A COMPREHENSIVE RESILIENCE FRAMEWORK FOR THE SEISMIC EVALUATION OF HYDRAULIC FILL DAMS IN NORTH TEXAS

by

SANTIAGO CABALLERO

Presented to the Faculty of the Graduate School of

The University of Texas at Arlington in Partial Fulfillment

of the Requirements

for the Degree of

DOCTOR OF PHILOSOPHY

THE UNIVERSITY OF TEXAS AT ARLINGTON

May 2017

Acknowledgements

The present work would not have been possible without the help and guidance of those involved, who provided valuable support, advice and assistance throughout this research work. First and foremost, I would like to offer my sincere gratitude to my advisor and mentor Dr. Anand Puppala, whose support, patient, advice and his exhaustive knowledge in geotechnical engineering were the main factors for the development of this work. A simple sentence is not enough to express my gratefulness to him because of his dedication and support to myself during my doctoral stay at UT Arlington. I extend a full honor the fact of working with him to develop the present comprehensive work.

I would like to thank my committee members and professors, Dr. Laureano Hoyos, Dr. Xinbao Yu and Dr. Shih-Ho Chao for their valuable academic contribution as well as their unconditional willingness to supervise this thesis work. Their extensive knowledge in all aspects of civil engineering aimed these work to be successful. I want to extend my special gratitude to Dr. Tejo V. Bheemasetti for his unconditional help, support and considerable advice to complete this research work. I would like to mention my advisor at CSU Fullerton, Dr. Binod Tiwari because of his continuous encouragement and support to pursue my doctoral degree.

Second and the greatest acknowledgement is extended to my parents, Patricia and Tarquino for their unconditional support, advice and daily blessings. I also want to thank my siblings, Andrea and Daniel for their never ending encouragement during this hard pathway. This work is dedicated to all of them and all my family in the United States and Ecuador for their vast support and love.

I would like to thank my friends and research co-workers at UT Arlington, Dr. Aravind Pedarla, Dr. Ujwalkumar Patil, Tom Taylor, Dr. Alejandro Pino, Dr. Raju Acharya, Dr. Pinit Ruttanaporamakul (Tom), Leila Mosadegh, Sayantan Chakraborty, Aritra

Banerjee, Nguyen Hai, Anu George, Rinu Samuels, Ali Shafikhani, He Shi (Dany), Jasaswee Das, Manikanta Saladhi, Sarat Congress, Puneet Bhaskar, Burak Boluk, Rice and Leopoldo Cardiel, for their constant support and help during my stay at UT Arlington. Also, a special dedication to my girlfriend Stefany for the unconditional support, love and strength and to all my friends and colleagues in Texas, California and Ecuador

Finally, I extend my acknowledgement to the entire faculty and staff in the Department of Civil Engineering at The University of Texas at Arlington for their exhaustive advice and suggestions during this career path. A special acknowledgement is extended to the Tarrant Regional Water District (TRWD) and its collaborators Louie Verreault and Dorota Koterba for financing this research project and for the extensive support and advice during the elaboration of this work.

March 31, 2017

Abstract

A COMPREHENSIVE RESILIENCE FRAMEWORK FOR THE SEISMIC EVALUATION OF HYDRAULIC FILL DAMS IN NORTH TEXAS

Santiago Caballero, PhD

The University of Texas at Arlington, 2016

Supervising Professor: Dr. Anand J. Puppala

Hydraulic filling is a construction procedure that was used for earthen structures during the mid-1800s to the early 1900s; however, dams and levees that were constructed by implementing this technique had a significant potential for geotechnical hazards. Historically, most of the failures of these structures were a result of the soil cyclic liquefaction phenomenon. This phenomenon occurs when excess pore water pressure develops during cyclic loading and causes loss of effective strength in the soil. The cyclic stress approach is one of the methods widely used to assess cyclic liquefaction; however, seismic parameters (loading conditions) and soil characterization (liquefaction resistance) must be characterized in a discreet and careful manner. The seismic resilience of hydraulic fill dams depend upon two main contributing factors which are the high variability of soil properties and the sudden increase of seismic activity in areas believed to have low seismicity (magnitude, location, and distance at which the earthquake occurs). Current slope stability and liquefaction analysis considers averaging the soil properties at a specific depth; they are considered as layered systems. However, such analysis is not suitable for hydraulic fill structures due to the high variability of the soil layers and the fact that failure can be triggered at any location within the structure.

Hence, a more rigorous approach is required for addressing the variability in soil properties and identifying potential liquefiable layers.

In this research study, a comprehensive seismic resilience framework for hydraulic fill dams was developed based on an enhanced soil characterization and 3D-visualization modeling using in-situ cone penetration testing and geotechnical borehole data. Eagle Mountain Dam located in Fort Worth, Texas was used for the present analysis. Geostatistics was used for modeling of the dam embankment section and these results are then used to assess liquefaction of dam embankment layers. Both deterministic and probabilistic hazard analyses using the recent earthquakes surrounding the test site are performed. Hypothetical scenarios based on source of seismicity, site-to-source distance, and focal depth of earthquakes were also assumed and analyzed. The cyclic liquefaction analysis showed that both deterministic and probabilistic analyses did not cause liquefaction of the layers in the current and natural field conditions. However, probabilistic analyses showed potential liquefaction of layers with an increase in the water elevations within the dam. This study can also be applied and used to evaluate liquefaction of similar structures where seismic activity has been either noted or expected.

Table of Contents

List of Illustrations

List of Tables

Chapter 1

Introduction

1.1 General Overview

Hydraulic fill construction procedures were commonly employed for building many earthen structures from the mid-1800s to the early 1900s. The methodology consists of generating an artificial fill composed of soils that are conveyed and deposited by hydraulic means (Valenzuela 2015). These fills are generally used to build construction platforms, to reclaim land, to generate beaches from the sea, and to build impoundment dams or levees. However, these types of structures are perceived negatively due to their history of failures associated with the original design. There is no specific date for the construction of the first hydraulic fill dam, but the methodology is associated with the construction of land reclamation dikes in the Netherlands (Hsu 1988) and with mining exploitation in California (Valenzuela 2015.)

Hydraulic systems enable large-scale extraction, transport, and placement of borrow soils in an economical manner (Valenzuela 2015.) However, the resilience and performance of several hydraulic fill dams and levees was affected by geotechnical failures that were due to unaccounted for factors in the design analysis (USNRC 1985). These failures are mainly attributed to the effects of seepage and liquefaction in seismically active areas. The difficulty of building the core, with respect to the shoulders, due to the variable contents of sand and fines in the borrowed material, generated a non-homogenous body after construction. A further difficulty of controlling the construction was that it allowed the sand material to slide from the shoulders towards the central core, introducing sand lenses into the “clayey” core, rendering it highly susceptible to liquefaction.

Over the past decades, several attempts have been made to analyze the cyclic liquefaction of hydraulic fill structures (Tezcan et al. 2001; Uddin and Baltz 2001; Bair et al. 2003). They were, however, performed based on spot-based measurements which did not consider the high variability of soil properties within the whole configuration of the dam or levee. It has been proven that the lack of incorporation of spatial variability within soil properties into the analysis resulted in a large number of uncertainties for geotechnical designs (Einstein and Baecher 1982; Laccasse and Nadim 1996).

Along with spatial variability, another important aspect of this analysis is to determine the appropriate seismic parameters, especially in low seismic areas, where some hydraulic fill structures are located in the United States. However, over the past eight years, some of the areas which were believed to be low seismic zones have experienced a sudden increase of seismic activity. The Central United States is such an area, and considerable seismic events, including some with high magnitudes (i.e., M5.8) have occurred in Oklahoma, Colorado, Arkansas, and Texas.

In November 2011, a sequence of earthquakes hit the area of Prague, OK (M 5.6 and three M > 4.0). Smaller events occurred in Texas (M3.6, Azle, TX 2013; M4.0 Venus, TX 2014; and M3.6 Irving, TX 2015). The main concern in the region is the lack of seismic hazard analyses for structures. Seismic hazard analyses are based on the known source of seismicity (i.e., commonly active faults). Only a few areas in central United States have developed a detailed mapping of faults so that the seismic hazard assessment for a site can be evaluated. In areas such as those in North Texas, where the increase of seismicity is evident, the lack of fault mapping makes the task of finding seismic sources more difficult.

Hence, it is vital to improve the geotechnical hazard assessments of existing old structures such as hydraulic fill dams and levees, considering both the high spatial variability within their configurations and developing a specific seismic hazard analysis for areas where no active faults have been encountered yet. In this research study, a comprehensive resilience framework based on soil characterization and 3D-visualization modeling was developed, using in-situ Cone Penetration Testing (CPT) data and Geostatistics tools. CPT results are further used to perform cyclic liquefaction assessment of hydraulic fill dam. The liquefaction analysis of these structures was complemented by integrating a seismic evaluation framework developed for the Central United States, using volumetric seismic sources that were based on the records obtained from the recent seismicity events in the region.

1.2 Research Objectives

The main objective of this research is to apply the principles of risk and reliability to assess the resilience of aging structures such as dams and levees. The principle of risk is associated with predicting the natural and man-made hazard events such as earthquakes, flooding and others. The reliability principles were applied to determine the realistic variation of soil properties by modeling the spatial variability using Geostatistics principles. These principles are then applied to assess the resiliency of an infrastructure. In this study, a comprehensive framework was developed to assess the resiliency of critical aging infrastructure such as dams by focusing on the liquefaction distress. In order to demonstrate the application of the framework, a hydraulic fill dam located in North Texas was considered as a prototype example for comprehensive analysis including risk based characterization of compacted dams and probabilistic seismic hazard analysis on

loading events. The following research tasks have been formulated for performing the above mentioned studies:

a) To develop a framework to assess the probabilistic seismic parameters based on previous and future seismic hazard events and specific site conditions in North Texas;
b) To develop a framework for soil characterization and to generate three dimensional (3D) visualization models of dams to identify the critical sections based on in-situ cone penetration testing measurements;
c) The incorporation of a) and b) for the comprehensive assessment of the liquefaction potential of dam structures.

As an attempt to demonstrate the developed approach, an analysis was performed on the Eagle Mountain Dam, a hydraulic fill dam structure located in North Texas. Extensive cone penetration soundings to borehole logs with laboratory tested soil parameters are available. This is presented along with available seismic records from USGS are used in performing the above specific tasks.

1.3 Thesis Organization

This thesis consists of six sections: Introduction (Chapter 1); Literature Review (Chapter 2); Formulation of a Simplified Seismic Hazard Analysis Framework for North Texas (Chapter 3); 3D Visualization in Geotechnical Engineering (Chapter 4); Liquefaction Evaluation of Eagle Mountain Lake Dam in Fort Worth, Texas based on 3D Visualization Models (Chapter 5); and Conclusions and Recommendations (Chapter 6).

Chapter 1 provides a general overview of hydraulic fill structures and their vulnerability to liquefaction in seismically active zones. The importance of soil

characterization of these structures is also highlighted, as is the necessity for using new visualization models to address soil variability when performing liquefaction assessments.

Chapter 2 includes a summary of the literature review pertaining to topics that are divided into several sub-chapters: A brief introduction of dams, Classification Types, Hydraulic Fill Dams, Geotechnical Hazards, Liquefaction analyses, and Seismic Hazards. A seismic hazard analysis is also introduced in this chapter, and includes basic concepts that will help in developing the seismic hazard analysis framework for North Texas. Finally, soil characterization and variability is included, with an explanation of uncertainties in geotechnical engineering, as well as descriptions of existing prediction models. A summary of 2D visualization models and technology is also highlighted to showcase the necessity of a 3D visualization for any geotechnical assessment.

Chapter 3 presents the steps required to develop a simplified seismic hazard analysis framework for North Texas. The generation of volumetric seismic sources, which plays an important role in assessing the seismic hazard parameters, is described, along with the final seismic hazard parameters.

Chapter 4 describes the methodology used to incorporate in-situ testing data to develop 3D visualization models, using Geostatistics. The in-situ test data available at a hydraulic fill structure located in North Texas was considered in this study to demonstrate that the 3D visualization model assesses the variability in soils and replicates the most appropriate field conditions.

Chapter 5 presents the liquefaction assessment of a hydraulic fill dam located in North Texas. This was performed by incorporating the seismic hazard analysis generated in Chapter 3 and the 3D visualization models and soil characterization developed in Chapter 4.

Chapter 6 summarizes the research, cites conclusions, offers recommendations for future research and define certain limitations of the framework presented.

Chapter 2

Literature Review

2.1 Introduction: Dams

Dams are structures built for water retention; flood control, recreational facilities, electricity generation, and a water supply source for irrigation purposes, drinking water, and other public facilities (Sharma 1991). They provide several societal, economic, and environmental benefits. Hence, their failure can be catastrophic, resulting in property loss and serious threat to different species of living beings. Dams are classified by three hazard levels: low, significant, and high (FEMA 2005). Most dams are considered to have low hazard potential because their failure does not cause any loss of human life. However, if the failure of the dam causes significant economic loss without loss of human life, it is considered a significant hazard. A high hazard classification refers to the probable loss of human life, economic loss, and harm to the environment.

According to the U.S. Army Corps of Engineers (National Inventory of Dams), there are approximately 91,000 dams in the United States, including some which were constructed before 1900 (USACE 2017). Of these, almost 28,000 dams are classified as having a high or significant hazard potential. According to the Association of State Dam Safety Officials, from January 1st, 2005 through June 2013, 173 dam failures and 587 incidents were reported (ASDSO 2017). Some of these were attributed to an inaccurate design or faulty construction process; others were a consequence of poor maintenance or inadequate operation. However, many of these failures resulted from unanticipated large floods and from intense earthquake tremors. In an effort to increase the resiliency of

these structures, over the past century, the design, construction, and maintenance of them have dramatically evolved.

The US Department of the Interior's Bureau of Reclamation has played a key role in the evolution of the design, construction, and safety of dams (Wiltshire 2002). Dams are subcategorized into different classes, according to the use of the dam, its hydraulic design, and the construction methodologies implemented (Wiltshire 2002).

Storage, diversion, and detention are the three main classification systems of dams based on their usage. Storage dams are constructed to retain water, over a long period of time, and serve as the water supply source for cities. Diversion dams are constructed to dodge water into ditches, canals, or other similar systems. Other dams are constructed as detention structures that control flood or runoff to minimize the effects of sudden floods (Wiltshire 2002). Dams can be also subdivided by their hydraulic design, and some are commonly called overflow dams, because they carry some discharge through spillways or over their crests. But the most common classification system is based on the materials used for the construction of the structure: concrete dams and earthen dams. The selection of a concrete dam or an earthen dam, rock-fill dam, or any other type depends on several factors which are presented in the following sections.

2.2 Factors Governing Selection of Dam Type

Dam projects, like any other civil engineering project, require special attention during the early stages of planning and design, including the selection of the site and type of dam. It requires special cooperation and coordination among experts from different disciplines such as, but not limited to, planners, geologists, hydrologists, and geotechnical and structural engineers to ensure the most adequate and economical design. According to the Manual of Small Dams (USDI 1987), several factors affect the

final selection of the type of dam, such as the protection of the spillway discharges, limitations of outlet works, the difficulty of diverting the stream during construction, availability of construction equipment and materials, the accessibility to the site, and physical characteristics of the site. It is important to have a good understanding of the characteristics of the site in order to evaluate its safety and to perform geotechnical assessment of existing dams. Therefore, this section presents an overview of the physical factors important to the selection of the type of dam and to being able to understand the potential problems during its operation.

2.2.1 Topography

The topography of the site plays a vital role in the selection of the dam. It includes the surface configuration of the site and the reservoir area, as well as the accessibility and availability of construction materials. In general, three rules for topography can be addressed when selecting the dam type: a) A narrow U-shaped valley (i.e., a narrow stream flowing between high rock walls) suggests a concrete overflow dam; b) An earth fill dam with separate spillways is suitable for low plain country; and c) A narrow V-shaped valley indicates the need for an arch dam.

Following the suggestions described, embankment dams can be built in almost any topography, although they are not constructed often in narrow canyons with steep abutments. A series of problems can be addressed when constructing earth fill dams in narrow canyons, such as the location of a spillway and the lack of availability of materials for its construction. However, there has been an increase in the construction of embankment dams in narrow valleys (Sharma 1991); several examples are the Esmeralda Dam and the Guavio Dam, both located in Colombia. The Esmeralda dam was built in a narrow V-shaped valley with a height of 237 m and a crest length ratio of 1

to 3. The Guavio Dam presented in Figure 2-5 is 264 m in height and is located over a similar topography (V-shaped valley).

Figure 2-1 Guavio earthen dam (Hydro Colombia Records)

2.2.2 Geology and Foundation Conditions

The foundation geology at the project site dictates the most suitable type of dam for that site. Earth fill or rock-fill dams can be built on any type of foundation since its long-term stability and operation directly depends on the construction material used; however, several considerations need to be addressed. The U.S. Bureau of Reclamation (USDI 1987) recommended several recommendations for classification of foundation soils for dams, based on their features and characteristics. The following sections present different foundation conditions and their effects on earthen dams.

2.2.2.1 Rock Foundations

If a solid rock foundation is present, the construction of any type of dam is acceptable due to its high bearing capacity and resistance against erosion and

percolation or seepage (USDI 1987). However, clayey shale, sandstones, or weathered basalt are considered unacceptable for the construction of high earth fill or rock-fill dams. The identification of shear zones or faults in the rock is a key factor that may lead to changing the dam type. Defects in the bedrock, such as shear zones or faults, affect the weathering, depths, slope stability, and seepage in high earth-fill dams.

2.2.2.2 Gravel or Alluvial Foundations

Well-compacted granular materials are usually able to withstand an embankment dam (USDI 1987). However, due to the high permeability of this material, several seepage problems might be encountered, and adequate seepage control must be provided, such as cut-off walls or seals.

2.2.2.3 Silt or Fine Sands

This category of soils can be suitable as foundations for low-height concrete gravity dams and some earth-fill dams, if they are properly designed, but they are not usually suitable for rock-fill dams (Kollgaard et al. 1988). Several problems might be encountered, such as non-uniform settlements, potential soil liquefaction or collapse upon saturation, uplift forces, piping, excessive percolation losses, and protection at the downstream toe from erosion (USDI 1987). If site stratigraphy is found to be composed of these type of materials, then it may be necessary to remove them, if economically feasible, or to improve them by artificial means such as vibro-compaction or heavy tamping techniques (Sharma 1991).

2.2.2.4 Clay Foundations

Clayey soils are suitable as foundation soil for embankment dams. However, careful consideration should be given to engineering properties, such as shear strength, permeability, mineralogy, and stress history. Due to the relative low strength of clayey

soils compared to rocks and other materials, relatively flat embankment slopes should be constructed, which greatly impacts the economy of the project. Concrete dams are not recommended for clayey foundations due to their heavy weight, which results in consolidation settlement. Several solutions can be provided to accelerate the consolidation of clayey foundation soils, such as vertical and horizontal drainage systems or blankets.

2.2.3 Availability of Materials

The availability of materials plays a vital role in governing the economy and performance of the project. The most economical type of dam is usually selected as the one for which a large amount of materials can be found within a reasonable distance from the project site. For a concrete structure, for example, the availability of suitable and high-quality sand and gravel is required. In the late 1800s and early 1900s, when construction equipment and technology were not properly developed yet, the availability of materials was one of the key factors in selecting the dam type.

Several embankment dams were constructed, using soil borrowed from sites, by transporting and compacting it, using hydraulic procedures (i.e., hydraulic fill dams). One of the objectives of this research is to address the origin of the hydraulic fill process and to attain a thorough understanding of the potential problems associated with it during its operation under external loading (i.e., seepage forces, earthquakes). Hydraulic fill structures were developed mainly due to the lack of materials locally and the constraints of construction and compaction equipment in that age. The following section describes in detail the configuration of embankment dams, specifically those constructed using the hydraulic fill procedure.

2.2.4 Spillway Location

The cost involved in the construction of a spillway is frequently a considerable portion of the total cost of a dam project. The size, type, and natural restrictions of its location are the controlling factors in the selection of the type of dam (USDI 1987). Some recommendations can be addressed based on the type of spillway used during the development of embankment dams. Generally, there are two types of spillways used with embankments. The “chute” type is most frequently used, and is constructed by excavating in one of the abutments (Sharma 1991). This type of spillway involves a lot of excavation, and the cost involved in its construction plays a key role in the selection of the type of dam.

The tunnel type is the other spillway that is used if a suitable site for a chute spillway is not available. Most of the time, when the topography presents a wide valley, a composite type of dam can used, with a concrete overflow spillway and an embankment dam as the main support of the reservoir. However, the practice of building overflow concrete spillways and earth-fill or rock-fill dams has generally been discouraged due to the conservative design assumptions, as well as the potential failures associated with it.

2.2.5 Earthquake (EQ) Prone Areas

Depending on the site of the project, which can lie in active seismic areas, earthquake considerations must be taken into account in the selection of the type of dam. This is especially true for dams constructed using hydraulic filling, where the liquefaction of soils has been reported (Wiltshire 2002; Seed et al. 1973). The design analyses should account for all of the expected or hypothetical scenarios, irrespective of dam type. Earthquake design considerations have been developed over last few decades, based on increasing research and what has been learned from historic failures. They play a key

role in the selection of the dam type, especially for those located in high seismic zones or areas.

2.2.6 Various Factors

Several other important factors, such as river diversion and/or the time available for construction, affect the selection of dam type. River diversion may affect both the location and cross section of the dam since some topography may be better suited for the construction of diversion tunnels or coffer dams. The cost of the project can be minimized by incorporating the upstream and downstream coffer dams in the shells of the dam section (Sharma 1991).

The time available for the construction is another important factor in the selection of the type of dam. The most economical dam is constructed by excavating and placing soil materials for its configuration. However, with limited construction time and the non-availability of materials, the designer may have to consider changing the dam type. On the other hand, if the embankment is constructed quickly, the pore pressure during construction might be an issue where slopes must be flatter or horizontal drainage must be provided to dissipate the pressure within the embankment.

Another important factor is the possibility of increasing the height of the dam in the future. When an embankment dam needs to be extended slightly, the new core is tied to existing structure; however, when the height increase is large, it is more economical to construct a new core section. This step is important due to the seepage problems that designers may encounter after their construction. Inclined core dams are more suitable than vertical core dams and present fewer problems.

The selection of the type of dam is governed by all of the factors discussed above. The following section provides a brief review of the different types of dams, with special attention paid to the earthen and rock-fill embankment dams.

2.3 Concrete Dams

Historically, concrete is the most common and strongest material used for the construction of many civil engineering projects. The design and construction of a concrete dam is expensive, and it is not always the most suitable option; however, depending on the use and the size of dams, concrete material results are often optimal. The construction of concrete dams introduced the concept of RCC (roller-compacted concrete), which has been developed and implemented over time (Kollgaard et al. 1988). Several types of concrete dams can be found in the literature, and their selection depends upon several factors explained in the following sections.

According to the US Army Corps of Engineers, gravity dams are solid concrete structures that maintain their stability from their geometric shape and the mass and strength of concrete (USACE 1995). Topography of the site is a key factor when selecting this type of dam, since they are generally constructed on a straight axis, although they can be slightly curved to accommodate site conditions.

The Manual of Small Dams Design developed by the United States Bureau of Reclamation (USBR) states that the construction of gravity dams is more acceptable for those sites where there is a sound rock foundation (USDI 1987). However, low-height structures may also be built on alluvial foundations, by providing reasonable cutoffs. Most often, gravity dams are used as overflow spillways for earth-fill and rock-fill dams (Figure 2-2), or as overflow sections of diversion dams.

Figure 2-2 Concrete gravity dam (Northern Water Conservancy District Records)

Concrete arch dams are dams suitable for special topography sites and for locations where the foundation at the abutments is composed of solid rock , which resists the arch thrust (USDI 1987). The stability of an arch dam is obtained by self-weight from the concrete material and by transmitting the loads of the arch shape into the abutments. Therefore, the geometry of the dam site is the most basic consideration in the selection of an arch dam (USACE 1994). The USACE also presents the importance of having strong abutments as a requirement for a site where an arch dam is to be constructed. However, it suggests that artificial abutments (i.e., thrust blocks) may be built in the absence of strong abutments. Figure 2-2 represents the single-arch and multiple-arch dams.

(a) (b)

Figure 2-3 (a) Single-arch design (Roosevelt dam - Phoenix, AZ): (b) Multiple-arch design (Bartlett dam - Phoenix, AZ) (USBR Records 2016)

Buttress dams are a special category of concrete dam. Unlike arch dams which have an arch shape on the upstream side of the structure, buttress dams have a flat deck and multiple arch structures as supports on the downstream side of the dam (Figure 2-4). Due to the shape of this structure, it requires about 60 percent less concrete than solid gravity dams; however, there is a significant increase of formwork and reinforcement steel required for construction of these dams.

Figure 2-4 Daniel Johnson Dam: Buttress dam in Quebec, Canada (Hydro-Quebec Records)

2.4 Embankment Dams

Embankment dams are constructed of earthen materials such as clay, silt, sand, and rock or gravel (Kollgaard et al. 1988). The term embankment dams includes both earth-filled and rock-filled dams, as well as a combination of the two (Sharma 1991). Earth-fill or rock-fill dams are the dams built most often, because of their low construction costs and adaptability to different geological conditions (Sharma 1991; Kollgaard et al. 1988). However, they are more susceptible than concrete dams to damage under different loading conditions from pore water pressures, flooding, seismic forces, and any human-induced forces.

In the United States, there are approximately 91,000 active dams, of which 79,000 are embankment dams (USACE 2017). Approximately, 28,000 earthen dams are considered to have “high” or “significant” hazard potential, and almost 50% are old structures, constructed from the mid-1800s to early 1900s. Figure 2-5 shows a schematic of the classification of dams briefly explained in this section.

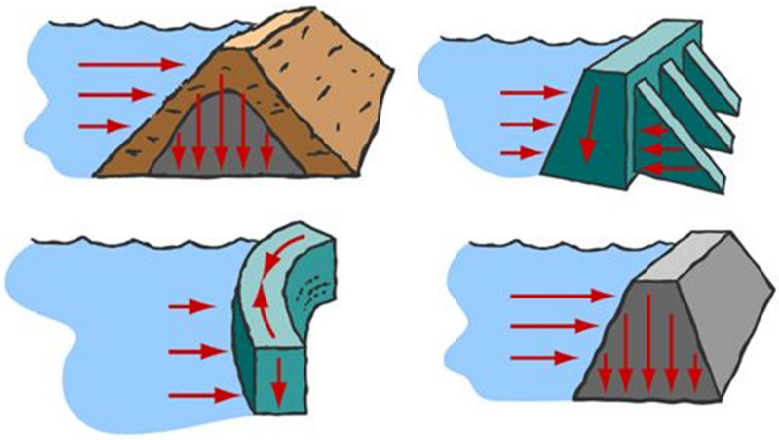

Figure 2-5 Clockwise from left top: Embankment dam, buttress dam, gravity dam and arch dam (Source: ASCE Ville 2016)

The popularity of earth-fill dams primarily resulted from three conditions: They can be constructed on top of any foundation system, they can be constructed using locally available soils, and they are more economical than either concrete or rock-fill dams. Another key aspect of why earthen dams are popular is that a properly designed earth-fill dam can be constructed on almost any site, as opposed to the stringent site limitations associated with concrete dams (Wiltshire 2002). This section presents information on earthen dams such as the history of their construction, the methodology used, and the stratigraphy configuration after their construction. A thorough understanding of these topics provides a better background for assessing the resiliency of these structures when they are subjected to various natural and man-made hazards.

The beginning of embankment dam construction, for both earth-fill and rock-fill dams, is primarily attributed to the needs of primitive civilizations (Wiltshire 2002). Several authors have compiled the history of dam evolution, and they found that the earliest documented dams were located in what is now Jordan (Billington et al. 2005). Figure 2-6 shows the earliest known design and construction of the Sadd el-Kafara embankment dam in Egypt, around 2900 B.C (Wilsthire 2002).

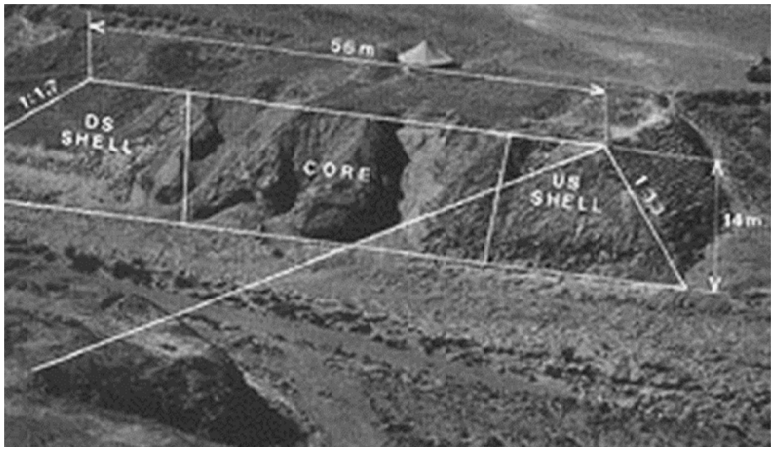

Figure 2-6 Sadd el-Kafara Dam in Egypt (Schnitter 1998)

The early use of embankment dams is reported in many countries, including India, China, and Iraq (Wiltshire, 2002). In North America, the Hohokam Indians began the construction of diversion works and canals along the Salt and Gila Rivers in Arizona in 300 B.C. The height of embankments gradually increased with time and experience, reaching a maximum of 79 ft. height. In the earliest dam project, 43 ft. was the maximum height for masonry dams. Earthen dams were constructed in six different ways: homogenous dams; an embankment with a central core of puddle (clay core); an embankment with the central core of masonry concrete; an embankment with puddle placed on its water face; an embankment of earth resisting an embankment of loose rock; and an embankment of earth, sand, and gravel sluiced into position by flowing water (hydraulic fill) (Wilson and Squier 1969).

In discussing the development of earthen dams engineering, it is necessary to understand basic design considerations that lead to a better assessment of geotechnical hazards of this type of structure. Several subsections can be defined such as layout, foundation conditions, materials for construction, cross sections, construction methods, site investigations, laboratory investigations, soil mechanics analyses, instrumentation, construction control, and monitoring. The following sections provide a brief overview of some of the key aspects of earthen dams that are limited to cross sections, materials, and construction methodologies used for old earth-fill dams.

2.4.1 Typical Cross Sections

The typical cross sections on earthen dams can be subdivided in two categories: homogenous dams and zoned dams. A homogenous dam, as the name implies, is built entirely of one type of material (except for slope protection) which should be sufficiently impervious to provide a proper seepage through the whole body of the dam. The soil

should also develop adequate shear strength after compaction and maintain most of its saturation after filling the reservoir (Sharma 1991). This type of earthen dam is usually constructed when only one material is locally available; however, due to the expected seepage at the downstream slope of the dam, additional seepage controls, such as a rock toe at the downstream, a foundation, blanket, or chimney drain are required, as shown in Figure 2-7.

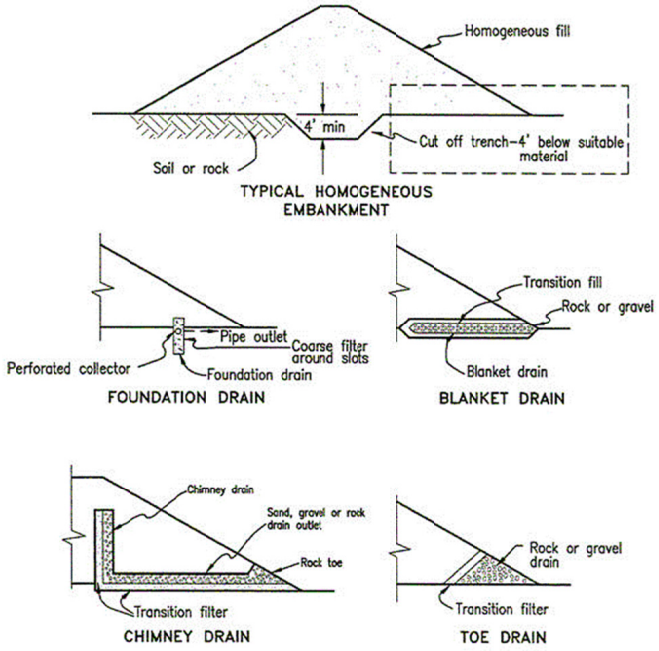

Figure 2-7 Homogeneous earthen dams with seepage controls

(USDA, Engineering Field Manual)

Unlike the homogenous earthen dam, a zoned earthen dam is designed using different materials or soils. The configuration of earth-fill dams consists of a central or sloping impervious core, as the impervious element, and the outer shells of pervious material to provide stability. This sort of construction is inevitable in the absence of homogeneous soil layers. Extreme care is required for these structures, especially with

regard to material variability, which can highly impact the performance of the structure. Several configurations of zoned earthen dams are shown in Figure 2-8. Despite the type of earthen dam selected, the materials that form their configuration play a key role in their overall future performance and are discussed in the next section.

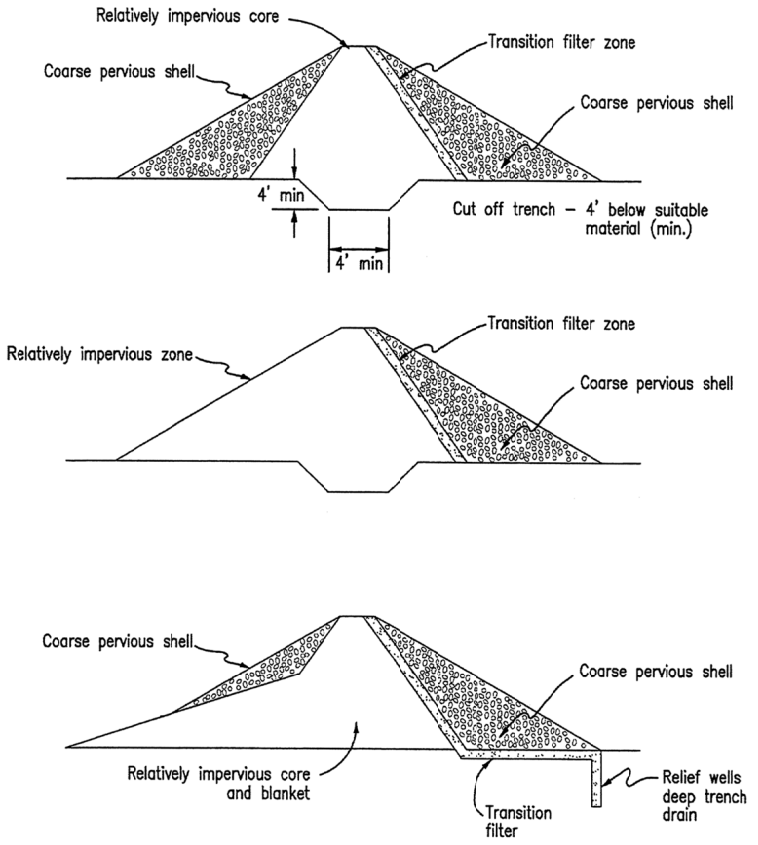

Figure 2-8 Zoned earthen dams (USDA, Engineering Field Manual)

2.4.2 Materials for Construction

The materials for the construction of earth-fill dams usually come from excavations or from borrow areas located reasonable distances from the project site. As discussed in previous sections, the selection of an ideal impervious material, whether it is coming from the excavation or from a borrow pit, is the main target for constructing any

type of earthen dam. Soils have infinite combinations of size, gradation, composition, and variation of properties, and their suitability is determined by performing laboratory tests.

2.4.2.1 Core Material: Impervious Materials

The core material, impervious in nature, may vary from clay soils of high plasticity to very well-graded materials of glacial till type with low plasticity (Lowe III 1970); (Kollgaard et al. 1988). These materials are preferred over silty sands and fine sands, where the seepage of water likely results in dam failure (Sharma 1991). Hence, a well-graded mixture of soils is suitable for ensuring both imperviousness and self-healing. In practice, a wide variety of soils, ranging from clays, silts, and fine granular soils with some silt to coarse-grained soils (i.e., glacial tills) have been used as the core of embankment dams (Sharma 1991).

In conclusion, the principal role of core material in an earthen dam is to provide imperviousness (Sherards and Dunnigan 1985). The basic design concept is more concerned with providing resistance to erosion against potential piping issues. Other control actions can be more suitable for controlling localized seepage, such as the construction of a filter downstream of the core (Sharma 1991; USDI 2012; Lowe III 1970).

2.4.2.2 Material for Shells in Zoned Earth-fill Dams

Zoned earth-fill dams are usually constructed in areas where several soil types are available, such as clays, silts, sands, gravels, and rock. Zoned embankments have the advantage of using all of the different native materials to their advantage in different components of the dam. The impervious core is flanked by transition zones; downstream filters; and drains; and the outer zones, named shells, are basically composed of gravel; rock; or random fill, which is considerably stronger than the core material.

The main purpose of shells is to provide stability for both downstream and upstream slopes of the dam. The upstream pervious zone has to be properly designed to provide protection against internal erosion or washout of the core during rapid drawdown (Sharma 1991). The downstream pervious zone serves as the filter, drain control of seepage, and leakage barrier, and prevents sediment transport through any cracks in the central impervious core.

Figure 2-9 presents a zoned earthen dam, where a coarse pervious shell was used. The material (i.e., clean sand, gravel, and cobbles, as at Oroville Dam in California, Figure 2-10) for the upstream shell should be free-draining; therefore, a coarse-grained material is desired to avoid liquefaction during earthquake events and slope stability issues during rapid drawdowns. The downstream shell of the dam is not expected to be saturated or subjected to drawdown. Several types of materials can be used, such as rock fill or gravel and cobbles, or top soil and seeding, which can function as filters and drain control seepage systems.

Figure 2-9 Eagle Mountain Dam, Fort Worth Texas USA (TRWD Records)

Figure 2-10 Oroville Dam, California (Source: Water Education Foundation)

Figure 2-11 shows an example of the difference in materials utilized on both downstream and upstream slopes in the Tinajones Dam in Peru. The latest special considerations of the materials for the construction of earthen dams can be found in the national standards developed by the U.S. Department of the Interior, Bureau of Reclamation (USDI 2012).

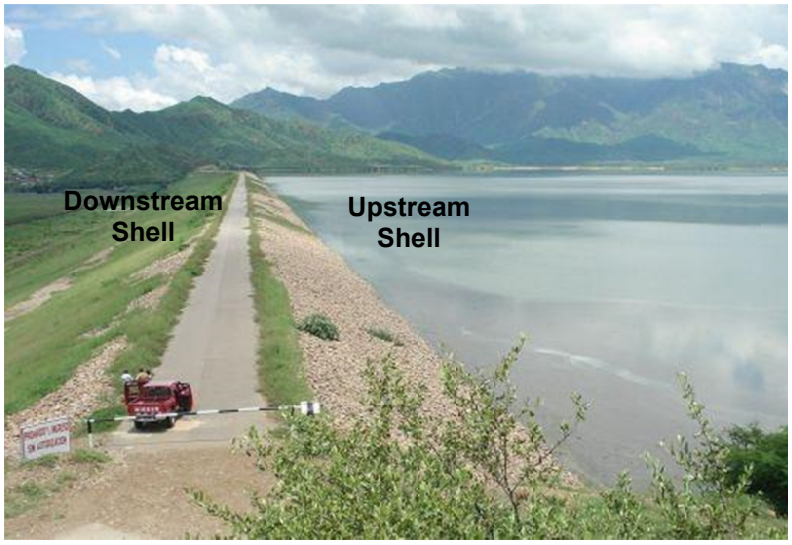

Figure 2-11 Tinajones Dam, Peru (Source: El Comercio, Peru 2016)

Since homogenous earthen dams are mainly constructed of only one impervious material, the construction methodology used does not affect the final configuration of the dam. For zoned earthen dams, where several materials are used for their construction, the placement of selected materials plays an important role in obtaining a configuration of the structure. Hence, the construction methodology plays a key role in evaluating the actual configuration of the dam structure, which impacts the geotechnical stability analyses. The following section presents the construction methodologies used for construction of an earth-fill dam.

2.4.3 Construction Methodology

The objective of this section is to describe the methodology used for the construction of earth-fill structures built during the late 1800s and the early 1900s (Valenzuela 2015). The construction methodologies of modern earth-fill and rock-fill embankment dams are far more sophisticated today than they were more than 100 years ago (USDA). During gold rush times, approximately in the 1850s, the lack of construction equipment was the main problem; therefore, the placement of soil for the development of tailing dams was performed by hydraulic means, which was the easiest way to construct embankments (i.e., hydraulic fill) (Kollgaard et al. 1988).

Over time, the traditional construction methodologies used in mid-19th century for mining (i.e., tailing dams) were slowly adapted to build storage earthen dams and reservoirs. A hydraulic fill procedure was adopted to construct several dams in the United States during the mid-19th century. For example, a zoned earthen dam, using hydraulic fill methodology, consists of depositing soils by hydraulic means: the silt and clay soils toward the center (core) and the sand and gravel in upstream and downstream sides to form shells. On the other hand, several other structures were constructed using

traditional compaction procedures, using the available primitive tools for compaction (Wiltshire 2002). These construction methods involved the use of horses or mules, drawn scrapers for excavation, as stated by Kollgaard and Chadwick (1988). The use of primitive tools for compaction was soon replaced by steam-powered shovels and steam locomotives. Compaction equipment evolved dramatically after World War I, with the inventions of gasoline and diesel. The increase of power and size of equipment made it more feasible to construct larger and higher dams (Kollgaard et al. 1988).

By the mid-20th century, dams for storage purposes were built using both hydraulic fill procedures and rolled compaction. However, the main challenge for the government agencies and engineers was not the construction of dams, but the safety of those already constructed. Several government agencies developed safety guidelines and procedures to ensure the safety and performance of existing dams, and the assessment of those still is a big concern. This research study focusses on hydraulic fill dams; hence, the following section provides more detailed information about hydraulic fill structures to facilitate a better understanding of the influence of this methodology on the performance of existing dams.

2.5 Hydraulic Fill Dams

The hydraulic fill procedure consists of generating an artificial fill composed of soils that are conveyed and deposited by hydraulic means (Valenzuela 2015). The basic principle of the methodology is to transform a constant fluid out of borrows, through pipes or sluice-ways. Soils are deposited to the corresponding dam section (i.e., zoned earthen dams) where they are separated into fines and coarse materials due to a sedimentation process that generates a self-compaction effect. The distribution of soil solids, methodology for placement of materials, water content, and compaction are considered

some of the most important variables that affects the construction of earth-fill embankments.

2.5.1 History of Hydraulic Fill Dams in the United States

The land reclamation dikes in the Netherlands are believed to be the first hydraulic structures that were constructed (Hsu 1988). Extensive hydraulic mining in the United States, followed by the discovery of gold in California in 1849, led to the utilization of the hydraulic fill procedure for the construction of dams. The hydraulic fill procedure provided a fast large-scale extraction, transport and placement of borrow soils in an economical manner (Valenzuela 2015). During the early 1900s, several dam projects using the hydraulic filling procedure were planned and executed in the United States.

The U.S. Army Corps of Engineers have first constructed important embankment projects in the United States by using this methodology and other compaction methods (Wiltshire 2002). The Van Noman Dam in California (Lower San Fernando Dam) and the Fort Peck Dam, along the Missouri River, were constructed between 1912 and 1915, using hydraulic filling (Figure 2-12). The lack of clear understanding of soil strength and implications from construction methodology resulted in massive slope failures in the Fort Peck Dam (Figure 2-13). The design criteria for the construction of these structures was based on the available concepts and guidelines (Schuyler 1907; Hazen 1920; Pail 1922; Holmes 1921).

Figure 2-12 Fort Peck Dam before the slide (U.S. Army Corps Records)

Figure 2-13 Slide occurred in Fort Peck Dam, Missouri (U.S. Army Corps Records)

2.5.2 Concept and Methodology

The basic objective of the hydraulic fill methodology in zoned earthen dams is to accommodate soils in the way that pervious material shells provide stability and drainage to the interior fluid mass of the soil (Sharma 1991). Initially, the core (impervious material) is in a fluid state and receives support and stability from the shells (pervious material). By sedimentation or gradual settlement following drainage, it becomes a solid mass capable of resisting water pressure from the reservoir. The methodology initiates with the excavation of materials, dredging with hydraulic giants, or drying by using a hog box. The methodology for excavation is selected based upon the cohesion of the soil, as well as the topography of the site. Shortly after the excavation, materials are transported in suspension, using different pipelines. Water and soil mixtures typically have 10-20% solids by volume or 25-50% solids by weight (Sowers and Sally 1962).

A schematic of hydraulic fill methodology for zoned earthen dams is shown in Figure 2-14. The filling starts by depositing the soil into two dikes located parallel to each other (starting dikes) which can be placed at or barely on the inner side of embankment toes, as illustrated in Figure 2-14(a). They commonly are the final and permanent rock toes which can also be constructed of rolled pervious soil. The pipelines, known as beach pipes are shortly after placed on top of the dikes which can be carried on low trestles above them as well. Several adjacent outlets are placed between dikes that allow the discharge of mixtures. Coarse materials settle close to the discharge points (forming shell), while the fine soils are carried to the center, still in suspension. A “pool” is generated between the “beaches” or shells just formed. Due the rate of sedimentation which is much lower for finer soils, the core level is below the beach level or outer side of shells, as shown in Figure 2-14 (a),

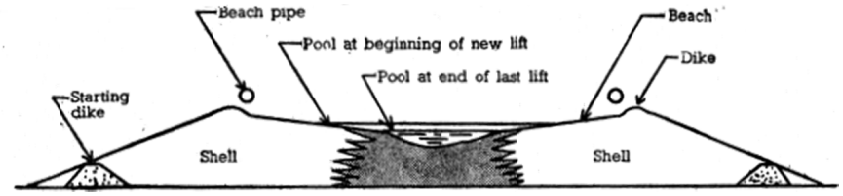

(a)

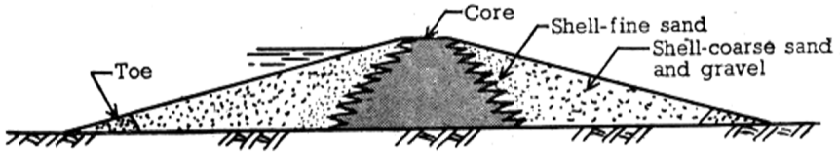

(b)

Figure 2-14 Hydraulic fill methodology: (a) Elements of H.F. and (b) Final configuration (Sowers and Sally 1962)

An important consideration is that the width of the core is constrained by the percentage of fines of the soil collected from borrow site as well as by the level of water in the core pool. After the placement of 3 to 6 ft., the level in the core pool is elevated producing a width slightly greater than the top limit of core in the shell. The filling process starts when coarser soils settle on the beach above the pool and intrudes into the pool limits. As soon as the beach gets elevated, the core pool narrows and deepens. The filling process stops after the pool width is slightly close to the minimum permissible core width given by the designer. The effect of this sedimentation process results into a core zone with jagged edges, as illustrated in Figure 2-14 (shadow zone).

It is expected that shells will not display the initial design dam shape due to variation of the deposition with the distance from the outlet. Therefore, a series of draglines are located on the outer edges of the shell to recover the initial dimensions of the dam defined on the design. The process is repeated as necessary to reach the desired height of the dam, and a pair of new dikes can be constructed if needed. Figure

2-15 shows a sketch of a typical cross-section of a hydraulic fill dam (a), and a case in which dredged material was used (b).

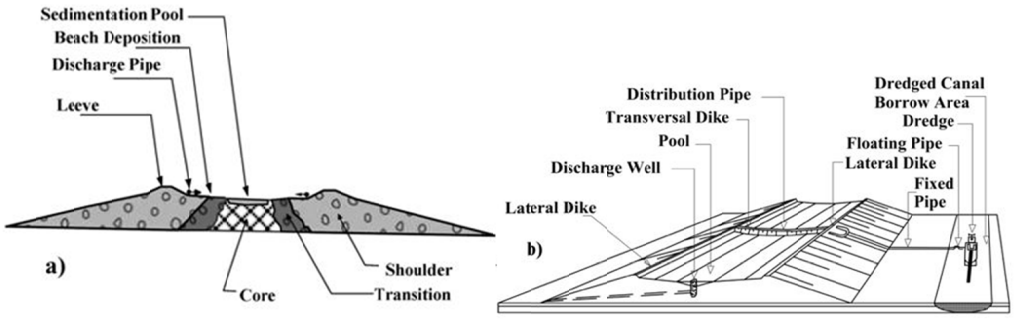

(a) (b)

Figure 2-15 (a) Typical section of a hydraulic fill dam; (b) Hydraulic fill and dredge perspective (Valenzuela 2015)

Several issues can arise during the hydraulic filling construction process. The jagged edges of the core or fingers can extend into the shell beyond established limits, which means that they must be cleared away by digging them out to be replaced with shell material. Similarly, the area where shell material falls within the core are likewise critical for the final configuration of the dam. Materials of shells can be displaced by slides due to a very deep core pool or due to the result of the fines content available in the borrowed soil being too small. If this issue occurs, a small hydraulic dredge can be used to excavate the core material and transport the mix back into the core pool to allow the coarse material to be widely dispersed again. However, performing this process that consists on reconfiguring the shell will also tend to minimize the loose structure which constitutes potential sources of failures and are a high hazard in hydraulic dam construction.

The San Pablo Dam in California was built between 1916 and 1920 as a 174 ft. high (maximum) hydraulic fill structure (Figure 2-16). The dam is still in operation, but it has undergone several modifications to reinforce the structure and to satisfy stricter design and acceptability criteria.

Figure 2-16 Construction of the San Pablo Dam, California (Bialek et al. 2007, Mitchell 2014)

The Fort Peck Dam in Missouri (Figure 2-12 and Figure 2-13) is another classic example of a hydraulic fill structure. The Van Norman Dam (Lower San Fernando Valley) in California is also a hydraulic fill that set a precedent for the development of guidelines for construction and safety in dam construction. Its failure after an earthquake event (M~6.8) in 1971 reinforced the perception that hydraulic fill dams are vulnerable to failures. A retrospective view of the development of hydraulic fill dams to serve as water reservoirs is of interest because their geotechnical performance is currently a concern among federal and state agencies. Their extensive use for dam construction in the late 1800s and early 1900s and their propensity for geotechnical failures over the past century are the main reasons that engineers want to adopt new methodologies to understand the complex soil configuration within this type of dam. A key component of a seismic resilient hydraulic fill structure is to have a robust framework that includes an

enhanced soil characterization with a proper characterization of external loadings (i.e., earthquake hazard) that potentially arrest geotechnical hazards in this type of structures.

2.5.3 Geotechnical Hazards in Hydraulic Fill Structures

The construction of an impoundment or a water diversion structure poses a high potential hazard to public safety in the event of failure (Lowe III 1970). Dam safety regulations have been developed over decades to identify potential hazards and minimize their effects to acceptable levels. These regulations and practices apply to all type of dams; however, embankment dams have more severe hazards than concrete dams due to their inherent variability of soil layers (USDI 1983).

In the United States, dam safety regulations vary significantly from state to state. However, in general, the safety requirements are tied to dam hazard classifications, according to the region or site of the project. According to the Manual of Risk Prioritization Tool for Dams (URS 2008), dam hazard classifications vary between the states but generally include three levels, based on estimated loss of life and whether the downstream damage is low, significant, or high. Figure 2-17 presents the total number of dams that are classified in each hazard category.

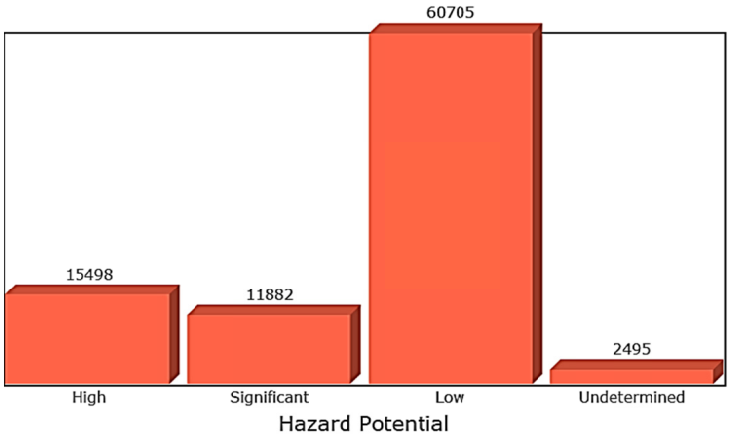

Figure 2-17 Dams by Hazard Potential in the US (National Inventory of Dams 2016)

From Figure 2-17, it can be observed that approximately 15,498 dams are classified as having “high” hazard potential. The National Inventory of Dams does not specify which dams are earthen structures; however, based on their classifications, there are approximately 78,000 earthen dams in the United States, which is 86% of the total number of dams in the United States (Figure 2-18). Therefore, the majority of “high” and “significant” hazard dams are earthen dams (homogenous or zoned earth-fill dams).

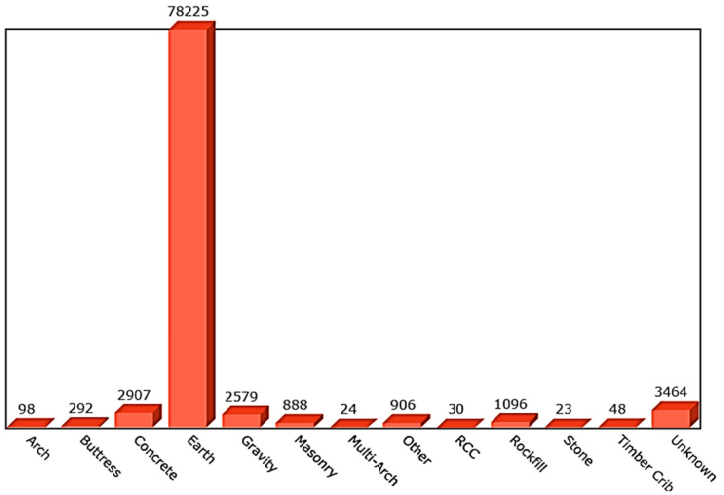

Figure 2-18 Number of Dams by type in the US (National Inventory of Dams 2016)

Another important fact to consider is the age of the “high” and “significant” hazard dams. The NID does not quantify structures which are considered old (i.e., late 1800s and early 1900s construction dates). However, several dams constructed in the late 1800s and early 1900s are still active and have been either replaced or significantly rehabilitated in order to ensure their full performance and operation. Aging earth-fill structures require a more complex assessment than conventional approaches to determine the safety factors. Over the past century, the vulnerability of hydraulic fill dams to failures was demonstrated by several historic failures. For earthen dams, hazards can be sorted depending upon the failure mode, such as piping or internal erosion, slope

stability, seepage failures, and global stability. Some of the areas to be revised are the ability to safely pass flood runoff without overtopping the embankment, control of seepage to prevent piping of materials, and the control of pore pressures within the embankment due to unexpected loadings (i.e., earthquakes or soil strength loss). This research is limited to those hazards (i.e., earthquakes) or physical mechanisms generated by failure modes that are more likely applicable to hydraulic fill structures.

A large number of hydraulic fill dams failed during strong seismic events (earthquakes) or due to numerous uncertainties that were not accounted for in the analyses. The instability of a dam could be caused by either static or dynamic loading. Static loading refers to the performance of the structure under construction with normal operating conditions (i.e., placement of soil layers, filling and emptying the reservoir, and constant seepage). Dynamic loading refers to those produced from earthquakes, pile driving, and geophysical exploration and blasting. Several hazards can be addressed, depending on the type of loading. The following sections present the most common failures that are associated with earthen dams, especially hydraulic fill dams.

2.5.3.1 Internal Erosion

The instability of a dam due to internal erosion usually occurs under static loading (i.e., normal operation) and is primarily caused by several problems, such as the construction materials, poor quality control during construction, lack of maintenance, or a change in the hydrological and environmental conditions. It is a progressive process that initiates by suffusion and induces additional hazards (Wan 2006). In hydraulic fill structures, a really complex configuration of soils is developed due to the construction process. There is a high degree of variability in the configuration of hydraulic fill dams, and soil materials fall into a broad particle-size range (Valenzuela 2015). Internal erosion,

briefly described in the following sections, has different mechanisms of failure (Figure 2-19), producing additional geotechnical hazards to the dam.

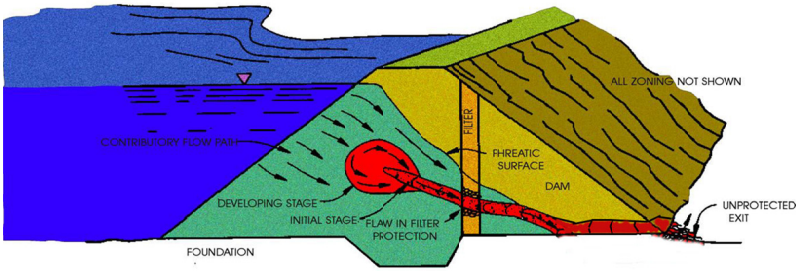

(a)

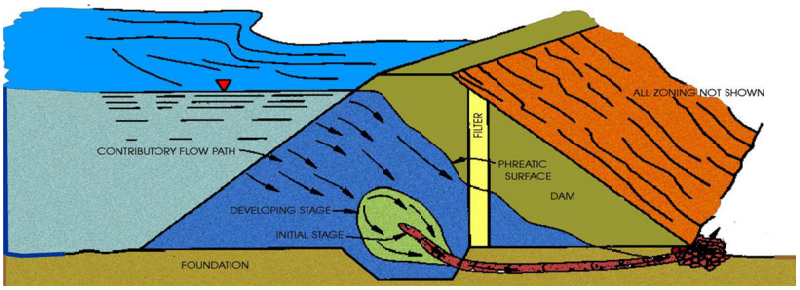

(b)

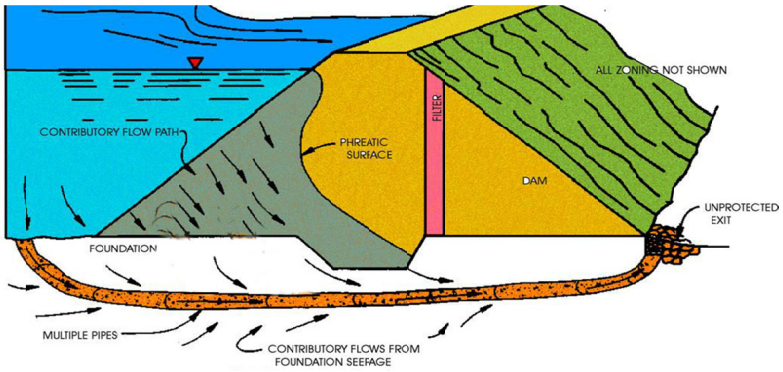

(c)

Figure 2-19 Mechanisms of failure under internal erosion. (a) Through the embankment, (b) Through cutoff trench and foundation and, (c) Through the foundation

(USDI 2010)

2.5.3.2 Slope Stability

Slope stability can be triggered under either static or dynamic loading. Under static loading, the internal erosion is associated with the initiation of slope instability at the downstream (Wan 2006), as illustrated in Figure 2-20. Slope stability can be an issue at the downstream face of the dam when there is an excessive loss of fine particles within the embankment during seepage. The localized pore water pressure can significantly increase, thereby resulting in decreased shear strength of the soil. This phenomenon causes landslides at the downstream face, and the process continues backward to the upstream slope. Slope stability can be also triggered under dynamic loading due to soil liquefaction. In the past decade, extensive studies have been performed to assess the stability of slopes in hydraulic fill dams (Dismuke 2002; Akhlaghi and Nikkar 2014; Hack, Alkema et al. 2007).

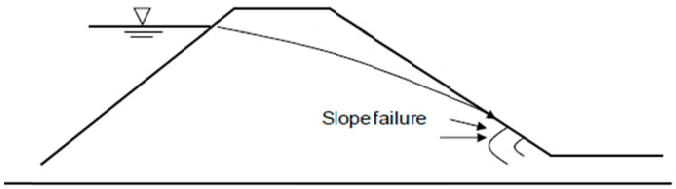

Figure 2-20 Downstream slope failure (Wan 2006)

2.5.3.2 Settlement and Sinkholes

An excessive settlement and the formation of sinkholes can be associated with both static and dynamic loading conditions derived from loss of freeboard. Internal erosion is the major cause of settlement and the formation of sinkholes at the crest and upstream of the dam, as illustrated in Figure 2-21 (Wan 2006). This can be attributed to the erosion of the cutoff wall or foundation soils, as described in Figure 2-20 (b) and (c) respectively. Foundations problems also occur in hydraulic fill dams due to the internal

erosion. The progressive loss of fine particles within the core or filters causes rearrangement of the particles within the soil mass and hence can lead to differential settlements. Also, due to the loss of fines within the permeable flow paths, fine particles are washed out along these paths. A change in the volume of a soil mass occurs within these flow paths, resulting in the formation of a sinkhole (Wan 2006). Hydraulic fill dams are old structures, and the soils have consolidated over decades; however, settlement and sinkholes can also occur under dynamic loading, constituting a direct hazard for hydraulic fill structures.

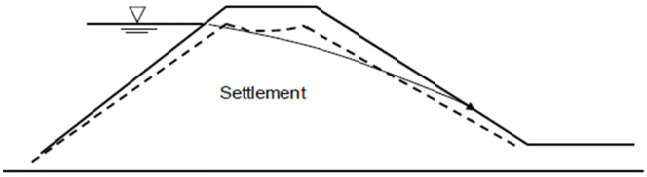

(a)

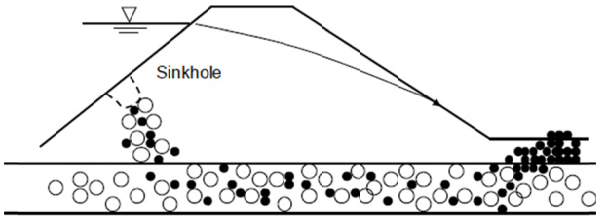

(b)

Figure 2-21 (a) Settlement of dam with loss of freeboard, (b) Sinkhole in upstream face, (Wan 2006)

A brief summary of geotechnical hazards in hydraulic fill dams was presented in the previous section. However, one of the major hazards of a hydraulic fill dam is associated with the soil liquefaction. The following sections present important concepts

and methodologies for evaluating liquefaction potential in hydraulic fill dams, as well as the description of some historic failures.

2.5.3.3 Liquefaction

Liquefaction is a term widely used by geotechnical engineers, especially in areas where seismic activity is highly present. It is a phenomenon that occurs when soil loses its strength and stiffness due to undrained (quick) loading and acts as a fluid (Kramer 1996). The term “soil liquefaction” was initially introduced by Hansen in 1920 (Hazen 1920) to describe the failure of the hydraulic fill dam at Calaveras in 1918 (Valenzuela 2015). Since then, hydraulic fill dams have experienced a series of failures, which are believed to have been caused by the loss of strength and stiffness under an undrained loading. Several research studies on soil liquefaction were conducted in the mid-20th century, after the occurrence of soil failures during seismic events (Mogami and Kubo 1953, Terzaghi and Peck 1967).

Extensive studies were performed to understand the liquefaction phenomenon in different soils and under different field conditions (Yoshimi et al. 1977; Seed 1979; Finn 1981; Ishihara 1993), and liquefaction improvement methodologies (Robertson and Fear 1994; Robertson and Wride 1998; Youd and Idriss 1998). The present work does not intend to describe the evolution of the liquefaction concept; it is limited to describing important concepts and understanding the traditional methods widely used for liquefaction assessment.

Liquefaction can be classified into two main groups, based on the performance of soil during an earthquake: *flow liquefaction* and *cyclic softening.* Both groups must be considered in assessing the liquefaction potential in hydraulic fill dams. Flow liquefaction is considered a major design issue for large soil structures such as mine tailings

impoundments and earth dams (Robertson 2010). Flow liquefaction refers to the strength loss potential of strain-softening soils either triggered by a monotonic (i.e., a sudden rise in groundwater level or rapid undrained loading), as well as by cyclic loading (i.e., earthquakes) (Robertson and Fear 1994).

For sloping ground structures (i.e., earthen dams), the flow liquefaction analysis becomes a challenge for geotechnical engineers since the ground could be subjected to a static driving shear stress and cyclic stress can induced even more loss of strength in soil. The term “spontaneous liquefaction was provided by Terzaghi and Peck (1967) to represent the rapid loss of strength of very loose sands which are the main cause of flow slides after a slender disturbance (Robertson 2010).

Flow or *static liquefaction* usually occurs when soils have a strain-softening response during undrained loading, resulting in approximately constant shear stress and effective stress (Robertson and Cabal 2012). In flow liquefaction, gravitational stresses must be higher than the undrained shear strength; a failure of soil mass will only occur, if a sufficient volume of material undergoes in strain softening (Robertson and Cabal 2012). The result consists on a flow failure, depending on the soil properties and ground topography, and the resulting deformations are primarily caused due to internal phenomena (i.e., internal erosion).

On the other hand, cyclic softening can only occur when enough excess pore water pressure is generated to overcome the effective stress of the soil triggered by a cyclic loading only. If no change in pore water pressure is present, hence in effective stress, then neither flow liquefaction nor cyclic softening will occur (Kramer 1996). *Cyclic softening* can be subdivided into two categories: *cyclic liquefaction* and *cyclic mobility,* and it applies to both strain-softening and strain-hardening soils, respectively (Robertson

and Fear 1994). Depending on the size and duration of the cyclic loading (i.e., earthquake), a stress reversal may occur.

If a stress reversal occurs, pore pressures suddenly build up, and the soil eventually reaches the condition of zero effective stress (Figure 2-22) (Robertson and Wride 1998). Stress reversal generally occurs if ground conditions are level or gently sloping; however, it also occurs during large earthquakes in steeply sloping ground (Pando and Robertson 1995). This phenomenon is known as *cyclic* or *seismic liquefaction*. The stress reversal state is often produced on saturated cohesionless soils subjected to a cyclic loading, which is the result of significant and sudden build-up of pore pressure (Kramer 1996). At that point, soil has very low stiffness, and large deformations are more susceptible to occur during cyclic loading (Robertson and Wride 1998).

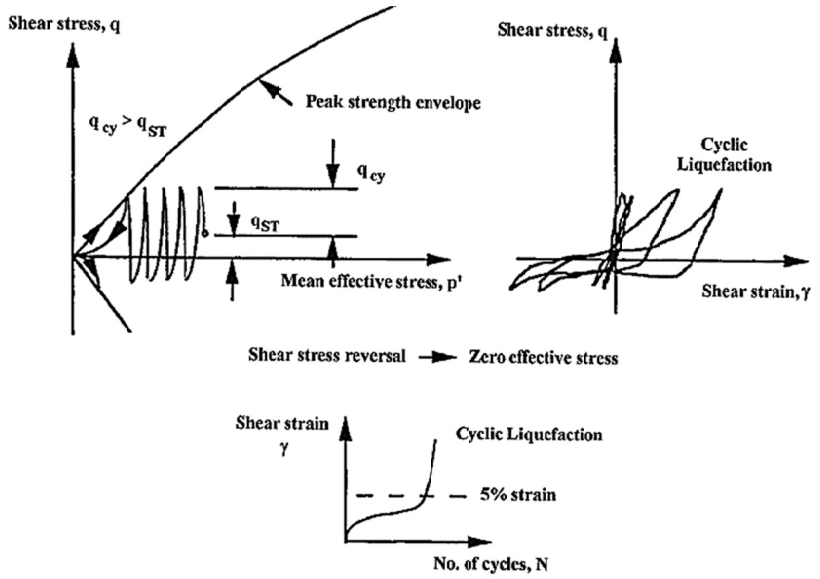

Figure 2-22 Undrained cyclic behavior of sand (Robertson and Fear 1994)

If a shear stress reversal does not occur (i.e., steeply sloping ground subjected to moderate cyclic loading), zero effective stress might not be reached, and the stress state may be slightly higher than zero as shown in Figure 2-23 (a) (b). In other words, *cyclic*

mobility occurs, and because the undrained cyclic loading includes shear stresses that are always greater than zero, only small or limited deformations are produced. However, this effect occurs only if the void ratio is below the critical state line (CSL) and the large strain response is strain hardening (i.e., the soil is not susceptible to a catastrophic flow slide) (Robertson and Fear 1994; Robertson and Wride 1998).

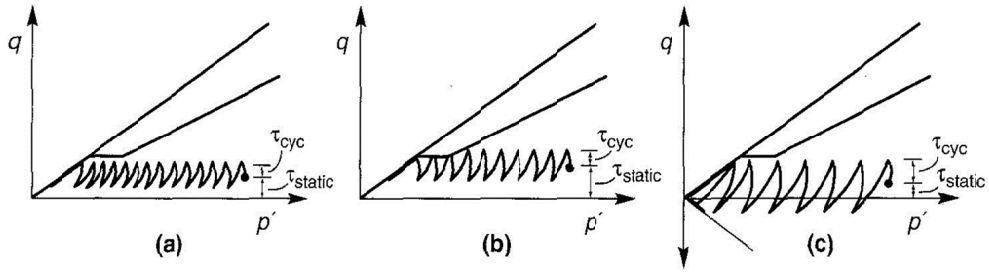

Figure 2-23 Three cases of cyclic softening (Kramer 1996)

2.5.4 Historic Failures in Hydraulic Fill Structures

Whether it is a flow or cyclic soil liquefaction, several hydraulic fill dams have experienced failures during earthquakes. In 1938, a massive landslide occurred at the Fort Peck Dam, a hydraulic fill dam constructed in the early 1930s (Figure 2-13). The final forensic investigation report stated that the shearing resistance of weathered shale and bentonite seams in the foundation were not sufficient to withstand the shearing force the foundation was subjected to (Billington et al. 2005). The flow failure of the Fort Peck Dam (Figure 2-24) in 1938 initiated studies of soil liquefaction. Professor Arthur Casagrande made several attempts to understand the mechanism that triggered the Fort Peck dam failure. Under his supervision, Gonzalo Castro (Castro 1969) discovered the flow condition by conducting a series of drained triaxial tests with deformation control (Valenzuela 2015). Liquefaction of sands in Fort Peck occurred under static loading conditions (i.e., flow liquefaction) and corresponded to what A. Casagrande named “true” liquefaction (Casagrande 1936), in which saturated cohesionless soils, under static or

dynamic loading, lose their resistance and acquire an internal structure that allows it to flow as a viscous fluid (Valenzuela 2015).

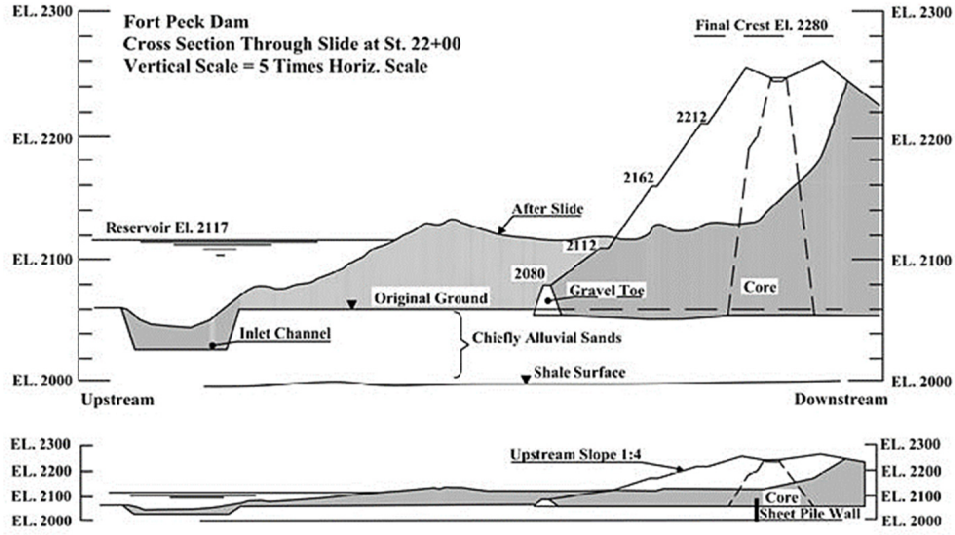

Figure 2-24 Transversal section and flow slide in the Fort Peck Dam, Station 22+00 (Casagrande 1975)

Despite the fact that liquefaction is present under static loading in hydraulic fill dams, the possibility of having a seismic event represents the greatest risk for liquefaction to occur. In 1971, an earthquake of M_L=6.6 in California caused the failure of the Upper and Lower Van Norman (San Fernando) Dam (Figure 2-25), confirming the negative perceptions about the vulnerability of hydraulic fill dams to liquefaction problems (Valenzuela 2015). Liquefaction in the San Fernando Dam occurred on the shell zones subjected to cyclic loading during the earthquake (i.e., cyclic liquefaction). Soils composed of coarse and fine sand layers, as well as clay layers were softened due to liquefaction and cyclic softening, respectively (Seed et al. 1973). Thus, the high variability of soil configurations, the non-uniform distribution of soil properties, and the loose

material resulting from the construction methodology employed in the San Fernando Dam were indicators for liquefaction failure.

Figure 2-25 Lower San Fernando Dam after M6.6 Earthquake in 1971

(NOAA/NGDC, E.V. Leyendecker, U.S. Geological Survey 1971)

2.5 Evaluation of Liquefaction

The evaluation of liquefaction susceptibility in dams became more feasible with the invention of in-situ tests (i.e., cone penetration tests and standard penetration tests). Several relationships and concepts on how in-situ tests can be applied for liquefaction assessment were addressed in different publications (Seed et al. 1985; Seed and Alba 1986. Robertson in 1994 (Robertson and Fear 1994), presented a general overview of the soil-liquefaction-triggering framework, which is still used today (Figure 2-26).

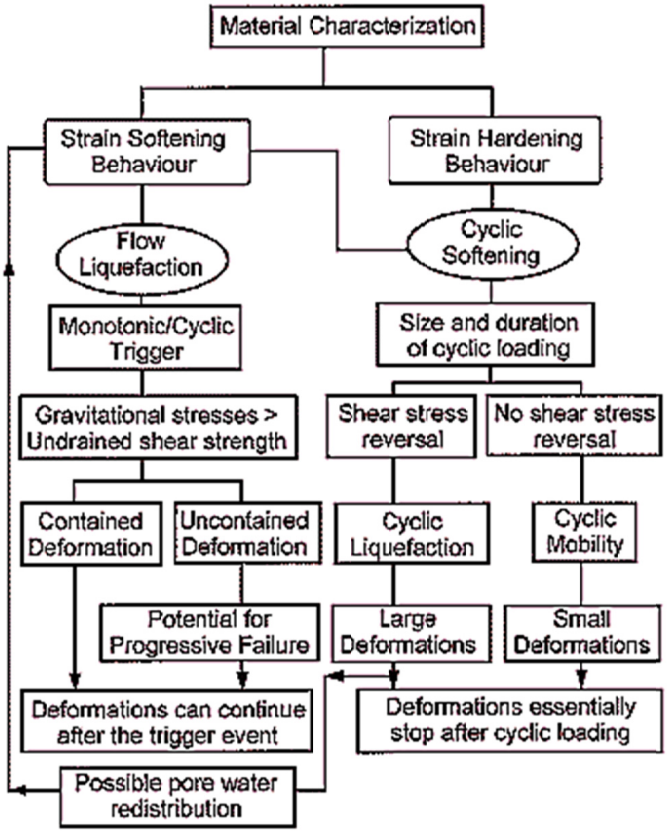

Figure 2-26 Suggested flow chart for evaluation of soil liquefaction

(Robertson and Fear 1994)

In 1996, several advances in soil liquefaction and included important work developed by Robertson and Wride (Robertson and Wride 1998) and Youd and Idriss (Youd and Idriss 1998) were presented to the National Center for Earthquake Engineering Research (NCEER) in the United States of America. The methodologies discussed are primarily those based on in-situ test methods (i.e., SPT and CPT methods). The in-situ test-based approach is the most suitable methodology for evaluating flow or cyclic liquefaction for existing dam projects. The advantage of this approach is that it refers to the field data, which has a greater representation of in-situ

conditions than soil sampling and laboratory-test-data based approaches. The present seismic resilience framework for hydraulic fill dams in this dissertation is primarily developed to address the cyclic liquefaction in hydraulic fill dams by using conventional in-situ cone penetration testing. Flow liquefaction or strength loss potential due to cyclic loading (i.e., cyclic mobility) is not covered in the present framework.

The cyclic liquefaction assessment is performed based on two factors, the quantification of external loading (i.e., earthquakes) and the resistance of soil against liquefaction and it will be discussed in the following section. The evaluation of the initiation of liquefaction was derived by different approaches over decades. The *Cyclic Stress* approach and the *Cyclic Strain* approach are the most common methodologies to estimate cyclic liquefaction. Several other approaches have been developed, such as the *dissipated energy approach* and the effective *stress-based response analysis* (Kramer 1996). The following sections present different approaches for assessing the liquefaction potential in soils.

2.5.1 Cyclic Stress Approach

The cyclic soil resistance concept was introduced by Professor Bolton Seed and his collaborators in the 1960s. The approach is based on the evaluation of the loading conditions required to trigger cyclic liquefaction. The loading is defined in terms of cyclic shear stresses, and the cyclic liquefaction potential is addressed on the basis of the amplitude and number of cycles of earthquake-induced shear stresses (Kramer, 1996). The stress-based approach for evaluating potential liquefaction compares two parameters: the earthquake-induced cyclic stress ratio (CSR) and the cyclic resistance ratio (CRR) (Boulanger and Idriss 2014). The earthquake-induced cyclic stress ratio (CSR) refers to the characterization of earthquake loading. The amount of excess pore

water pressure required to initiate liquefaction directly depends on the amplitude and duration of earthquake loading (i.e., higher CSR). Earthquake loading can be estimated by using two approaches: by generating a detailed ground-response analysis or by using a simplified approach. The CSR is usually estimated based on the probability of an occurrence of an earthquake and is referred to as a simplified approach (Seed and Idriss 1971). The simplified approach for evaluating CSR is based on the maximum ground surface acceleration (a_{max}) at the site of interest, as shown in Equation 2.1.

$$CSR = \frac{\tau_{AV}}{\sigma'_{VO}} = 0.65 \left[\frac{a_{max}}{g}\right] \left(\frac{\sigma_{vo}}{\sigma'_{vo}}\right) r_d \quad (2.1)$$

A cyclic stress ratio profile is developed based on the average cyclic shear stress (τ_{av}) expressed by the simplified approach, based on the peak ground acceleration (a_{max}), and the total (σ_{vo}) and effective (σ'_{vo}) vertical overburden stresses. A factor of r_d is also considered as a depth reduction factor (i.e., earthquake loading reduces with depth). Soil liquefaction resistance is represented by evaluating the cyclic resistance ratio (CRR). A methodology for estimating CRR was first developed by Seed (Seed and Alba 1986) for clean sands, based on the standard penetration test (SPT) and using data of liquefied soils. In-situ tests are considered the most appropriate methods for addressing liquefaction potential at a test site. Cone penetration test (CPT) is the most popular tool for estimating CRR values because of their continuous and reliable nature of data (Youd and Idriss 1998; Robertson 2009). The susceptibility of soils to liquefaction was developed by considering sand-like behavior and clay-like behavior (Boulanger and Idriss 2004). Figure 2-27 shows the criteria suggested by Bray and Sancio's method, which is based on the plasticity of soils (Bray et al. 2004).

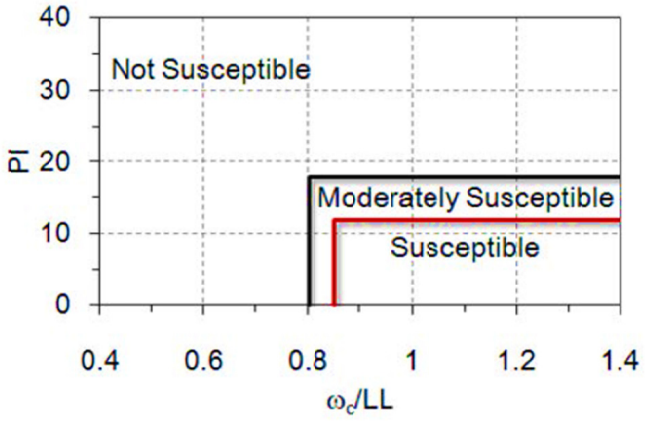

Figure 2-27 Liquefaction susceptibility criteria based on soil plasticity

(Bray et al. 2004)

2.5.1.1 Cyclic Stress Approach based on CPT

Since the cyclic stress approach is used for the present study, it is necessary to understand various methodologies developed for evaluating liquefaction, based on in-situ tests, specifically on cone penetration tests (CPT). Earthquake loading, referred to as CSR, can be directly determined by using the simplified approach, based on the maximum horizontal acceleration (a_{max}) obtained from a comprehensive seismic hazard analysis. However, soil liquefaction resistance, CRR, can be derived by using different approaches, based on conservative assumptions (Seed et al. 1985; Seed and Alba 1986); Robertson and Wride 1998; Youd and Idriss 1998; Boulanger and Idriss 2014). The cyclic resistance ratio is directly evaluated by plotting case histories of soil liquefaction occurrences. Robertson (Robertson and Wride 1998; Robertson 2009) estimated the CRR by normalizing the cone tip resistance from the CPT. Figure 2-28 shows the CRR chart and Figure 2-29 presents a framework for evaluating liquefaction developed by Robertson (2009).

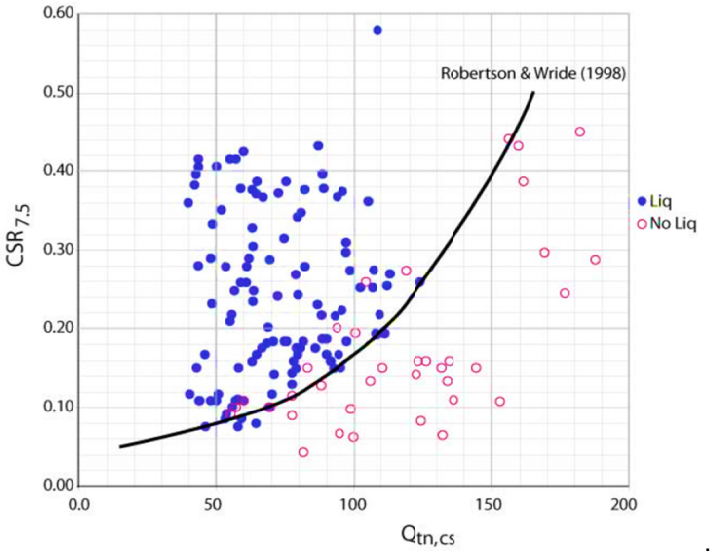

Figure 2-28 Cyclic resistance ratio ($CRR_{7.5}$) from CPT normalized clean sand equivalent cone resistance ($Q_{tn,cs}$) (Robertson 2009)

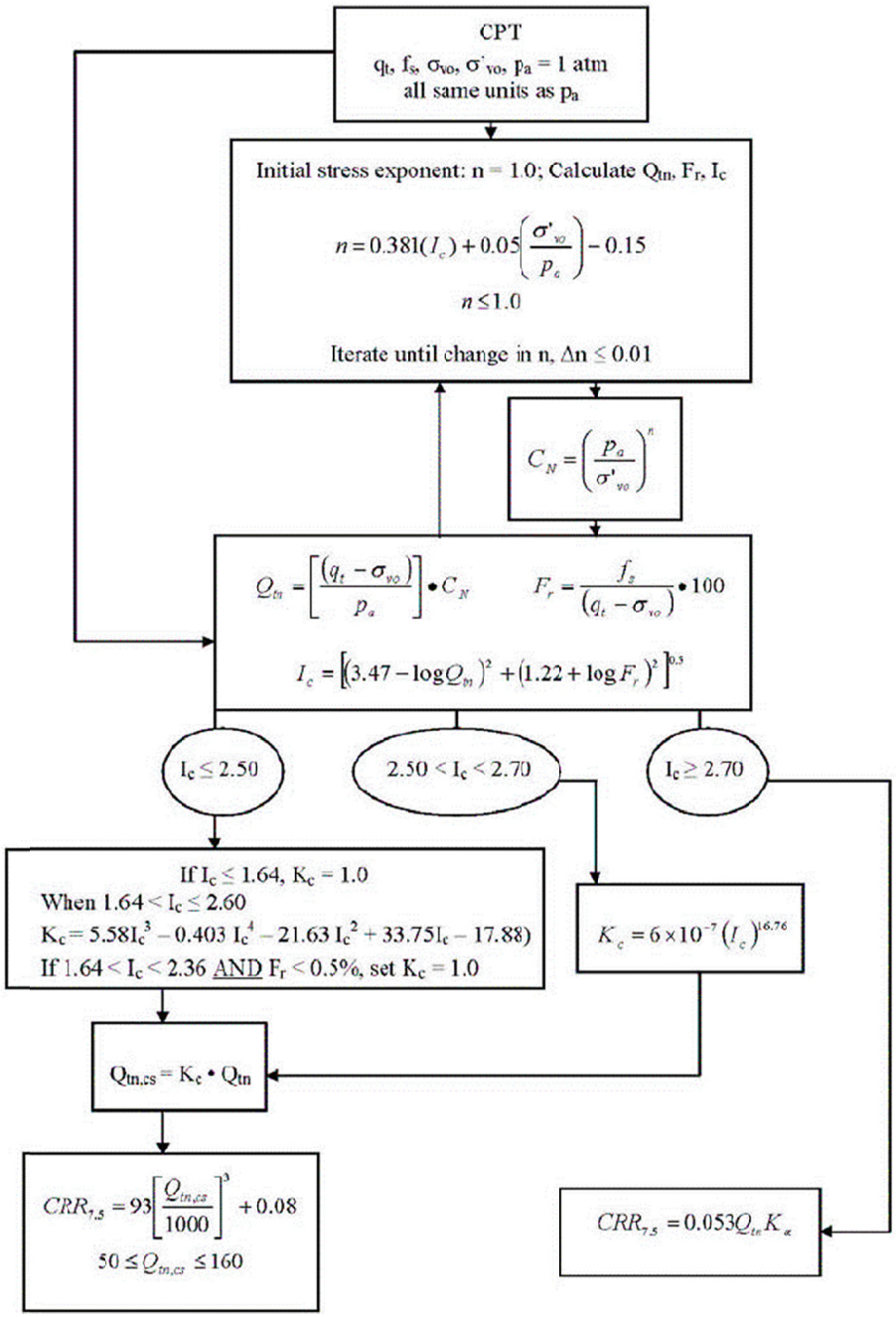

Figure 2-29 Framework to evaluate cyclic resistance ratio ($CRR_{7.5}$) from CPT (Robertson 2009)

The second approach for evaluating CRR is based on the study performed by Boulanger and Idriss (2014), which includes an updated database of CPT-based liquefaction/no liquefaction case histories. It also considers a revised MSF (magnitude scale factor) that incorporates functional dependency on the soil characteristics. This study was an update of the research presented in 2008 by the same authors (Idriss and Boulanger 2008), and the outcome of their analysis is illustrated in Figure 2-30. A comprehensive analysis of both approaches is presented by incorporating CPT interpolated data into the liquefaction evaluation, and is described in Chapter 5.

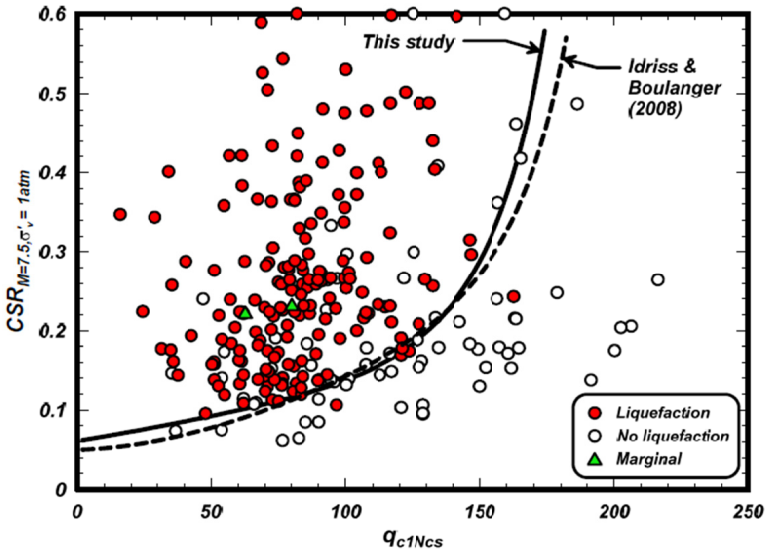

Figure 2-30 CRR evaluation model (Boulanger and Idriss 2014)

2.5.1.2 Cyclic Stress Approach based on Shear Wave Velocity, V_s

Several methodologies of in-situ shear wave velocity measurements are also used in the evaluation of liquefaction resistance in soils (Stokoe et al. 1994; Tokimatsu et al. 1991). However, shear wave velocity of granular soils (i.e., clean sands) is insensitive for factors including soil fabric, over-consolidation ratio, and prior cyclic straining, which are known to be liquefaction resistant (Kramer 1996). Therefore, shear wave velocities

obtained directly from soil deposits may not be suitable for evaluating the liquefaction of all deposits (Verdugo 1992; Jamiolkowsky and LoPrsti 1992). Despite the fact that shear wave velocity measurements alone are not a convenient approach to addressing their liquefaction, the present research utilizes the shear wave velocity obtained from few SCPTu as well as from raw CPT data correlations, which gives a more reliable and continuous profile of any soil parameter by correlations. The liquefaction assessment is developed by using the cyclic stress approach, and by evaluating CRR based on CPT and shear wave velocities correlations. CRR can also be estimated by using normalized shear wave velocity, V_{s1}, shown in Figure 2-31 (Kayen, Moss et al. 2013).

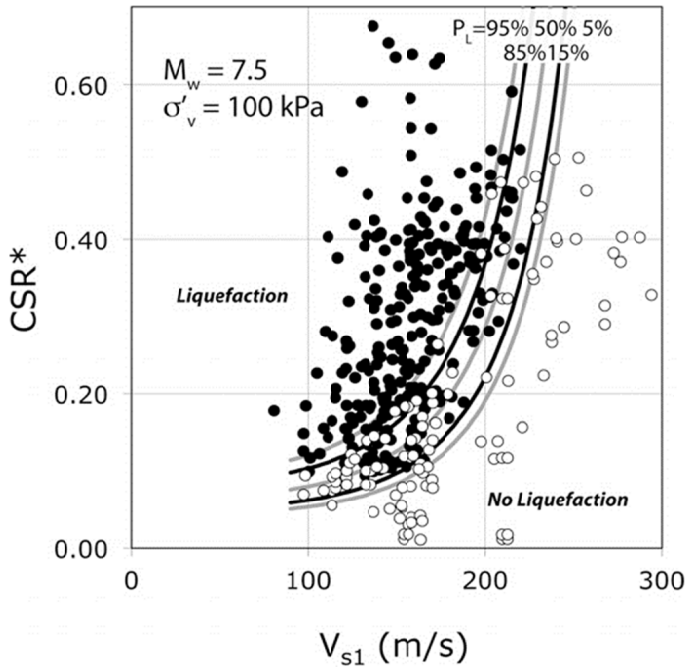

Figure 2-31 CRR evaluation model based on normalized shear wave velocity (Kayen et al. 2013)

2.5.2 Other Traditional Approaches

The influence of different factors on the cyclic stresses required to produce liquefaction are difficult to identify due to its conservative assumptions. Soils, especially sands, tend to densify due to the generation of excess pore water pressure and are fundamentally related to cyclic strain rather than cyclic stresses (Kramer 1996). Other approaches for evaluating the initiation of liquefaction are found in the literature. The cyclic strain approach was developed on experimental results that showed densification of dry sands which were controlled by cyclic strains rather than by cyclic stresses (Silver and Seed 1971; Youd 1972). It is also based on the existence of the threshold volumetric shear strain where densification does not occur below this point. Thus, the convenience of using this approach is the strong relationship between pore pressure generation and cyclic strain amplitude.

The excess pore water pressure during cyclic loading can be estimated more accurately by determining cyclic strains rather than cyclic stresses (Kramer 1996). Other approaches are identified as the *energy dissipation approach* and the *effective stress-based response analysis approach,* which are not widely used due to the lack of calibration. The former method has the advantage of considering both cyclic strains and cyclic stresses to address the liquefaction resistance, as well as stochastic earthquake ground motions for evaluating the earthquake-induced loading. The latter approach is more complex since the excess pore water pressure can be predicted by applying advanced constitutive models by describing models based on cyclic nonlinear stress-strain (Kramer 1996).

Despite the methodology used to evaluate the liquefaction potential, the success of their application can be demonstrated in several hydraulic fill dams' post-earthquake

evaluations. However, choosing the methodology is not the primary concern for liquefaction assessment in hydraulic fill dams. The significant number of liquefaction failures in hydraulic fill dams is primarily due to the uncertainty of the soil configuration after the construction. This was demonstrated by the research work performed by Seed (Seed et al. 1973) on soil samples collected from the San Fernando Dam after the earthquake. Liquefaction in the San Fernando Dam occurred in layers of mixed soils (coarse, fine sands, and clays) and in soils with D_{50} ranging between 0.05 and 1.00 mm and relative density (D_R) ranging from 40% to 70% (Valenzuela 2015).

Although the application of the hydraulic fill methodology was discontinued in the United States due to the extensive number of failures, some hydraulic fill dams are still operating and require a comprehensive liquefaction assessment. Therefore, it is important to perform a comprehensive interpretation of the soil configuration within the embankment to characterize its properties by considering the variabilities encountered in hydraulic fill dams. The following sections present various approaches to studying soil characterization and variability.

2.6 Soil Characterization and Variability

2.6.1 Introduction

The key aspect to any geotechnical assessment is to understand the geology and soil conditions at the site of interest. Soils are inherently heterogeneous; therefore, their stratigraphy can present high variabilities in the soil properties. Geotechnical variability is a complex attribute, resulting from different sources of uncertainties (Phoon and Kulhawy 1999). Uncertainties in geotechnical designs are the result of not incorporating the spatial variability of soil properties into geotechnical analyses (Einstein and Baecher 1982; Laccasse and Nadim 1996). In other words, soil properties vary from

location to location in the space as well as in time, and past research analyses did not include incorporation of spatial variability of soil properties (Bheemasetti 2014). Spatial variability recognition is a vital task that helps to categorize the distances over which it occurs, compared to the scale of the data of interest (Whitman 1984). According to Lacasse (Laccasse and Nadim 1996), uncertainties in soil properties can be formally grouped into *aleatory* and *epistemic* uncertainties, with subdivisions as shown in Figure 2-32. Extensive studies were performed to address the uncertainties associated with soil properties by using different statistical parameters (Phoon and Kulhawy 1999). Of all the uncertainties, spatial variability is the most challenging and is the key for proper evaluation of the safety of a structure. The following sections present a brief review of spatial variability of soil properties.

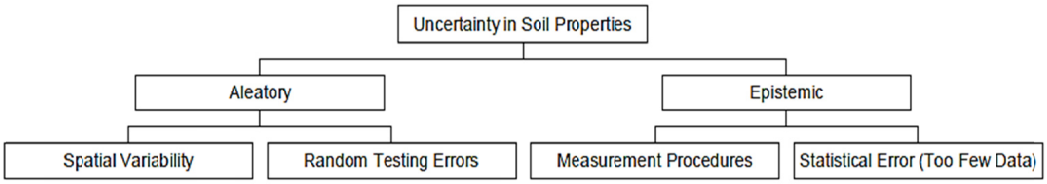

Figure 2-32 Sources of uncertainty in geotechnical soil properties (adapted from Whitman, 1996; Jones et al. 2002)

2.6.2 Spatial Variability of Soil Properties

Spatial variability refers to measured values of a random variable that changes within the space (Bheemasetti 2014). Characterization of the spatial distribution of soil properties necessitates the use of *regionalized variables,* which are required to be correlated (Jones et al. 2002). The term when a variable is correlated to itself is known as *autocorrelation*; it depends on the relative positions of sample values both in distance and direction, and on the particular property which is being evaluated. The size, orientation, shape and spatial distribution of samples is consider as support of the regionalized

variable; thus, the regionalized variable is directly affected if any of these factors change (Davis 1986).

The spatial variability of soil properties directly depends upon the soil type and soil deposition and formation (Jones et al. 2002). It also depends on the values of the parameters collected and used to evaluate spatial variability due to the potential influence of measurement errors. Considering spatial variability in developing geologic models based on collected soil properties enhances the prediction of subsurface materials so that realistic estimates can be performed. The following sections present different approaches used to determine the spatial variability in soils.

2.6.2.1 Trend or Drift

Trend or commonly named drift refers to the constant path or fit belonging to a soil property variation along a subsurface profile or with respect to depth (Bheemasetti 2014). The trend can be computed by considering the weighted average of all points within the region around that point (Davis 1986). Least-square techniques can be used to model trends or drifts as linear, quadratic, or higher-order functions in one or two dimensions (Jones et al. 2002). The trend or drift has to be minimized or removed by several techniques (i.e., ancillary data) to achieve spatial variability, and more importantly to enhance the prediction of soil properties (Minasny and McBratney 2007). The method for estimating the trend or drift function in spatial observations was developed by several researchers (Davidoff et al. 1986; Arutyunyan et al. 1996).

2.6.2.2 Scale of Fluctuation

Unlike the trend or drift, the scale of fluctuation grant a measure of how fast a parameter changes with position about a trend. In other words, this fluctuation estimates maximum distances over which a random variable (i.e., soil property) shows strong

correlation. A larger value of the scale of fluctuation, δ, indicates the slowly varying nature of the property about the trend (low spatial variability) (Jones et al. 2002). The study presented by Jones in 2012 includes an application example to facilitate understanding of the estimation of the scale of fluctuation for the tip resistance obtained from CPT along the subsurface profile presented in Figure 2-33.

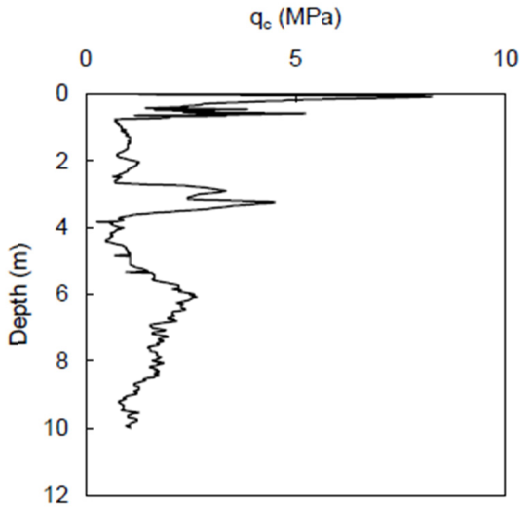

(a)

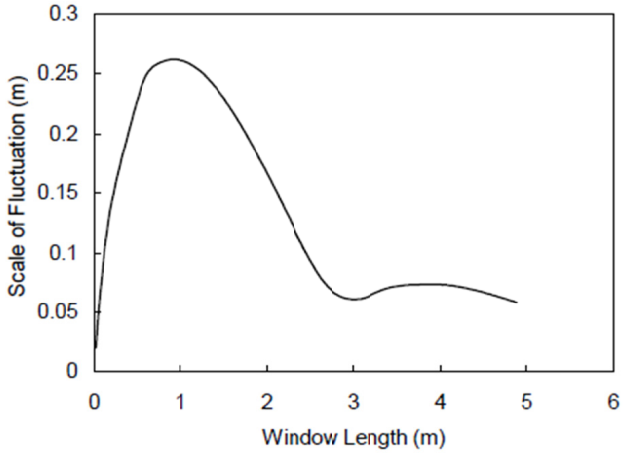

(b)

Figure 2-33 (a) CPT tip resistance log, (b) Plot of scale of fluctuation

(Jones et al. 2002)

2.6.2.3 Correlation Functions for Spatial Variability

Correlation functions are commonly used to quantify the spatial variability of a variable by using *h-scatter plots.* These type of plots consist of the relationship between the value of one single variable and the value of the same variable at nearby locations, that is separated by a distance "h" called *lag distance* (Isaaks and Srivastava 1989). Figure 2-42 presents two plots, where the lag distance is zero and two. It can be observed that as the lag distance increased, the scatter in the plots also increased.

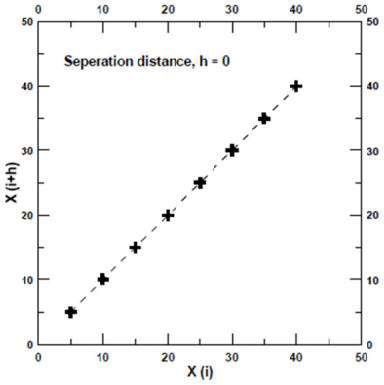

(a)

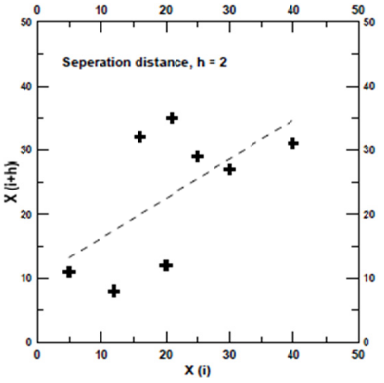

(b)

Figure 2-34 (a) h-scatter plot for a separation distance of 0 m, (b) h-scatter plot for a separation distance of 2 m (Bheemasetti 2014)

Covariance function is a relationship between the covariance of an *h-scatter* plot and *h* (Isaaks and Srivastava 1989). The covariance, a basic statistic parameter, is primarily used to identify the sameness between two random variables; however, in geostatistics the covariance function (Equation 2.2) allows the estimation of the maximum lag distance by using Equation 2.2 which exhibits the spatial correlation data.

$$Cov(X_i, X_{i+h}) = \frac{[\sum X_i X_{i+h}] - \frac{1}{n-h}\sum X_i \frac{1}{n} X_{i+h}}{n-h-1} \quad 2.2$$

Autocorrelation functions are plotted in terms of the lag distance to generate the auto-correlogram (Jones et al. 2002). Various models have been developed to address autocorrelation function models between the scale of fluctuation and the lag distance (Li and White 1987; Davis 1986). For example, the autocorrelation function of the covariance is generally obtained by normalizing the auto-covariance with respect to the variance of the same random variable by using Equation 2.3 (Bheemasetti 2014). (See Figure 2-35.)

$$r_h = \frac{cov(X_i, X_{i+h})}{V(X)} \quad 2.3$$

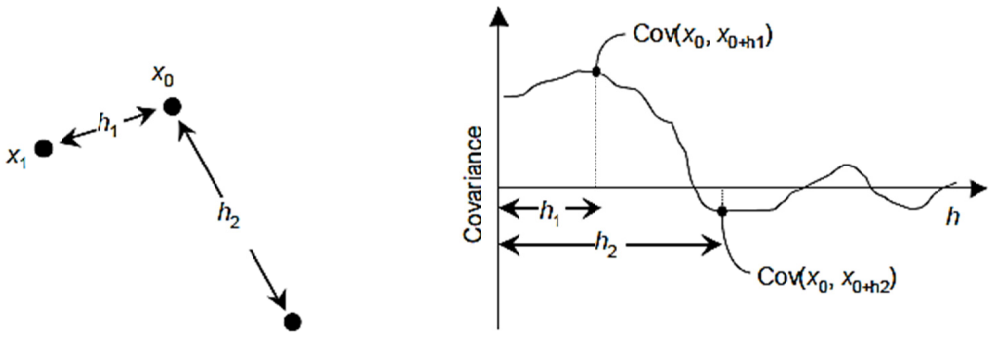

(a) (b)

Figure 2-35 (a) Spatial covariance represented by data points, *x*, and separation distances of *h*; (b) Hypothetical data showing that autocorrelation should be higher for low h than for high *h* (Jones et al. 2002)

2.6.2.4 Variogram Model

Several concepts can be found in the literature for describing the *variogram* and *semi-variogram* (Amundaray 1994; Isaaks and Srivastava 1989). The semi-variogram is one-half of the variogram (Equation 2.4), and it provides the spatial variability present in the property of interest (i.e., soil parameter). Spatial continuity of data can be described by variograms in earth science applications. Mathematically, the variogram can be expressed as the expected squared difference between two data values separated by a distance vector, *h,* in the variogram (Gringarten and Deutsch 2001).

$$\gamma(h) = \frac{1}{2n(h)}\sum_{i=1}^{n(h)}[z(x_i + h) - z(x_i)]^2 \qquad 2.4$$

Figure 2-36 illustrates a typical sample semi-variogram for which three main characteristics can be often defined: Range, sill and nugget (Isaaks and Srivastava 1989). The *range, a,* refers to the value of the x-axis of the variogram that is related to the lag distance, *h*. Thus, by increasing the separation distance between pairs, the range value in the semi-variogram will also increases. It is also described as the distance in the x-axis where the semi-variogram function reaches approximately a constant value in the y-axis. The sill, ($C+C_0$), is the vertical distance value in the y-axis, starting from the origin of the semi-variogram to the value of the y-axis, where the function tends to be constant. The nugget, C_0', is discontinuity from the origin, as shown in Figure 2-36, and is primarily caused by sampling error and very short scale variability, causing sample values to get separated by excessively short distances (h) (i.e., nugget effect).

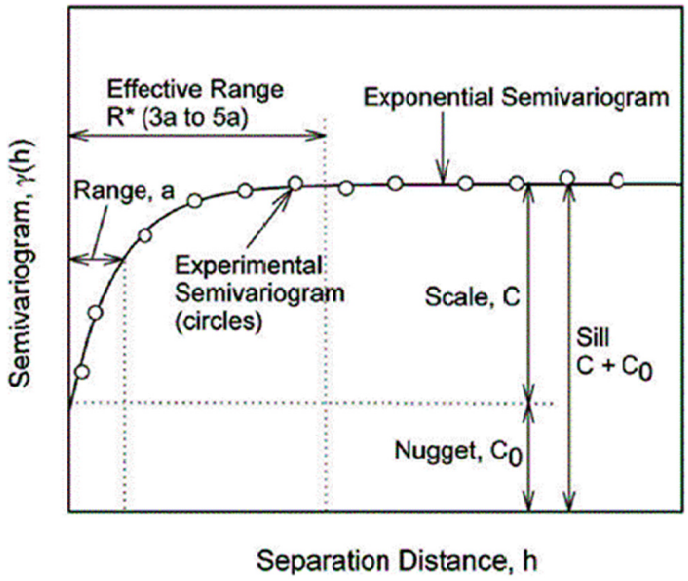

Figure 2-36 Typical semi-variogram (Gringarten and Deutsch 2001, Vennapusa et al. 2010)

Variograms are developed based on mathematical models or functions that typically are positive definite (Jones et al. 2002). Some variogram functions that include simple linear, spherical, exponential, and Gaussian regression models are also called *"transition models with sill."* Figure 2-37 illustrates the various types of variogram functions. The present research uses the exponential and Gaussian models to consider a fully three-dimensional anisotropy (spatial anisotropy) model, described in the following section.

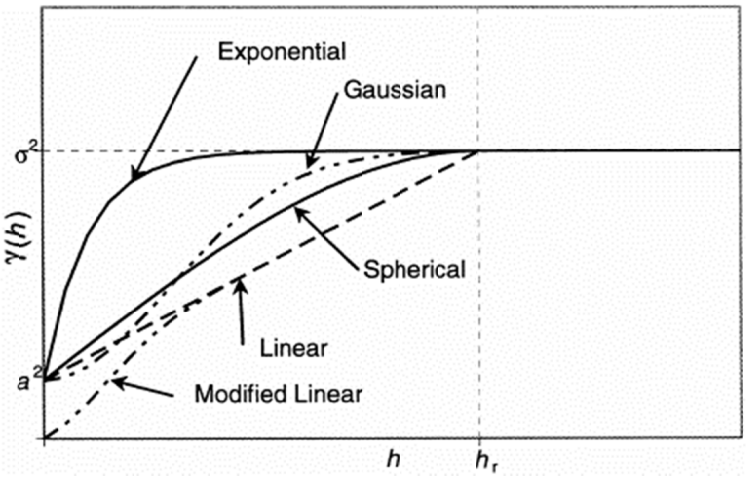

Figure 2-37 Typical semi-variogram (Gringarten and Deutsch 2001, Vennapusa et al. 2010)

2.6.3 Simulation and Estimation of Spatial Variability

In geotechnical engineering, the main objective of a spatial variability analysis is to determine the value of a soil property at a random location, based on existing soil property data at different locations. The present section presents several researches developed to replicate the actual field conditions, by either estimating or by simulating field conditions. The concept of estimation and simulation are totally different and it is important to address its difference. The objective of estimation techniques is to produce an unbiased estimation with minimal variance based on the actual data collected; however, estimated data does not always reproduce the true variability of the property. On the other hand, simulation produces a group of data with its corresponding mean, covariance (second moment statistics), and spatial variation (semi-variogram) as the known distribution (Jones et al. 2002).

Simulation of a field condition is a complex methodology used to model soil conditions. Several research studies have focused on the application of slope stability

(Vanmarcke 1977). Since the present research focuses on the application of prediction methodologies to address spatial variability, estimation methods are described in later sections. Various techniques for simulating soil variability are briefly presented.

2.6.3.1 Random Field

A random field quantifies the uncertainty in probabilistic terms and is used in geotechnical engineering to replicate the actual field conditions by incorporating spatial variability. Several researches have been developed based on statistical tools (i.e., correlation distance, scale of fluctuations, and coefficient of variation) that simulate a random field (Vanmarcke 1977; Fenton 1999a; Huang et al. 2010; Cho 2012; Zhu et al. 2013). Several methodologies for generating a random field were summarized by Jones (Jones et al. 2002), based on the work performed by different researchers (Vanmarcke 1984; Yamazaki and Shinozuka 1988; Hasofer 1993). On large number of simulation methodologies, fields are generated approximately or exactly in form of Gaussian models, and the assumption of having a Gaussian behavior simplifies the stochastic problems (Jones et al. 2002).

2.6.3.2 Monte Carlo Simulation Methods

The Monte Carlo methods (MCM) model the simulation of soil properties by generating suitable random numbers and identifying the portion of values that satisfy a single soil property or several properties. The implementation model was compiled by Yang (Yang et al. 1993), and it requires a series of iterations that are dependent on the number of variables to be simulated. By using computational algorithms, the results can be determined in a faster way. For example, MCM can be used in probabilistic slope stability analysis for the determination of a critical slope surface, and the calculation is based on the mean value of the input shear strength parameters combined with

appropriate deterministic analyses (i.e., limit equilibrium or finite element analyses). A probabilistic approach is performed by considering the variability of input parameters (i.e., mean and standard deviations) on the critical slip surface, which in most cases, the designer has already specified. Iterations are performed during MCM, and a normalized random number is used for updating input parameters. The final result is that the factor of safety includes the corresponding mean and standard deviation, thus, the probability distribution function can be calculate. As a general rule, the required trails tend to increase based on the increasing of variables as well as on the decreasing of expected probability of failure (Jones et al. 2002). It not common practice to perform several trials to reach a reasonable level of confidence when using a Monte Carlo probabilistic slope stability analysis (Mostyn and Li 1996).

2.6.4 Predictions using Geostatistics

The present study incorporates spatial variability in geotechnical projects by using geostatistics, which is a stochastic interpretation tool that evaluates the spatial variability of data sets. According to Isaaks and Srivastava (1989), spatial analysis or spatial variability refers to those techniques that define data sets with respect to space. Several examples of considering spatial variability are the definition of the location of extreme value, the overall trend or the degree of continuity. Geostatistics incorporates both the statistical distribution of the sample data and the spatial correlation among the sample data.

A hypothetical example is presented in a study performed by Bheemasetti (2014), as shown in Figure 2-38. The value (z) is predicted by considering data provided, A, B, C, and D. However, by performing univariate statistics, the value of (z) can be estimated as the average of the nearby values. Geostatistical methods predict the value

of (z) by considering both the location of samples (i.e., spatial distribution) and the weightage of each sample (i.e., magnitude of soil property), and by constructing and modeling a semi-variogram combined with a Kriging algorithm described later in this section.

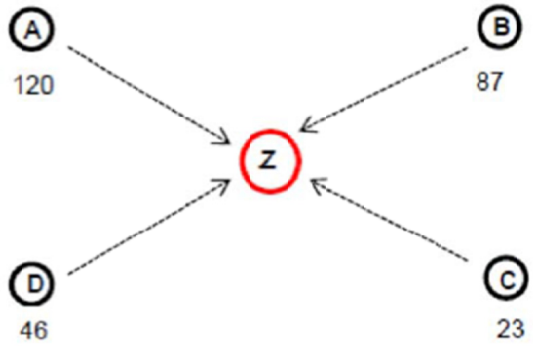

Figure 2-38 Hypothetical example for highly varying random variables (Bheemasetti 2014)

The prediction of value (z) can also be attained by traditional methods in statistics. However, depending on the data provided, these methodologies are not appropriate for performing an interpolation. Usually, an increase in sample quality or density affects the selection of the interpolation methodology. The current research study uses the geostatistical theories; hence, the Kriging, a geostatistical interpolation technique, is reviewed in the following section.

2.6.4.2 Kriging Interpolation

Kriging is a geostatistical procedure that uses the semi-variogram model to incorporate the spatial continuity of the input data to estimate values at unsampled locations (Isaaks and Srivastava 1989). Kriging can also be defined as the weighted, moving average interpolation or extrapolation procedure that reduces the error variance of the interpolated or extrapolated value, based on the linear weighted average of nearby

values (Jones et al. 2002). The weighted factors, as well as the variance of the data set, are analyzed by the semi-variogram to address spatial variability. The present research is based on the application of the Kriging interpolation method to predict soil parameters at unsampled locations by using collected data at specific locations. However, different types of Kriging are found in the literature, which are briefly described in this section

Simple Kriging is considered the simplest type of all the Kriging methods, and consists on assuming the covariance as a second-order stationary which means that the trend or drift component is constant and the mean or average is known. It is commonly used in the mining industry, where the mean of mining panels is a known value (Armstrong 1994; Bheemasetti 2014). The accuracy of the simple Kriging is considered to be very low as compared with other kriging types; it only assumes the first order moments constant (Olea 2009).

Ordinary Kriging is a form of Kriging also known as BLUE (best linear unbiased estimator) (Isaaks and Srivastava 1989). Ordinary Kriging is “linear,” because its estimates are weighted linear combinations of the available data. It is called unbiased because it tends to have the residual mean or error equal to zero, and it is the best because it reduces the variance of the errors. Bheemasetti (2014) defined ordinary Kriging as the method when the first and second order moments are constant values, which means that the second order stationarity is satisfied (Haining 2010; Olea 2009). The work also presents the application of ordinary Kriging for predicting soil properties in two dimensions models. Ordinary Kriging is most successful when the anistropy is properly described and when the variogram is locally customized (Isaaks and Srivastava 1989). Therefore, the present research uses ordianry Kriging and also considers the anistropy to generate more realistic variograms.

Universal Kriging (Regression Kriging) is a variant of ordinary Kriging and is used when the mean is not constant and the weights of the nearby values are estimated by considering locally varying means values (Bheemasetti 2014). Additionally, intrinsic stationarity must be satisfied in this approach (Hohn 1999; Olea 2009). *Fractional Kriging* is developed based on a variogram filtering technique (Matheron 1982). It consists to be a multivariate geostatistical technique that needs to minimize the noise present in data (Magneron et al. 2009). Several applications are suitable for using factorial Kriging, such as petroleum and mining engineering. The technique is limited to when the data is non-stationary and reducing the noise is a big challenge to constructing the variogram (Bheemasetti 2014). Various research projects have used Kriging for the prediction of variables at unsampled locations. Mesic (2016) presented an example of depth interpolation to describe which Kriging technique is most suitable in a specific application, as shown in Figure 2-39 (Mesic 2016).

Overall, Kriging has several advantages over conventional interpolation methods. Kriging accounts both for the clustering of nearby samples and for their distance to the point being estimated (Isaaks and Srivastava 1989). Additionally, by considering statisitcal distance (Kriging) through the variogram, rather than the euclidean distance (straight-line) distance used in conventional methods, it offers a siginifcant advantage for customizing the estimation method to a particular problem by considering the spatial continuity (spatial anisotropy). The incorporation of anisotropy or spatial continuity is used in the present research as part of the construction of variograms for the interpolation of several soil parameters in three dimensions by using ordinary Kriging. The following section presents a compilation of the advances of geostatistics in geotechnical engineering and its application for creating two-dimensional models.

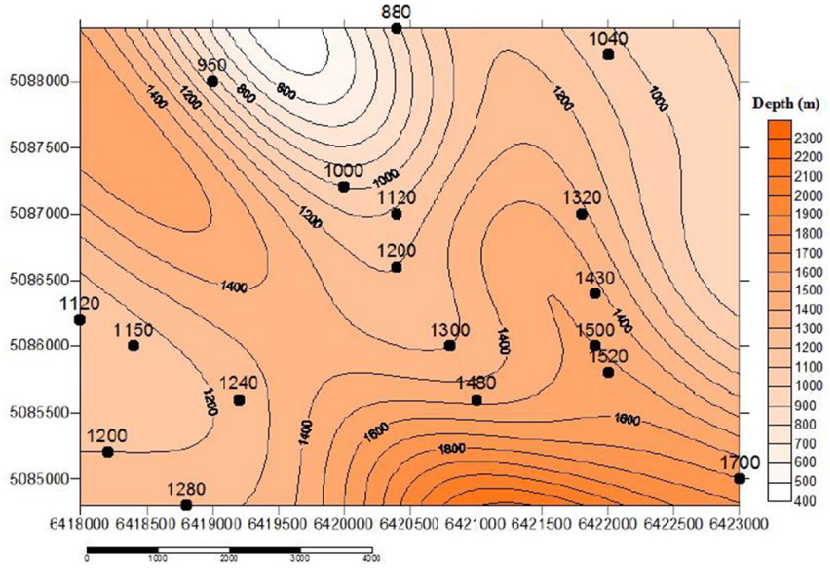

(a)

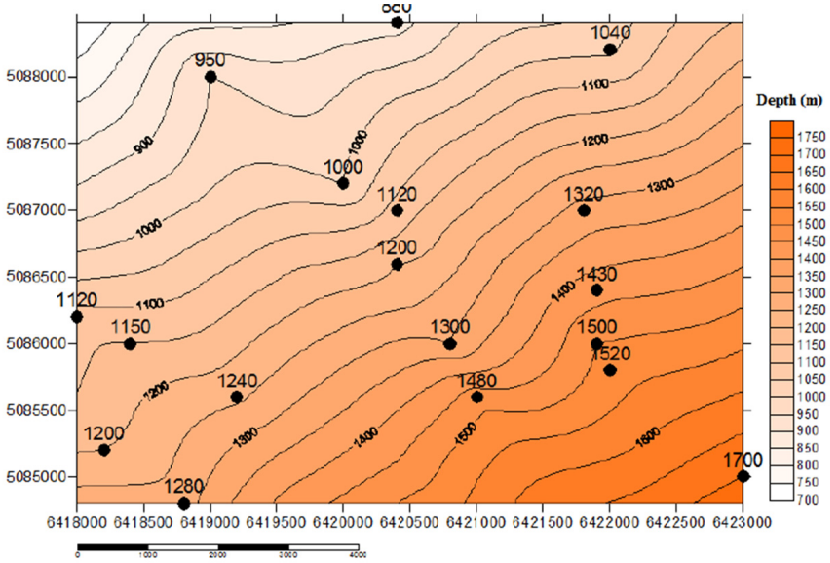

(b)

Figure 2-39 Depth of geologic data (a) Ordinary Kriging, (b) Universal Kriging (Mesic 2016)

2.6.5 Geotechnical Data Visualization

Geotechnical data visualization is a valuable task for hazard mitigation and disaster response (Ellis and Vessely 2015), and it can include a wide list of available tools to collect, interpret, analyze, and represent geotechnical features to address hazards. However, many of the existing researches present a gap between the interpretation of collected data and enhanced visualization tools, which could range from simple two dimensional X-Y plots to more interactive three-dimensional modeling of the subsurface conditions. Geotechnical engineers are looking for innovative tools which can improve the design and evaluation to handle uncertainties and variations inherent in soil and rock properties in a more favorable manner (Hammah and Curran 2006).

Geotechnical hazards of hydraulic fill dams were widely covered in the last section, and a vital step for addressing those hazards is to understand the soil configuration of this type of structure, which presents high variability in its properties. Enhanced visualization tools are necessary to overcome the uncertainties inherent in soil properties. Broad-based applications of geostatistics facilitate easier incorporation of the inherent uncertainty of soil mass into numerical models (Hammah and Curran 2006). The following sections present an overview of geotechnical visualization techniques traditionally used by practitioners to better understand the subsurface before conducting any geotechnical hazard assessment.

2.6.5.1 Conventional Geotechnical Visualization Techniques

A tremendous challenge for geotechnical engineers deals with the access, view and the interpretation of geotechnical data in a consistent and favorable format (Ellis and Vessely 2015). Visualization techniques for soil subsurface can be addressed based on high-quality data collected over a specific site. Geotechnical data can vary in type and

can be stored and accessed by different methods, such as reconnaissance; exploration; and testing (i.e., CPT, SPT); instrumentation (i.e., piezometers, inclinometers); remote sensing devices (i.e., gravimetric surveys); and geophysical devices (i.e., seismic refraction). Whether or not a specific type of collecting data method is used, the vital step to modeling geotechnical data is to apply available tools in an efficient and realistic manner.

Data visualization tools varies from typical X-Y graphing software to sophisticated systems that combines multiple graphic tools based on complex database and image acquisition tools. A report prepared by Hollie et al. (2015) includes a basic list of existing geotechnical visualization technologies that includes the following.

Spreadsheets and *boring log generators* are considered and used for visualization of geotechnical data by generating x-y graphs which will be useful for the illustration of data relationships such as CPT and SPT data interpretations. Spreadsheets are mainly created to interpret general geotechnical information based on existing correlations by inputting users' data (i.e., shear strength based on tip resistance). A boring log generator is often referred to as software that employs user data input, and uses existing correlations to output a completed log interpretation (Ellis and Vessely 2015), as shown in Figure 2-40.

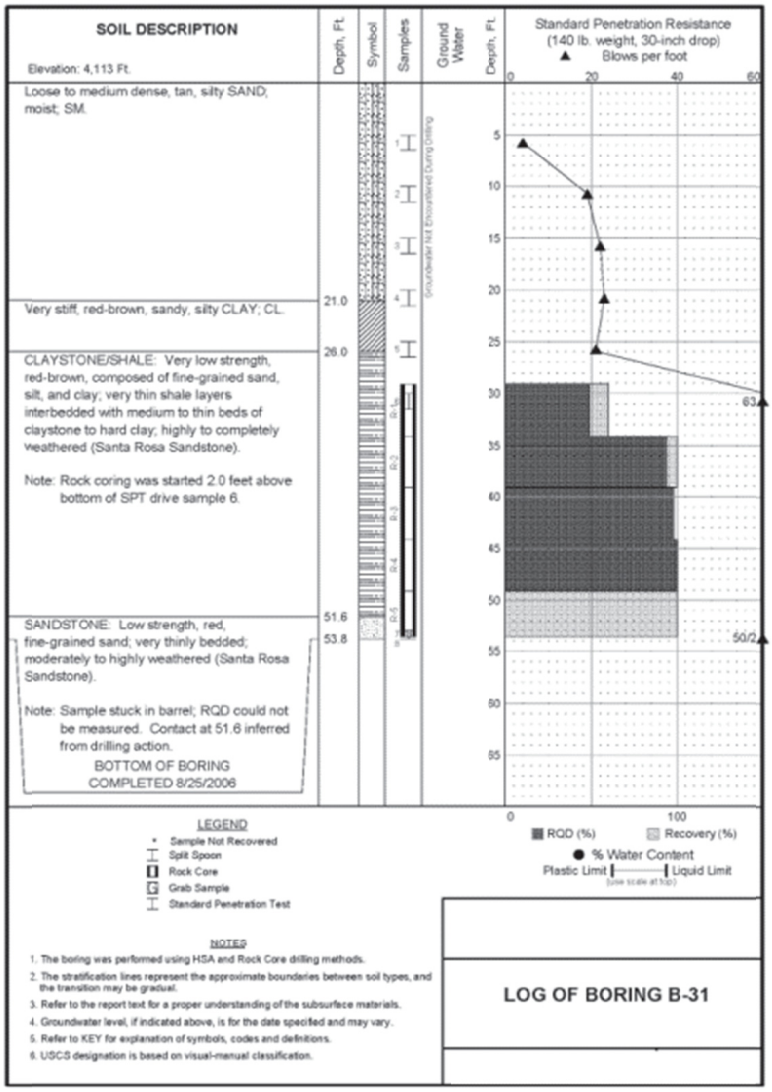

Figure 2-40 Typical boring log (Ellis and Vessely 2015)

A boring log is considered the simplest way to visualize collected data in geotechnical engineering. However, the interpretation of single boring logs is not the most adequate approach to understanding the subsurface before any geotechnical assessments. Therefore, it is necessary to collect data from several boring logs, perform

a correct interpretation, and incorporate visualization tools to combine the analyzed information.

The traditional technique used to interpret boring logs is known as *Fence Diagrams.* Fence diagrams integrates the information from different subsurface explorations and create a cross-sectional view of soil configuration or stratigraphy with corresponding soil properties and ground water location, as shown in Figure 2-41 (Ellis and Vessely 2015). Fence diagrams are often created by predicting soil layers based on the conventional statistical methods covered in the last sections. They are usually generated by commercial software that uses input from boring log data (i.e., SPT or CPT) to interpret and visualize data by performing basic interpolations. More advanced interpolation techniques, such as geostatistics interpolation methods, have recently been used for the prediction of subsurface by the creation of fence diagrams (Bheemasetti 2014), and are summarized in the following sections.

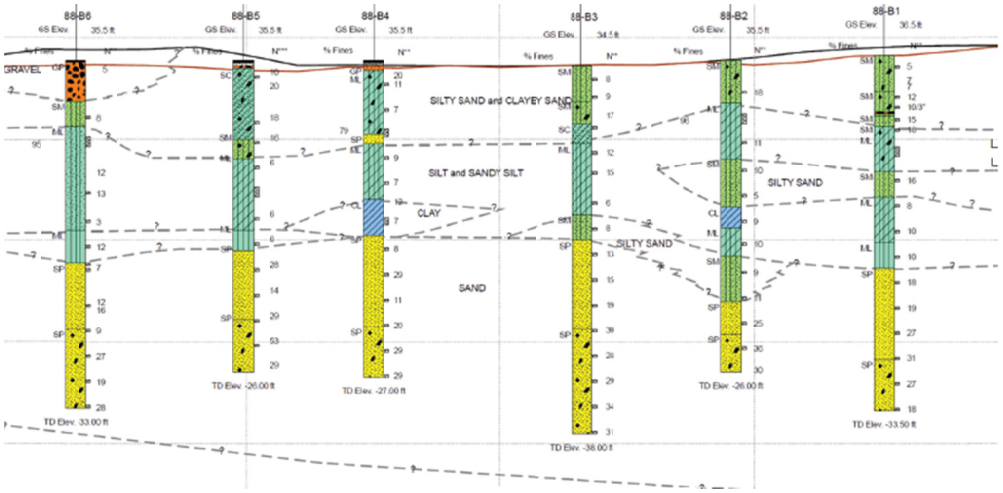

Figure 2-41 Typical fence diagram (Ellis and Vessely 2015)

Several other techniques are also considered as visualization tools, such as *laboratory software* that interprets laboratory data and converts it into relevant

engineering units to visualize and present laboratory results; The scheduling, collection, processing and visualization of data can also be obtained from installed instruments at the site (i.e., inclinometers, piezometers) by using *instrumentation software*; *geographical information systems* (GIS); *image analysis software;* and *web-based imaging systems.* These tools are primarily used to visualize surface areas (i.e., create interactive maps, ground penetrating radar, GPR, and LiDAR). Whether or not specific visualization tools are used, soil modeling has been primarily considered only in two dimensions in the existing literature; little research has considered soil as a three-dimensional mass that can vary in all three directions. Most of the available research using three-dimensional models was created by using conventional interpolation methods after data collection. The following section includes several applications for visualizing and modeling soil based on geostatistical methods.

2.6.5.2 Geotechnical Data Visualization using Two-Dimensional Models based on Geostatistics

There are several benefits of employing geostatistical analyses in geotechnical engineering. It provides powerful tools for performing relatively simple but accurate models of non-homogenous materials based on limited sample data. Also, it contains techniques for optimizing sampling locations and the methodologies for estimating geotechnical properties at unsampled locations, with minimum estimation errors. Hammah (2005) presented a study that includes an application of geostatistics in a channel tunnel project, where optimization studies were performed along the alignment of the tunnel based on a Kriging interpolation of geologic layers.

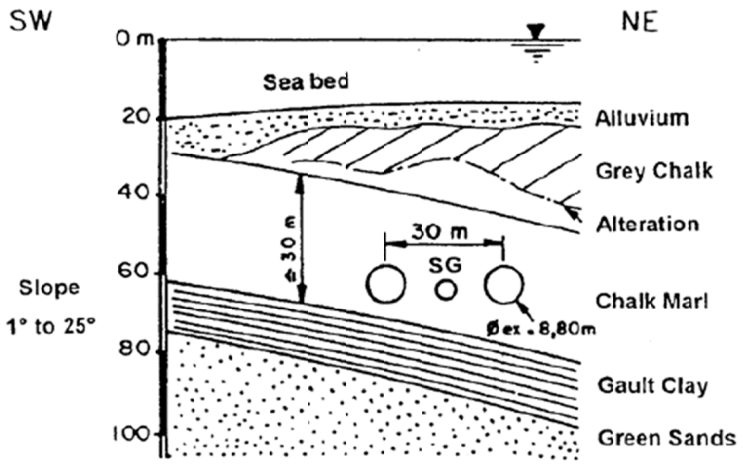

Figure 2-42 Geological cross-section of the Channel Tunnel project (Hammah and Curran 2006)

The two-dimensional Kriging interpolation allows engineers to determine the boundary between two different types of soil stratigraphy along the tunnel and to improve the tunnel's alignment, as shown in Figure 2-42. Bheemasetti (2014) presented a framework for applying geostatistics in geotechnical engineering projects, and demonstrated several studies where two-dimensional interpolation for different soil properties was obtained. The analyses consisted of predicting the stiffness values of a controlled low strength material (CLSM), which was used around an underground pipe to overcome bedding material issues. Geostatistics was primarily used to study the variations in CLSM stiffness properties with time (Bheemasetti 2014). Figure 2-43 illustrates the two-dimensional Kriging interpolation of data collected along the pipe.

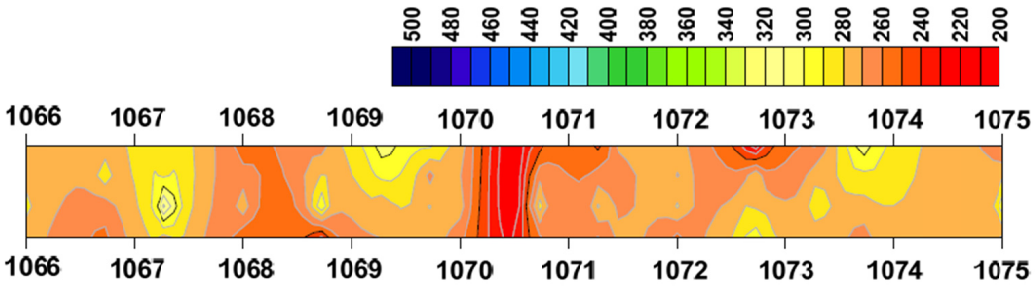

(a)

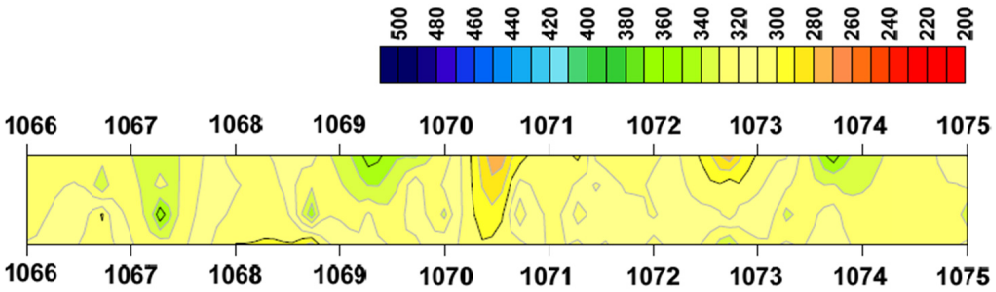

(b)

Figure 2-43 Kriging analysis map for stiffness (MPa); (a) After 3 days during period, (b) After 7 days curing period (Bheemasetti 2014)

A regression co-Kriging approach was performed by Heuvelink (Heuvelink et al. 2016) to map soil properties simultaneously for multiple soil horizons. Omran (2012) performed a study that compared how Kriging was more suitable than conventional interpolation methods for addressing soil properties in a study area in Egypt. Universal Kriging was compared with other methodologies that clearly demonstrated its accuracy.

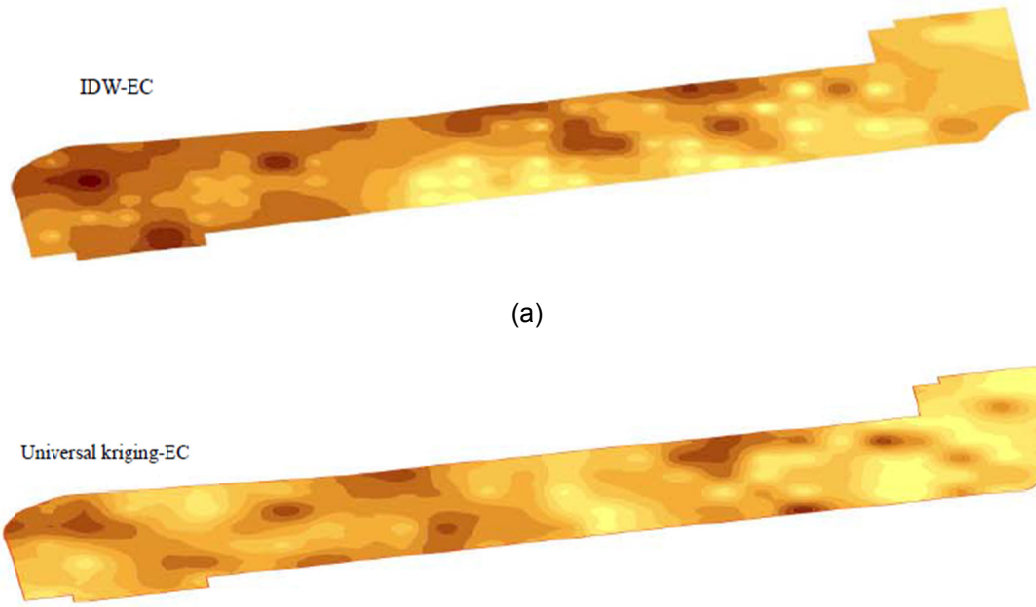

Figure 2-44 (a) Inverse distance interpolation, (b) Universal Kriging interpolation.

Electrical conductivity of soil (Omran 2012)

Limited research is available on modeling soil properties in three-dimensions by using Geostatistics. Due to the complexity of algorithms for interpolations, software is required for performing such calculations. In 2005, Choi and Park (Choi and Park 2006) introduced an integration of Geographical Information System (GIS) and 3D geostatistical methods for geotechnical characterization of soil properties. The latest work developed by Caballero (2016) presented an introductory study, based on in-situ-collected data, on the visualization of aging embankment structures by using the Kriging interpolation through the use of innovative software capable of performing estimations with a high number of data (Caballero et al. 2016).

Three-dimensional visualization of property variability in space is a tremendous benefit of geostatistical analysis (Hammah and Curran 2006). When it is properly

implemented, such analysis allows different hypotheses and assumptions on variability to be readily tested. The present study presents a framework that results in visualization models based on a geostatistical prediction that considers spatial variability and spatial continuity of data collected from a hydraulic fill dam. Visualization models were predicted by Ordinary Kriging and by considering spatial anisotropy of data, as well and present soil properties models, based on interpolation of CPT data collected from dams at different locations.

Three-dimensional visualization modeling can also enhance evaluations of geotechnical hazards. Liquefaction was defined as one of the most important hazards for hydraulic fill structures located in seismic areas. Although the hazards may vary from one location to another, the effective use of geotechnical data visualization tools and methodologies in one location can be applied to a series of conditions, events, and objectives in another location (Ellis and Vessely 2015). The present research also presents a visualization model of liquefaction assessment based on in-situ test data interpretation performed by existing liquefaction triggering methodologies described in earlier sections.

Several hydraulic fill dams are actively in operation and located in areas where seismic activity was previously non-existent. However, areas such as the Central United States have been subjected to seismicity over the past decade. Three-dimensional visualization models are developed based on the liquefaction assessment for hydraulic fill dams located in specific regions within the Central United States. A simplified seismic hazard analysis is generated to combine liquefaction evaluations with the generation of three-dimensional visualization models. The following section presents a brief review of seismic hazard analysis.

2.7 Seismic Hazard Analysis

2.7.1 Introduction

A seismic hazard is described as a natural, earthquake-generated phenomenon such as ground shaking, fault rupture, and soil liquefaction (Kramer 1996). Several hydraulic fill dam failures have occurred after strong and long-duration seismic events. The vulnerability of hydraulic fill dams to accidents and failures from long-duration seismic ground motions was clearly demonstrated during the 1971 San Fernando, California earthquake (National Research 1983). Seismic hazard analysis is often developed in areas where the threat of natural earthquakes is constant (i.e., California, New Madrid area).

Other areas, such as the Central United States, were previously considered as non-seismic regions due to their location in the middle of the intercontinental plate. However, the sudden increase of seismic activity alerted engineers to perform safety evaluations for all civil infrastructures in this region, especially in areas like Oklahoma, Texas, Colorado, and Arkansas. The present research develops a simplified seismic hazard analysis for the area of North Texas where several hydraulic fill dams are still active and require surveillance and safety evaluations.

2.7.2 Recent increase of Seismic Activity in Central United States

Earthquake activity within the Central United States has suddenly increased more than an order of magnitude since late 2009 (Rubinstein and Mahani 2015). Such rate of increase is having dramatic implications for the seismic hazards throughout the regions like Oklahoma, Colorado, and Texas, where the existing infrastructures were not designed to sustain seismic events. Significant damages were reported from the 5.7 magnitude (M) earthquake that occurred in 2011 in Prague, Oklahoma, as well as several

more recent events, such as the M5.8 Pawnee and M5.0 Cushing earthquakes in Oklahoma during late 2016. Recent studies have demonstrated the importance of having a modern seismic hazard for this region by considering induced and natural earthquakes.

Holland et al. (2013) presented a probabilistic seismic hazard assessment for the Arcadia, Oklahoma, Dam site, based on the rate of seismic activity from 2009 to 2013 (Holland et al. 2013). Results showed that the ground motion for the M5.7 Prague, OK earthquake exceeded the 2,000 year ground motion at the Arcadia, Dam site calculated by past researchers (Lawson 1985). Figure 2-45 illustrates a cumulative record of earthquakes (M>3) from 1973 to April 2015 and the sudden increase in seismicity which has been present since 2009 in areas of Oklahoma, Arkansas, and Texas.

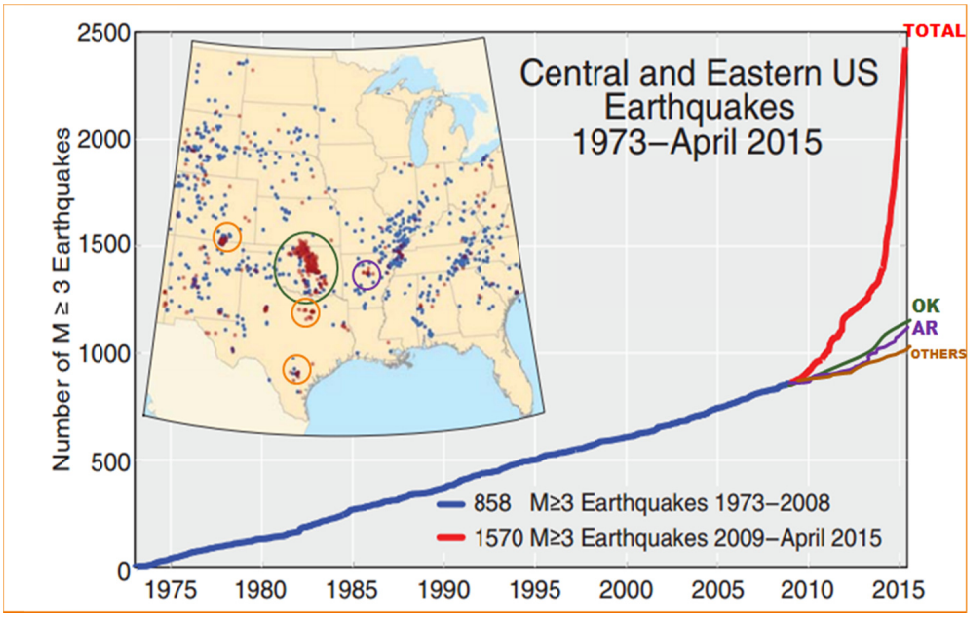

Figure 2-45 Increase of seismic activity in Central US (Rubinstein and Mahani 2015)

Several seismic hazard maps have been presented by the United States Geological Survey (USGS), as shown in Figure 2-46. However, such maps do not

consider the recent seismic activity in the Central US and cannot be used for seismic hazard assessment.

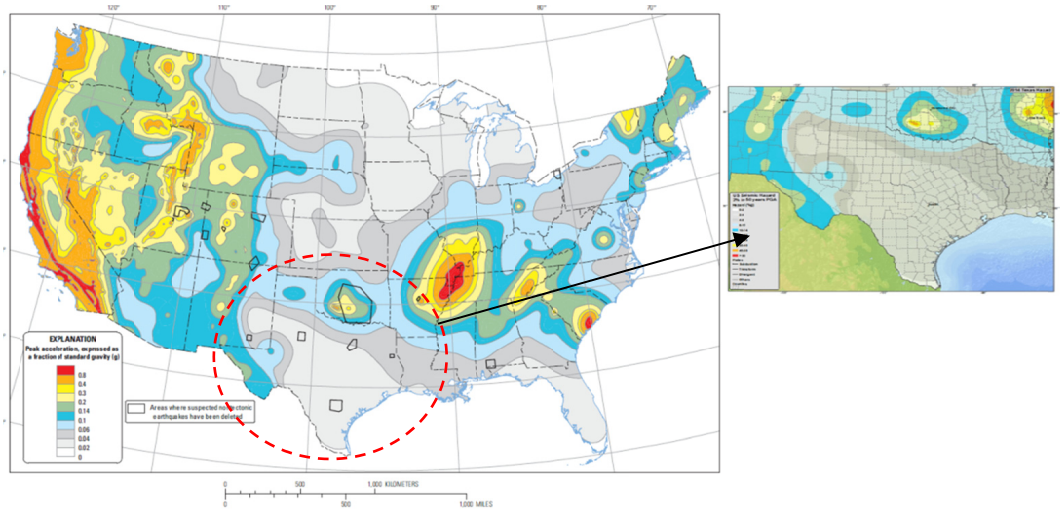

Figure 2-46 Seismic hazard in US. Two-percent probability of exceedance in 50 years (USGS 2005)

USGS initiated a compilation of seismic records by installing several seismometer systems around the Central United States, including areas such as Oklahoma and Texas. An updated map of seismic events recorded was released by USGS in late 2015, illustrating the increase of seismic events from 2009-2015, as shown in Figure 2-47. The cause of the increased seismic activity in the region can be attributed to several things, which are being currently discussed and studied. However, the present research does not intend to define causes for the increase of earthquakes, but to consider the available records to determine a simplified seismic hazard analysis based on the concepts of geotechnical earthquake engineering. Figure 2-47 also illustrates specifically the region of North Texas where there has been an increase in the number of

earthquake events, but where civil infrastructures were not previously designed to sustain seismic forces.

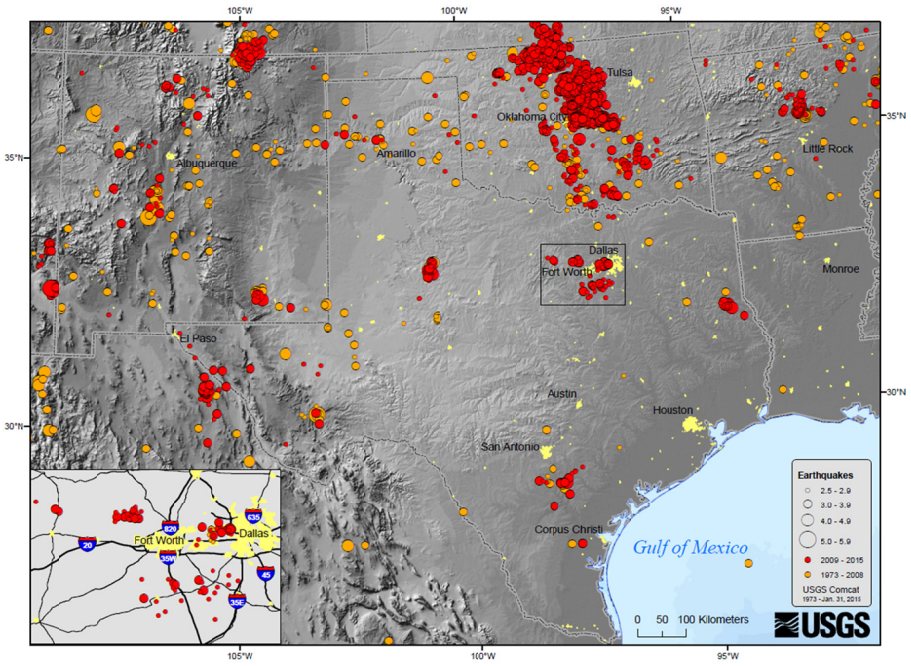

Figure 2-47 Seismic events recorded by USGS during different periods of time in Central United States (USGS 2015)

According to Kramer (1996) a seismic hazard analysis involves the quantitative estimation of ground shaking at a particular site. Seismic hazards analyses may be defined deterministically, when a particular earthquake scenario is assumed; or deterministically, when uncertainties are considered in earthquake size, location, and time of occurrence (Kramer 1996). The following sections present the methodology often use to address seismic hazard analysis. The goal of the present section is to introduce a simplified approach for the identification and characterization of earthquake sources, which becomes an issue due to the lack of fault mapping in those regions.

2.7.3 Identification and Evaluation of Earthquakes sources

A seismic or earthquake source is described as a geologic structure or domain within which the spatial and temporal occurrances or seismic events are approximately uniformily distributed (Kramer 1996). Potential sources that may generate future strong ground motion must be identified and evaluated. Identifying sources becomes an easy step where modern seismographs and seismographic networks are present (Kramer 1996). However, seismographic networks have been deployed only to areas where there has been constant seismicity and/or expected earthquakes are likely to occur (i.e., California, New Madrid area). In areas where seismicity is rarely present, there is no reason for engineers to install equipment to make observations and interpretations; therefore, mapping of potential seismic sources has not been generated. North Texas is one of such areas where seismic activity was previously non-existent, but it now shows an increase of seismicity, demonstrated by earthquakes that occurred few years ago (i.e., M3.6 Azle TX, M4.0 Venus TX, and M3.6 Iriving TX).

Seismic sources are generally identified by the use of instruments; however, in the absence of instrumental seismic records, several other types of identification may be useful, such as the geologic and tectonic evidence or historical seismicity (Kramer 1996), as shown in Figure 2-48. In areas where seismic activity is often present, the identification of sources becomes an easy task. For the Central United States, several seismograph network were installed after seismic events in Oklahoma (i.e., M5.7 Prague, OK earthquake). Since seismic activity continues to increase, the data recorded by seismographs has identified several active faults that were not easily found before. However, it is part of an extensive and time consuming work, and faults are identified after the earthquakes occur. Regions with a recent increase of seismicity (i.e., North

Texas and Arkansas), where no seismograph networks are available, do not have detailed fault mapping or seismic sources.

Figure 2-48 Tectonic evidence of seismic sources. Strike Slip Fault, Turkey (Bachuber 2010)

Seismic sources are required to be characterized geometrically, which is a relatively easy task for areas where faults have been identified. Several types of seismic sources can be considered for the calculation of seismic hazards in a specific region, based on their geometry. A *point source* refers to volcanos or distant short faults, and has a constant source-site distance. A *linear source* refers to shallow and distant faults and is correlated to only one geometric parameter that controls that distance (i.e., depth of fault). An *areal source* is related to a constant depth crustal source, where two geometric parameters control the distance (i.e., width and length). Unlike the last three seismic sources described, the *volumetric sources* refer to those where three geometric parameters control the distance (i.e., x, y, and depth). In areas of North Texas where low

seismic activity is recorded, determining the seismic source or domain for calculating the seismic hazard is challenging. Kramer (1996) stated that *"areas where earthquake mechanisms are poorly defined, or where faulting is so extensive as to prelude distinction between individual faults, can be treated as three-dimensional volumetric sources."*

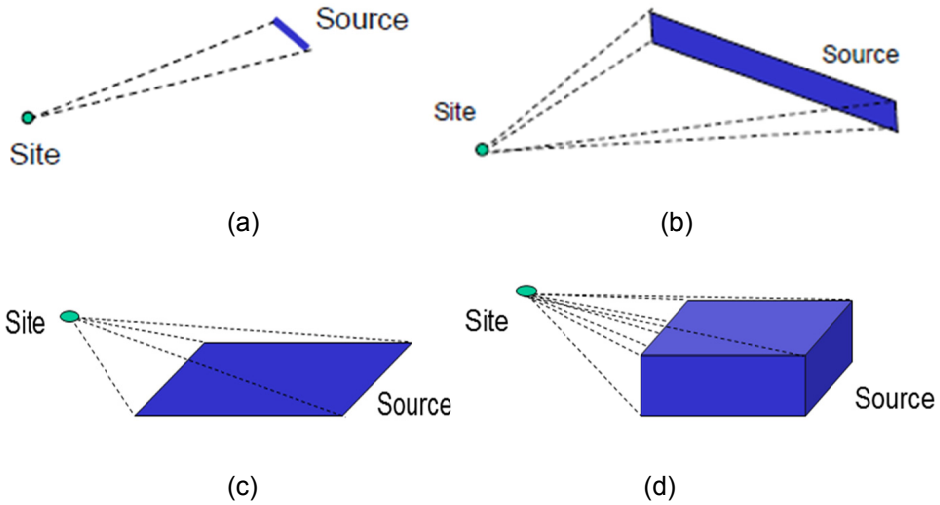

Figure 2-49 Seismic sources geometric characterization (Tang 2015)

The present research developed a seismic hazard analysis for North Texas based on the generation of *volumetric sources*. Spatial and temporal normalization is an important characteristic of seismic sources (Kramer 1996); therefore, univariate statistics were used to evaluate the normalization of data sources.

2.7.3.1 Histograms

Histograms produce a relatively good interpretation of the dispersion encountered in any type of data (i.e., geotechnical data). In general, it is a statistical tool that relates to the distribution of seismic events within one specific source (Figure 2-50). The extent of each bin refers to the number of observations falling within a particular bin size or range of values. Bheemasetti (2014) presented the mathematical equations used

for the generation of a histogram found in the literature. The class interval (CI) can be defined by the Equation 2.5 (Sturges 1926):

$$No.of\ Class\ Intervals = 1 + 3.3log_{10}N \quad 2.5$$

Where N is the total number of samples or observations in the data set (i.e., distances to the fault). After the class interval (CI) is defined, the bin size is obtained by using Equation 2.6. It is noted, that the bin size can be rounded off to the nearest decimal point in the histogram plotting settings.

$$Bin\ Size = \frac{Maximum\ Value - Minimum\ Value}{Number\ of\ Class\ Intervals} \quad 2.6$$

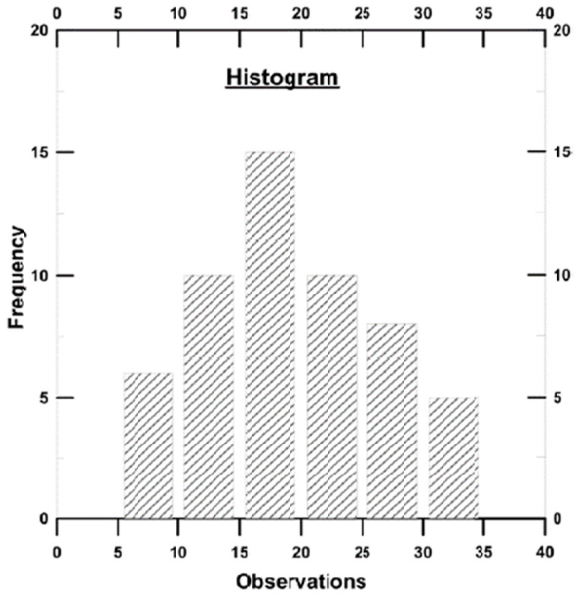

Figure 2-50 Plot of histogram (Bheemasetti 2014)

2.7.3.2 Chi-Square Test

The majority of statistical tests are based on normal distribution, therefore, normal distribution of the soil properties data should be checked (Bheemasetti 2014). Since a seismic source is characterized by the spatial and temporal normalization of data, the distribution of distances from the source to the site, as well as the occurrence of

earthquakes within a source, must be checked for having normal distribution. There are several tests for checking the normalization of data found in the literature, such as the Normal-Quantile plot (n-q plot) and the Shapiro-Wilk test. However, the present study used the Chi-Square test, a strong test for checking normalization of data, for the analysis of distribution and characterization of the source.

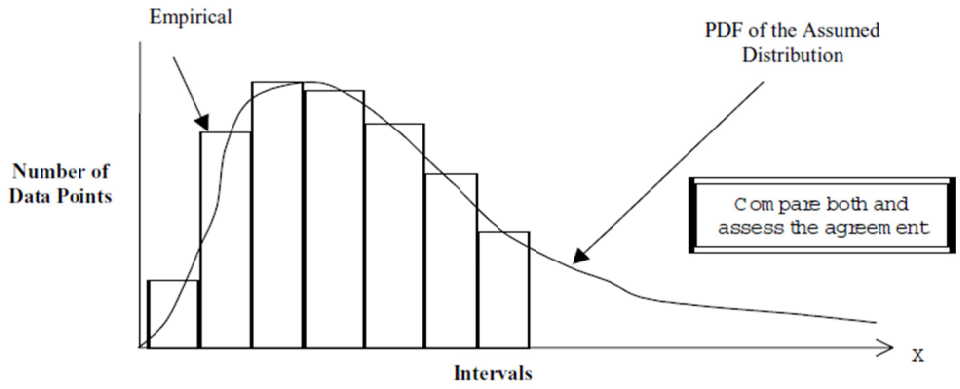

Figure 2-51 Area Goodness of Fit Test (START 2003)

The Chi-Square test is a simple test, and is suitable for a large set of data. The concept of this test is based on the probability density function (PDF) of an assumed distribution. The PDF (yielding an area of unity) should closely encompass the data range only if the assumed distribution is correct. For example, the selected convenient values in the data range in Figure 2-51 are divided into several intervals. Then, the number of data points is computed for each interval, which are called “observed” values. Once the observed values are obtained, the “expected” values are calculated. Based on the PDF of the assumed distribution, the expected values are those that ranged within the same subintervals. The Chi-Square test requires at least five of them in subintervals.

Finally, a comparison between two sets of values is performed, and the assumed distribution is supported only if both set of values agree probabilistically. The name of the

Chi-Square test comes from the statistical formula that uses the difference between "expected" and "observed" values and follows a Chi-Square distribution (Equation 2.7).

$$\chi^2 = \sum_{i=1}^{k} \frac{(e_i - o_i)^2}{e_i} \sim \chi^2_{k-1-nep} \quad 2.7$$

Where,

e_i: expected number of data point in cell I (e_i>5)

o_i: actual (observed) number of data points in cell I;

k: total number of cells or subintervals in the range;

n: sample size for implementing the Chi-Square test (n>25*K)

k: total number of cells or range subintervals

k-1: No. estimated parameters (nep); Chi-Square degrees of freedom (DF>0)

χ^2_γ: Chi-Square distribution (table) with DF=γ

2.7.4 Ground Motion in Central United States

The effect of earthquakes is primarily characterized by the strong motion produced at one specific site, and can be quite complicated to describe (Kramer 1996). The evaluation of any seismic hazard analysis is described by the ground motion expected at that specific site, and it is measured by using Ground Motion Predicting Equations (GMPEs) (Atkinson 2015). Ground motion is generally described by ground motion parameters in two groups: amplitude parameters, such as peak ground or horizontal acceleration (PGA or PHA), peak ground velocity (PGV), or peak ground displacement; and frequency content parameters (ground motion spectra) that include the Fourier spectra, power spectra, and response spectra. There are several others that fall into a different group, such as the spectral parameters (bandwidth, central frequency, and shape factor (Kramer 1996).

Despite the fact that seismic parameters are considered for the seismic hazard analysis, they are generally obtained based on the application of GMPEs of a specific site. GMPEs are mainly developed by using regression models that relate any ground-motion parameters (the most commonly used is the peak ground acceleration, PGA, and the pseudo-spectral acceleration, PSA) to seismological parameters of a specific region, such as earthquake magnitude, source-to-site distance, local site conditions, and style of faulting (Pezeshk et al. 2011).

In the Central US, and due to the past low seismicity, the generation of GMPEs has been a challenge. For regions in the Central US, such as Oklahoma, Texas, Arkansas, and Colorado, various characteristics of seismic activity can be determined based on a collected earthquakes record. According to the USGS classification, earthquakes in this region are considered shallow earthquakes, since their hypocenters are located at shallow depths (4-20 km) compared to other regions where hypocenters are located at higher depths (>40 km) (i.e., California). It is believed that earthquakes can be attributed to human activities (i.e., mining and oil-extracting activities) or natural causes (i.e., reactivation of faults).

A key requirement for the accurate assessment of seismic hazards and risks is to develop ground-motion-predicting equations (GMPE) for a specific site of interest. Several studies have developed GMPEs by using catalogs of earthquakes believed to have originated from mining or oil extracting activities. Edwards et al. (2013) predicted ground motions from induced earthquakes that occurred in areas where geothermal energy was developed for electrical power production (Edwards and Douglas 2013). Douglas (2011) presented a report gathering GMPEs developed from 1964 to 2010 and commonly used for seismic hazards in the Central United States (Douglas 2011).

However, those GMPEs did not consider the new catalog of earthquakes that was compiled for the increase of seismic activity in the region that occurred in 2009 and thereafter. Atkinson (2015) presented an updated study where GMPEs were developed based on induced seismicity in the United States and were also combined with the existing catalog of earthquakes. The study was mainly focused on small-to-moderate events (M3-6) at relatively short hypocenter distances (less than 40 km). The present research considers the development of the seismic hazard for a site located in North Texas. Ground motion calculated for the site of interest was based on the study developed by Atkinson (2015) described earlier, which was drawn from the Next Generation Attenuation-West 2 (NGA-West 2) database. GMPEs depend directly on the magnitude and source-to-site distance and various coefficients defined by Atkinson (2015), after the statistical regression.

$$\log Y = C_0 + C_1 M + C_2 M^2 + C_3 \log R \qquad 2.8$$

in which Y is the ground-motion parameter (specifically, the orientation-independent-horizontal component 5% damped pseudo-spectral acceleration [PSA] at a given frequency, or the PGA, or PGV); logs are in base 10; M is moment magnitude; and R is an effective point-source distance that includes near-source distance–saturation effects using an effective depth parameter (see Atkinson and Silva, 2000; Boore, 2009; Yenier and Atkinson, 2014) shown in Equation 2.9.

$$\mathrm{R} = \sqrt{\mathrm{R}_{\mathrm{hypo}}^2 + \mathrm{h}_{\mathrm{eff}}^2} \qquad 2.9$$

$$h_{eff} = \max(1.10^{(-1.72+0.43M)}) \qquad 2.10$$

To constrain near-source behavior, Atkinson established Equation 2.10, in which the distance-saturation parameter, h_{eff}, is as determined by Yenier and Atkinson (2014) from stochastic modeling of a range of global events of M ≥6:0 (Yenier and Atkinson

2014). Note that a minimum value of h_{eff} = 1 km is specified. A limitation of the GMPE derived herein for seismic hazard application is that the simplicity of the selected functional form restricts its applicability to distances less than about 60 km. In conclusion, GMPEs derived by Atkinson (2015) induce a significant and larger ground motion than the GMPEs commonly used for the Central United States.

Table 2-1 Coefficients of Equation 2.8 (Atkinson 2015)

PSA at Frequency	*c*0	*c*1	*c*2	*c*3	σ-intra	σ-inter	σ-total
0.2	−4.321	1.08	0.009376	−1.378	0.25	0.18	0.31
0.33	−3.827	1.06	0.009086	−1.398	0.24	0.22	0.32
0.5	−4.462	1.485	−0.03815	−1.361	0.24	0.23	0.33
1	−4.081	1.742	−0.07381	−1.481	0.26	0.22	0.34
2	−3.873	2.06	−0.1212	−1.544	0.29	0.2	0.35
3.33	−2.794	1.852	−0.1078	−1.608	0.3	0.19	0.36
5	−2.266	1.785	−0.1061	−1.657	0.3	0.21	0.37
10	−1.954	1.83	−0.1185	−1.774	0.29	0.25	0.39
20	−2.018	1.826	−0.1192	−1.831	0.28	0.3	0.41
33	−2.283	1.842	−0.1189	−1.785	0.28	0.27	0.39
PGA	−2.376	1.818	−0.1153	−1.752	0.28	0.24	0.37
PGV	−4.151	1.762	−0.09509	−1.669	0.27	0.19	0.33

Equation (1) predicts 5% damped horizontal-component pseudospectral acceleration (PSA, in cm=s2) for B/C site conditions, peak ground acceleration (PGA, in cm=s2), and peak ground velocity (PGV, in cm=s). The standard deviation of residuals (σ-total) and its intra-event and inter-event components are also given.

Several other GMPEs were also used for addressing the deterministic seismic hazard analysis (Torild van et al. 2006; Pezeshk et al. 2011). For probabilistic hazard analysis, GMPEs from Atkinson (2015) were used. Once the ground motion at a specific site has been defined, the seismic hazard can be calculated based on two basic approaches: deterministic and probabilistic seismic hazards. Both use the same basic body of information to establish the design earthquake. The major difference is that the probabilistic methodology systematically examines the uncertainties and includes the

likelihood of a specific earthquake exceeding the design ground motion. All of the elements of a deterministic analysis are included in the probabilistic approach. The present research includes both analyses for the seismic hazard at the site of interest, and then they are compared to select the worst case scenario to use for geotechnical assessments. A brief example of final results for both approaches is presented below.

An example of a *deterministic seismic hazard* is: “The seismic hazard for the site of interest consist on a peak ground acceleration of 0.22g that resulted from an earthquake magnitude of M5.0 with a hypocenter on the San Andreas Fault located at a distance of 6 miles from the site.” On the other hand a *probabilistic seismic hazard* output is: “The seismic hazard for the site consists on a peak ground acceleration of 0.28g with a 2 percent probability of being exceeded in a 50-year period.” The following section includes the steps for calculating the seismic hazard by using both approaches.

2.7.5 Deterministic Seismic Hazard Analysis

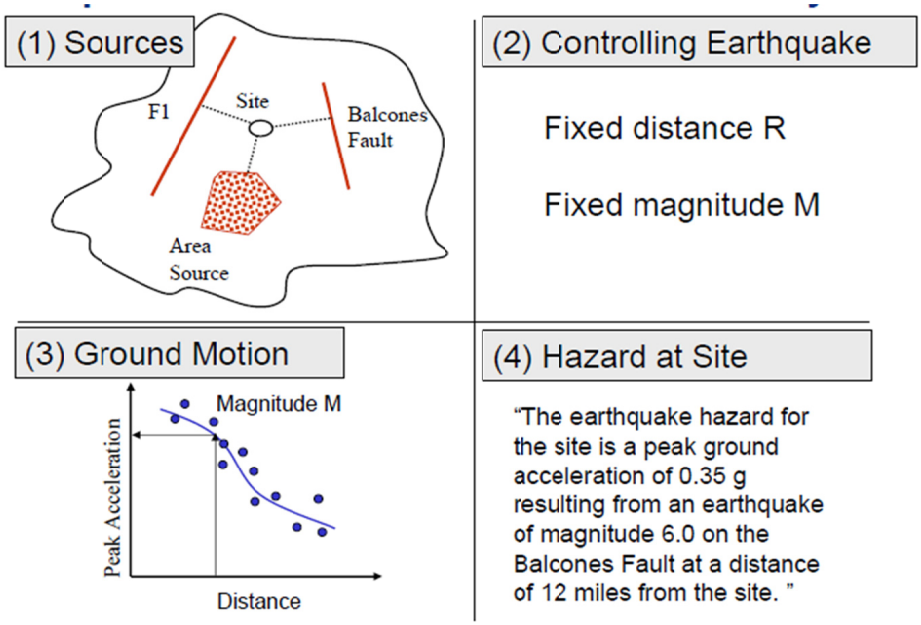

Figure 2-52 Steps for deterministic seismic hazard analysis (FEMA 2007)

According to the US Army Corps of Engineers (USACE 2016), the DSHA approach uses the known seismic sources that can affect the site, along with the available historical seismic and geological data to generate *discrete, single-valued* events or models of ground motion at the site of interest. It mainly considers that earthquakes occur at the source closest to the site. In deterministic analysis, the closest source-to-site is commonly used to determine the ground motion. A vital step in any seismic hazard is to apply right attenuation relationships that are characteristic to the local geology.

Figure 2-52 illustrates the basic steps in the deterministic analysis. The initial step consists on the identification of all the possible sources capable of producing significant ground motion described in earlier sections. Some of these will be easy to identify (e.g., a known active fault); however, others may be more complicated to spot and characterize (i.e., North Texas region). Each seismic source is characterized by the selection of a source-to-site distance parameter for each seismic source. In most DSHAs, the calculation of the ground motion is primarily in terms of the shortest distance from the source to the site (R_{min}).

Also, each source is usually characterized by the maximum credible earthquake (MCE), which is considered as the largest earthquake magnitude that could occur along a recognized fault or within a particular seismic source (FEMA 2005). The loading resulting from the MCE often is exceeded for probabilistic methods for high-return period faults (i.e., San Andreas Fault). However, it involves various subjective and intuitive decisions, particularly regarding earthquake potential that may require expertise from professionals who already perform seismic hazards at similar sites.

The second step consists of selecting the controlling earthquake (i.e., earthquake that is expected to produce the strongest level of shaking), which is generally expressed

in terms of any ground motion parameter (i.e., PGA or PGV) (Kramer 1996). Therefore, the ground motion using GMPEs based on MCE and R_{min} must be calculated for each source identified in Step 1. The selection is performed by comparing the different levels of shaking produced by seismic sources, as shown in Figure 2-53. Finally, the hazard is defined by using the controlling earthquake obtained from the comparison.

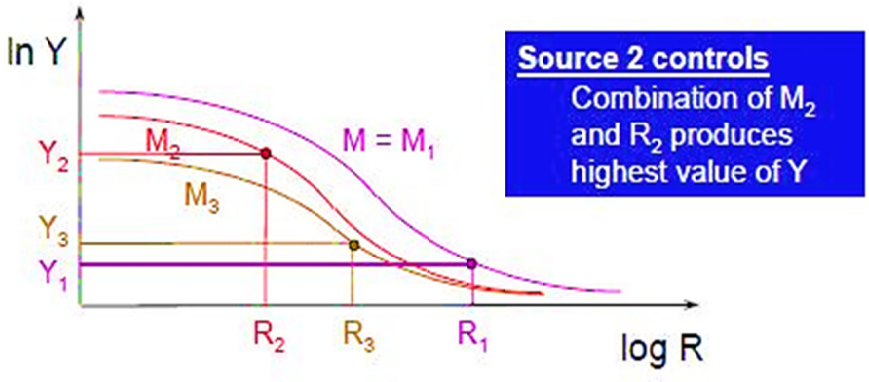

Figure 2-53 Selection of controlling earthquake (FEMA 2005)

The deterministic approach is quite simple; however, DSHA provides no indication of how likely the design earthquake (i.e., MCE) is to occur during the life of the structure (FEMA 2005). Design earthquakes may occur every 200 years in some places, or every 10,000 years in others. Note that nothing is being said about probability of occurrence. In the present research, it is expected that the deterministic seismic hazard analysis will result in very low ground motion at the site of interest since the maximum magnitudes are very low. The probabilistic seismic hazard approach is more appropriate for the Central United States.

2.7.6 Probabilistic Seismic Hazard Analysis

Several concerns and conceptual problems can arise when deterministic approaches are used, such as the variability in the design event (i.e., design earthquake)

and the variability of ground motion intensity for a given earthquake event (Baker 2008). In this section, a probability-based framework is described, including concepts and mathematical approaches to incorporate those conceptual problems.

A PSHA does not search for the elusive worst-case ground motion intensity as the DSHA does. Rather, it considers all possible earthquake events and resulting events including their corresponding probability of occurrence, to finally find the level of ground motion intensity exceeded with some sufficiently low rate (Baker 2008). In general, the PSHA is established based on four steps:

1. Identification of all earthquake sources of producing significant ground motion;
2. Characterization of the distribution of earthquake magnitudes (rates at which earthquakes of various magnitudes are expected to occur). Characterization of all source-to-site distances associated with potential earthquakes;
3. Prediction of the resulting distribution of ground motion intensity in terms of each magnitude and source-to-site distance combinations found in Step 2;
4. Combination of all uncertainties in earthquake size, location, and ground motion intensity, using the total probability theorem computation (Baker 2008).

The final result is a full distribution of levels of ground shaking intensity and corresponding rates of exceedance, which can be illustrated with seismic hazard curves developed for the site of interest. PSHA results can be used to identify a ground motion intensity having an acceptably small probability of being exceeded.

2.7.6.1 Identification of Earthquake Sources

Unlike in the DSHA, where seismic sources are focused on identifying the one which causes the largest possible earthquake, the identification of earthquake sources in a PSHA intends to recognize all earthquake sources capable of producing significant damaging ground motions at the site. Once all sources are identified, the distribution of magnitudes and source-to-site distances associated with earthquakes from the sources are defined.

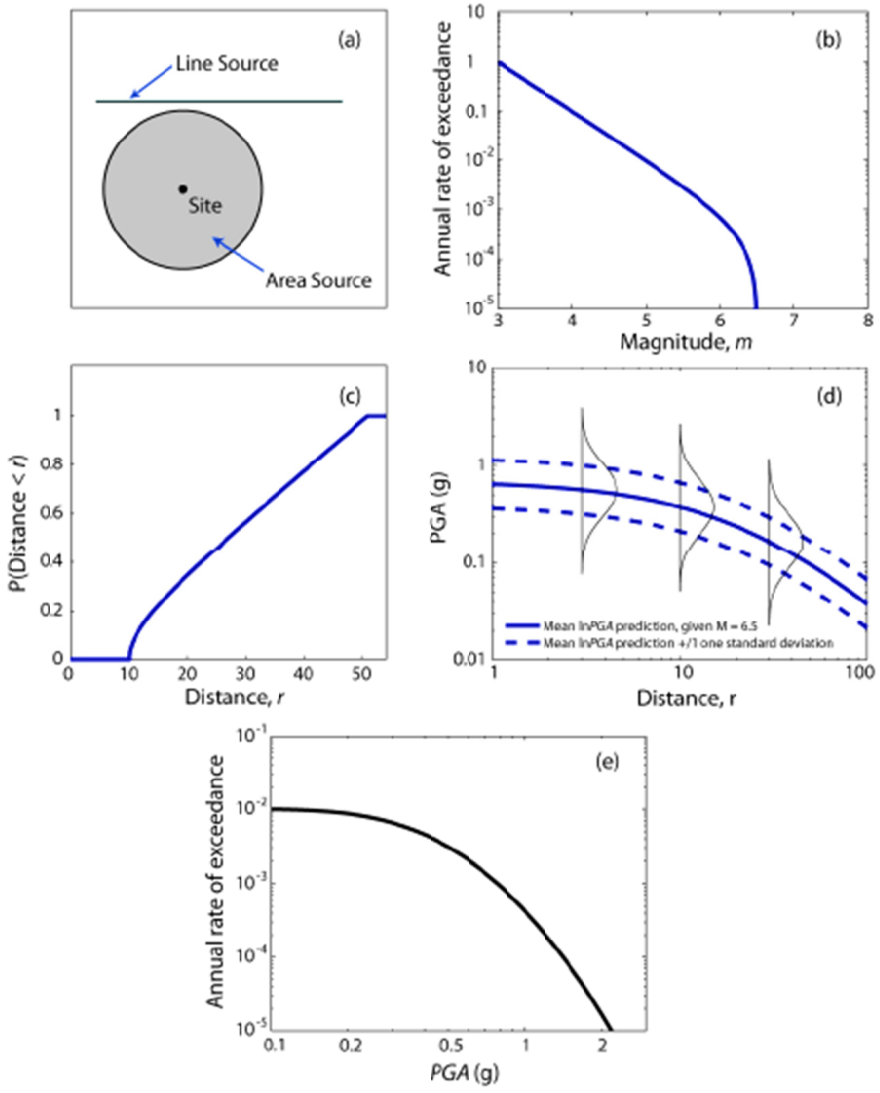

Figure 2-54 Steps for PSHA calculation (Baker 2008)

2.7.6.2 Size Uncertainty

Size uncertainty refers to the distribution of earthquake magnitudes from all sources. Tectonic faults are able to produce earthquakes of various sizes (i.e., magnitudes) (Baker 2008). Gutenberg and Richter (1944) performed their study on observations of earthquake magnitudes, and defined that the distribution of the size of

these specific earthquakes in a region generally follows a particular distribution (Guttenberg and Richter 1944), that is given by Equation 2.11:

$$\log \lambda_m = a - b.m \qquad 2.11$$

Where λ_m is the rate of earthquakes with magnitudes greater than m, and "a" and "b" are constants. This equation is called the *Gutenberg-Richter recurrence law*. Figure 2-54 illustrates typical observations from a fault or region, along with the Gutenberg-Richter recurrence law, given by Equation 2.11.

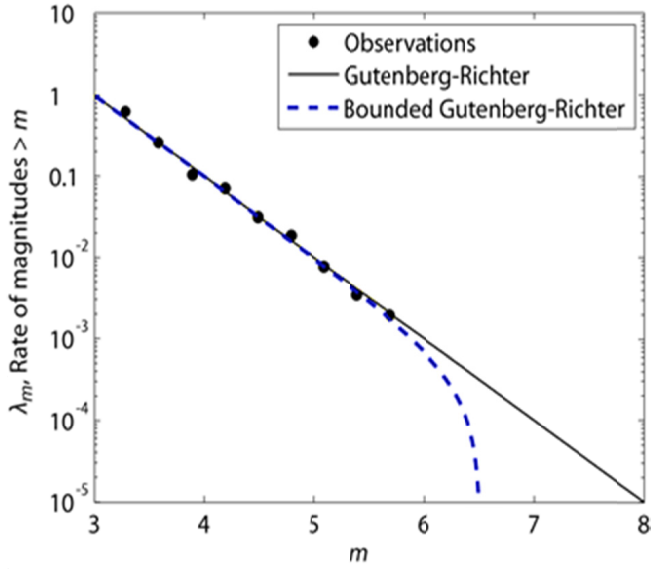

Figure 2-55 Typical distribution of observed earthquake magnitudes (Baker 2008)

The *a* and *b* parameters shown in equation 2.11 are estimated using statistical analysis of historical observations and based on additional constraining data produced by different types of geological evidence. The *a* value refers to the overall rate of earthquakes present in a region, and the *b* value represents the relative ratio of small and large earthquake magnitudes (typical *b* values are approximately equal to 1). However, by fitting just a straight line (i.e., G-R recurrence law), the actual mean rate of small

earthquakes will be under-predicted, and the mean rate of large earthquakes will be over-predicted (Kramer 1996). Several other methods have been introduced (Stepp 1972; Weichert 1980; EPRI 1986) to overcome with incomplete records and to correct the trend or path.

The bounded Gutenberg-Richter recurrence law (Figure 2-55) was introduced to overcome the over-prediction of large earthquakes. Generally, a limitation is present on the upper bound of earthquake magnitudes in a region, and it primarily attributed to the finite and predefined size of the source faults. (Earthquake magnitude is related to the area of the seismic rupture. McGuire and Arabasz (1990) expressed a new version of the recurrence law that overcomes the overestimation for large earthquakes (McGuire and Arabasz 1990), as shown in Equation 2.12.

$$\lambda_m = \nu \frac{\exp[-\beta(m-m_0)]-\exp[-\beta(m_{max}-m_0)]}{1-\exp[-\beta(m_{max}-m_0)]}; \qquad m_0 < m < m_{max} \qquad 2.12$$

Where, "v" is the temporal distribution of earthquake recurrence; β = 2.303b; b=parameter obtained by regression of the database of seismicity from the source of interest; m_0=minimum magnitude (m_0=1.5); m_{max}= maximum magnitude assumed in our model; and λ_m is the mean annual rate of exceedance.

Several other recurrence laws are found in the literature and can be used for specific cases. The Gutenberg-Richter Law represents the behavior of a single source only and has been questioned by some authors (Schwartz and Coppersmith 1984) (Schwartz 1988). For example, for some specific faults which produce earthquakes of similar size, the *characteristic recurrence law* is more appropriate (Figure 2-56). This can be addressed when enough geologic evidence of the fault is present (Kramer 1996). Geologic evidence refers to the fact the characteristic earthquakes occur more often than would be implied by extrapolation of the G-R Law from high exceedance rates (low

magnitude earthquakes) to low exceedance rates (high magnitude earthquakes). The characteristic recurrence law commonly predicts lower rates of exceedance at lower magnitudes than the characteristic earthquake magnitude and higher rates at magnitudes located near the characteristic earthquake magnitude.

One of the main characteristics of earthquakes in the Central US is that they are moderate seismic events (M 3-5). Therefore, a simplified seismic hazard analysis can be developed based on the Guttenberg-Richter recurrence law to consider the size uncertainty.

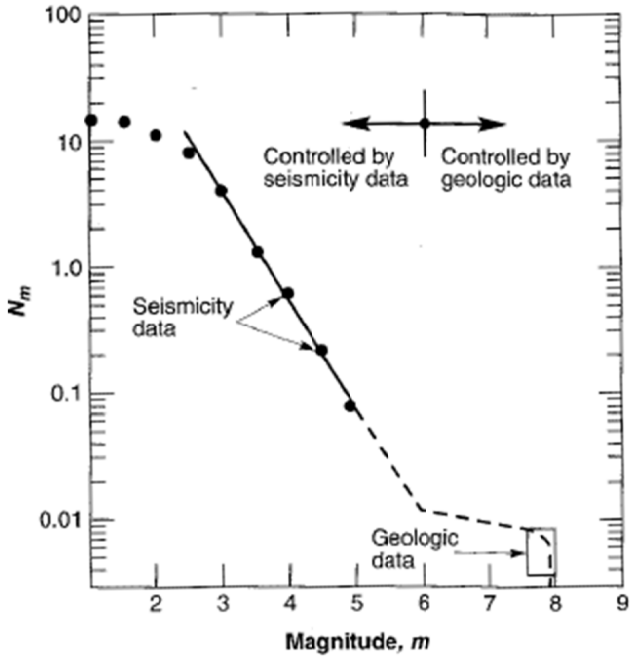

Figure 2-56 Inconsistency of mean annual rate of exceedante determined from seismicity and geologic data (Youngs and Coppersmith 1985)

2.7.6.3 Spatial Uncertainty

In the PSHA, earthquakes are usually considered to be uniformly distributed within a particular source zone. In other words, they are considered equally likely to occur

at any location (Kramer 1996). The evaluation of distribution of source-to-site distances is mandatory when predicting the ground shaking at a site using PSHA approach (Baker 2008). For each earthquake source encountered in the region, earthquakes are assumed to occur with equal probability at any location on the fault. Based on this fact and providing locations with a uniform distribution, the identification of the distribution of source-to-site distances can be defined by using only the geometry of the source. Since GMPEs define ground motion parameters in terms of source-to-site distance, the spatial uncertainty within each seismic source must be described. Based on the geometric characterization of seismic sources illustrated in Figure 2-49, several functions can be calculated to model the spatial uncertainty. Kramer (1996) presented different examples of variations of source-to-site distance for different source geometries (Figure 2-57).

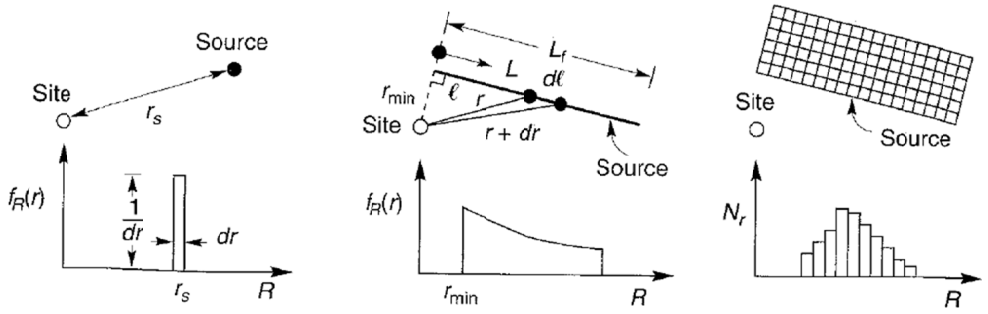

(a) (b) (c)

Figure 2-57 Variaions of source-to-site distance distribution for different seismic sources geometries (Kramer 1996)

For a point source (Figure 2-57a) the distance, R, is known to be r; thus, the probability that $R=r_s$ is assumed to be 1 and the probability that $R \neq r_s$ is zero. For linear (Figure 2-57 b) or areal seismic sources, the definition of probability is not that simple. The probability function for a linear seismic source is described as shown in Equation 2.13.

$$f_R(r) = f_L(l)\frac{d_l}{d_r} \quad 2.13$$

The present research uses volumetric models to characterize seismic sources within the area of study in North Texas. Kramer (1996) described a simplified methodology to compute the spatial uncertainty for volumetric sources, as shown in Figure 2-57(c). For volumetric sources, it is appropriate to evaluate $f_R(r)$ by numerical rather than analytical methods (Kramer, 1996). The task can be accomplished by dividing the irregular zone into a large number of discrete elements of equal area to generate a histogram $f_R(r)$, where R corresponds to the distance to the center of each element in the source. This approach assumes that the energy from the source rupture is released at the hypocenter of the earthquake.

2.7.6.4 Ground Motion Intensity Uncertainty

Quantification of the distribution of potential earthquake magnitudes and locations has been described; however, the objective is to analyze ground motions, not earthquakes at one specific site. Therefore, the following step is quantify the ground motion by using a ground motion prediction model (GMPE), which was described in earlier sections. However, seismic parameters can be scattered after using GMPEs, as shown in Figure 2-58, and the uncertainty of events to occur requires an evaluation.

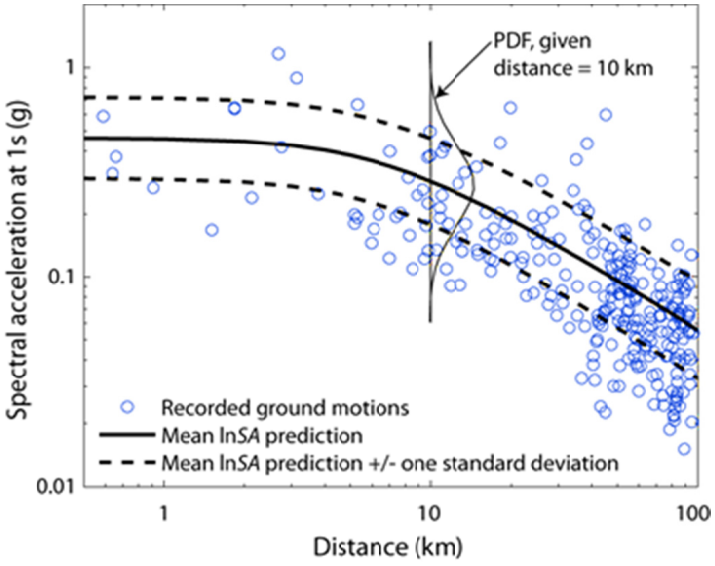

Figure 2-58 Observed spectral accelerations, 1999 Chi-Chi, Taiwan earthquakes (Baker 2008)

The significant scatter in observed ground motion intensities can be illustrated in Figure 2-58. It is noted that the scatter shown is after considering the effect of magnitude and distance. For this reason, the prediction must be combined with a probability distribution for multiple intensities, instead of only a single intensity. This can be done by combining with a Poisson model as shown in Figure 2-58. It is an important step because PSHA calculations are required to consider a possibility of unlikely outcomes, such as extreme intensities much larger than the predicted mean (Bommer and Abrahamson 2006). Equation 2.14 describe the prediction model use to describe this probability distribution:

$$\ln IM = \ln IM(M, R, \theta) + \sigma(M, R, \theta) \cdot \varepsilon \qquad 2.14$$

Where lnIM is the natural log of the ground motion intensity measure of interest (i.e., peak ground acceleration), the term ln*IM* is evaluated as a random variable, which can be represented by a normal distribution in a reasonable manner.

The terms $\ln IM\,(M, R, \theta)$ and $\sigma(M, R, \theta)$ are the result of the ground motion prediction model; both terms refer to the predicted mean and standard deviation, respectively, of the term ln*IM*. As shown in the Equation 2.14, both terms are function of earthquake magnitudes (M), source-to-site distance (R) and other parameters which can be constants from regression models developed for GMPEs that typically are referred to as "θ". On the other hand, ε is a standard normal random variable that provides the variability in the prediction model of $\ln IM$. Positive values of ε produce larger values than average of $\ln IM$, while negative values of ε produce smaller values than average values of $\ln IM$.

In PSHAs, the definition of ground motion brings inevitable scatter results from using GMPES. Causes for the scattering in results are attributed to the randomness in the mechanisms of rupture and from variability and heterogeneity of the source, travel path, and variable site conditions. The values of the confidence limits (Campbell 1985) or by considering the standard deviation of the predicted parameter in the regression model of GMPEs (Kramer 1996) can be used as quantitative parameters in the scattering of data. An easier way to address the uncertainty is to consider the standard deviation of the logarithm model of the predicted parameter. Once the seismic parameter is calculated, using GMPEs for an specific m and r, the probability of that various target peak acceleration level will be exceeded and must be calculated using Equation 2.15.

$$z^* = \frac{lny^* - lnPHA}{\sigma_{lny}} \qquad 2.15$$

Where y* is the target peak acceleration or seismic parameter and σ is the corresponding standard deviation for the GMPE model. Figure 2-59 illustrates the

probability that a particular ground motion parameter, Y, exceeds a certain value, y* produced by an earthquake magnitude, m and that occurs at a distance, r from the site.

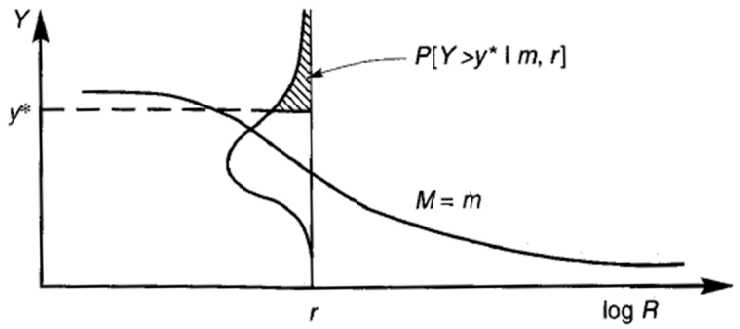

Figure 2-59 Conditional probability of exceedance of a particular value of ground motion parameter (M and R) (Kramer 1996)

In probabilistic terms, Equation 2.16 described the illustration in Figure 2-59.

$$P[Y > y^*|m,r| = 1 - F_y(z^*) \quad 2.16$$

Where $F_Y(z)$ is the value of the CDF of Y at specific m and r. The value of $F_Y(z)$ depends on the probability distribution used to represent Y (Kramer 1996).

2.7.6.5 Seismic Hazard Curves Computation and Finite Time Period

Seismic hazard curves can be calculated for individual seismic sources or be integrated to express the cumulative hazard for a particular site. The computation concept for developing seismic hazard curves is quite simple (Kramer, 1996). It primarily refers to the calculation of probability of exceeding a particular value of y*, that was calculated for a ground motion parameter Y with a specific earthquake that occurs at one possible source location, multiplied by the probability that this particular magnitude earthquake would occur at that specific location. The process is then repeated for all possible magnitudes and locations obtained from the spatial and size distribution.

Several math calculations overcome the most commonly associated equation for PSHA. Equation 2.17 integrates the fact about rates of occurrence of earthquakes, the expected earthquake magnitudes and sour-to-site distances, as well as the distribution of ground shaking intensity produced by those given earthquakes.

$$\lambda(IM > x) = \sum_{i=1}^{n_{sources}} \lambda(M_i > m_{min}) \sum_{j=1}^{n_M} \sum_{k=1}^{n_R} P\left(IM > x \middle| m_j, r_k\right) P\left(M_i = m_j\right) P(R_i = r_k) \quad 2.17$$

Where, M_i and R_i represents the magnitude and distance distributions for a given source I; $m_j=m_0$ + (j-0.5) (mmax+m0)/N_m; rk=r_{min}+(k-0.5) (r_{max}-r_{min})/N_r; IM=Y and $n_{sources}$ Is the number of sources considered.

Once PSHA calculations are performed, it is easy to combine the seismic hazard curve with the Poisson model to estimate probabilities of exceedance in finite time intervals (Kramer 1996). Equation 2.18 defines the probability of exceedance of y* in a time period, T.

$$P[Y_T > y^*] = 1 - e^{-\lambda_{y^* T}} \quad 2.18$$

2.8 Summary

This chapter presents a comprehensive literature review on earthen dams, hazards, soil variability, and seismic hazard analysis. Geotechnical evaluation for hydraulic fill structures is required, especially in areas where high seismicity is present. Several failures of hydraulic fill dams were presented, showing that liquefaction is the primary hazard that affects this type of structure. Also, hydraulic fill dams present high soil variability in their configuration, which was demonstrated by several researchers. The main objective of the research is to develop a comprehensive soil characterization by generating 3D visualization models based on the theory of Geostatistics, a method that considers spatial variability, and by incorporating in-situ test data (i.e., CPT) for

characterization of soil. Kriging interpolation is used based on the generation of variograms that incorporates spatial continuity combined with the anisotropy in the data.

This research integrates an application study for the Central United States, where a sudden increase of seismicity has become an issue. A seismic geotechnical evaluation for this type of dam is also performed by addressing the cyclic liquefaction potential for the case study. The following chapter presents an approach to determine seismic parameters in areas where sudden increase of seismic activity has become an issue. First, a simplified seismic hazard analysis is developed by generating volumetric seismic sources for the area of North Texas, due to the lack of fault mapping.

Finally, three-dimensional visualization models are presented for characterizing soil properties and cyclic liquefaction potential, based on CPT data collected and Geostatistical interpolation.

Chapter 3 Formulation of a Simplified Seismic Hazard Analysis for North Texas

3.1 Introduction

The main objective of this research is to apply the principles of risk and reliability to develop a framework to assess the resiliency of critical aging infrastructure such as dams and levees. The Eagle Mountain Dam, a hydraulic fills structure located in North Texas was considered for comprehensive seismic analysis including risk based characterizations of compacted dams and probabilistic seismic hazard analysis on seismic loading events. The whole framework of development and analysis was done by using a real example of Eagle Mountain Dam located in North Texas. This chapter presents the development of a seismic hazard analysis by using the recent earthquake events in North Texas. Seismic parameters obtained from this analysis are used for the calculation and assessment of liquefaction potential at the EM dam internal soil layers.

The sudden increase of seismic activity in the central United States raises a concern for the stability of critical lifeline structures such as dams and levees. Due to low seismic activity in these regions, many of the civil infrastructures were not designed to sustain seismic loading conditions. Significant damages were reported during the M5.7 (magnitude) earthquake occurred in 2011 at Prague, Oklahoma (Holland et al. 2013). Latest seismic events, in the Oklahoma area such as the M5.8 Pawnee, OK and the M5.0 Cushing, OK earthquakes, caused several geotechnical and structural damage (Clayton et al. 2016). Other important earthquakes in this region are: M5.3 Trinidad, Colorado earthquake, the 2012 M4.8 Timpson, Texas earthquake, the 2011 M4.7 Guy, Arkansas earthquake. The National Earthquake Information Center (NEIC) reported 27 earthquakes near the cities of Azle and Reno, Texas including two main M3.6 events Figure 3-1.

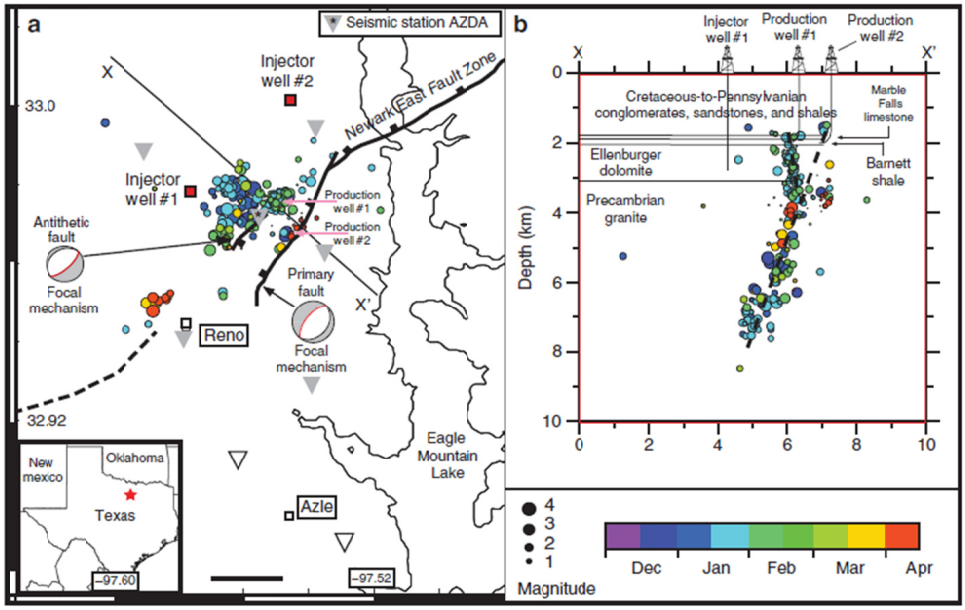

Figure 3-1 Azle Earthquakes locations and regional geologic structure (Hornbach et al. 2015)

In North Texas, several earthquakes of lower intensity as compared to other places were reported. These earthquakes started to occur in 2013 along a mapped ancient fault system near Azle, Texas (Hornbach et al. 2015). Although it is true that these seismic events are relatively low in magnitudes (M<6.0) as compared with areas with high seismicity (i.e., California, New Madrid), the concern is that their rate has suddenly increased. In addition, the shallow nature of these earthquakes could induce more problems to infrastructure.

A M3.6 earthquake occurred in Irving, Texas in January 2015 and the levels of shaking were felt in the area of North Texas. In May 2015, another M4.0 earthquake occurred in the area of Venus, Texas and according with USGS officials (USGS 2016), it is considered as the strongest to ever hit in North Texas. According to Ellsworth (2015), the central and eastern United States have seen an unprecedented increase in

earthquake rate since 2009, and many of these earthquakes are believed to be induced (Ellsworth et al. 2015). The main objective of this study is to address a seismic hazard analysis based on the latest seismicity in the region and it does not intend to define the causes of earthquakes. However, it is important to understand the possible causes to characterize earthquakes (i.e., depth and rate of occurrence).

A shallow earthquake can cause significant damage to civil infrastructure and even more damage than those larger earthquakes at higher depths. Hydraulic fill structures can result into significant damage if the ground motion expected overcomes the seismic design of the dam. Several existing hydraulic fill dams and other important civil infrastructure are present in the area of North Texas. In order to develop and demonstrate the proposed research frame work, a hydraulic fill dam located in Fort Worth, Texas was considered in this study. This work is done as a part of comprehensive research evaluation and this study should be considered as a proactive approach/assessment to evaluate potential concerns on the stability of the dam.

Figure 3-2 Eagle Mountain Dam Lake Site: Dam and Levee

Eagle Mountain lake dam and its associated structures are located at the city of Fort Worth and currently supplies water for nearly 2 million North Texas residents. The main dam consists on a semi-hydraulic fill dam (i.e., hydraulic fill and wetted and rolled). This dam was constructed in 1932 and according to the U.S. Army Corps of Engineers, such dams are considered as a “High” to “Very High” hazard structure consequence dams from seismic activity. Therefore, the Eagle Mountain Dam is considered to be susceptible for potential geotechnical hazard caused by seismic activity and hence a seismic hazard analysis is required to address geotechnical hazard evaluation (i.e., liquefaction or dynamic slope stability) of the dam.

A simplified seismic hazard is therefore compiled and presented for the North of Texas region by considering the recent seismicity and by generating volumetric seismic sources due to the lack of specific faults that may cause the existing seismic activity. A general framework of the seismic hazard for the Eagle Mountain Dam is illustrated in Figure 3-3.

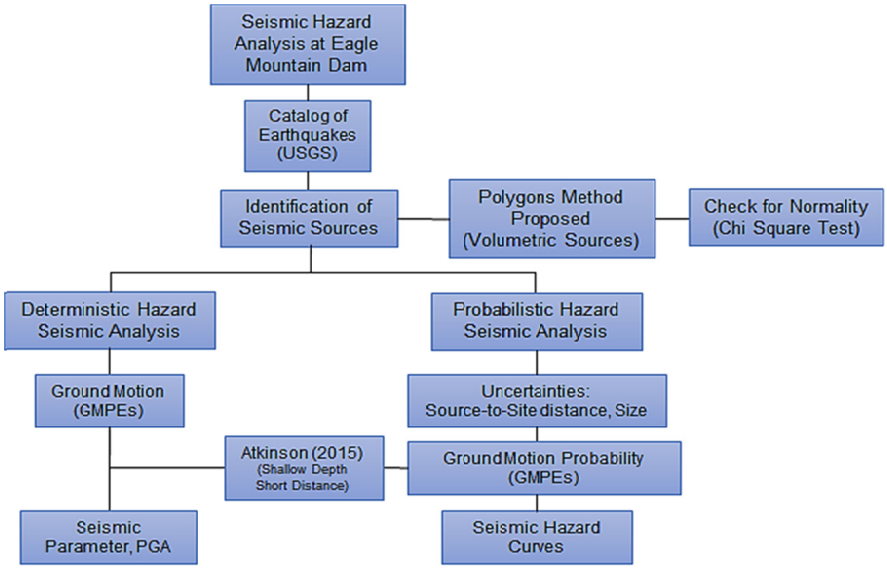

Figure 3-3 General seismic framework for the EM Dam (North Texas)

Both, deterministic and probabilistic seismic hazard analyses, DSHA and PSHA respectively, are performed for this site to obtain the seismic parameters. However, based on the maximum earthquake magnitude recorded within the area, the DSHA appears to underestimate the seismic hazard at the site; however, PSHA complements and addresses those uncertainties coming from DSHA analysis. Initially, the analysis was performed based on two different approaches:

- earthquakes with a short radius (R_{max}=40 miles) from Eagle Mountain Dam
- earthquakes with larger radius (R_{max}=200 miles) from Eagle Mountain Dam

Both approaches were selected based on the current seismicity near the site and also the potential effect of earthquakes in further areas such as Oklahoma. Corresponding ground motion predicting equations shall be used for each approach. The main characteristic of earthquakes in central US is considered by USGS in the category of minor to moderate earthquakes (M1-M5) or also called shallow or small magnitude earthquakes. The ground motion required was calculated based on ground motion predicting equations (GMPEs) developed for specific earthquake conditions (i.e., magnitude) as well as based on the source-to-site distance (R).

Chapter 2 presented a compilation of GMPEs which can be applicable for the central United States; however, none of the correlations consider distances more than 35-40 miles (50-60 km) for similar ground conditions of North Texas. A correlation for magnitudes M4-M8 and distances up to 1600 miles is found in the literature (Pezeshk et al. 2011); those GMPEs were developed for hard rock sites in Eastern United States and are not applicable for the region of interest where soft rock is mainly present.

Despite the fact that it is unknown the cause oh earthquakes, it is not expected to have large events in North Texas as compared with areas like California or New Madrid

where faults are well known to trigger larger seismic events. Two main events occurred in Oklahoma (i.e., Prague, OK 2011; Pawnee, OK 2016) approximately 250 miles away from EM. Ground accelaration produced by shallow earthquakes which likely occur at short distances from the site (50 miles maximum) produce hgiher ground acceleration thatn those which occur at larger distances (>50 miles). Therefore earthquakes within short distance from EM will have more effect than those ocurred in Oklahoma with that magnitude size expected. Thus, a seismic hazard analysis is developed here by considering those seismic sources that can be generated within 40 miles distance from the Eagle Mountain Dam.

Figure 3-4 illustrates the initial catalog of earthquakes for both approaches. However, as stated above the 40 miles (60 km) radius approach is used for the calculation of seismic hazard analysis of the Eagle Mountain Dam site. The catalog of earthquakes was obtained from the database of the USGS based on the geographic coordinates of the Eagle Mountain dam (N: 32.8732; E: -97.4865).

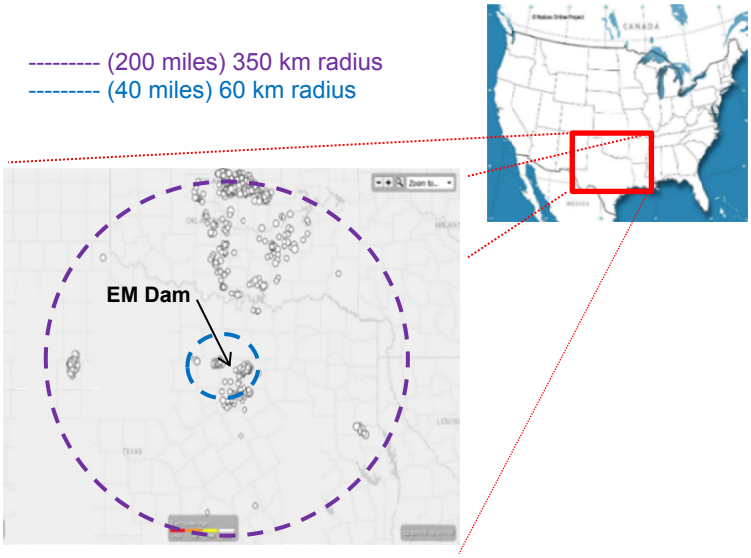

Figure 3-4 Initial catalog of earthquakes collected from USGS until November 2015

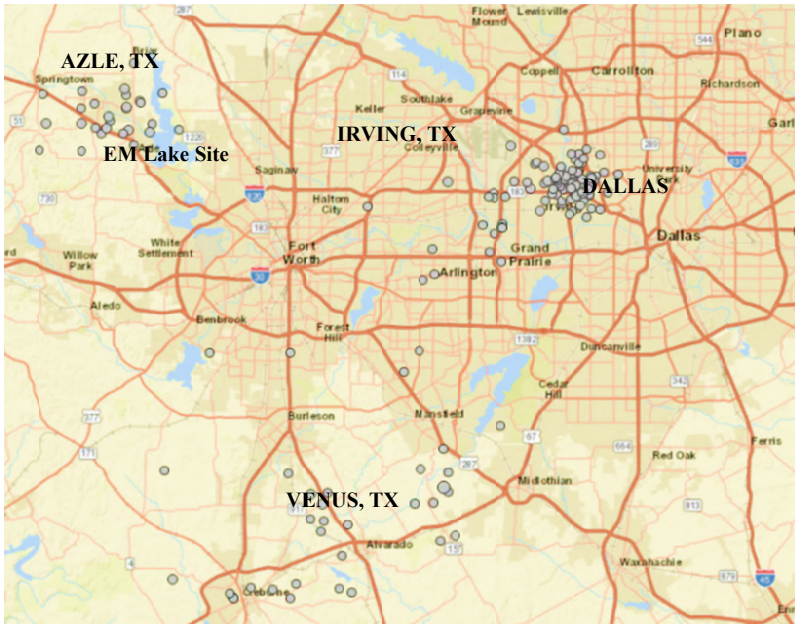

Figure 3-5 Earthquake catalog within 60km from EM dam

Therefore, the present seismic hazard analysis assumes that earthquakes within short distance (R_{max}=40 miles) from EM will have higher strong motion than those occurred at larger distances. Earthquake catalog within 40-mile radius from the site of interest are shown in Figure 3-5. Once the catalog of earthquakes is obtained from USGS, the identification and characterization of seismic sources have to be defined. It should be noted that no information about faults is found in North of Texas as illustrated in Figure 3-6. A new methodology for defining seismic sources is developed based on the generation of volumes or prisms.

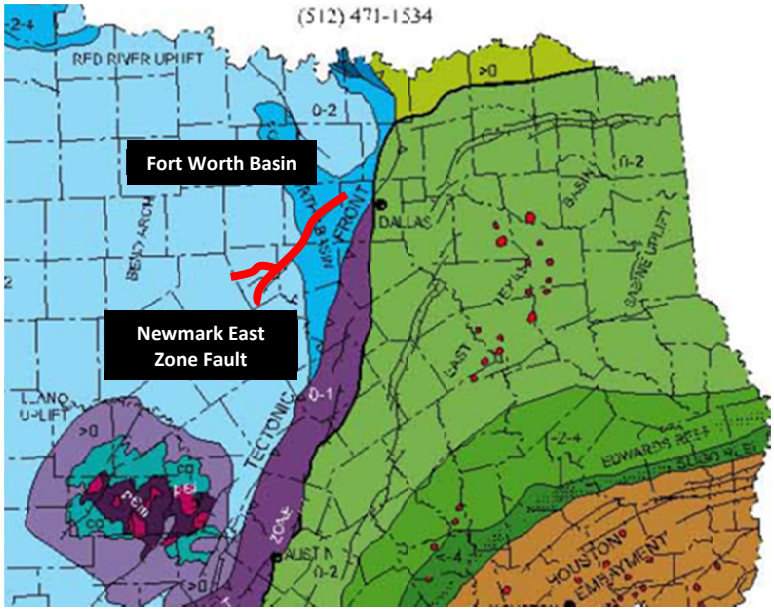

Figure 3-6 Fault Map for the North of Texas (UT Austin 1997)

3.2 Identification and Characterization of Seismic Sources

The increase of earthquake activity in the midcontinent presents particular challenges to assess a seismic hazard analysis. Conventional seismic hazard analyses are commonly developed in areas where known active faults or seismic sources have been identified. Seismic sources are dentified in areas where modern seismographs and seismographic networks are installed which can provide earthquake magnitude, locate the rupture surface, and some can even defined some source parameters (Kramer 1996).

The seismic hazard presented includes a new methodology to create volumes or prisms as seismic sources due to the lack of fault mapping in the region of North Texas. The simplified methodology can be applied to areas where recent seismicity is present and faults have not been mapped yet. A seismic or earthquake source is described as a geologic structure or as a domain within which the spatial and temporal occurrances or seismic events are approximately uniformily distributed (Kramer, 1996). The normaility of

source-to-site distance is evaluated for normaility por each prism generated to satisfy the statement defined by Kramer (1996).

The seismic hazard of EM is based on the assumption that earthquakes occuring at short distances (40-mile radius) will have more impact that those occurring at larger distances. The simplified model also assumes that Newmark East Zone fault identified in the area of North Texas is part of the volumetric seismic sources generated. The assumption is based that no information of fault rupture type has been documented for this type of fault; therefore it cannot be considered as seismic source for potential damage.

3.2.1 Geometric Characterization

Earthquake catalog was obtained within 40-mile radius from EM site from USGS database. Epicenter coordinates, hypocenter distances (depth) and magnitude of all the seismic events were recorded (See Appendix A). It was expected that the depth of earthquakes within this catalog ranges from 2.25-10 km approximately as shown in the catalog in which earthquakes are categorized as shallow events according to USGS. Figure 3-7 presents a sketch of the proposed methodology to generate volumetric seismic sources. It consists of generating two-dimensional polygons by connecting earthquake epicenters over a random area. Epicenters include the information of corresponding depth and hypocenters are easily identified for the creation of volumes or prisms. The polygon is then divided in a reasonable number of elements with the same volume capable to produce a good number of data for the check of normality. The process performs different iterations with different random polygons and prism created and normaility is checked for each.

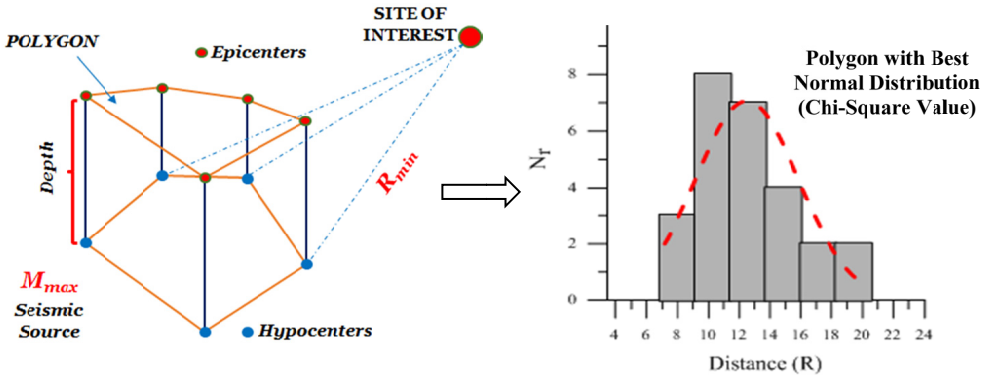

Figure 3-7 Polygon method for generating volumetric sources

The concept is based on the generation of random polygons that connects epicenters (i.e., ground surface) with corresponding hypocenters (i.e., underground surface). Surfaces were connected as shown in the sketch in Figure 3-7 and various examples of the process are shown in the following illustrations. Source 1 refers to the group of earthquakes occurred near the area of Azle, TX; Source 2 includes earthquakes near Irving, TX and Source 3 compiles all records from the area of Venus, TX as shown in Figure 3-5. It may be noted that Venus, TX area is located outside the 40 mile radius; however, the present work considers that the seismic activity in this region is crucial for developing the seismic framework and it is further considered as part of the seismic sources capable of producing significant ground motion. The goal of geometric characterization is to provide an overview of earthquakes likely to occur within specific boundaries. The source-to-site distance distribution changes for every single trial and polygon using the proposed methodology, therefore the check of normaility of its distributions is a vital step for validation of the method.

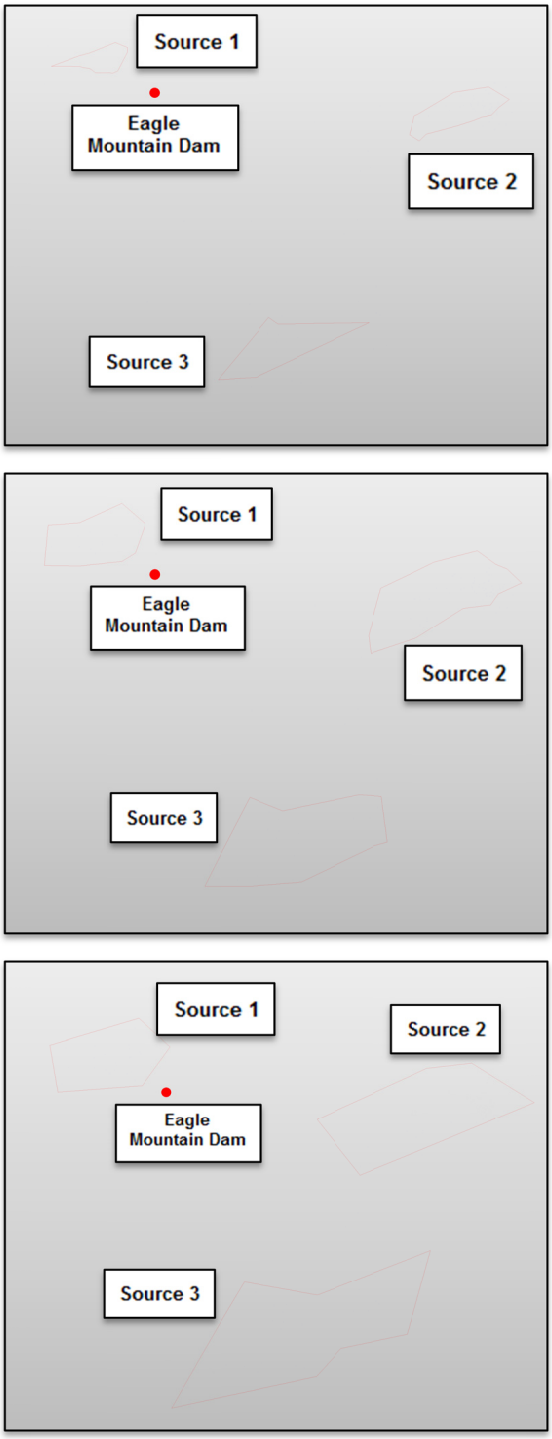

Figure 3-8 Generation of various polygons (S_1, S_2 and S_3)

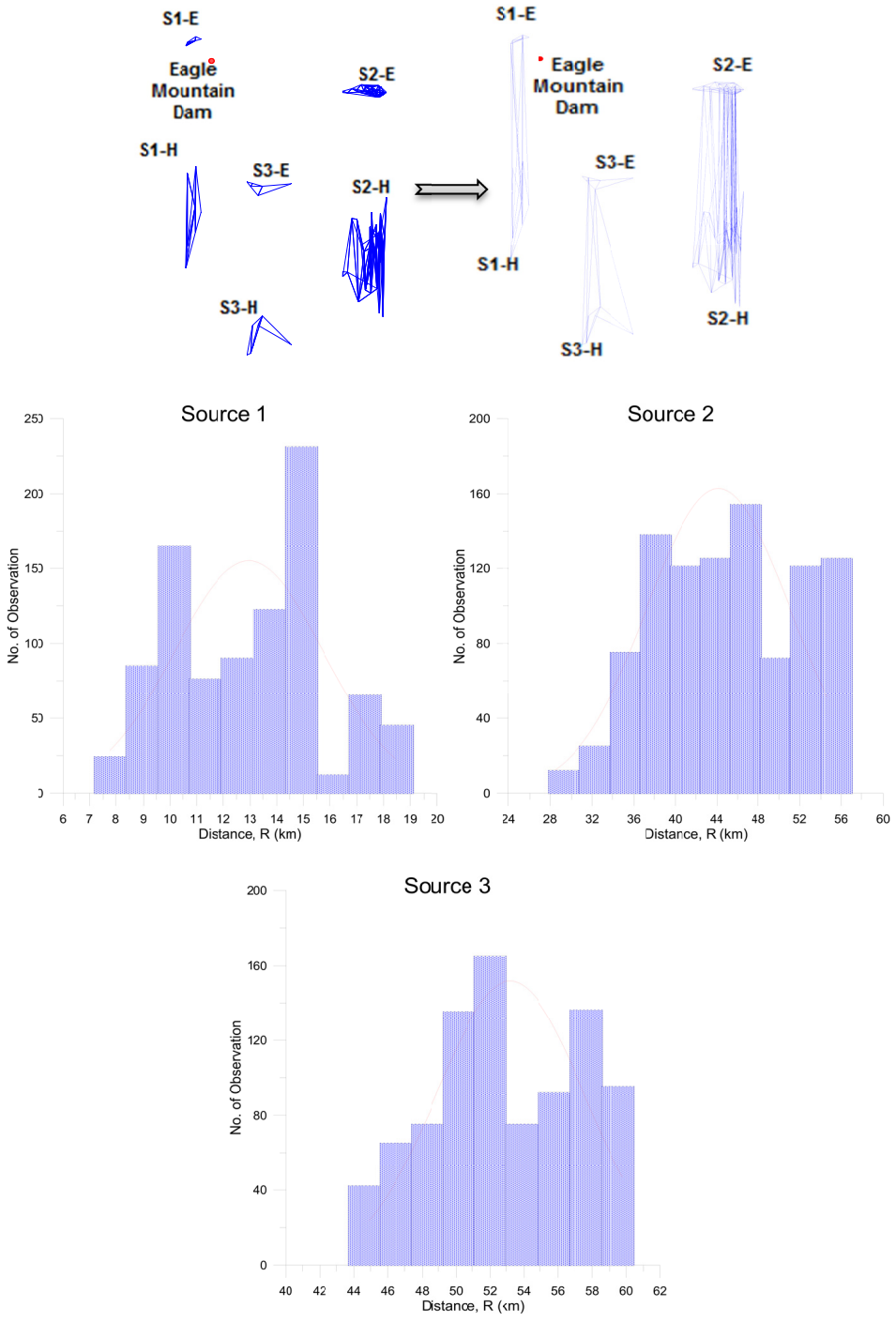

Figure 3-9 Sample trial of polygons (Data with low normality)

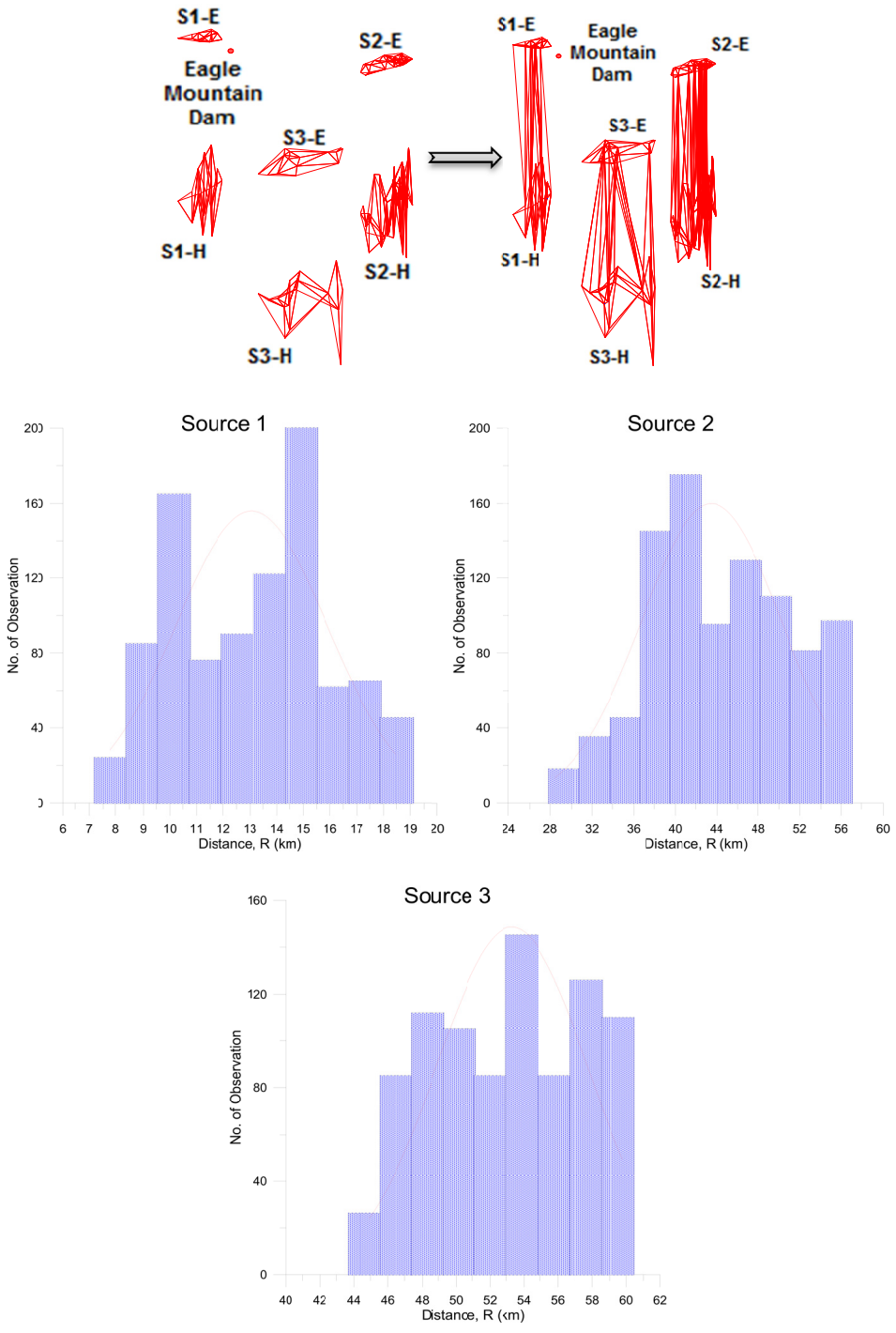

Figure 3-10 Sample trial of polygons (Data with medium normality)

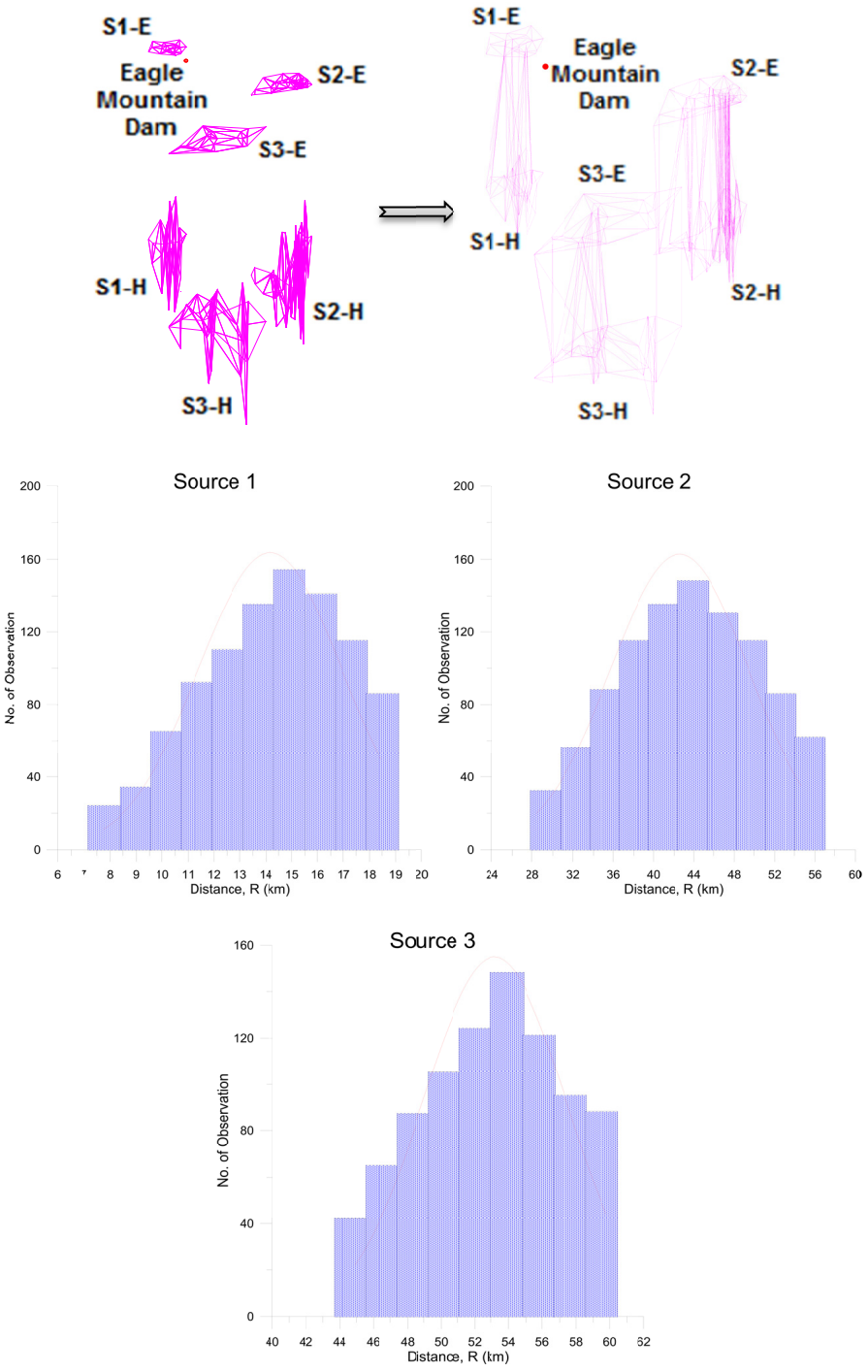

Figure 3-11 Sample trial of polygons (Data with acceptable normality)

3.2.2 Check for normality – Chi-Square Test

The Chi-Square goodness of fit test is used to test the hypothesis that data comes from a normal distribution. It basically consists on comparing the observed values with the expected values by evaluating using the Chi-square function as described in Chapter 2. The statistical method to verify the normality is sufficient to consider the source-to-site distance for the generation of seismic sources since the number of elements is 1000 for each seismic source. Results of the chi-square analysis for sources shown in Figure 3-9, Figure 3-10, Figure 3-11 and tabulated in Table 3-2.

Table 3-1 Check of Normality in Seismic Sources

Description	p-value (Chi-Square test)		
	Low Normality	Medium Normality	Acceptable Normality
Source 1	13.16%	23.25%	76.11%
Source 2	1.79%	19.86%	65.73%
Source 3	10.78%	32.19%	70.29%

The proposed methodology aims the identification of seismic sources when faults or other potential sources have not been identified in a specific region. The seismic hazard presented herein includes this methodology as part of the computation of both, deterministic and probabilistic seismic hazard analysis which are described in the following sections.

3.3 Deterministic Seismic Hazard Analysis (DSHA)

The assessment of DSHA consists of determining the occurrence of an earthquake of a specified magnitude (controlling earthquake) at a specified location from the site of interest (FEMA 2005). This section presents the deterministic seismic hazard analysis performed for Eagle Mountain Lake site.

The DSHA performed is based on the steps described in Chapter 2. The first step consisted of identifying and characterizing seismic sources which refers to the definition of source-to-site distances and maximum earthquakes within each source. Three volumetric seismic sources (S_1, S_2 and S_3) are considered within the 40-mile radius of EM Lake. The Maximum Credible Earthquake (MCE), defined as the maximum earthquake found within each source for assessing DSHA was determined for all the sources (M_{max}).

One of the main steps of DSHA is to address a threshold ground motion parameter value (minimum value of ground motion that causes a seismic hazard at the site). A threshold value is important to check whether all sources are actually capable or not to produce damage at the site of interest. It is usually calculated by using the minimum magnitude (M_{min}) and the maximum source-to-site distance (R_{max}) out of all sources. However, a threshold value is defined as a decluttering tool when a high number of seismic sources are present around the site of interest.

Since there are only three sources (S_1, S_2 and S_3) within the 40-mile radius from EM, it is assumed that all of them could cause significant hazard at the site. Figure 3-12 shows a sketch of seismic sources with corresponding MCE (M_{max}) and the shortest source-to-site (R_{min}) to EM site. Recorded seismic events are represented as blue dots and the red solid lines represent the boundary for each seismic source. S.I units are used herein for the ground motion calculation for the easiness of applying GMPEs developed for those specific units.

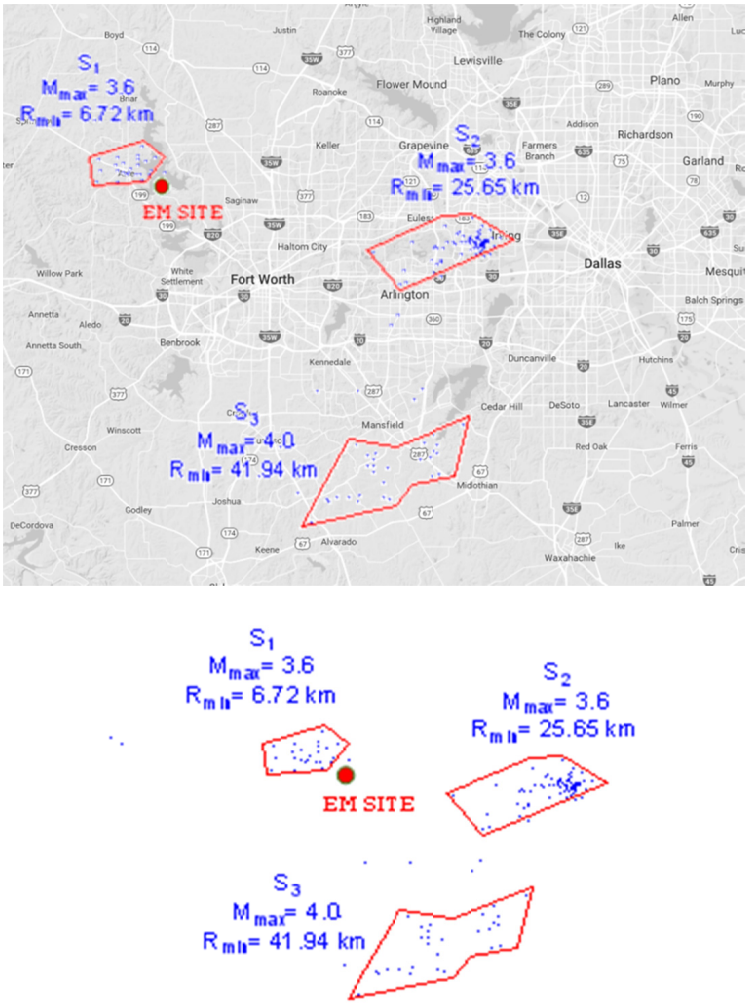

Figure 3-12 DSHA schematic at EM

The calculation of ground motion produced by each source is characterized based on corresponding M_{max} and $R_{min.}$ Ground motion is calculated by using GMPEs developed by Atkinson (2015) described in Chapter 2. The set of GMPEs presented are relatively valid for calculating ground motion in terms of a seismic parameter (PGA) within short distances (40 km) and it is applicable for low seismicity regions (M 3-6) where earthquakes are likely to be occurred at shallow depths (4-10 km), similar conditions as

related to North Texas seismicity. Table 3-2 shows the results from the calculation of ground motion using Atkinson (2015) equations.

Table 3-2 Ground motion at Eagle Mountain Lake site (DSHA)

Source	M_{max}	Ground Source-to-site distance (Km)	Depth (km)	R_{eff} (Km)	h_{eff}	R_{min} (km)	PGA (cm/s^2)
S1	3.6	4.3	5.05	6.6	0.98	6.7	17
S2	3.6	25.1	5.01	25.6	0.98	25.7	1.6
S3	4	41.6	4.92	41.9	1.00	41.9	1.6

A primary objective of DHSA to address maximum potential damage from all sources is to select the controlling earthquake, earthquake that is expected to produce the strongest level of shaking which is obtained by quantifying the maximum ground motion parameter (Y, PGA) at the corresponding minimum source-to-site distance (R_{min}) from Table 3-2. The hazard at the site is usually defined by different ground motion parameters. The present study only shows the evaluations of PGA as the critical ground motion parameter and does not contemplate the calculation of peak ground velocity (PGV) or spectral acceleration (PSA). The seismic hazard at the site is dependent on the earthquake magnitude (M_{max}) and minimum distance from source to site (R_{min}) that produces the highest value of PGA (cm/s2). The seismic hazard curve generated by S_1 and S_2 is shown in red line and was developed with M_{max}=3.6; however the R_{min} is different for each source (i.e., R_{min1}=6.7 km; R_{min2}=25.7 km) and therefore the PGA generated by S_1 is much higher than S_2 (i.e., PGA_{S1}=17 cm/s2). The seismic hazard curve produced by S_3 is shown in blue, and it was generated with M_{max}=4.0; however, the corresponding R_{min3}=41.94 km produces a small value of PGA which is not able to be shown in Figure 3-13.

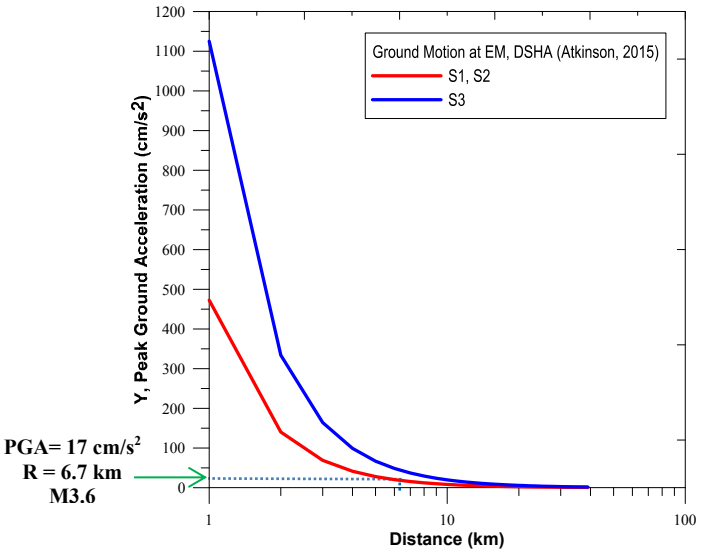

Figure 3-13 Deterministic Seismic Hazard Analysis (DSHA) at EM

Results from DSHA showed that the earthquake hazard for the EM site has a peak ground acceleration (PGA) of approximately 0.02g (17 cm/s^2) resulting from an M3.6 earthquake located at Source 1 (Azle, TX) at a distance of 6.7 km from the site. DSHA produces a relatively low seismic parameter (PGA) to generate a moderate or significant damage. However, the DSHA is not considered appropriate to estimate seismic hazard in North of Texas particularly when the rate of earthquakes is not constant. Therefore, a probabilistic seismic hazard analysis is more suitable by considering several uncertainties which are not considered in DSHA.

3.4 Probabilistic Seismic Hazard Analysis, PSHA

Seismic activity in North Texas is primarily characterized by the uncertainty of an earthquake to occur in both time and space. The recent increase of seismic events does not provide an overall view to define a final seismic hazard for sites at this region. However, the best approach to assess a seismic hazard at these sites is to use the probabilistic concepts that allows considering uncertainties in the size, location and rate

of recurrence of earthquakes and in the variation of ground motion characteristics with earthquake size and location (Kramer 1996). The present PSHA approach is developed based on the assumption that rate of earthquakes remains stationary in both time and space. Although, this assumption might not reflect the reality of seismic activity in the region but it can forecast seismic hazard within a short and finite period of time (1 year).

PSHA calculation is usually described as a specific ground motion parameter with 2% probability of exceedance in 50 years at sites where representative seismic information is available. In other words, it commonly describes the 2% probability for a computed seismic parameter (i.e., PGA) to be exceeded in 50 years. The present model is valid for the calculation of ground motion parameter with 1% of probability of exceedance in one year to consider the rate of earthquakes stationary and it is valid to forecast seismic hazard in 2016 for similar structures located at this region. The developed PSHA approach provides a simple framework which allows identifying, quantifying and combining uncertainties in an easy manner to have a better picture of seismic hazards in North Texas.

The PSHA methodology described in this section is based on deeply ingrained methods developed by different authors (Cornell 1968; Algermissen et al. 1982) which primarily consists of four steps (Reiter 1990) similar to DSHA. The following sections presents the detailed analysis on determining the seismic parameters using PSHA approach described in Chapter 2. The identification and characterization of sources is defined as the first step of PSHA which has same considerations as provided for deterministic analysis. However, a PSHA requires careful attention for characterizing a seismic source to consider uncertainties of the earthquake potential to the site. Therefore, characterization of an earthquake source is defined based on the

consideration of the spatial distance, size and time earthquake distribution within each source.

3.4.1 Spatial and Size Uncertainty

Seismicity has a peculiar characteristic in North Texas and several assumptions are required for the calculation of uncertainties in both, space and size, within seismic sources. The generation of volumetric sources primarily describes that earthquakes of different magnitudes (M) can occur at any location of the volumetric source (prism) with a certain source-to-site distance (R). PSHA considers those uncertainties by using univariate statistics to characterize the spatial and size uncertainty. Spatial distribution refers to the uncertainty in source-to-site distance and can be evaluated by a probability density function fR(r) (i.e., frequency of earthquakes within the source). This task was described in Chapter 2 and it is the same methodology used for evaluating a volumetric source by using univariate statistics (i.e., histograms). The distribution of earthquakes within each sources is shown in Figure 3-14.

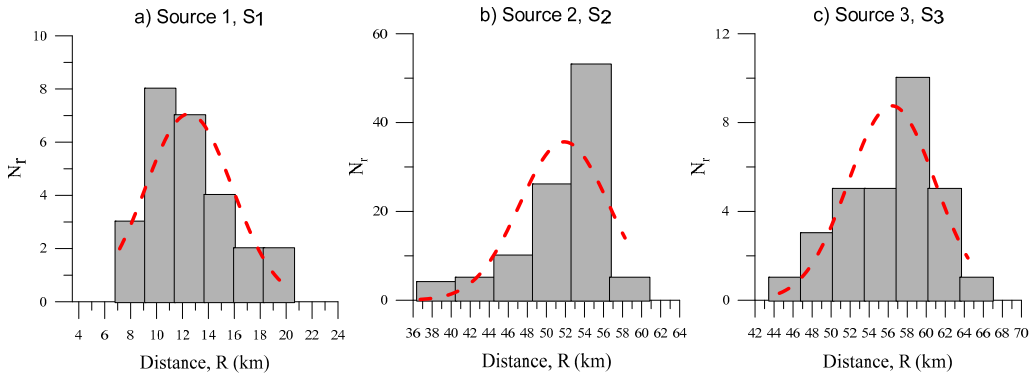

Figure 3-14 Spatial uncertainty illustration (Histograms) S_1, S_2 and S_3

A PSHA examines all possible seismic events and resulting events integrating their corresponding probability of occurrence within a source to finally establish the level of ground motion intensity that exceeds with a threshold value (i.e., tolerably low rate.) As

GMPEs are developed in terms of distances (R) and magnitudes (M), both parameters need to be addressed statistically. First, distances are obtained from histograms which are generated using number of samples on the y-axis and can be transformed to probability by assuming the maximum number of samples within a bin as one; Ground motion calculations is performed for every average distance at every single combination of bin size for each seismic source.

On the other hand, the size uncertainty can be determined by using recurrence law models described in Chapter 2. PSHA approach makes the assumption that the recurrence law obtained from past seismic events is applicable for the prediction of future seismic events (Kramer 1996). In other words, a recurrence law describes the mean annual rate (λ_m) for a specific catalog of earthquakes which will be used later for probability calculations for different combinations of ground motion, magnitude and source-to-site distance as part of PSHA. The seismicity rate model assumes that rates of earthquakes (M 1.5 – 4.5) can be used along with a Bounded Gutenberg-Richter magnitude-frequency distribution (Guttenberg and Richter 1944). The Bounded G-R model is developed based on the Standard G-R model (Guttenberg and Richter 1944) which characterizes seismic sources by obtaining parameters from regression of the database of seismicity from the source of interest (i.e., “a” and “b” parameters; Guttenberg and Richter 1944).

Parameters “a” and “b” are obtained based on the equation found from the Standard G-R model (Figure 3-15) and results are tabulated in Table 3-3. Parameters “a” and “b” will be used for the calculation of the temporal distribution of earthquakes “ν”. The model assumes a maximum earthquake M_{max}6.0 to be associated with all sources and a minimum earthquake M_{min}1.5 assuming that earthquakes of magnitude less than 1.5 do

not produce significant ground motion that contributes to the seismic hazard at EM site. The value "ν" is used for the calculation mean annual rate of exceedance for each source of the Bounded G-R recurrence model (McGuire and Arabasz 1990) defined by the Equation 3.1:

$$\lambda_m = \nu \frac{\exp[-\beta(m-m_0)]-\exp[-\beta(m_{max}-m_0)]}{1-\exp[-\beta(m_{max}-m_0)]}\ ; \qquad m_0 < m < m_{max} \qquad 3.1$$

Where, ν is the temporal distribution of earthquake recurrence; β=2.303*b*; b=parameter obtained by regression of the database of seismicity from the source of interest; m_0=minimum magnitude (m0=1.5); m_{max}= maximum magnitude assumed in our model (m_{max}=6.0); and λ_m is the mean annual rate of exceedance

Table 3-3 "a" and "b" parameters (Figure 3-15) (S1, S2, S3)

Source	Parameters from Regression (Earthquake catalog) Standard G-R model		ν
	a	B	
S1	2.53	0.76	24.2
S2	2.93	1.00	27.1
S3	2.61	0.99	13.5

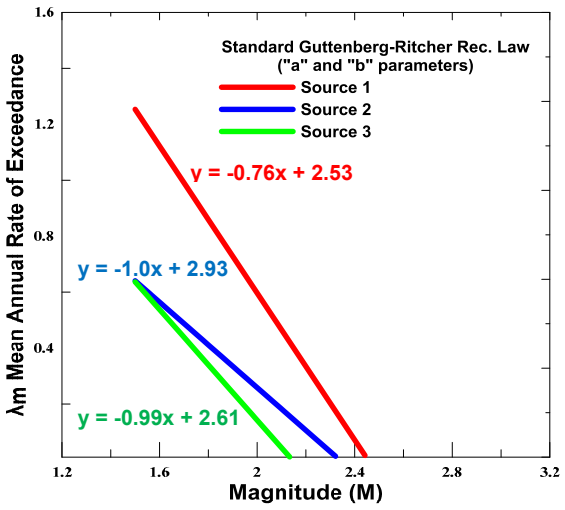

Figure 3-15 Standard G-R model for S_1, S_2 and S_3 at EM

Table 3-4 summarizes values the calculations based on the G-R recurrence model described in Chapter 2. Figure 3-16 illustrates the Bounded G-R recurrence model for each source capable of producing considerable ground motion at the Eagle Mountain Dam.

Table 3-4 Gutenberg-Richter Recurrence Law calculation (S_1, S_2, S_3)

Years (Data collected)		8	Source 1					
Range	M	Description	# Eqs	N_m	λ_m	log λ_m	ν	λ_m (Bounded)
1.5							10.5	10.50
2	2-2.5	M>2	5	26	3.25	0.51		4.37
2.5	2.51-3	M>2.5	14	21	2.63	0.42		1.81
3	3.01-3.5	M>3	5	7	0.88	-0.06		0.75
3.5	3.51-4	M>3.5	2	2	0.25	-0.60		0.31
4	4.01-4.5	M>4	0	0	0	-		0.13

Years (Data collected)		8	Source 2					
Range	M	Description	# Eqs	N_m	λ_m	log λ_m	ν	λ_m (Bounded)
1.5			8	104	13	1.11	27.1	27.07
2	2-2.5	M>2	50	96	12	1.09		3.35
2.5	2.51-3	M>2.5	35	46	5.75	0.76		1.07
3	3.01-3.5	M>3	10	11	1.38	0.14		0.34
3.5	3.51-4	M>3.5	1	1	0.13	-0.90		0.11
4	4.01-4.5	M>4	0	0	0	-		0.03

Years (Data collected)		8	Source 3					
Range	M	Description	# Eqs	N_m	λ_m	log λ_m	ν	λ_m (Bounded)
1.5							13.5	13.52
2	2-2.5	M>2	17	30	3.75	0.57		4.33
2.5	2.51-3	M>2.5	9	13	1.63	0.21		1.39
3	3.01-3.5	M>3	3	4	0.5	-0.30		0.44
3.5	3.51-4	M>3.5	1	1	0.13	-0.90		0.14
4	4.01-4.5	M>4	0	0	0	-		0.045

PSHA computations are primarily based on the temporal distribution of earthquake recurrence "ν" and probabilistic calculations that are described in the following sections. Source-to-site probability distribution can be directly obtained from

histograms (Figure 3-14). Results for the source-to-site probability distribution are summarized in Table 3-5.

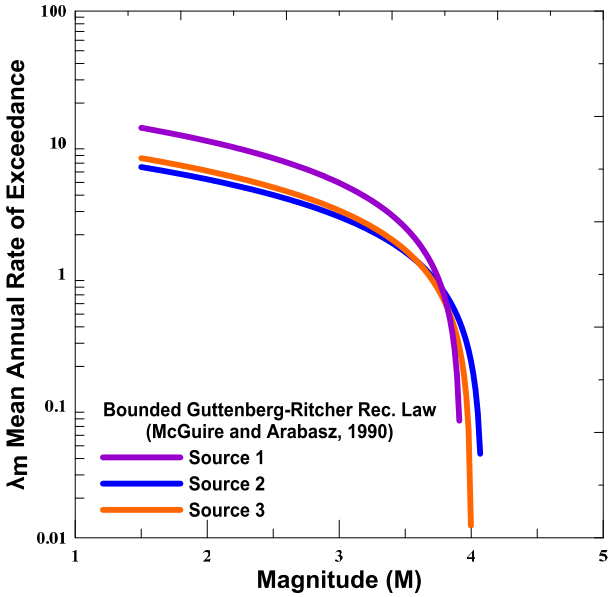

Figure 3-16 Bounded G-R model for S_1, S_2 and S_3 at EM

Table 3-5 Source-to-site probability distribution (S_1, S_2, S_3)

Description	Source-to-Site Probability Distribution							
	Source 1 (26 observations)							
Bin Limits (km)	6.9	9.2	11.4	13.7	16.0	18.3	20.6	-
Range of Limits (km)	6.9 - 9.2	9.2 -11.4	11.4 -13.7	13.7 - 16	16 - 18.3	18.3 - 20.6	-	-
Frequency	4	8	6	4	2	2	-	-
Probability	0.15	0.31	0.23	0.15	0.08	0.08	-	-
	Source 2 (103 observations)							
Bin Limits (km)	36.5	40.5	44.6	48.6	52.6	56.7	60.8	-
Range of Limits (km)	36.5-0.5	40.5 - 4.6	44.6 - 48.6	48.6-52.6	52.6 -56.7	56.7 - 60.8	-	-
Frequency	4	5	10	26	53	5	-	-
Probability	0.04	0.05	0.1	0.25	0.52	0.05	-	-
	Source 3 (31 observations)							
Bin Limits (km)	43.5	46.9	50.2	53.5	56.9	60.2	63.5	66.9
Range of Limits (km)	43.5-46.9	46.9-50.2	50.2- 53.5	53.5-56.9	56.9-60.2	60.2- 63.5	63.5- 6.9	-
Frequency	1	3	5	5	10	6	1	-
Probability	0.032	0.097	0.161	0.161	0.323	0.194	0.032	-

Several assumptions are used to derive the seismic hazard at EM. Since, the earthquake catalog for the site is limited and it is not possible to generate an adequate magnitude probability distribution for seismic sources at EM, the magnitude probability distribution is simplified by assuming to be the same for all three sources. Intervals of 0.5 of magnitude from the range of M1.5 to M6.0 (i.e., 1.5-2.0; 2.0-2.5; 2.5-3.0) are used to estimate the probability of size within seismic sources. The magnitude probability distribution function is given by Equation 3.2 (Guttenberg and Richter, 1944) and results are tabulated in Table 3-6.

$$f_M(m) = \frac{\beta \exp[-\beta(m-m_0)]}{1-\exp[-\beta(m_{max}-m_0)}$$ 3.2

Table 3-6 Magnitude probability distribution S_1, S_2 and S_3

Magnitude (M)	M_{ave}	Probability (Eq. 3.2)
1.5	-	-
2	1.75	0.32
2.5	2.25	0.31
3	2.75	0.16
3.5	3.25	0.07
4	3.75	0.03
4.5	4.25	0.01
5	4.75	0.004
5.5	5.25	0.002
6	5.75	0.001

3.4.2 Ground Motion Probability Calculations

The goal of PSHA is primarily to use GMPEs by considering the probability of occurrence of any size of earthquake at any possible point in each source using the probability distribution for both source-to-site and magnitude computed in previous sections. The inherent uncertainty present in the predictive equation (GMPE) is also

considered for the computation of PSHA by using its standard deviation in calculations. As discussed in previous sections, ground motion at EM Lake is calculated in terms of magnitude and source-to-site distance by using GMPEs developed by Atkinson (2015). GMPEs developed by Atkinson (2015) are described in Chapter 2 (Eq. 2.8; Eq. 2.9 and Eq. 2.10) as well as coefficients for PGA calculation described in Table 3-7. The calculation of ground motion for each source is performed for every average source-to-site distance value (R_{ave}; Table 3-7) and average magnitude (M_{ave}) obtained from the average of bin limits shown in Table 3-6. The computation of ground motion for three seismic sources are tabulated in Table 3-8.

Table 3-7 R_{ave} calculation used in GMPE (S_1, S_2 and S_3)

Description	Average Source-to-site distance, R_{ave} (km)							
	Source 1							
Bin Limits (km)	6.7	9.2	11.4	13.7	16.0	18.3	20.6	-
R_{ave} (km)	8.00	10.3	12.6	14.9	17.2	19.4	-	-
	Source 2							
Bin Limits (km)	36.5	40.5	44.57	48.6	52.9	56.7	60.9	-
R_{ave} (km)	38.5	42.6	46.6	50.7	54.70	58.8	-	-
	Source 3							
Bin Limits (km)	43.5	46.9	50.2	53.5	56.9	60.20	63.5	66.9
R_{ave} (km)	45.2	48.5	51.9	55.2	58.5	63.5	65.2	-

Table 3-8 Log (PGA) Calculation for S_1, S_2 and S_3 (cm/s^2)

Source	M	h_{eff} (Km)	Distance R_{hypo} (Km)					
			8.0	*10.3*	*12.6*	*14.9*	*17.2*	*19.4*
1	1.75	1	-1.13	-1.32	-1.48	-1.60	-1.7	-1.81
	2.25	1	-0.46	-0.64	-0.8	-0.92	-1.03	-1.13
	2.75	1	0.16	-0.03	-0.18	-0.30	-0.41	-0.51
	3.25	1	0.72	0.54	0.39	0.26	0.15	0.06
	3.75	1	1.23	1.04	0.90	0.77	0.66	0.56

Source	M	h_{eff} (Km)	Distance R_{hypo} (Km)					
			38.5	*42.5*	*46.6*	*50.7*	*54.7*	*58.8*
2	1.75	1	-2.33	-2.40	-2.47	-2.53	-2.60	-2.65
	2.25	1	-1.65	-1.72	-1.80	-1.86	-1.91	-1.97
	2.75	1	-1.03	-1.10	-1.17	-1.24	-1.29	-1.35
	3.25	1	-0.46	-0.54	-0.61	-0.67	-0.73	-0.78
	3.75	1	0.042	-0.033	-0.10	-0.17	-0.22	-0.28

Source	M	h_{eff} (Km)	Distance R_{hypo} (Km)					
			45.2	*48.5*	*51.9*	*55.2*	*58.5*	*63.5*
3	1.75	1	-2.45	-2.50	-2.55	-2.60	-2.64	-2.71
	2.25	1	-1.77	-1.82	-1.87	-1.92	-1.97	-2.03
	2.75	1	-1.15	-1.20	-1.25	-1.30	-1.35	-1.41
	3.25	1	-0.59	-0.64	-0.69	-0.74	-0.78	-0.84
	3.75	1	-0.08	-0.13	-0.18	-0.23	-0.28	-0.34

PSHA results can either be illustrated by seismic hazard curves or seismic hazard maps (Kramer 1996). The present study presents results by generating seismic hazard curves for the Eagle Mountain Lake site. Seismic hazard curves illustrate the annual probability of exceedance (λ) of several values of a ground motion parameter previously selected (i.e., PGA). Then first, the probability that various target peak

acceleration levels will be exceeded can be initially calculated by evaluating the standard normal variable (z*) (Equation 2.15) and by using the cumulative distribution function (CDF) of a Gaussian distribution as described in Chapter 2.

Sample calculations are tabulated in Table 3-9 for the probability of exceedance (z*) 0.10 cm/s^2 by using Equation 2.15 described in Chapter 2. The probability that various target peak acceleration levels will be exceeded is then calculated by using the standard normal variable (z*) as part of a Gaussian cumulative distribution function. The probability that peak ground acceleration within the sources will exceed a specific given PGA value is summarized in Table 3-10 for PGA=0.1 cm/s^2. Finally the Mean rate of exceedance (λ) is calculated based on Equation 2.17 by multiplying the temporal distribution recurrence of earthquakes "v" (Table 3-3), the source-to-site probability (Table 3-5), the magnitude or size probability assumed (Table 3-6) and the probability of exceedance a given PGA value (Table 3-10).

Table 3-9 Standard normal variable (z*) for CDF (PGA=0.1 cm/s^2)

Source	M	Distance R_{hypo} (Km)					
		8.0	*10.3*	*12.6*	*14.9*	*17.2*	*19.4*
1	1.75	8.5	8.96	9.37	9.71	10.01	10.26
	2.25	6.62	7.13	7.54	7.88	8.17	8.43
	2.75	4.94	5.45	5.86	6.20	6.50	6.75
	3.25	3.42	3.93	4.34	4.68	4.95	5.23
	3.75	2.05	2.56	2.97	3.32	3.61	3.87

Source	M	Distance R_{hypo} (Km)					
		38.5	*42.5*	*46.6*	*50.7*	*54.7*	*58.8*
2	1.75	11.67	11.87	12.06	12.23	12.39	12.54
	2.25	9.83	10.04	10.23	10.40	10.56	10.70
	2.75	8.16	8.36	8.55	8.72	8.88	9.03
	3.25	6.63	6.84	7.03	7.20	7.36	7.50
	3.75	5.27	5.47	5.66	5.83	5.99	6.14

Source	M	Distance R_{hypo} (Km)

		45.2	48.5	51.9	55.2	58.5	63.5
3	1.75	0.12	0.12	12.28	12.41	12.53	12.70
	2.25	0.10	10.31	10.45	10.58	10.70	10.86
	2.75	0.09	8.63	8.77	8.90	9.02	9.19
	3.25	0.07	7.14	7.25	7.38	7.50	7.67
	3.75	0.06	5.75	5.88	6.01	6.134	6.30

Table 3-10 Probability of exceedance $P[Y > 0.1\ \mathrm{cm/s2}|m, r| = 1 - F_y(z^*)$

Source	M	Distance R_{hypo} (Km)					
		8.0	10.3	12.6	14.9	17.2	19.4
1	1.75	0E+00	0E+00	0E+00	0E+00	0E+00	0E+00
	2.25	2E-09	6E-11	3E-12	2E-13	1E-14	0E+00
	2.75	5E-05	3E-06	3E-07	3E-08	5E-09	9E-10
	3.25	4E-02	5E-03	9E-04	2E-04	4E-05	1E-05
	3.75	2E+00	6E-01	2E-01	6E-02	2E-02	7E-03

Source	M	Distance R_{hypo} (Km)					
		38.5	42.5	46.6	50.7	54.7	58.8
2	1.75	0E+00	0E+00	0E+00	0E+00	0E+00	0E+00
	2.25	0E+00	0E+00	0E+00	0E+00	0E+00	0E+00
	2.75	3E-14	0E+00	0E+00	0E+00	0E+00	0E+00
	3.25	2E-09	6E-10	2E-10	5E-11	1E-11	5E-12
	3.75	1E-05	3E-06	1E-06	4E-07	2E-07	6E-08

Source	M	Distance R_{hypo} (Km)					
		45.2	48.5	51.9	55.2	58.5	63.5
3	1.75	4.5E-01	4.5E-01	0.0E+00	0.0E+00	0.0E+00	0.0E+00
	2.25	4.6E-01	0.0E+00	0.0E+00	0.0E+00	0.0E+00	0.0E+00
	2.75	4.7E-01	0.0E+00	0.0E+00	0.0E+00	0.0E+00	0.0E+00
	3.25	4.7E-01	5.8E-13	2.1E-13	8.2E-14	3.3E-14	9.0E-15
	3.75	4.8E-01	4.6E-09	2.0E-09	9.3E-10	4.4E-10	1.5E-10

Finally, the process is repeated to calculate the probabilities for various target peak acceleration levels coming for each source. The total seismic hazard analysis at the Eagle Mountain Lake site is the summation of the hazard caused of each source. Seismic

hazard curves developed for the Eagle Mountain Lake site is shown in Figure 10 for three sources (S_1, S_2 and S_3) within the 60 km radius.

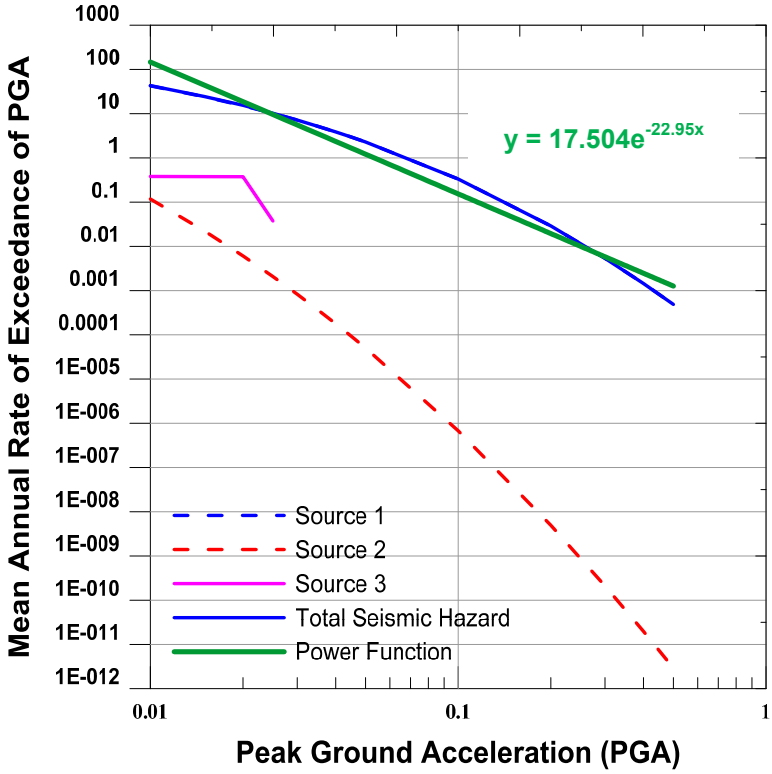

Figure 3-17 Seismic Hazard curves for EM site (2016)

3.4.3 Finite Time Period

The total seismic hazard curve obtained can be integrated with the Poisson model to define probabilities of exceedance in finite time intervals (Equation 2.18). The model proposed is valid for probabilities of exceedance in one-year since the rate of earthquakes is non-stationary in the region; however, model considered stationary until 2016 and short time periods are more suitable for this uncertainty. Finally, the

probabilistic seismic hazard analysis for the Eagle Mountain Dam is a peak ground acceleration of 0.325g with a 1% probability of being exceeded in a 1-year period.

3.3 Validation of Seismic Hazard Analysis

Seismic hazard curves presented in this study for the Eagle Mountain Lake site are validated with the recent "2016 One-Year Seismic Hazard Forecast for the Central and Eastern United States from Induced and Natural Earthquakes" report released by USGS (Petersen et al. 2016). USGS reported seismic hazard curves using a different methodology and considering a large earthquake catalog covering areas like Oklahoma.

Seismic hazard curves developed by USGS are presented in Figure 3-18 and the validation of the proposed simplified model is compared with the seismic curve developed for the city of Dallas, TX which is the closest location to the Eagle Mountain Lake site. USGS also provided seismic hazard maps for the one-year hazard forecast for Central United States as shown in Figure 3-19. The area of North Texas shows a hazard of approximately 0.25-0.28g with 1% probability of being exceeded in one-year. From the PSHA approach developed, the probability of exceedance is computed for a value of PGA=0.32g by using 2.18 and it is compared with USGS seismic hazard. Based on the calculation, the probability of exceedance 0.27g is 1% for one-year forecast. The simplified seismic hazard analysis can be used for analyzing civil infrastructure in similar regions.

PSHA computations present more suitable results for the evaluation of seismic hazard in North of Texas as compared with those resulting from DSHA that underestimate the hazard. Geotechnical seismic evaluation of structures can use the present simplified approach for different application such as liquefaction analysis, pseudo-static slope stability and lateral spreading. An important limitation of the

methodology is that the rate of earthquakes is assumed to be non-stationary. Central United States including the North Texas region are subjected to an increase of seismicity without a defined or constant rate of earthquakes. Therefore, an update catalog of earthquakes is required if the simplified seismic hazard will be used in the future.

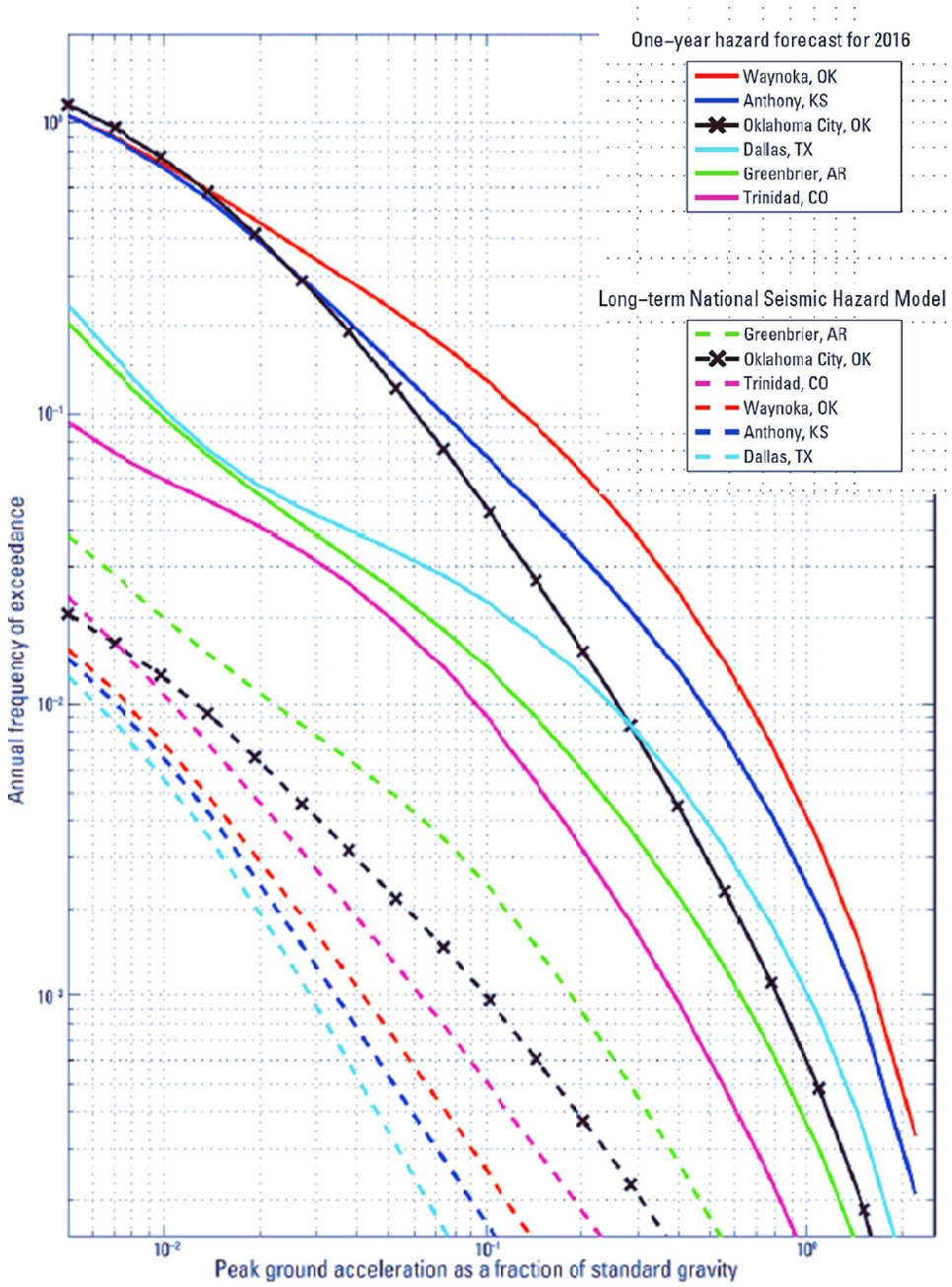

Figure 3-18 Seismic Hazard curves for central US (Petersen et al. 2016)

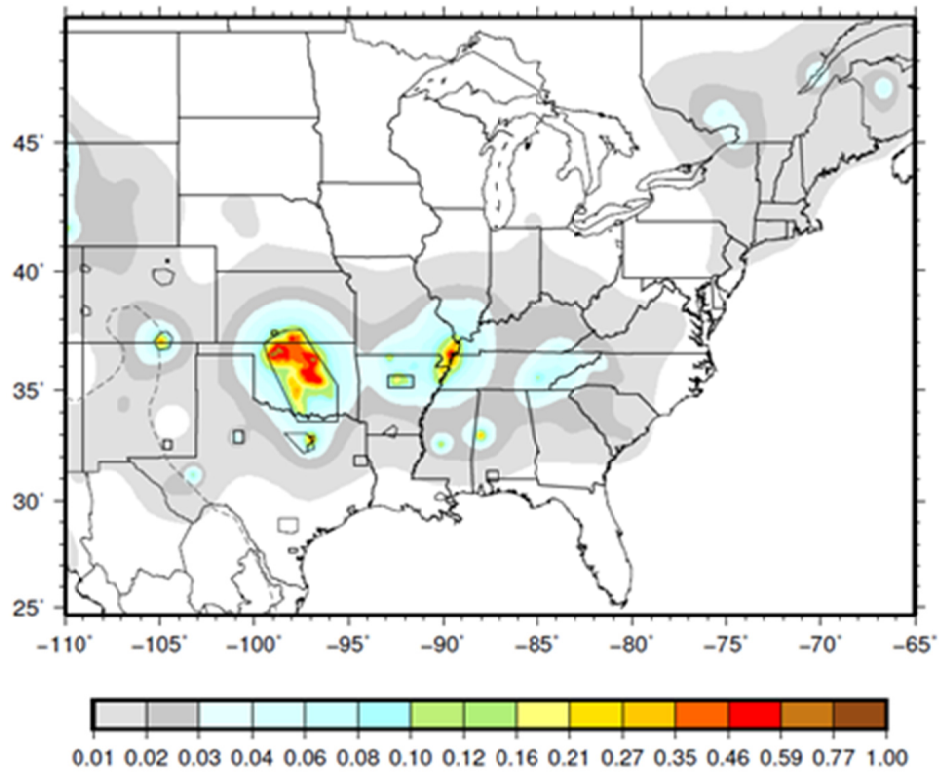

Figure 3-19 PGA for 1% probability of exceedance in one-year (Petersen et al. 2016)

The present research uses the computed probabilistic seismic hazard analysis for the estimation of the earthquake loading to assess the cyclic liquefaction potential in hydraulic fill dams. The following Chapter includes the estimation of the liquefaction soil resistance based on the spatial variability encountered in soils at Eagle Mountain Dam and the cyclic liquefaction at this site will be evaluated based on a peak ground acceleration of 0.3g. The PGA of 0.3g is selected based on the average of acceleration values obtained from both, the calculations using the present seismic hazard analysis for (i.e., 0.32 g) and the seismic hazard released by USGS (i.e., 0.28g) at the Eagle Mountain Dam Site (Petersen et al. 2016).

Chapter 4 Soil Variability Characterization using 3D Geostatistics and Visualization Models

4.1 Introduction

Soil characterization preludes geotechnical evaluation of site conditions. Traditionally, soil is characterized by interpreting soil data from the site using different in-situ methodologies (i.e., SPT and CPT), and by conducting laboratory tests on the soil samples. Over the years, researchers and practitioners have relied mostly on the in-situ tests to understand the soil behavior types and other geotechnical properties. The constraints of a soil investigation program pose inevitable challenges to engineers in interpreting the soil properties between two or more bore holes or in-situ tests.

In the last decade, several researchers have demonstrated the applicability of probabilistic theories to address this variability of soil properties. However, these studies are used to interpret the soil properties in two-dimensional (2D) models, and in the case of hydraulic dams, the variability pertains to three-dimensional (3D) models. The variability of soil properties in hydraulic fill dams has been demonstrated by several researchers (Seed et al. 1973). This chapter presents a methodology for developing a 3D visualization model of a hydraulic fill dam by incorporating the spatial variability of soils. In order to demonstrate the methodology, Eagle Mountain Dam, a hydraulic fill dam located in Fort Worth, Texas, was considered for this study.

The Eagle Mountain Dam is situated on top of a geologic formation known as the Fort Worth Basin (Bend Arch-Fort Worth Basin). The Fort Worth Basin is a geologic formation located in North Central Texas and Southwestern Oklahoma that has a north-south orientation, it is elongated in shape, relatively shallow in depth, and covers around 15,000 miles^2 (38,100 km^2) (Montgomery et al. 2005) as shown in Figure 4-1. The Eagle

Mountain Dam is located on top of Mississippian deposits, which consist of alternating shallow-marine limestones and black organic-rich shales (Fernandez 2013). The area is underlain by the 1000 ft. thick Barnett Shale formation that contains significant limestone (Pollastro 2003).

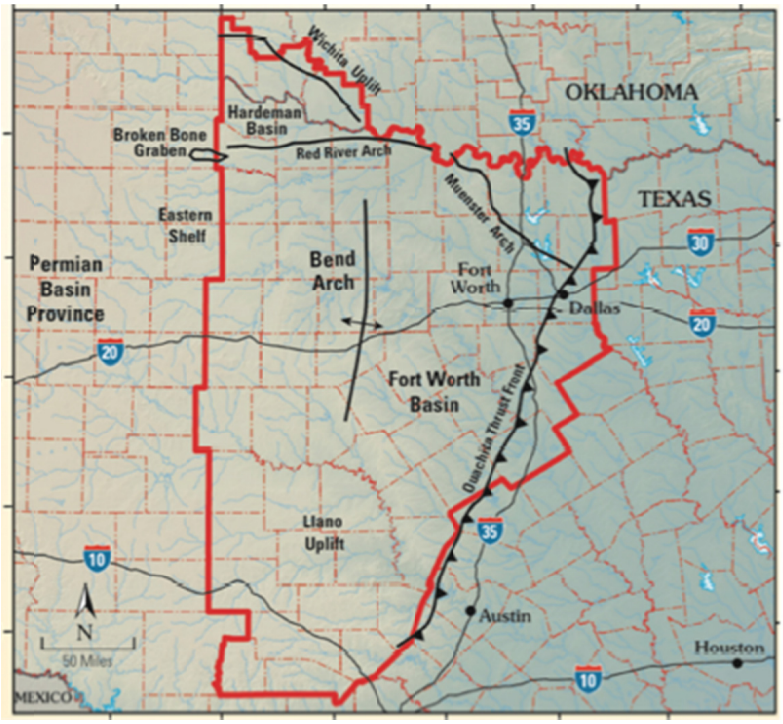

Figure 4-1 Bend Arch-Fort Worth Basin Province (Red line) (USGS 2013 after Pollastro 2003)

The soils in the Fort Worth Basin primarily consist of gently tilted sediments of mostly Cretaceous age. Several groups of soils can be found in North Texas, specifically in the DFW area, where the site of interest is situated, as shown in Figure 4-2. Based on the location of the Eagle Mountain Dam, it can be inferred that the soils in this area are Washita and Woodbine sandstone geological formations. Soils in the Washita group include thick clay units and thin limestone units, whereas the Woodbine soils consist of

marine beds of sand, clay, sandstone, and shale (USGS 2016). The Eagle Mountain Dam was constructed by excavating soils near the site and by placing them, using hydraulic fill and wetted and rolled construction procedures. The following section presents a comprehensive soil variability characterization of the hydraulic fill dam, based on interpretation of in-situ tests (i.e., CPT) and using existing correlations in the literature. The interpretations of these results were combined with Geostatistics to incorporate the spatial variability of the soil in the generation of three-dimensional models of the Eagle Mountain Dam.

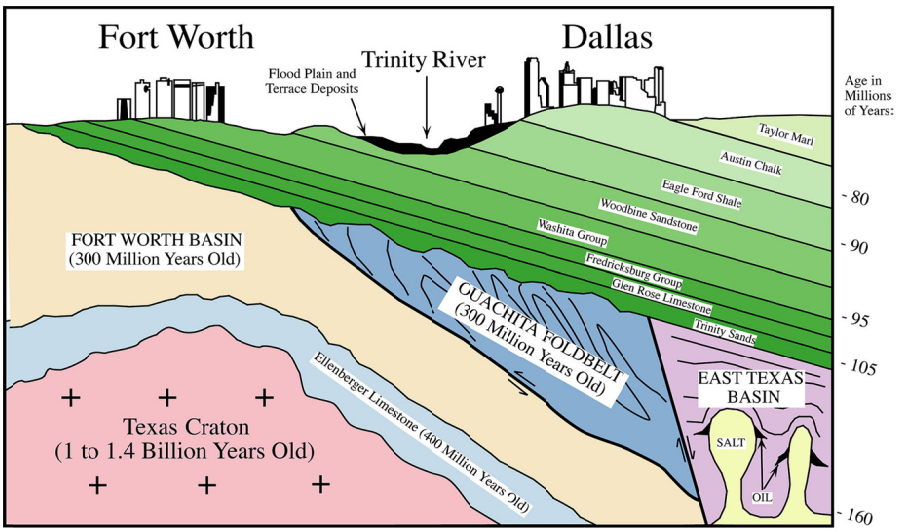

Figure 4-2 Schematic E-W section of DFW (CC BY-SA 3.0, Creative Commons)

4.2 Three-Dimensional Soil Characterization of the Eagle Mountain Dam

4.2.1 Data Collection

The Eagle Mountain Lake (Figure 4-3) is impounded by a main dam and a levee. It is situated about 12.5 miles northwest of downtown Fort Worth, Texas. The length of the dam is approximately 4400 ft., with a height of about 85 ft. (crest approximately El+682).

Figure 4-3 Aerial view of EM Dam (Courtesy: Tarrant Regional Water District, TRWD Records)

According to construction records (Appendix B), the clay core of the main dam and part of the shells were constructed by the hydraulic fill method. A few of the sections also depict layers of soils placed in lifts with mechanical compaction (wetted and rolled). A sheet of sheet pile cutoff wall was installed along the main dam centerline, across the embankment foundation, and a core wall was added in the 1960s due to the presence of seepage problems (Figure 4-4).

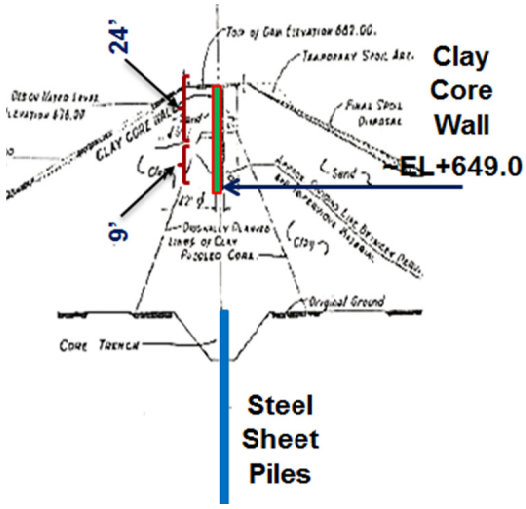

Figure 4-4 Typical cross section (TRWD Records - after Freese and Nichols 1957-1958)

As part of routine maintenance, inspections, and safety evaluations, a series of cone penetration test soundings (61) and exploratory borings (11) were performed at the site, as shown in Figure 4-5. Cone penetration tests with pore water measurements (CPTu) were performed on the crest (30), dry side toe (25), and far downstream of the dry toe of the dam (6). The CPTs at the crest were staggered to the upstream and downstream of the crest centerline to investigate conditions both downstream and upstream of the sheet pile cutoff, based on the assumption that the sheet pile was located directly on the crest centerline.

CPT with pore water pressure measurements and exploratory boring coordinates are provided based on North American Datum (NAD83). An extensive review of the CPT profiles was performed, and soil properties were determined by using conventional CPT correlations developed over the past two decades (Robertson 2009; Robertson and Cabal 2012). The following section includes the application of Geostatistics to the generation of three-dimensional models of several soil properties at the Eagle Mountain Dam.

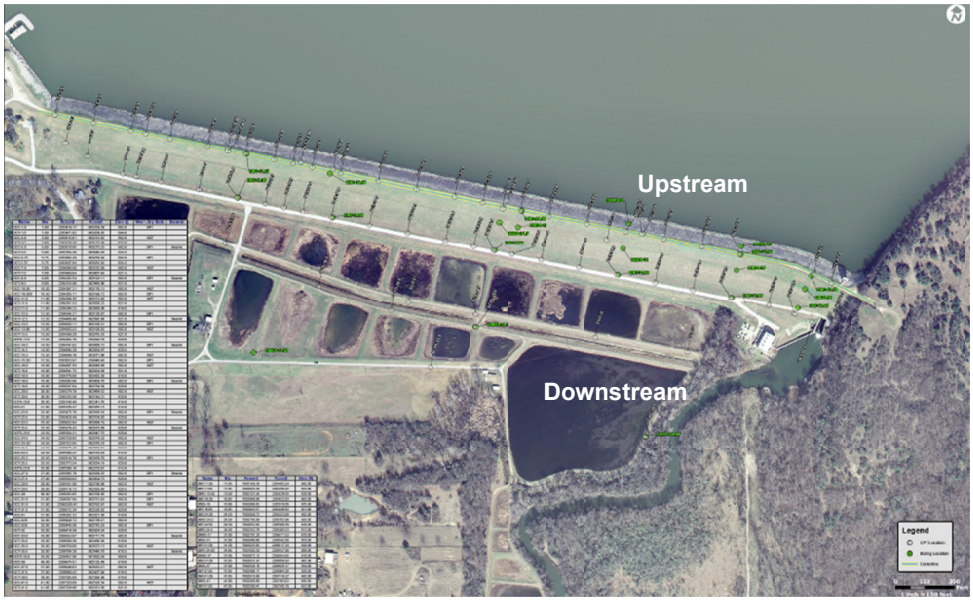

Figure 4-5 CPT and exploratory boring logs at the EM Dam (Courtesy: Tarrant Regional Water District, TRWD Records)

4.2.2 Soil Variability

As a part of the data collection, construction drawings from the 1930 were used to understand the soil configuration within the dam. Thirty (30) as-built drawings were collected from archives and were arranged by station numbers located along the centerline of the dam. Figure 4-6 shows a sketch of the station locations along the dam.

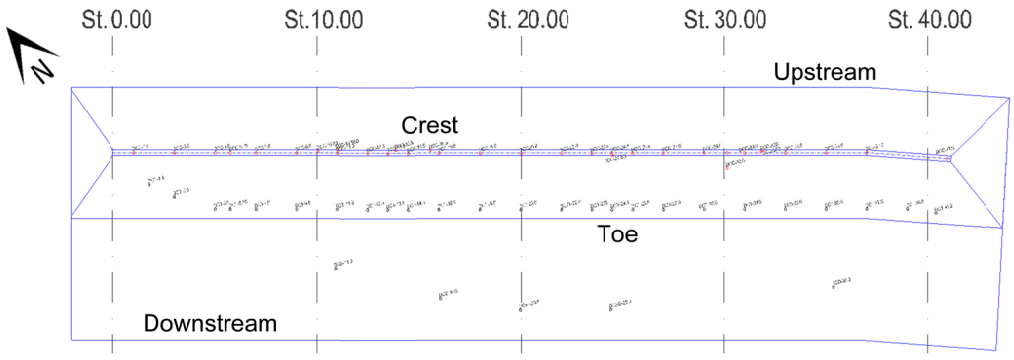

Figure 4-6 Station arrangement of EM Dam

Soil variability in the Eagle Mountain dam was visualized by creating two-dimensional fence diagrams from CPT data collected along the crest of the dam. The construction of the core wall, shown in Figure 4-4, was part of a mitigation plan in the 1960s. Since tests were performed downstream and upstream of the centerline of the dam (core wall), CPTs are assumed to have been aligned with each other before the interpolation. Soil behavior type (SBT) obtained from the Robertson (1986 updated 2009) chart was used to classify the types of soils within the dam (Robertson 2009). The interpolation between two CPT's was performed by using the Ordinary Kriging method, and results depicted that the dam presents significant soil variability as illustrated in Figure 4-7.

Four stages of the construction process developed in the 1930s were identified from this interpolation. The maximum height of the dam is located in Sector 3 (H~100 ft.), and the largest amount of hydraulic fill is also at this location. Sand lenses, as well as clay layers, can be identified embedded in Sector 3, at depths of approximately 60 to 80 ft. from the crest of the dam. Sector 1 also presents high soil variability in its configuration, and sand and silt lenses can be seen embedded where the hydraulic fill dam was placed, as per to construction drawings. It may be noted that vertical scale in Figure 4-7 has been increased to have a better visualization of the soil configuration within the dam.

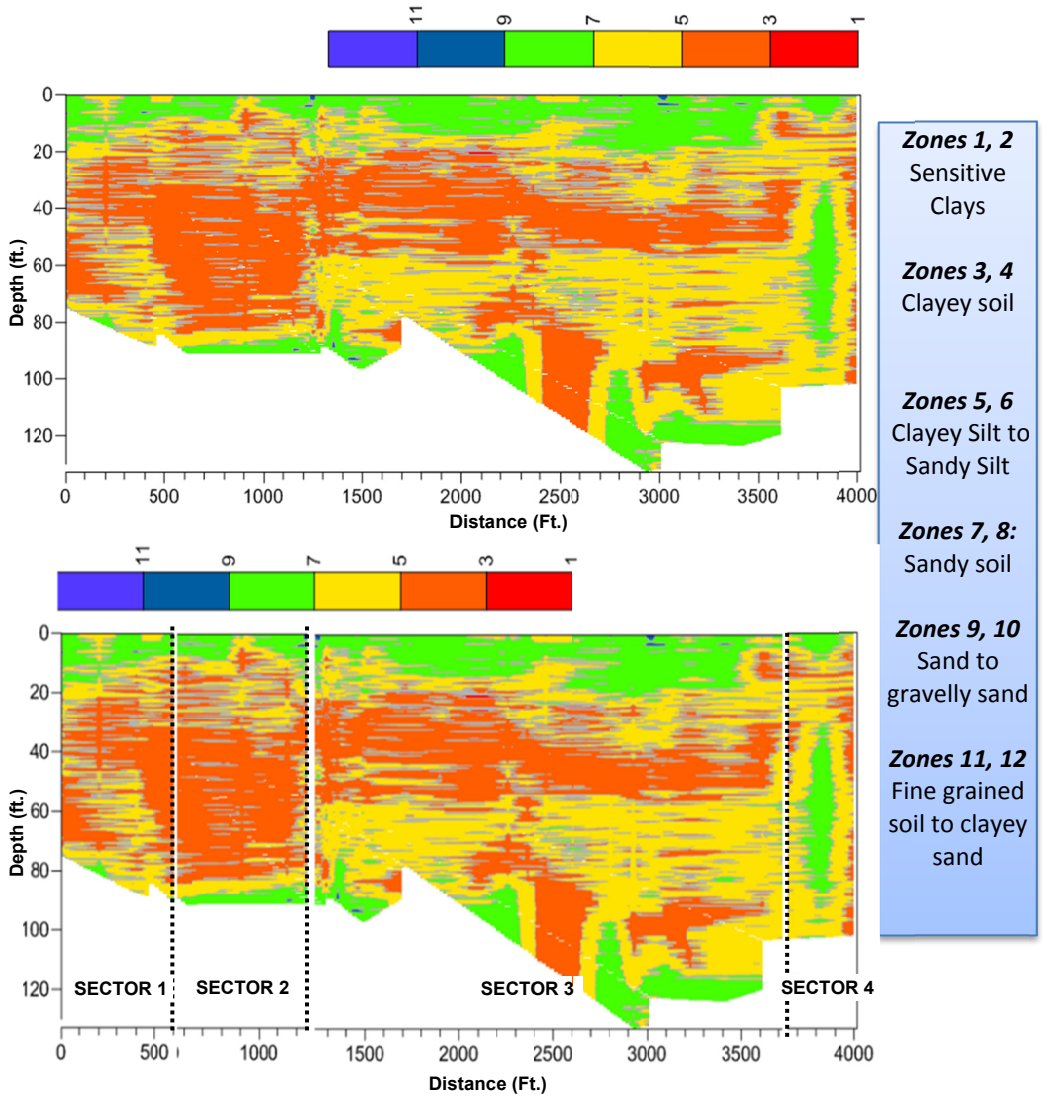

Figure 4-7 Two-dimensional fence diagram along the crest

Soil variability in the configuration of the dam was also addressed by comparing the variation of normalized tip resistance (Q_{tn}) variation with depth in specific depth ranges with the data from construction drawings of the same depth ranges. The analysis was performed on two stations located at about 2500 to 3500 ft., due to the high amount of hydraulic fill placed in those locations. The construction of the Eagle Mountain dam was performed in several stages, as shown in as-built drawings which present different contour colors depicting the thickness of the layers deposited at different times during construction.

The first approach was conducted by considering the assumption that each layer deposited by the contractor was of the same soil type and was applied for the evaluation of Station 25.00 (Figure 4-8). Based on construction drawings, the soil variability analysis performed at this station depicts that eight layers were placed in that specific section. The normalized tip resistance (Q_{tn}) was evaluated by sorting values within depth ranges according to the construction drawings. Histograms were generated for each layer and the coefficient of variation (COV) was computed for each layer. The COV ranges from approximately 18% to 100% in Station 25.00, and values were lower at elevation approximately El+640 to El+650, where it was expected that unique materials form the dam core. COV values continued to increase as the depth increased (i.e., EL+620 to El+629) due to the high amount of hydraulic fill placed in those locations.

The second approach was performed in Station 30.00 by assuming that the soil was placed in different layers, following a design criterion (i.e., clayey core and more granular top layers). Therefore, the construction drawing at Station 30.00 was divided into three ranges of depth, with two layers at the top, the first approximately from El+647 to El+662; the second layer from El+662 to the elevation of dam crest ~El+682; and the

third layer underneath the last two, approximately from El+600 to El+647. The COV was computed for all three layers, and it was found that the soil variability was higher in the deep layers, where the hydraulic fill was placed. Table 4-1 shows the COV values for every range of depth found in the analyses for both stations along the dam. Spatial variability was considered in this study by generating variograms before performing the Kriging interpolation. By performing conventional interpolation methods, problematic soils, such as sand lenses or small clay seams, might not be found due to the lack of spatial variability consideration.

Table 4-1 COV at Different Ranges of Depth at St. 25.00 and St. 30.00

Station	Elevation Range (ft.)	COV (%)
25.00	620-625	100
	625-629	72.0
	629-635	30.3
	635-642	18.4
	642-647	64.2
	647-650	46.6
	650-662	82.5
	662-682	100
30.00	600-647	100
	647-662	69.7
	662-682	46.4

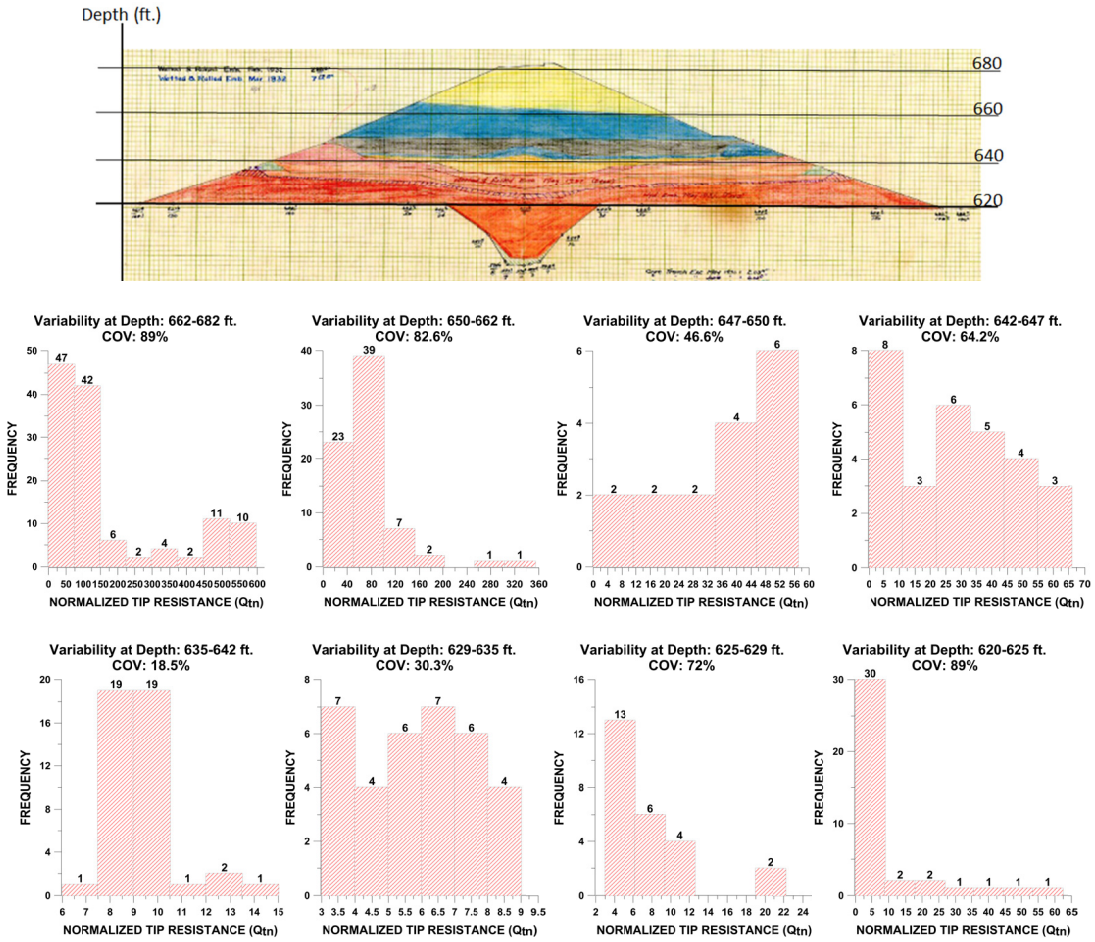

Figure 4-8 Soil variability estimation – Station 25.00

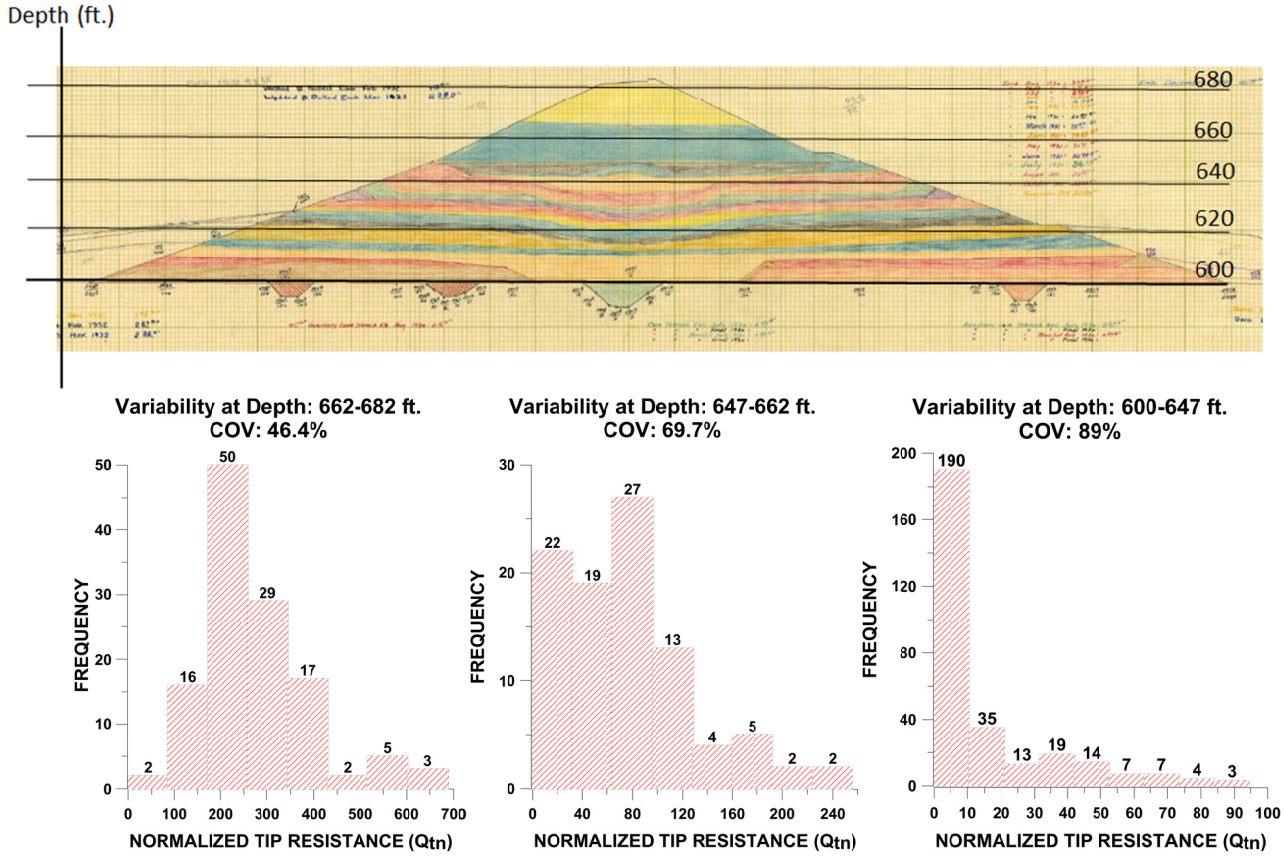

Figure 4-9 Soil variability estimation – Station 30.00

4.2.3 Interpretation of Soil Properties

This section presents the interpretation of soil properties within the dam configuration. Soil properties can be estimated by using existing correlations in literature based on collected data from in-situ tests. CPT records indicate that they were performed at an average interval of 200 ft. from each other, and the depths of the tests varied within the dam. The cone tip resistance (q_c), sleeve friction (f_s), and pore water pressure information (u_2) were collected, as shown in the sample CPTu result provided the local agency (Figure 4-10).

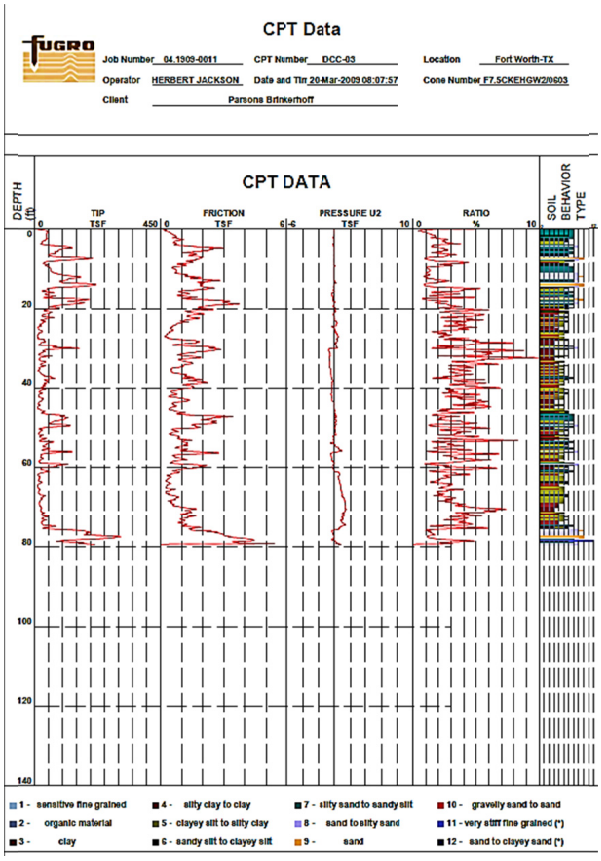

Figure 4-10 CPT data provided (Courtesy: Tarrant Regional Water District, TRWD Records)

Several soil properties were estimated based on the data collected from CPT and by using existing correlations found in the literature (Robertson and Cabal 2012). Soil behavior type (SBT), soil behavior type index (Ic), friction angle (ϕ), undrained shear strength (Su) and modulus of elasticity (E) were obtained by using different correlations. Soil type was determined by considering two different approaches. The first was presented by Robertson (1986) and is depicted in Figure 4-11a. It considered the tip resistance (q_c) and friction ratio (R_f). The second approach evaluated the soil behavior type Index (Ic) which considers the effect of depth by normalizing both the tip resistance and the friction ratio (Q_{tn} and F_r) (Figure 4-11b).

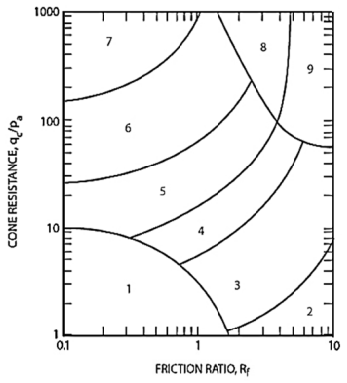

Zone	Soil Behavior Type
1	Sensitive, fine grained
2	Organic soils - clay
3	Clay – silty clay to clay
4	Silt mixtures – clayey silt to silty clay
5	Sand mixtures – silty sand to sandy silt
6	Sands – clean sand to silty sand
7	Gravelly sand to dense sand
8	Very stiff sand to clayey sand*
9	Very stiff fine grained*

* Heavily overconsolidated or cemented

P_a = atmospheric pressure = 100 kPa = 1 tsf

(a)

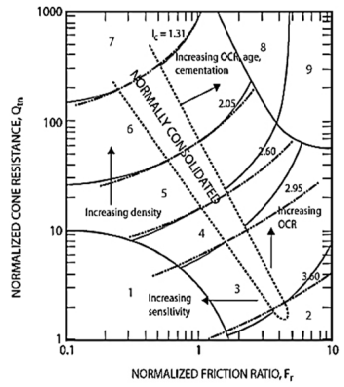

Zone	Soil Behavior Type	I_c
1	Sensitive, fine grained	N/A
2	Organic soils – clay	> 3.6
3	Clays – silty clay to clay	2.95 – 3.6
4	Silt mixtures – clayey silt to silty clay	2.60 – 2.95
5	Sand mixtures – silty sand to sandy silt	2.05 – 2.6
6	Sands – clean sand to silty sand	1.31 – 2.05
7	Gravelly sand to dense sand	< 1.31
8	Very stiff sand to clayey sand*	N/A
9	Very stiff, fine grained*	N/A

* Heavily overconsolidated or cemented

(b)

Figure 4-11 Soil type (a) Non-normalized CPT SBT chart (Robertson et al. 1986, updated by Robertson 2010) and (b) Normalized CPT SBT chart, Qt – F (Robertson 1990, updated by Robertson 2010)

The soil strength is often controlled by the effective stress frictional envelope, and the parameters obtained from the Mohr-Coulomb model: effective friction angle, ϕ' and effective cohesion intercept, c'. For sand, the effective drained friction angle can be evaluated by using Equation 4.1, developed by Robertson and Campanella (1983) (Robertson and Campanella 1983).

$$\Phi' = \arctan\left[0.1 + 0.38log\left(\frac{q_t}{\sigma_{vo}'}\right)\right] \quad 4.1$$

The strength of the clayey soils located within the core of the dam was evaluated by Equation 4.2, which was developed by theoretical solutions that provided some valuable insights (Robertson and Campanella 1983).

$$Su = \frac{q_t - \sigma_v}{N_{kt}} \quad 4.2$$

The modulus of elasticity (E) was determined by using empirical correlations compiled within the NCHRP report (Mayne 2007). Equations 4.3 and 4.4 were used to determine the constrained modulus for cohesionless and cohesive soils, respectively.

$$E_S = \begin{Bmatrix} 4q_C & q_{c<10MPa} \\ 2q_c + 20\ (MPa) & 10MPa < q_c < 50MPa \\ 120\ (MPa) & 50MPa < q_c \end{Bmatrix}; \text{ Cohesionless Soils} \quad 4.3$$

$$E_S = 8.25 * (\frac{q_t}{\sigma_{vo}})\ ; \text{ Cohesive Soils} \quad 4.4$$

Where, q_c represents the tip cone resistance, q_t represents the corrected tip resistance for pore water effects; σ_{vo} represents overburden pressure; σ'_{vo} represents effective overburden pressure; σ_{atm} represents reference stress ~1atm considered for the analysis and N_{kt} represents bearing capacity factor ~15 considered in this study.

4.2.3 Grid Generation

Visualization models are primarily generated by incorporating information that depicts the geometry of the site by using different methods: LiDAR, Unmanned Aerial

Vehicles (UAV) and even original construction drawings. The visualization of Eagle Mountain Dam was generated by utilizing the original “as-built” drawings from 1930 and incorporating them into a reasonable geometry. Coordinates for points at each section were generated as two main surfaces, top and bottom, shown in red and blue, respectively, in Figure 4-12. Various sections were obtained along the dam and interpolated, using Kriging, to generate a three-dimensional grid or mesh of the dam. Figure 4-12 illustrates the process used to develop the surfaces of the dam. Contour colors of surfaces denote the elevation of each surface.

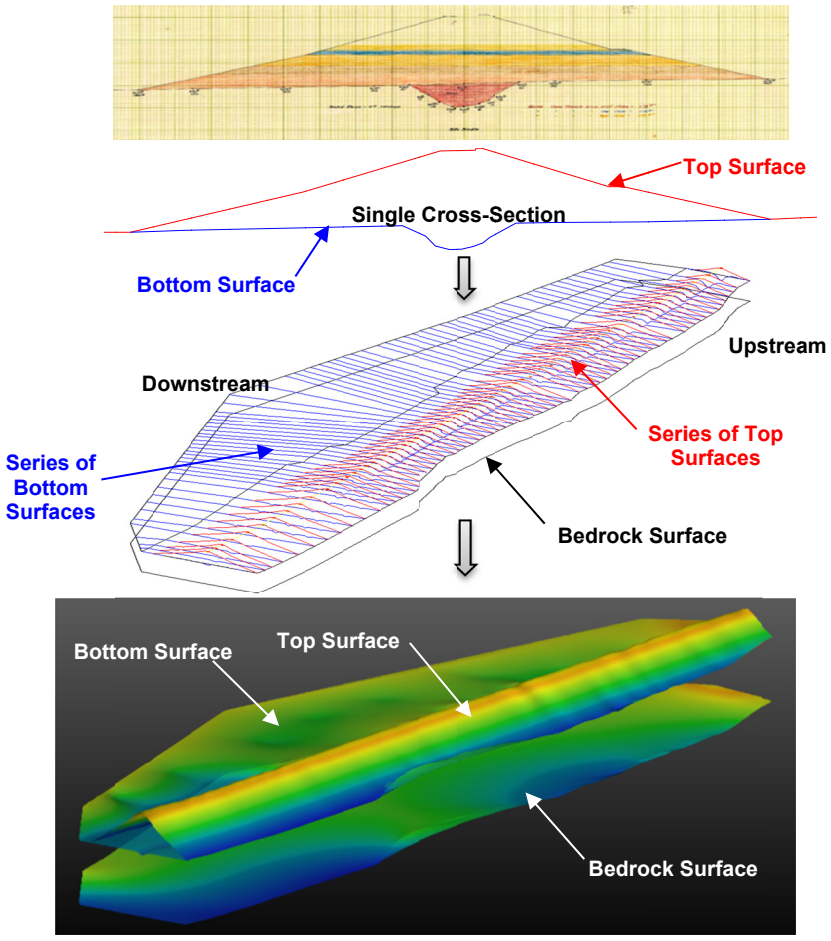

Figure 4-12 Generation of sections for geometric mesh

The final volumetric grid was generated by interpolating surfaces (as shown in the Figure 4-12), by using Kriging interpolation as well. Unlike other interpolation methods, Kriging produces a smoother geometry of the surface rather than showing spikes at locations where there is a lack of geometric information. The model was improved by incorporating some additional features, such as the group of sheet piles placed in 1932 at the bottom trench of the dam to control seepage underneath the dam. Additionally, a core sheet wall was placed at the top of the dam along the centerline of the dam after several seepage issues occurred in 1960. Interpolation of any data (i.e., soil parameters) can be performed within the volumetric grid herein generated.

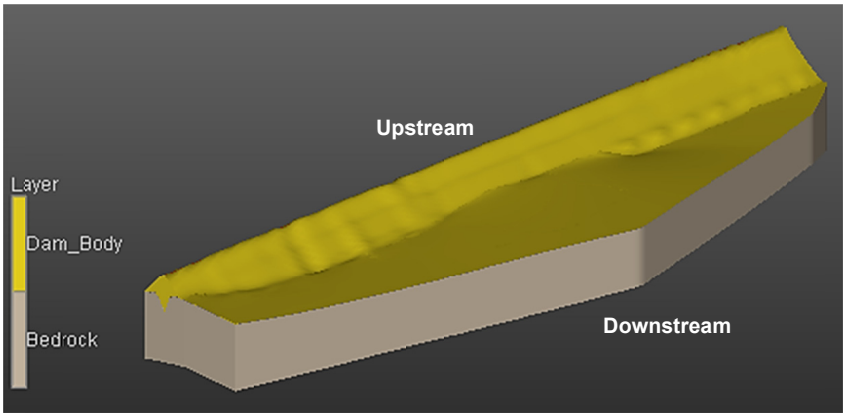

Figure 4-13 Final volumetric grid used for interpolation of soil data

Cone penetration test results were incorporated in the volumetric grid by using their corresponding coordinates. Visualization models are shown in the following section by evaluating the variogram for each soil property evaluated.

4.2.4 Three-Dimensional Visualization Models of Soil Properties

Visualization models were developed by using results obtained from the Kriging interpolation of CPT data correlations and by the generation of the semi-variograms. Semi-variograms were developed by considering the spatial variability, anisotropy of

data, and lag-distance distribution evaluated by the histograms. Ordinary Kriging was performed by combining the variogram analysis and its mathematical algorithm.

A visualization tool software was used for the interpolation of the data, using Kriging. The data collected had approximately 25,000 points to be interpolated within the volumetric grid generated in earlier sections. The Ordinary Kriging approach is prone to unacceptable results when the input data is highly clustered and/or oversampled in one or even two directions. It has to be computed within one single and unique matrix in order to obtain a complete interpolation of data. However, the capacity of the software is limited, and Kriging can be performed with a moderate amount of data (approximately 7000 data points). A data reduction tool is described in the following section to minimize the oversampling or the high cluster presented in data at some locations.

4.2.4.1 Data Reduction Tool

In statistics, it seems reasonable to assume that more data is always better. However, depending on how the data is used and interpreted, this is often not true. In general, reducing oversampling has several benefits including generating the model faster model and getting better quality of results. However, it is important to understand that the primary objective is to reduce the data without modifying the original raw input data.

The present analysis includes a data reduction tool to minimize the oversampling of CPT data collected. Several approaches can be used to reduce the data such gradient optimization, average at geometric centroid, extremes of samples, and maximum of samples and minimum of samples approach. The average of a geometric centroid is a useful method when there is noise in the data. This algorithm extracts different mean values along the distance intervals resulting in effective filtering. The main parameter is

the group size (linear distance). The extreme of samples preserves the minimum and maximum values along several distance intervals, and the primary parameter is the group size (linear distance). The “Max and Min of Samples” approach presented in the software preserves maximum and minimum values along the distance intervals, and the main parameter is the group size (linear distance). A data log process is also available, which generates the plot with log axes; it is useful for data spanning several orders of magnitude.

The gradient optimization approach of the software (Figure 4-14) uses a complex curve-fitting algorithm to fit the gradients in the user’s data with as few points as possible. The main parameters are epsilon and minimum distance. The epsilon value is a dimensionless parameter that describes how large gradients are allowed to exist along the bore line. In other words, it controls how finely the data is reduced. Larger values result in fewer points, and smaller values result in a higher number of data points. The minimum distance is used when several values remain the same for a large depth.

Setting the minimum distance with a high value ensures that there is at least one sample value within that large depth range. Group size is also present in this method; however, it has less direct influence on the results, and hence is not used for reducing the data in this approach. This approach is applied for each CPT before the interpolation of each soil property. The output of data minimized is the same, regardless of the approach used, for reduction of data in the software.

Figure 4-14 illustrates a sample of the data reduction tool used for the present study. The original raw data obtained from CPT DCD-24.5 originally contained 25,000 points. The gradient optimization described above was used for accommodation and reduction of data. It is a vital step since software is limited to a certain amount of data.

Kriging must be interpolated in one single matrix, and if a large number of samples values is present, this may not occur. For CPT data where high soil variability is present, a small value of epsilon (0.02-0.05) and a higher value of minimum distance (5-10 ft.) for the optimization of data in the software substantially reduced the data (5000 points), as shown in Figure 4-14. However, the reduced data of each boring log (red line) has to be checked to avoid missing meaningful original values.

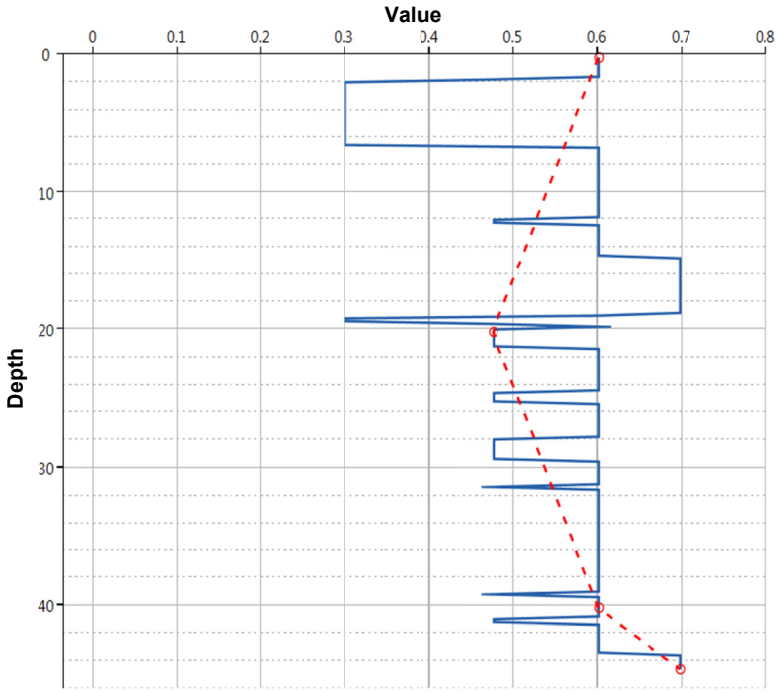

(a)

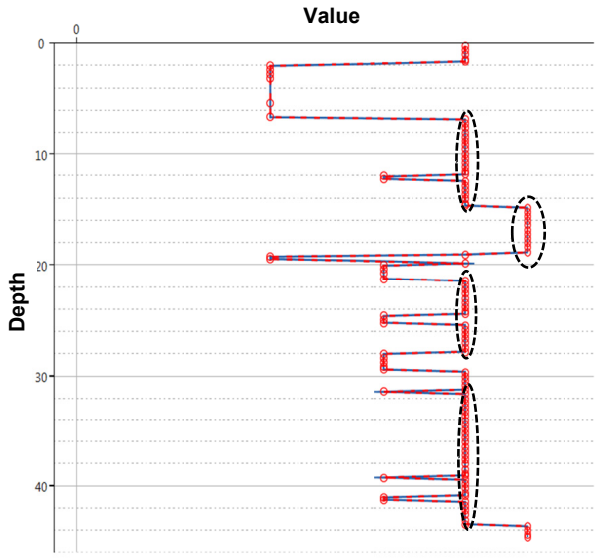

(b)

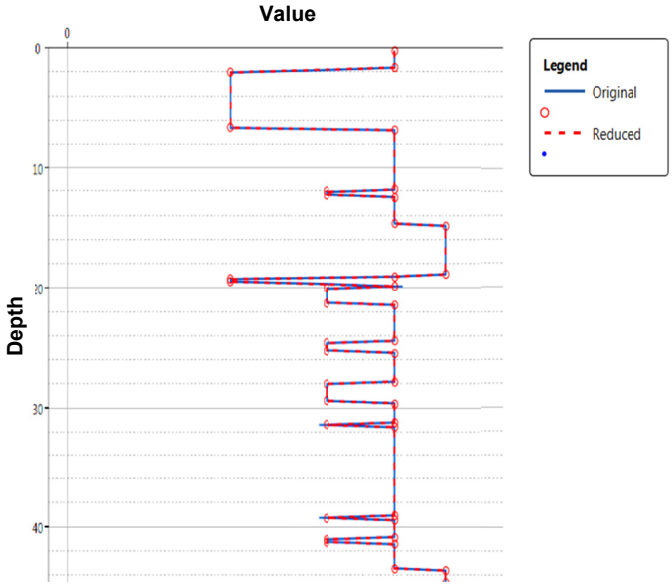

(c)

Figure 4-14 Reduction of oversampling data by gradient optimization

(EVS visualization Software)

4.2.4.2 Soil Type Visualization Model

Soil type visualization models are developed by using data obtained from two different CPT correlations (Robertson et al., 1986, 2009; Robertson 1990, 2010). The first approach interpolates the soil behavior type (SBT) value obtained from non-normalized values of tip resistance and friction ratio. The variogram was constructed by using reduced data generated by the methodology described in the last section. Since some zones did not exist in the data (i.e., Zone 1 and Zone 9), they were grouped into a new material type, as shown in Table 4-2.

Table 4-2 SBT Values Grouped into a New Material Type

SBT Values Robertson (1986)		Material Type	
Min (>=)	Max (<)		
1	2	1	Sensitive, fine grained
2	4	2	Organic soils - clay; Clays - Silty clay to clay
4	6	3	Silt mixtures - clayey silt to silty clay; Sand mixtures - silty sand to sandy silt
6	9	4	Sands - clean sand to silty sand; Gravelly sand to dense sand; Very stiff sand to clayey sand*
9	12	5	Very stiff fine grained *

The variogram could not be generated by using isotropic data conditions due to high scatter in the data which preludes the creation of an exponential or any other type of variogram function. Therefore, the variogram was constructed by considering advanced anisotropy in the data described in Chapter 2. Values to model anisotropy are tabulated in Table 4-3. A histogram of lag-distance distribution was also developed to verify the normality of the data distributed in the space. Variogram construction and lag-distance distribution for the material type obtained from SBT are illustrated in Figure 4-15.

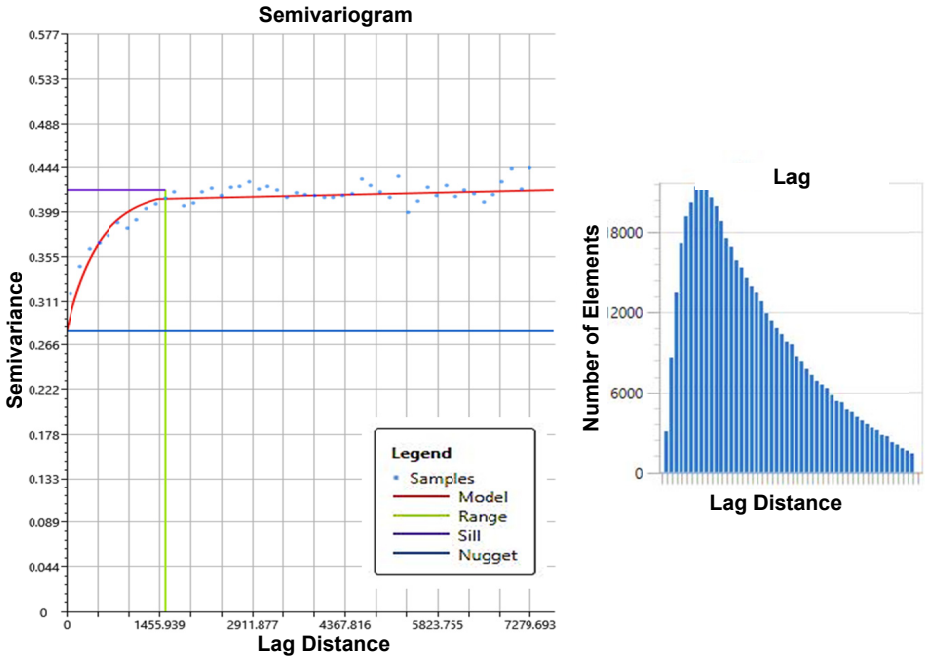

Figure 4-15 Variogram generated for material type (SBT)

The second approach consists of evaluating the soil type by using the Soil Behavior Type Index (I_c), based on the normalized values of tip resistance and friction ratio of CPT. The variogram was developed by using advanced anisotropy. Values for modelling anisotropy are tabulated in Table 4-3. The variogram used for the modeling is illustrated in Figure 4-16.

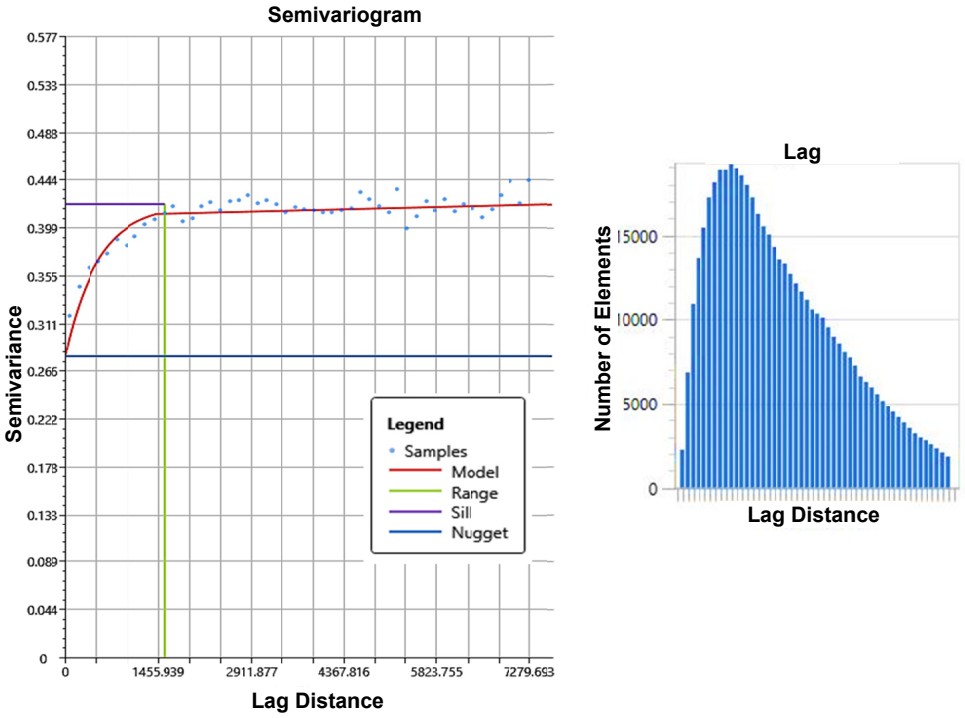

Figure 4-16 Variogram generated for I_c

Table 4-3 Variogram Modeling for Visualization of SBT and I_c

Description	Model Type	*Anisotropy*				*Variogram*		
		Secondary Ratio	Primary Ratio	Heading	Dip	Range	Sill	Nugget
Material Type (SBT)	Exponential	50.0	0.62	349.8	2.15	1550	0.14	0.28
Soil Behavior Index (I_c)	Exponential	50.0	0.6	312.2	1.83	1550	0.26	0.35

Kriging interpolation depicts four stages or sectors of construction of the Eagle Mountain dam adopted during 1930s. The visualization of three-dimensional SBT or I_c values obtained by CPT correlations presents a detailed configuration of soils within the dam. In both cases, the clay core was illustrated by filtering data within ranges of $2<SBT<3$ and $2<I_c<4$, and results are shown in Figure 4-17. A gap of clayey soils at the core was found at the transition of the third and fourth sectors. The dam was subjected to

seepage issues during the 1960s, and leakage problems were found at these locations. The visualization model depicts some silty and sandy soils at this location where the design demands a clayey core. The clay core wall, constructed as a mitigation measurement, effectively controlled the seepage and the lack of clayey soil at this depth. The possibility of having sands or silty soils in that section is corroborated by the visualization of other soil properties (i.e., friction angle and undrained shear strength).

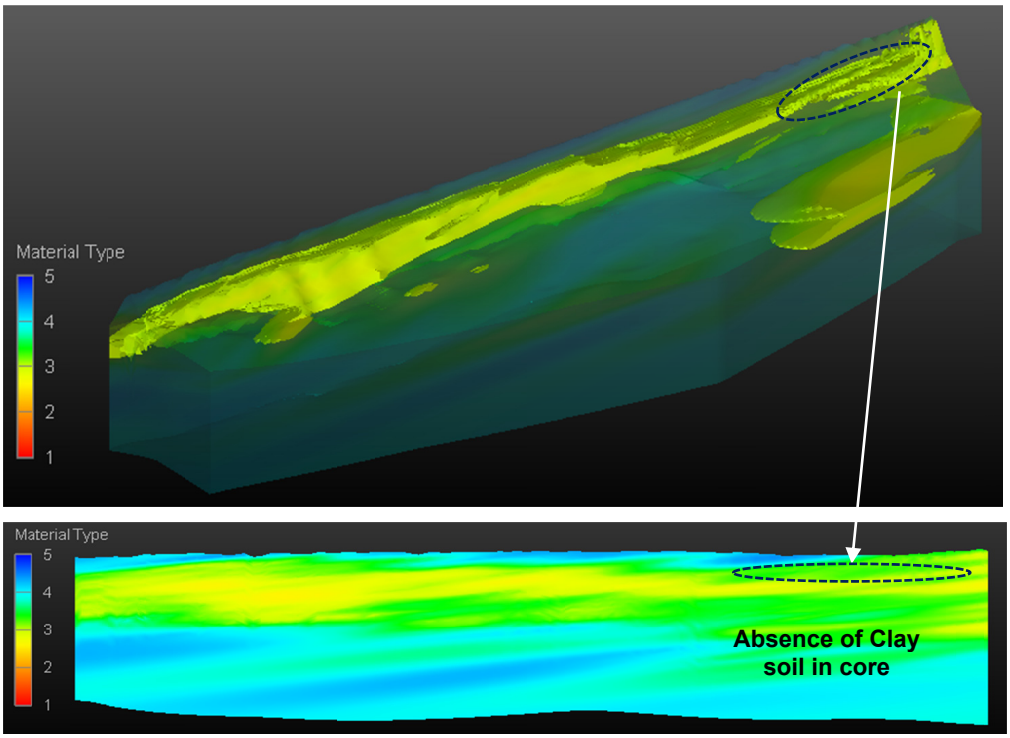

Figure 4-17 Clayey core of the dam (2<SBT<3) – No clayey soil in the core at Sector 3

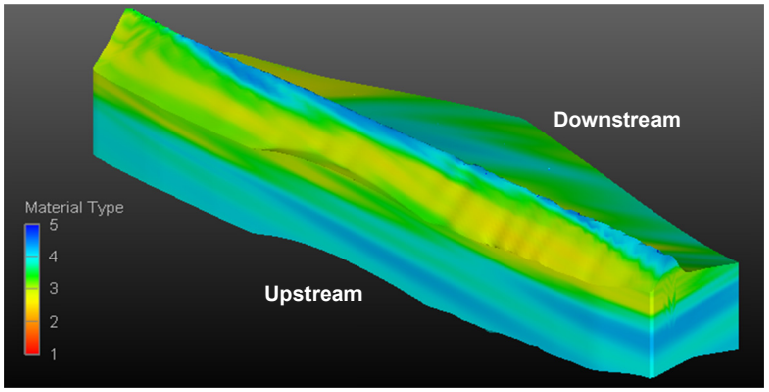

(a)

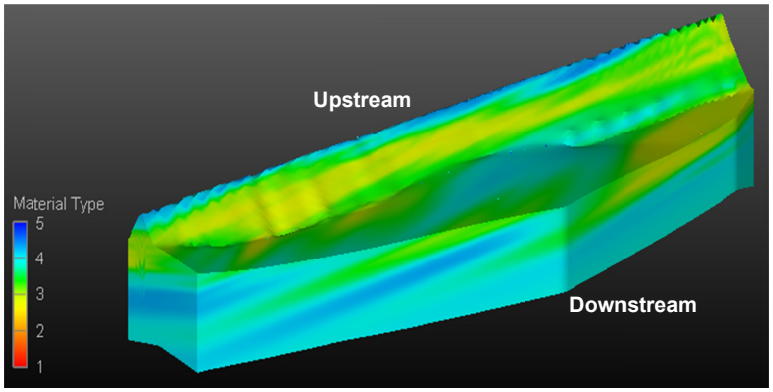

(b)

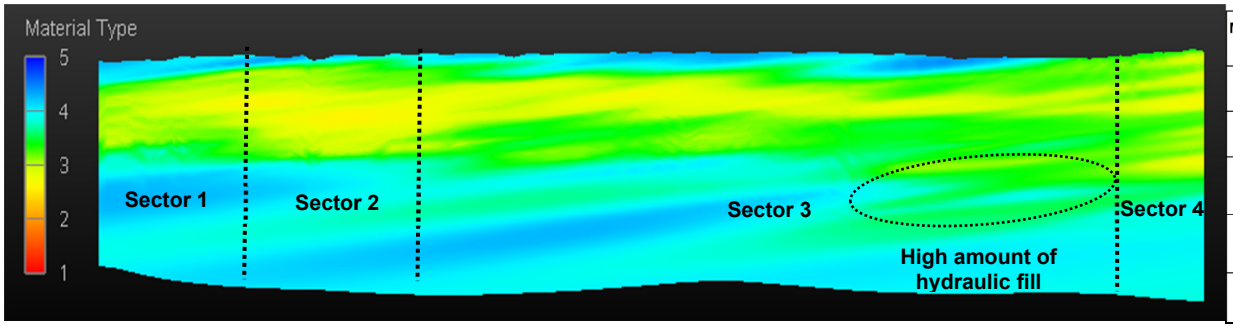

Material Type	Soil Behavior Type
1	Sensitive, fine grained
2	Organic soils - clay; Clays - Silty clay to clay
3	Silt mixtures - clayey silt to silty clay; Sand mixtures - silty sand to sandy silt
4	Sands - clean sand to silty sand; Gravelly sand to dense sand; Very stiff sand to clayey sand*
5	Very stiff fine grained *

(c)

Figure 4-18 (a) and (b) Soil type 3D-visualization model of EM – SBT, (c) Section along the center line of the dam

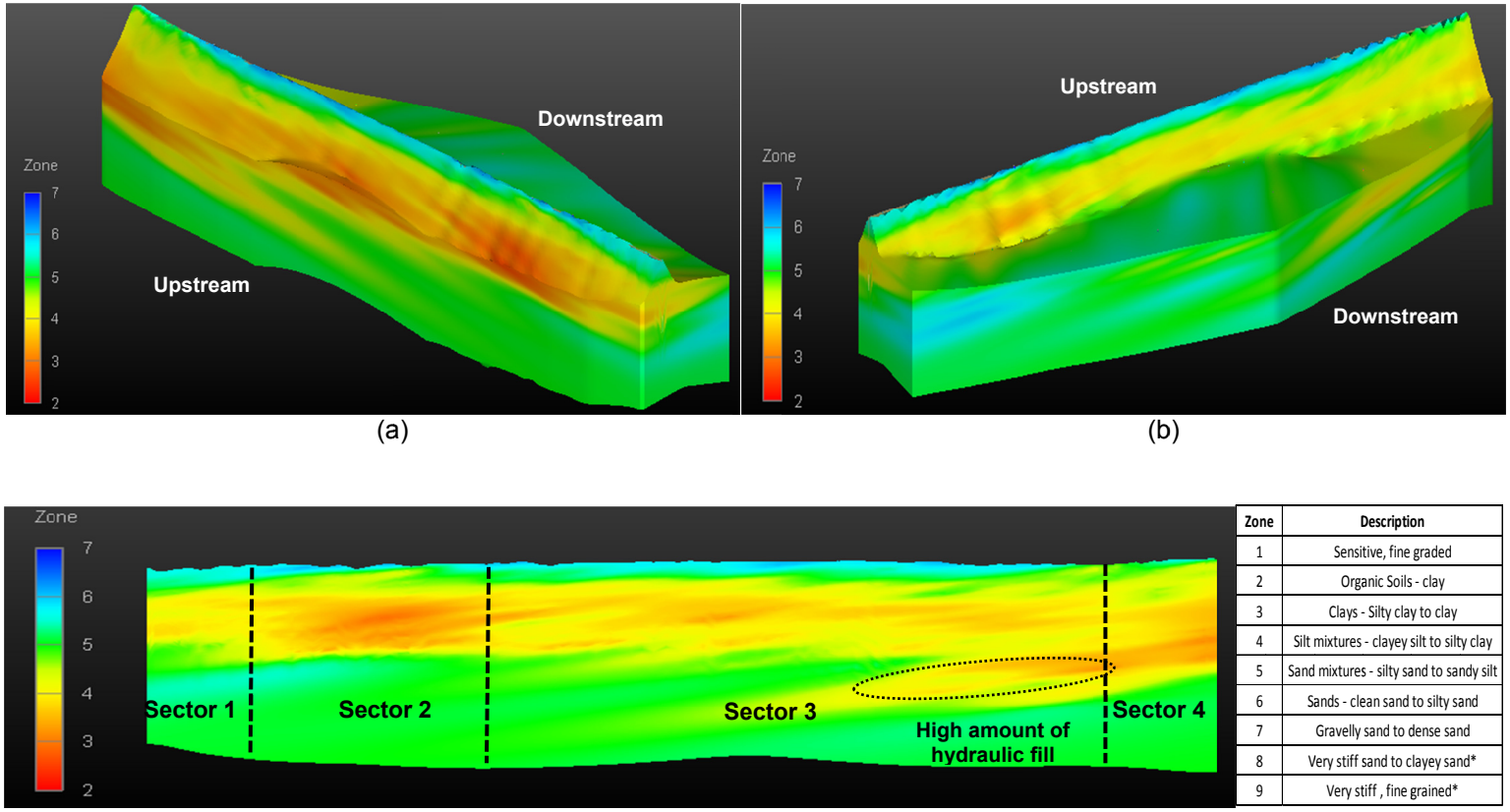

Zone	Description
1	Sensitive, fine graded
2	Organic Soils - clay
3	Clays - Silty clay to clay
4	Silt mixtures - clayey silt to silty clay
5	Sand mixtures - silty sand to sandy silt
6	Sands - clean sand to silty sand
7	Gravelly sand to dense sand
8	Very stiff sand to clayey sand*
9	Very stiff , fine grained*

Figure 4-19 (a) and (b) Soil type 3D-visualization model of EM – I_c, (c) Section along the center line of the dam

4.2.4.3 Shear Strength - Effective Friction Angle (ϕ')

The effective shear strength can be estimated for relatively granular soils or clean sands. Estimation can be performed by evaluating the effective friction angle (ϕ'), based on CPT correlations described in earlier sections. The friction angle can be used as an input for slope stability calculations at critical sections found in the model. Raw data was reduced by using data reduction techniques and a variogram was generated, incorporating spatial continuity or anisotropy in the model. Table 4-4 shows values used for modelling anisotropy in the generation of the variogram for the estimation of spatial variability of the friction angle.

Table 4-4 Variogram Modeling for Visualization of Effective Friction Angle (ϕ')

Description	Model Type	Anisotropy				Variogram		
		Secondary Ratio	Primary Ratio	Heading	Dip	Range	Sill	Nugget
Friction Angle (ϕ)	Exponential	25.0	0.9	224.5	0.0	1550	0.14	0.28

Data distribution analysis was generated by the histogram presented in Figure 4-20 to establish interpolation limit values. Friction angle results values, Φ'<22° and Φ'>45° are relatively low in the data distribution plot (Figure 4-20). Therefore, limit values of interpolation are defined as 20° < ϕ < 45° for the Kriging interpolation and generation of the visualization model.

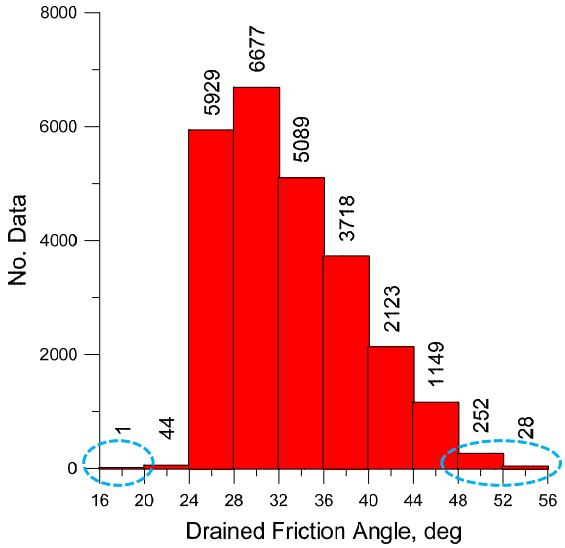

Figure 4-20 Drained friction angle variability, ϕ' (deg)

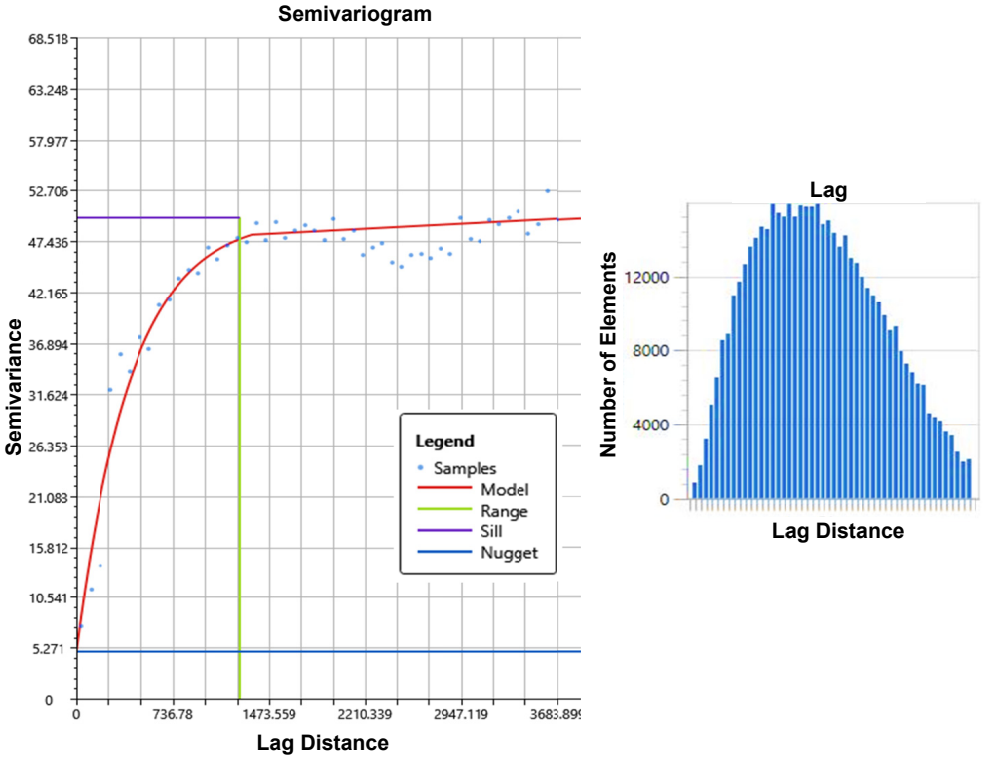

Figure 4-21 Variogram generated for effective friction angle

Visualization results for the interpolation of effective friction angle are shown in Figure 4-22, presenting several sections of the dam. The clayey core was formed by silts and clayey soils, depicting relatively small friction angles as expected. Based on the classification described in Table 4-5, visualization results also showed the presence of sands and silts in Sector 3, as shown in Figure 4-22. Sand lenses were identified at these locations, which may be susceptible to liquefaction or slope stability problems. Foundation soils were primarily composed of compact and dense sands; therefore, significant settlement are not expected to occur at the dam. Surface layers on the crest depict the presence of sands with high drained friction angle, as illustrated in Figure 4-23. The gap in the clayey core, from approximately Station 38.00 to Station 40.00 observed in soil type visualization models, was verified by the presence of high effective friction angle corresponding to silty or sandy soils (ϕ'~25-30°), and shown in the longitudinal section in Figure 4-22. Overall, Sector 3 is one of critical locations for addressing geotechnical hazards. Table 4-6 also shows strength properties for all types of soils and can be used as reference for the visualization model generated.

Table 4-5 Strength Properties for Sands (Das 1998)

State of Packing	Relative Density (%)	Friction Angle, ϕ' (deg.)
Very loose	<20	<30
Loose	20-40	30-35
Compact	40-60	35-40
Dense	60-80	40-45
Very dense	>80	>45

Table 4-6 Strength Properties (Drained) for Soils (Ortiz and Serra 1986)

Material	Cohesion		Friction Angle (degrees)	
	lb/ft^2	lb/in^2	Peak	Residual
Gravel	-	-	34	32
Sandy gravel with few fines	-	-	35	32
Sandy gravel with silty or clayey fines	-	-	35	32
Mixture of gravel and sand with fines	21	0.15	28	22
Uniform sand - fine	62	0.44	32	30
Uniform sand – coarse	-	-	34	30
Well-graded sand	-	-	33	32
Low-plasticity silt	42	0.29	28	25
Medium to high plasticity silt	62	0.44	25	22
Low plasticity clay	125	0.87	24	20
Medium plasticity clay	167	1.16	20	10
High plasticity clay	208	1.45	17	6
Organic silt or clay	146	1.02	20	15

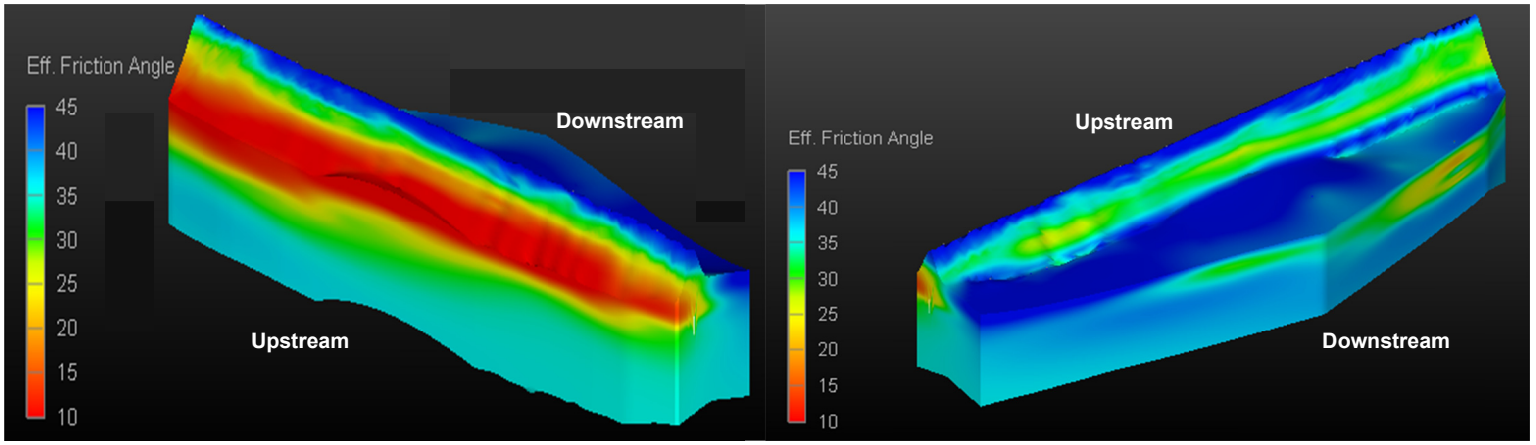

(a) (b)

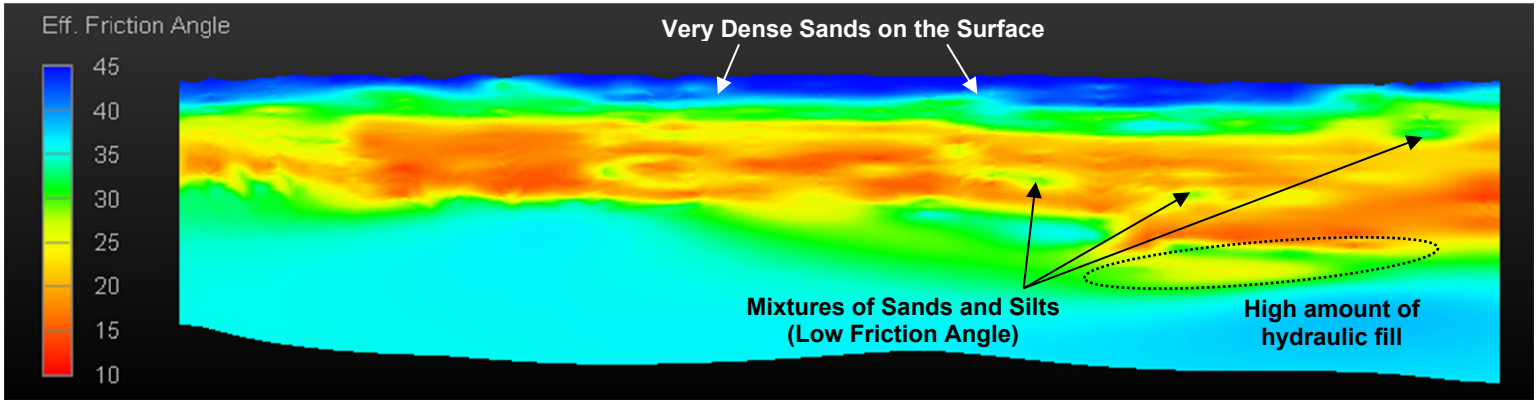

(c)

Figure 4-22 Visualization model of effective friction angle, ϕ' – Identification of sand lenses

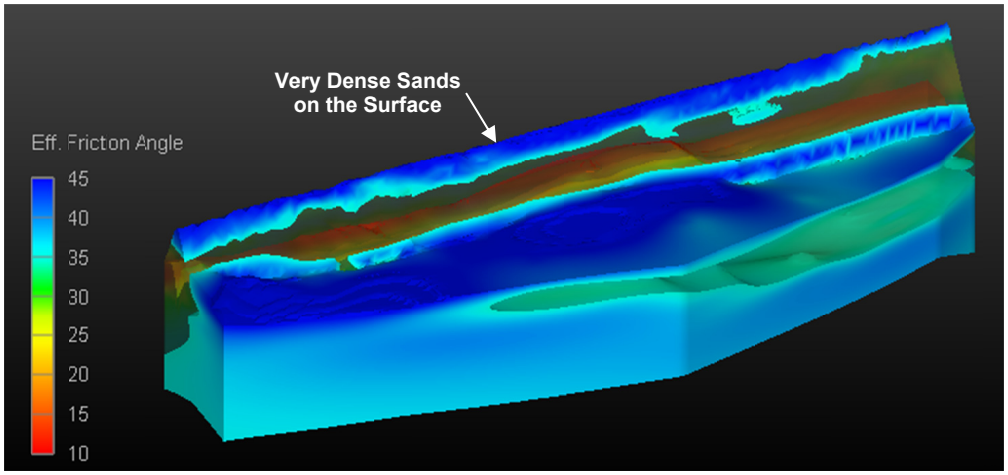

Figure 4-23 Sands at surface at the crest of the dams – High drained strength (ϕ')

4.2.4.4 Undrained Shear Strength (Su)

The undrained shear strength was evaluated on clays and silts primarily to assess the condition of the core of the dam. Undrained shear strength values were obtained by using CPT correlations described in the earlier section. Data distribution analysis was performed to establish limit values for the interpolation, as shown in the data distribution represented by the histogram shown in Figure 4-24.

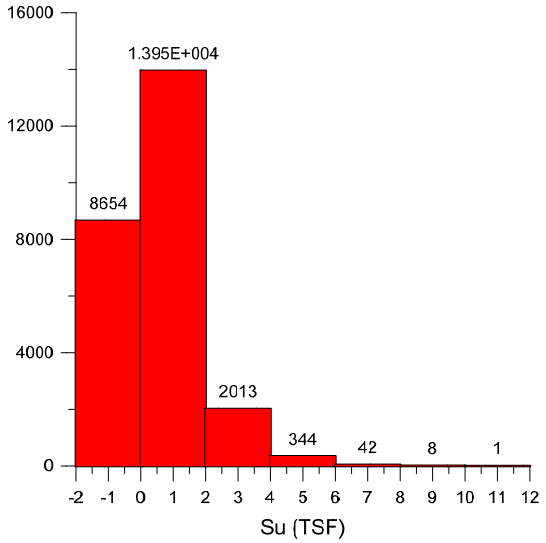

Figure 4-24 Undrained shear strength variability, S_u (TSF)

It was noted that the data contains several “zero” values (Figure 4-24). Therefore, the variogram was generated by accounting for data distribution and anisotropy. Data was interpolated from values of S_u, which ranged from 0.12 to 2 TSF. Anisotropy parameters are shown in Table 4-7, and the variogram constructed for the interpolation of Su is shown in Figure 4-25.

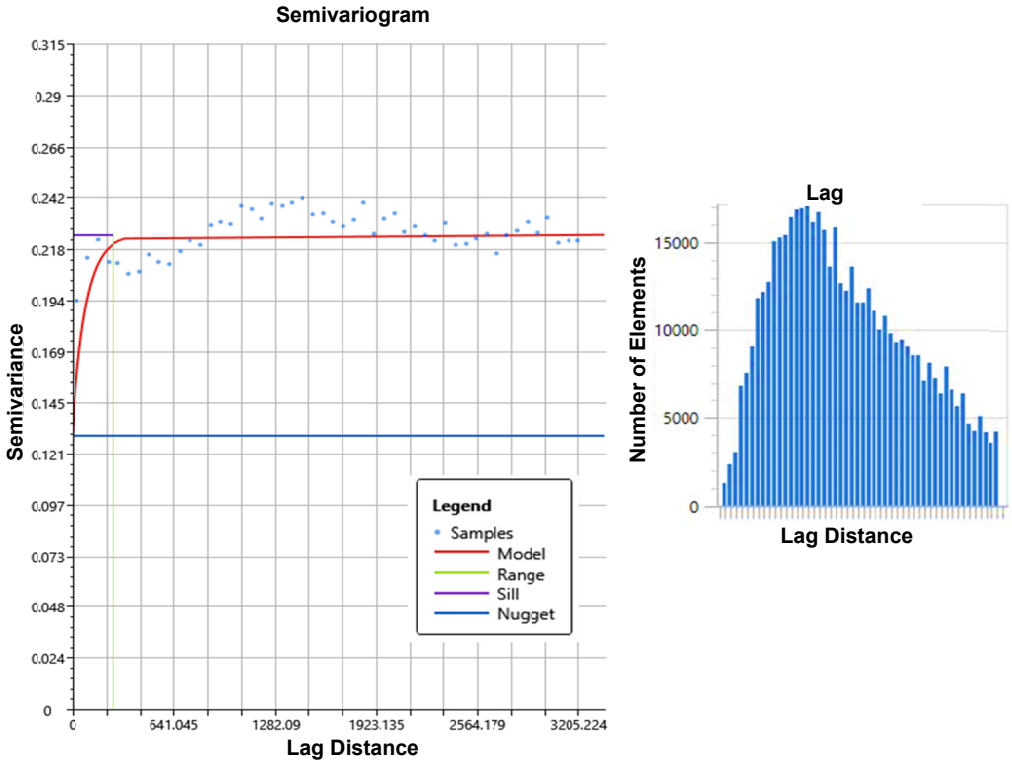

Figure 4-25 Variogram generated for undrained shear strength (Su, TSF)

Table 4-7 Variogram Modeling for Visualization of Undrained Shear Strength (Su) TSF

Description	Model Type	Anisotropy (Simple)				Variogram		
		Secondary Ratio	Primary Ratio	Heading	Dip	Range	Sill	Nugget
Undrained Shear Strength	Exponential	15	1	0	0	254	0.095	0.13

Terzaghi and Peck (1967) presented a general classification of the consistency of clays based on their undrained shear strength values (Table 4-8) (Terzaghi and Peck

1967). Several red zones (Su<0.2 TSF) were found on the surface layers of the crest, depicting soil layers as soft clays, as shown in Figure 4-26; however, SBT, I_c and friction angle visualization models defined those locations as sands with high drained effective friction angles. Those red regions depict cohesionless soils, and only drained shear strength parameters must be considered for any geotechnical assessment. The hydraulic fill placed in Sectors 2, 3, and 4 was mainly composed of medium stiff clay which was verified using with results obtained from SBT and I_c visualization models.

The major part of the dam has very stiff soil, highlighting a stiff-to-very-stiff puddled clay (1<Su<2, TSF) core, as shown in Figure 4-27. The lack of clay soil in the core is identified in Sector 3 and 4 where possible seepage problems occurred in the 1960s, as shown in Figure 4-26. The undrained shear visualization model defined the presence of some cohesionless soils in Sector 3 that may be susceptible to liquefaction. This area had already been identified by the visualization models of SBT, I_c and effective friction angle.

Table 4-8 Undrained Shear Strength (Terzaghi and Peck 1967)

Consistency	Undrained Shear Strength, TSF (KPa)	Unconfined Compressive Strength, TSF (KPa)
Very Soft	<0.125 (<12)	<0.25 (<24)
Soft	0.125-0.25 (12-24)	0.25-0.50 (24-48)
Medium	0.25-0.50 (24-48)	0.50-1.0 (48-96)
Stiff	0.50-1.0 (48-96)	1.0-2.0 (96-192)
Very Stiff	1.0-2.0 (96-192)	2.0-4.0 (192-383)
Hard	>2.0 (>192)	>4.0 (>383)

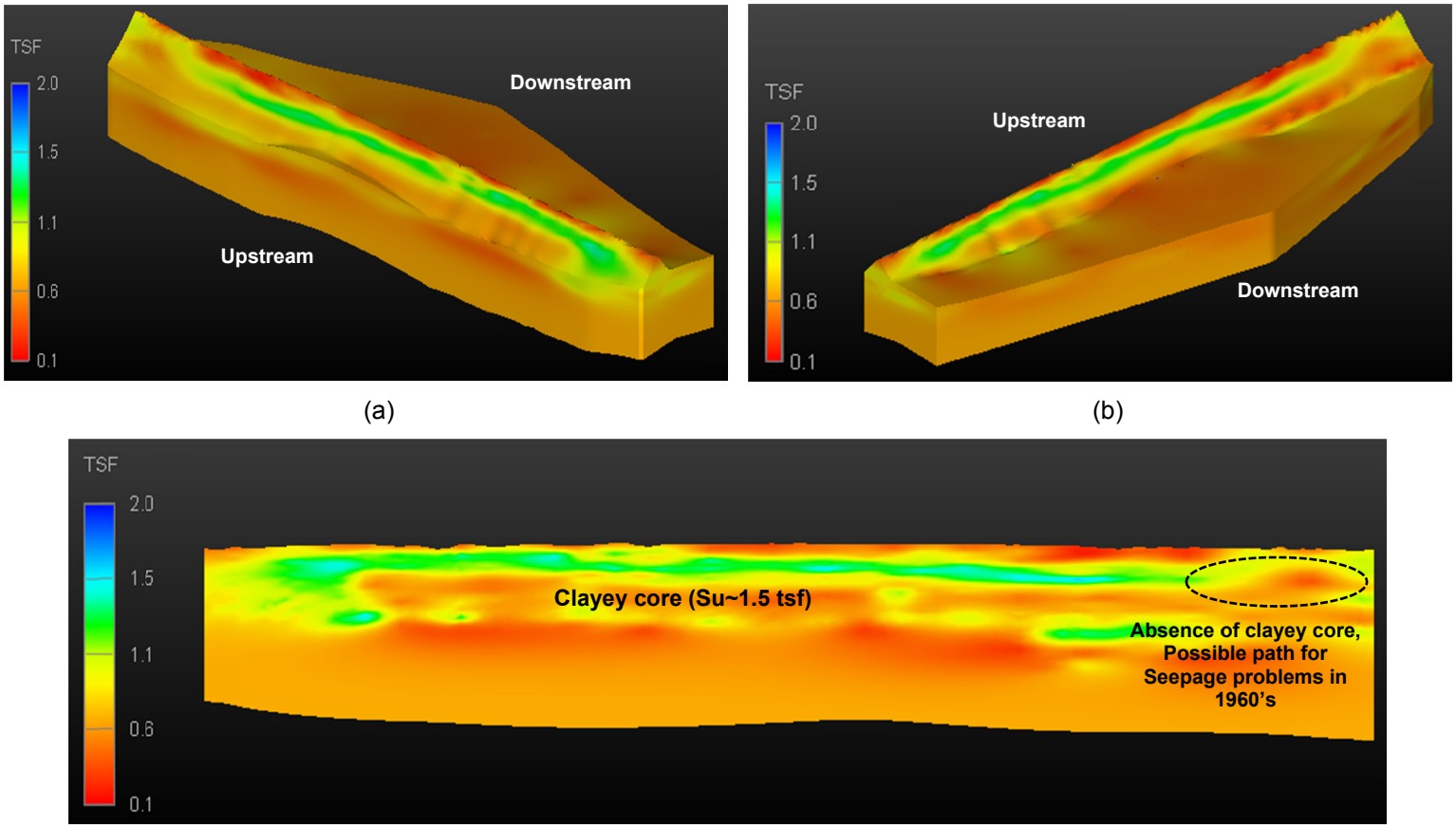

Figure 4-26 Visualization model of undrained shear strength (Su) – Identification of clay core

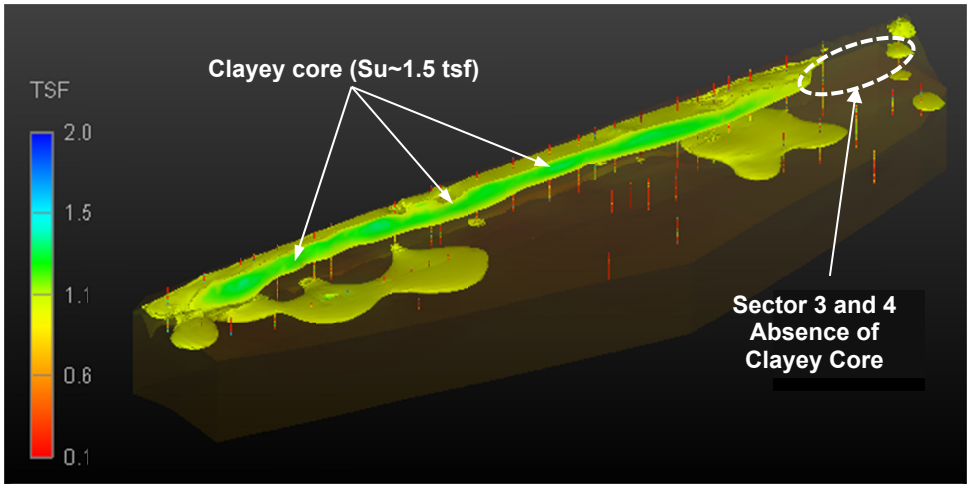

Figure 4-27 Clayey core of the dam (1<Su<2, TSF)

4.2.4.5 Young's Modulus of Elasticity (E)

The constrained modulus (E) was obtained by using CPT correlations for cohesionless and cohesive soils shown in earlier sections. Deformation analysis can be performed by incorporating the modulus of elasticity when evaluating slope stability or lateral spreading. Data distribution analysis was performed by generating the histogram shown in Figure 4-28. Since there were only a few values present on the maximum extreme side of the histogram, interpolation values were approximately 80<E<1200, TSF.

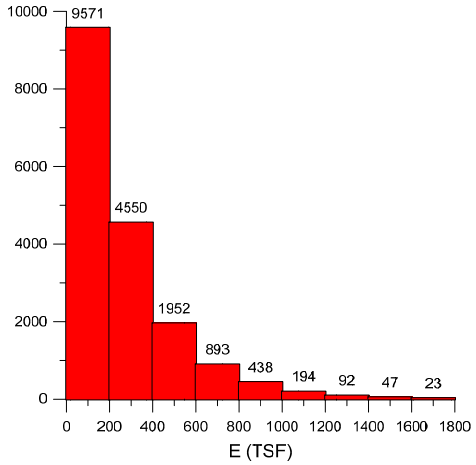

Figure 4-28 Variability of modulus of elasticity, E (TSF)

The visualization model of elastic moduli accommodates a Gaussian function for the generation of a variogram. Advanced anisotropy was also considered and the parameters used are shown in Table 4-9. The corresponding variogram is illustrated in Figure 4-29.

Table 4-9 Variogram Modeling for Visualization of Elastic Moduli (E), TSF

Description	Model Type	Anisotropy (Simple)				Variogram		
		Secondary Ratio	Primary Ratio	Heading	Dip	Range	Sill	Nugget
Elastic Moduli (E)	Gaussian	20	0.1	26.12	0.40	2000	28500	14100

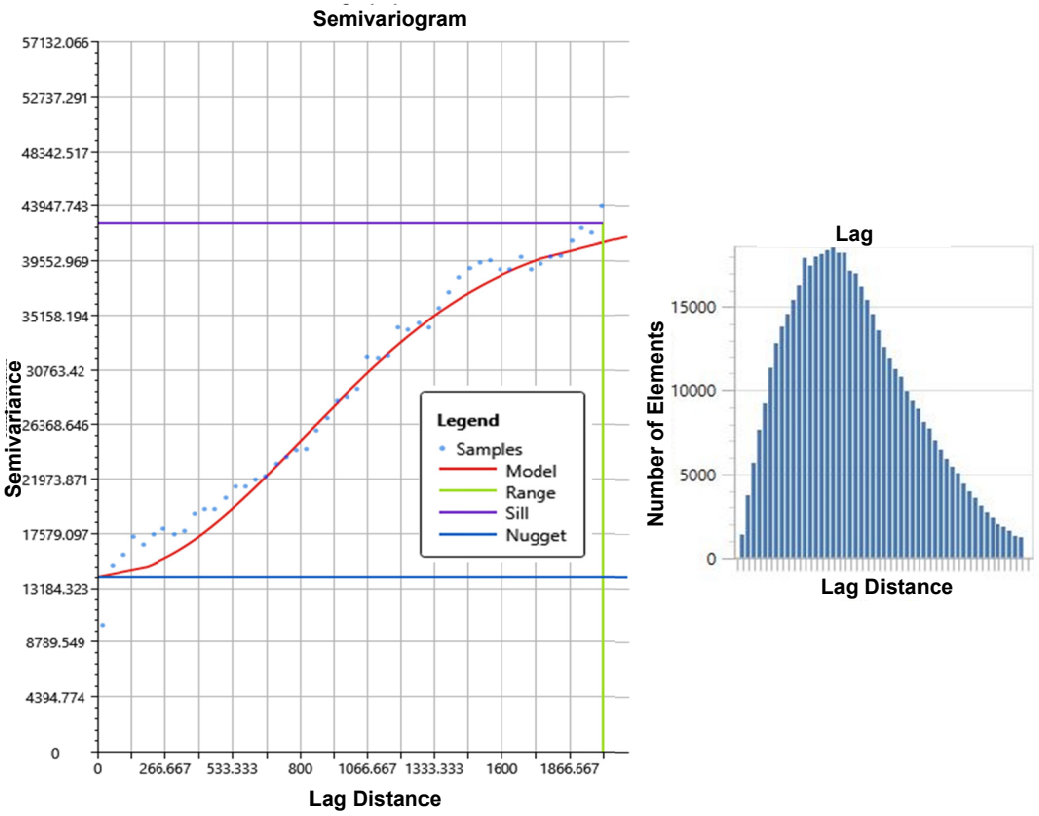

Figure 4-29 Variogram generated for elastic moduli (E, TSF)

According to USACE (USACE 2016), typical elastic moduli of soils are described in Table 4-10 based on their type and consistency/density. It was noted that it could

range from 5 to 2000 TSF. From the generated visualization model of the elastic moduli (TSF), it is observed that very low values at the area where sands are present instead of a clayey core (Sectors 3 and 4). These zones, with relatively low moduli values, can be susceptible to large deformations in case of a liquefaction phenomenon and can be identified as critical sections. The elastic moduli interpolated can be further used for modeling slope stability deformation analysis at those critical sections and incorporating corresponding values from interpolation for assigning properties to the model.

Figure 4-30 shows the visualization model of elastic moduli within the dam. Sector 3, which is shown to be a composition of sands and silts from previous models, depicts low values of E. Since sands and silts are highly susceptible to liquefaction, it is important to identify the elastic moduli at this location for further deformation analysis.

Table 4-10 Typical Elastic Modulus of Soils (USACE 2016)

Soil	**E_s (TSF)**
Very soft clay	5-50
Soft clay	50 - 200
Medium clay	200 - 500
Stiff clay, silty clay	500 - 1000
Sandy clay	250 - 2000
Clay shale	1000 - 2000
Loose sand	100 - 250
Dense sand	250 - 1000
Dense sand and gravel	1000 - 2000
Silty sand	250 - 2000

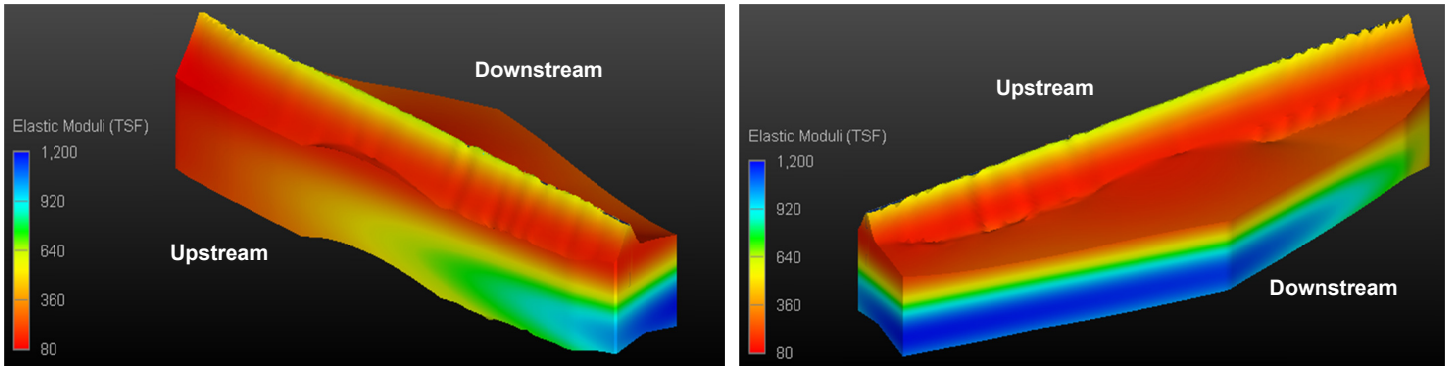

(a) (b)

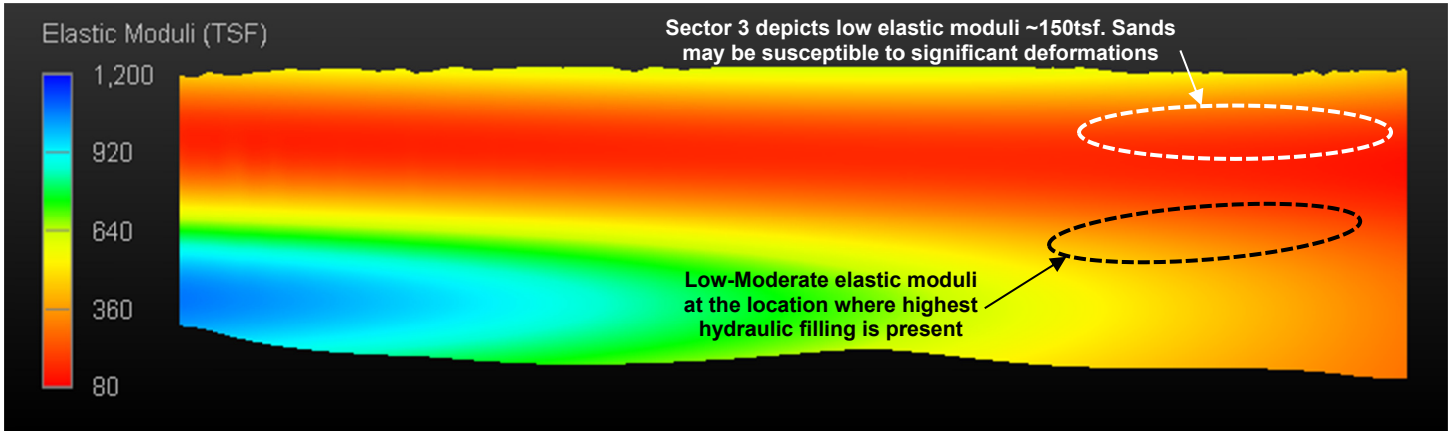

(c)

Figure 4-30 Visualization model of elastic moduli (E), TSF

4.2.3 Validation of Visualization Models

This section presents the validation studies that evaluated the accuracy of soil property interpolations performed by using 3D Geostatistics. This was done by comparing the interpolation results with the laboratory test results. Several borings were performed at the EM site for collecting soil samples. Basic laboratory tests such as sieve analysis, Atterberg limits, consolidation tests and strength tests were conducted. The laboratory results were used to validate the visualization models generated by interpolation using Geostatistics. Figure 4-31 and Figure 4-32 illustrate the results from the visualization model of the undrained shear strength, (Su, TSF) and effective friction angle, ϕ' (deg.) interpolations.

A boring located at Station DBC-16.05 was considered for the validation purpose. Sample "U24" collected at a depth of 51.5-52.2 ft. was subjected to strength laboratory tests and results were compared with values obtained from visualization models. Undrained shear strength (S_u) shown a value of Su=0.5 tsf (1.1ksf) in laboratory results as compared with the value obtained from the visualization model Su~0.0.55 tsf (1.23 ksf). The effective shear strength of the same sample was found to be ϕ'=19.1° based on laboratory results, whereas the visualization model showed a value of ϕ'~18°.

A similar comparison was performed at Station DBC-37.05, with samples collected at a depth of 10 to 12 ft. Laboratory test results at that location indicated a value of Su= 0.36 tsf (0.81 ksf) and ϕ'=31.9° as compared to values of Su= 0.4 tsf (0.9 ksf) and ϕ'=32° obtained from interpolation and visualization. Visualization results were in consonance with the laboratory data and suggest the presence of some sand lenses at that depth that may be susceptible to liquefaction.

Deeper layers were also evaluated, exhibiting some dense silty to sandy materials in Sector 3. Visualization model results indicate very dense sands at deeper

layers. Figure 4-33 and Figure 4-34 illustrate the visualized values of undrained shear strength and effective friction angle at Station 37.05 (10-12 ft.). Laboratory results for both locations are shown in Appendix B.

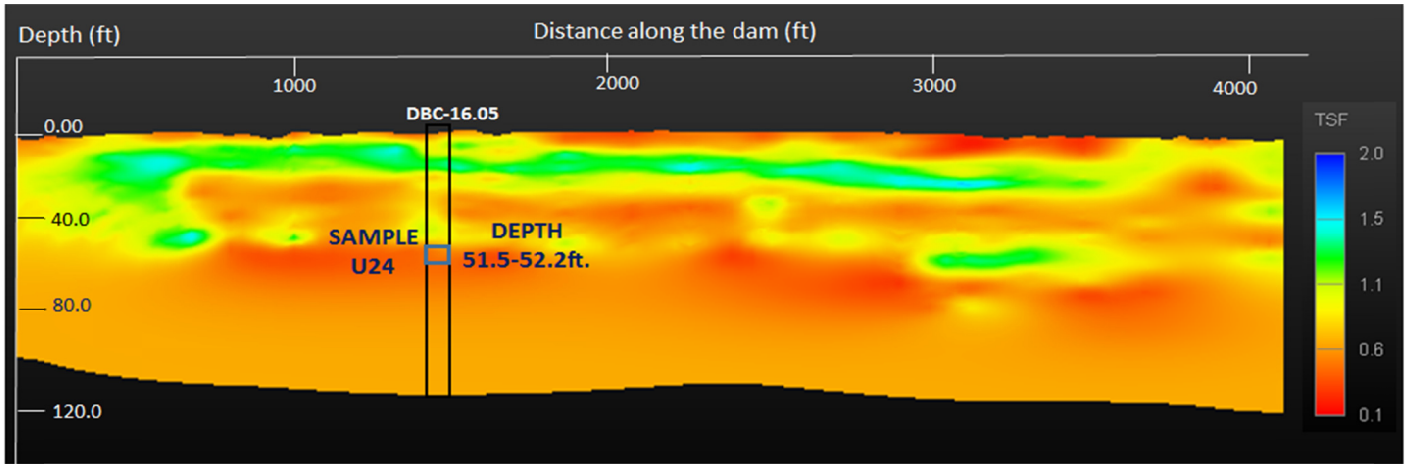

Figure 4-31 Validation of Su (TSF), Station 16.05 – Sample U24

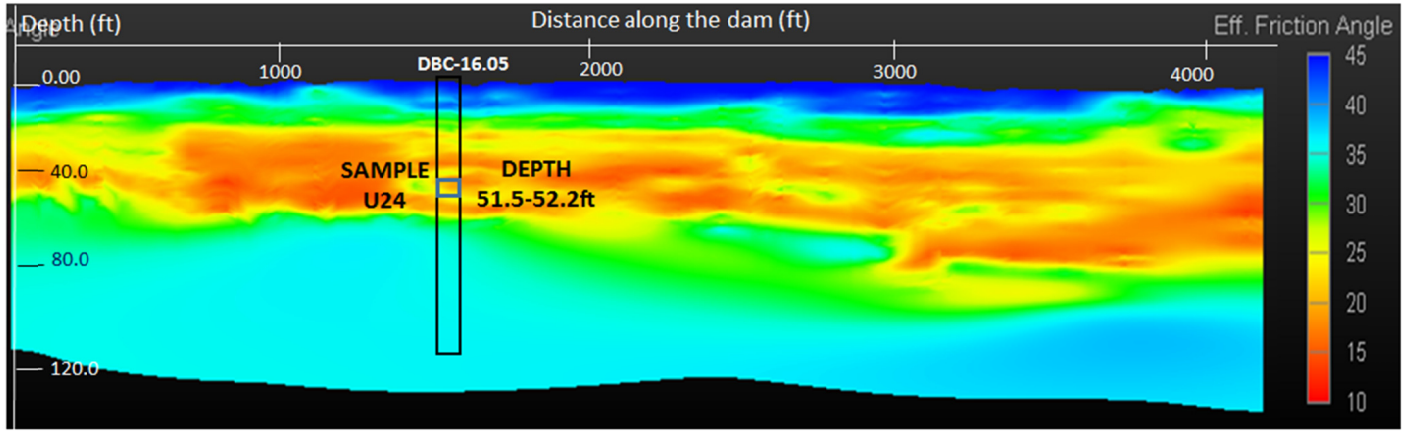

Figure 4-32 Validation of ϕ', Station 16.05 – Sample U24

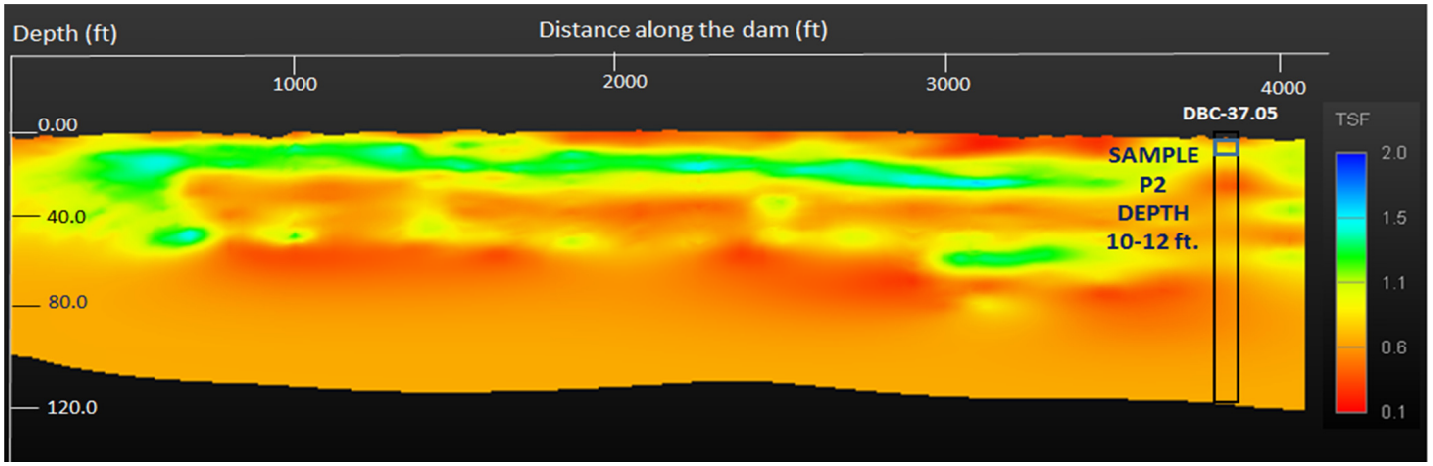

Figure 4-33 Validation of Su (TSF), Station 37.05 – Sample P2

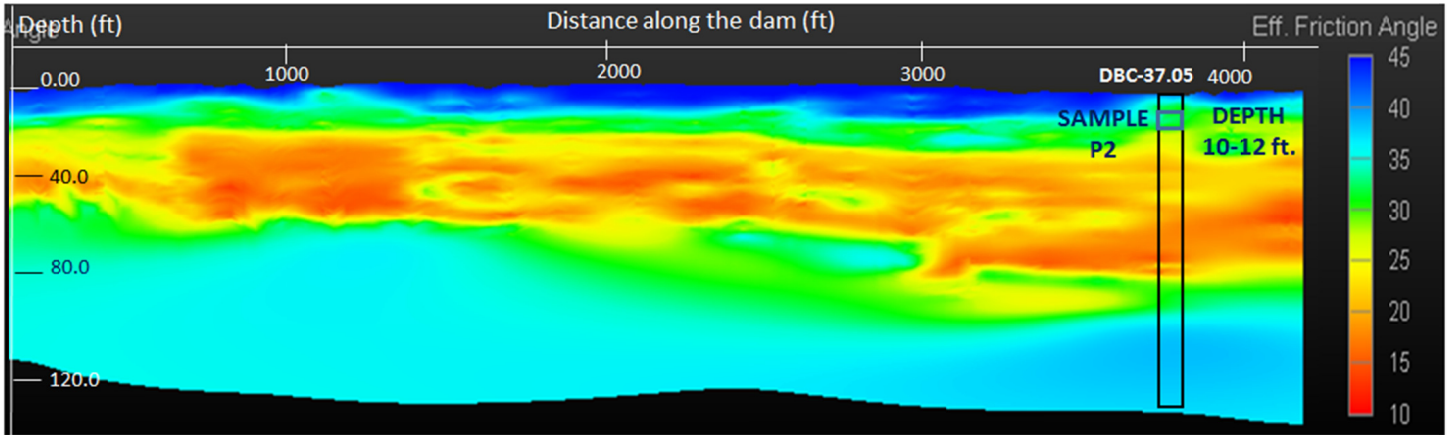

Figure 4-34 Validation of of ϕ, Station 37.05 – Sample P2

Three-dimensional visualization models were successfully generated by using Geostatistics to consider spatial variability in the soil data. The key to the generation of models is the construction of a very detailed variogram based on the spatial continuity or anisotropy of the data. Data cannot be assumed to be isotropic in the space and special parameters have to be considered for the anisotropy to be considered for variogram construction. Visualization models can be used to identify critical sections that may be affected by geotechnical hazards such as liquefaction or slope stability assessments. Sector 3 seems to be the location most susceptible to geotechnical hazard assessment.

4.3. Insights from Visualization Models for the Eagle Mountain Dam - Summary

Three-dimensional visualization models of the Eagle Mountain Dam offer a complete understanding of soil configuration within the dam body. Several soil properties were calculated based on CPT correlations and visualized by computing variograms which considered data anisotropy and distribution. Critical sections were identified from visualization models. A comprehensive analysis of all models developed (i.e., SBT, I_c, ϕ', Su, and E) were considered for the final interpretation of the soil configuration within the dam. The Eagle Mountain dam consists of a stiff clayey core (1<Su<2, TSF) surrounded by sandy material on the upstream and downstream side of the dam. Surface layers at the crest consist of very dense and compacted sands (Figure 4-23), and foundation soils show relatively dense sands as well (Figure 4-22).

Sector 3, specifically the location from Station 35.00 to Stations 40.00, has sand pockets or lenses at locations where a clayey core was supposed to be constructed (Figure 4-26). Laboratory tests obtained near this location (i.e., DBC 37.05) were used to verify this information. As shown in Figures 1-22 and 1-30, low effective shear strength combined with relatively low elastic moduli at locations where sand pockets are found,

can produce large deformations if geotechnical hazards occur (i.e., liquefaction or slope failures).

The following section includes a comprehensive three-dimensional visualization framework of the liquefaction assessment of the Eagle Mountain dam to understand the seismic behavior of the soil structure within the dam. Liquefaction soil resistance can be calculated by employing traditional CPT procedures, and interpolation of factor of safety can be performed by applying Geostatistics. Earthquake loading is characterized based on the probabilistic seismic hazard analysis included in Chapter 3 of the present work.

Chapter 5 Liquefaction Evaluation of the Eagle Mountain Dam based on 3D Visualization Models

5.1 Introduction

In the previous chapters, the vulnerability of several hydraulic fill dams to liquefaction and ground displacement in the event of earthquakes was presented. Historically, liquefaction is categorized as a geotechnical hazard that is capable to produce significant damage in hydraulic fill dams. This phenomenon can produce large deformations by triggering landslides even if small soil lenses lose their strength due to the increase of pore pressures (Holchin and Vallejo 1995). This chapter presents the resiliency of the EM dam against cyclic liquefaction in the event of different earthquake magnitudes. The analysis considered a hypothetical situation of a larger magnitude earthquake in the North Texas region (i.e., M6-7). Considering the age and hazard consequences of EM dam, it is important to evaluate its vulnerability to future hypothetical natural and man-made hazards.

In this research study, the cyclic stress approach is used for evaluating the cyclic liquefaction potential in the EM dam. The cyclic stress approach is valid for gentle slope or level ground surfaces (i.e., slopes<5 degrees), therefore cyclic liquefaction will be evaluated up to El+625 at the EM Dam. Flow liquefaction evaluation is outside of the scope research, however since factor of safety is interpolated using Geostatistics, several liquefiable zones are identified (FOS_{liq}<1.0) within the dam body at higher magnitudes (i.e., M5.5 or higher) and higher accelerations than the PSHA (i.e., 0.4g and 0.5g). The cyclic stress approach consists of comparing the cyclic stress ratio (CSR) resulting from the earthquake loading with the cyclic resistance ratio (CRR) resulting from the in-situ soil property conditions. The Factor of Safety (FS_{liq}) for the calculation of cyclic liquefaction potential in sand-like soils is calculated as the ratio of CRR of soils and the earthquake-

induced CSR as shown in Equation 5.1. Both, CRR and CSR values directly depend on the earthquake magnitude (M) chosen for the analysis and the in-situ effective overburden stress condition. Most of the methodologies convert the earthquake-induced CSR into the reference condition application to M=7.5 and σ'_{vo} = 1 atm (i.e., σ'_{vo}/p_a=1) (Robertson 2009) as shown in Equation 5.2.

$$FS_{liq} = CRR_{M,\sigma'_{vo}}/CSR_{M,\sigma'_{vo}} \quad 5.1$$

$$FS_{liq} = CRR_{M=7.5,\sigma'_{vo}=1}/CSR_{M=7.5,\sigma'_{vo=1}} \quad 5.2$$

Where: $CRR_{M=7.5,\sigma'_{vo}=1}$ = Cyclic Resistance Ratio applicable to M = 7.5 and an effective overburden stress of σ'_{vo}= 1 atm., sometimes presented as simply $CRR_{7.5}$.

$CSR_{M=7.5,\sigma'_{vo}=1}$ = earthquake induced Cyclic Stress Ratio adjusted to the equivalent CSR for the reference values of M = 7.5 and an effective overburden stress of $_{7.5,\sigma'_{vo}}$ = 1 atm., sometimes presented as simply $CSR_{7.5}$.

Earthquake-induced CSR can be estimated using the following simplified correlation described by Seed and Idriss (1971) shown Equation 5.3.

$$CSR = \frac{\tau_{AV}}{\sigma'_{VO}} = 0.65\left[\frac{a_{max}}{g}\right]\left(\frac{\sigma_{VO}}{\sigma'_{VO}}\right)r_d \quad 5.3$$

Two main correction factors were later introduced by Boulanger and Idriss (2014) as shown in Equation 5.4 (Boulanger and Idriss 2014). The expression must be expressed through an earthquake magnitude scaling factor, MSF and an effective stress scaling factor K_σ.

$$CSR = \frac{\tau_{av}}{\sigma'_{vo}} = 0.65\left[\frac{a_{max}}{g}\right]\left(\frac{\sigma_{vo}}{\sigma'_{vo}}\right)r_d\left(\frac{1}{MSF*K_\sigma}\right) \quad 5.4$$

The soil's CRR is dependent on the duration of shaking and effective overburden stress conditions at a site. Corresponding conditions at the site are evaluated by correcting CRR due to the magnitude and effective stress scaling factors. Methods for estimating CRR depend mainly on normalized tip resistance or shear wave velocity

properties. CRR estimation by different methods and researchers mainly differ on the amount of data used, soil conditions and properties and the use of corrections factors.

In this research study, the liquefaction potential at EM dam is evaluated using two CPT-based approaches developed by Robertson (2009) and Boulanger and Idriss (2014), and one shear wave velocity based approach developed by Kayen et al. (2013) (Robertson 2009; Boulanger and Idriss 2014; Kayen et al. 2013). Three-dimensional visualization models of liquefaction potential (Factor of Safety, FOS) are generated by incorporating spatial variability of soil properties such as fines content and cyclic resistance ratio. Overall, the liquefaction evaluation of the EM dam was performed based on the following scenarios:

- The first scenario is a realistic case which considers the actual lake water level as in field conditions (i.e., elevation of the lake El+649.0) combined with an earthquake of magnitude M4.0 (~max. earthquake occurred in North Texas) which produced a ground motion of 0.3g (i.e., PSHA for the north Texas region)
- Several hypothetical scenarios were considered to evaluate the resiliency of the EM dam for liquefaction analysis. The variables considered are as follows:
    - Lake water level is as in field conditions but the dam is subjected to higher earthquake magnitudes namely M4.5, M5.5 and M6.5 that produced ground motions of 0.3g, 0.4g and 0.5g
    - Lake water level at the time of earthquake to be ~10 ft. below the crest (soils within the dam embankment are saturated) combined with earthquakes of same magnitudes that produce a ground motion of 0.3g at the site.

In order to highlight the importance of geotechnical visualization tools, 3D visualization models were generated for the results obtained from liquefaction analysis to

identify liquefiable zones. Finally, the effect of liquefiable zones on slope stability analyses is considered for slope stability analyses. The following sections provide brief descriptions of all three methods used to determine liquefaction potential at EM dam followed by results, analyses and discussion.

5.2 Approach I: Robertson (2009)

Robertson (2009) provided a simplified method to assess cyclic liquefaction by using Cone Penetration Test (CPT) data. This is an updated approach developed by Robertson and Wride (1998) (Robertson and Wride 1998) which primarily estimates grain characteristics from CPT and combine this concept with methods for determining resistance to cyclic loading (Cyclic stress based approach) (Robertson and Fear 1994). The estimation of CSR is performed using Equation 5.4. The determination of a_{max} can be obtained from PSHA analysis is presented in Chapter 3. The stress reduction factor r_d can be estimated using the following tri-linear function (Equation 5.5), originally proposed by Seed and Idriss (1971).

$$\begin{aligned} r_d &= 1.0-0.00765z && \text{if } z<30 \text{ ft.} \\ &= 1.174-0.0267z && \text{if } z=30 \text{ to } 75 \text{ ft.} \\ &= 0.744-0.008z && \text{if } z= 75 \text{ to } 100 \text{ ft.} \\ &=0.5 && \text{if } z>100 \text{ ft.} \end{aligned} \qquad 5.5$$

Magnitude Scaling Factor, MSF can be calculated based on Equation 5.6 and overburden correction factor (K_σ) is assumed to be unity. On the other hand, cyclic resistance ratio, CRR can be directly obtained from laboratory tests. Robertson (2009) initially proposed several equations for estimating CRR. However, a more updated version of their work is presented in Robertson (2009) by combining their initial approach for cohesionless sand-like soils by adding Boulanger and Idriss (2008) recommendations for cohesive clay-like soils (Idriss and Boulanger 2008). Therefore, it is possible to

provide a simple set of recommendations to estimate $CRR_{7.5}$ from CPT results using the normalization of tip resistance, Q_{tn}, and for a wide range of soils expressed by the Soil Behavior Type Index, I_c (Robertson 2009).

$$MSF = \frac{174}{M^{2.54}} \quad 5.6$$

CRR equations developed for all soils and their use directly depends on the Soil Behavior Type Index (I_c). For sand-like soils ($I_c \leq 2.60$) and for transition regions, sand-like to clay-like soils ($2.60 < I_c < 2.60$), the normalized tip resistance (Q_{tn}) is first corrected using a correction factor, K_c. The K_c factor is dependent on the I_c and refers to the soil plasticity, fines content, mineralogy, soil sensitivity, and stress history. The corrected normalized tip resistance ($Q_{tn,cs}$) values for sand-like soils and transition regions are calculated using the following criteria. If $I_c \leq 2.60$ (sand-like soils), the correction factor K_c is determined by the following set of equations:

If $I_c \leq 1.64$, $K_c=1.0$

$1.64< I_c < 2.60$, $K_c= 5.581I_c^3 – 0.403I_c^4 – 21.53I_c^2 – 33.75I_c -17.88$

$1.64< I_c <2.36$ AND $F_r<0.5\%$, set $K_c-=1.0$

If $2.60 < I_c < 2.70$ (transition regions), the K_c is computed as shown is Equation 5.7:

$$K_c = 6 \times 10^{-7}(I_C)^{16.76} \quad 5.7$$

Thus, normalized tip resistance Q_{tn} can be corrected by K_c using the following Equation 5.8:

$$Q_{tn,cs} = K_c \times Q_{tn} \quad 5.8$$

Where Q_{tn} is the normalized tip resistance obtained from CPT. The estimation of $CRR_{7.5}$ for sandy-like soils and transition regions can be estimated by in terms of the corrected normalized tip resistance, $Q_{tn,cs}$ using Equations 5.9 and 5.10:

$$CRR_{7.5} = 0.833\left[\frac{Q_{tn,cs}}{1000}\right] + 0.05 \qquad \text{If } Q_{tn,cs} < 50 \qquad 5.9$$

$$CRR_{7.5} = 93\left[\frac{Q_{tn,cs}}{1000}\right]^3 + 0.08 \qquad \text{If } 50 \le Q_{tn,cs} \le 160 \qquad 5.10$$

For clay-like soils (Ic ≥ 2.70), the cyclic softening expected is also evaluated. $CRR_{7.5}$ can be estimated using Equation 5.11 in terms of the normalized tip resistance, Q_{tn} obtained from CPT.

$$CRR_{7.5} = 0.053\, Q_{tn} K_\alpha \qquad 5.11$$

Where, Kα is a correction factor to account for static shear stresses. For structures considered well-designed, where the factor of safety for static loading is relatively large, Kα is generally close to 0.9 (Robertson and Cabal 2012). A value of K_α = 0.9 is considered by reasonably assuming that the Eagle Mountain dam presents a high FOS against static loading; and is therefore used for the evaluation of cyclic softening in clay-like soils. A different traditional CPT-based liquefaction triggering approach developed by Boulanger and Idriss (2014) is also used for the assessment of cyclic liquefaction and brief details of this method is described in the following section.

5.3 Approach II: Boulanger and Idriss (2014)

A more advanced liquefaction analysis framework was presented by Boulanger and Idriss (2014) which is based on the procedure established in Idriss and Boulanger (2008) with some additional features. The present section summarizes the methodology for liquefaction assessment using Boulanger and Idriss (2014) approach.

The magnitude scaling factor (MSF) is modified to be a function of earthquake (EQ) magnitude, soil type and denseness (Boulanger and Idriss 2014). A recommended relationship and approach for estimating fines content from CPT data is also described. CRR can be estimated using Equation 5.4 previously described. However, the magnitude

scaling factor is modified based on an equivalent clean-sand value, $q_{C1N_{CS}}$ using Equation 5.12:

$$MSF_{max} = 1.09 + \left(\frac{q_{C1N_{CS}}}{180}\right)^3 \leq 2.2 \quad 5.12$$

$$q_{C1N_{CS}} = q_{C1N} + \Delta q_{C1N} \quad 5.13$$

Where: $q_{C1N_{CS}}$= equivalent clean sand term; q_{C1N}= corrected tip resistance with overburden pressure and Δq_{C1N} = adjustment for CPT-based correlation based on the fines content, FC = 80 x (I_c + C_{FC}) – 137; 0% ≤ FC ≤ 100%. Soil Behavior Type Index, Ic is calculated by using correlations described by Robertson (2009) by using Normalized CPT values (Q_{tn} and FR); C_{FC} = 0.0, -0.29 and 0.29, corresponds to a fitting parameter (i.e., standard deviation of the regression) that can be adjusted based on site-specific data when available. The present study uses C_{FC} as zero.

The equivalent clean sand term, $q_{C1N_{CS}}$ can be expressed in terms of the tip resistance, q_c, the atmospheric pressure, p_a, and the effective overburden stress, σ'_v as follows:

$$q_{c1N} = \frac{C_N \times q_c}{Pa} \quad 5.14$$

$$C_N = \left(\frac{p_a}{\sigma'_v}\right)^{1.530 - 0.247\left(q_{c1N_{CS}}\right)^{0.264}} \quad 5.15$$

Combining Equation 5.13 and 5.14, Equation 5.16 for q_{c1N} is formulated:

$$q_{c1N} = \frac{\left(\frac{p_a}{\sigma'_v}\right)^{1.530 - 0.247\left(q_{c1N_{CS}}\right)^{0.264}} \times q_c}{Pa} \quad 5.16$$

The adjustment term, Δq_{C1N} is expressed in terms of the fines content correlation developed by Boulanger and Idriss (2014) using Equation 5.17:

$$\Delta q_{C1N} = \left(11.9 + \frac{q_{c1N}}{14.6}\right) exp\left(1.63 - \frac{9.7}{FC+2} - \left(\frac{15.7}{FC+2}\right)^2\right) \quad 5.17$$

The term Δq_{C1N} can be described in terms of $q_{C1N_{CS}}$ by combining Equation 5.15 and 5.16 to finally calculate the equivalent clean sand, $q_{C1N_{CS}}$ in terms of the fines content (FC), atmospheric pressure (p_a), overburden pressure (σ'_v) and tip resistance (q_c). The MSF is then computed by using Equation 5.12 to calculate cyclic stress ratio CSR.

CRR is estimated by using the equivalent clean sand term resulting from the regression presented by Boulanger and Idriss (2014) based on Equation 5.18.

$$CRR_{M=7.5,\sigma'_v=1atm} = exp\left\{\frac{q_{C1N_{CS}}}{113} + \left(\frac{q_{C1N_{CS}}}{1000}\right)^2 - \left(\frac{q_{C1N_{CS}}}{140}\right)^3 + \left(\frac{q_{C1N_{CS}}}{137}\right)^2 - 2.80\right\} \qquad 5.18$$

Factors of Safety are calculated by comparing CRR and CSR values as described in Equation 5.1. The methodology described is applied to each CPT collected at the Eagle Mountain dam to evaluate liquefaction potential and for comparison with other methods. This is a modern CPT approach that incorporates important soil information (i.e., FC and I_c) into the development of correction factors as well as the probability of liquefaction P_L implicitly considered in the model of 15%.

The third approach for liquefaction potential assessment was based on the shear wave velocity, V_s measurements in soil layers and this method is described in the following section. Kayen et al. (2013) presented a methodology that incorporated the direct measurements of V_s into the cyclic stress approach for liquefaction assessment. It should be noted that select cone test soundings on the dam has produced seismic shear wave data as these tests were conducted using a seismic piezocone.

5.4 Approach III: Kayen et al. (2013)

A more innovative approach based on the measurement of shear wave velocity, V_s is provided by Kayen et al. (2013). Measurements of shear wave velocity are considerably less sensitive to problems regarding to the soil compression and reduced penetration resistance when soil fines are present. Therefore, the approach based on

shear wave velocity measurements does not require major corrections for fines content, FC. Traditional means of estimating V_s of soil uses an instrumented borehole such as the Seismic CPT (SCPT) to measure the travel time of shear waves with respect to depth. In this study, four SCPTs (4) that were performed at Eagle Mountain Dam along the crest were considered to perform the liquefaction analysis using this approach. The shear wave velocities obtained from SCPT at these locations are combined with the estimation of V_s by using Standard CPT-based correlations provided in the NCHRP report (2007) to perform interpolations and visualization model of liquefaction potential.

Shear wave velocity, V_s can be determined from Standard CPT by using the empirical correlation provided by Mayne (2006b) as presented in Equation 5.19, which is developed from well-documented experimental sites that includes, saturated clays, silts and sands:

$$V_s = 118.8\ log(f_s) + 18.5\ (m/s) \quad 5.19$$

Where, f_s = sleeve friction reported in unites of KPa.

Shear wave velocity obtained from Standard CPT as well as shear wave velocity data collected from four SCPTs along the dam are corrected to be used for computation of cyclic resistance ratio $CRR_{7.5}$. It can be estimated using the normalized shear wave velocity, V_{s1} as described by Kayen et al. (2013) using Equation 5.20.

$$CRR = exp\left\{\frac{\left[(0.0073.V_{S1})^{2.8011} - 2.6168.\ln(M_w) - 0.0099.\ln(\sigma'_{vo}) + 0.0028.\mathrm{FC} - 0.4809.\Phi^{-1}(P_L)\right]}{1.946}\right\} \quad 5.20$$

Where, M is the magnitude of earthquake; σ'_v is the effective stress; V_{S1} is the normalized shear wave velocity obtained by $V_{S1} = \left({p_a}/{\sigma'_v}\right)^{0.25}$ and ϕ-1(PL) the model for probability developed in this approach which can be computed using Equation 5.21 as follows:

$$P_L = \phi\left\{-\frac{\left[(0.0073.V_{S1})^{2.8011} - 1.946.\ln(CSR) - 2.6168.\ln(M_w) - 0.0099.\ln(\sigma'_{vo}) + 0.0028.(FC)\right]}{0.4809}\right\} \quad 5.21$$

On the other hand, $CSR_{7.5}$ can be computed using Equation 5.3; however the stress reduction factor r_d is estimated based on a statistical model of ground response analysis results provided in this approach based on the Equation 5.22 and the MSF or (DFW – duration weighting factor defined by Kayen) using Equation 5.23.

$$R_d\left(d, M_w, a_{max}, V^*_{s,12m}\right) = \frac{\left(1 + \frac{-23.013 - 2.949.a_{max} + 0.999.M_W + 0.0525.V^*_{s,12m}}{16.258 + 0.201.e^{0.341,\left(-d + 0.0785.V^*_{s,12m} + 7.586\right)}}\right)}{\left(1 + \frac{-23.013 - 2.949.a_{max} + 0.999.M_W + 0.0525.V^*_{s,12m}}{16.258 + 0.201.e^{0.341,\left(0.0785.V^*_{s,12m} + 7.586\right)}}\right)} \pm \sigma_{\varepsilon rd} \quad 5.22$$

$$MSF(DFW) = 15{M_W}^{-1.342} \quad 5.23$$

Where, d=depth in meters, measured at the midpoint of the critical layer; $V_{s12.2m}$=average Vs in the upper 12.2 m (40 ft) of the soil column; and a_{max}=PGA in units of gravity.

For the deterministic assessment of liquefaction susceptibility, this approach recommends the P_L=15% contour for use as the single deterministic boundary for V_{s1}-based liquefaction evaluation shown in Figure 2.31. Thus, the factor of safety is computed using Equation 5.21.

$$FS_{liq} = \frac{CRR_{PL(15\%)}}{CSR} \quad 5.21$$

Transitions zones are considered for the first two approaches (Robertson 2009; Boulanger and Idriss 2014). By considering transition zones in the analysis, lateral and vertical displacements using CPT data are commonly overestimated. However, the objective of the present study is not to evaluate the displacements expected after liquefaction, but to provide more qualitative information on liquefaction related FOS values (ratios of CSR and CRR values). It should be noted a FOS value of 1 indicates a significant potential for liquefaction in a soil layer whereas higher FOS values indicate no

liquefaction in the soil layers. Hence, in order to have a better interpolation using Geostatistics, the FOS values obtained for all three approaches on selection cone soundings are determined and then interpolated by geostatistics and used for the generation of three-dimensional models of liquefaction potential. The following sections present a comprehensive liquefaction evaluation of the Eagle Mountain dam by presenting three different scenarios described earlier.

5.4 Liquefaction Potential of EM Dam: Actual Field Conditions

This first scenario refers to the liquefaction evaluation by using the present field conditions at the Eagle Mountain dam. The ground water level or phreatic line within the dam plays a vital role on the assessment of liquefaction within the dam. An excess of pore water pressure must be developed within the soil mass in order for liquefaction to occur. Therefore, if soils are above the phreatic line (unsaturated zone), they are less susceptible to liquefaction. According to the United States Geological Survey (USGS) along with the information from Tarrant Regional Water District (TRWD), the conservation pool elevation is estimated to be approximately El+649.0 ft. The dam is assumed to have a reasonable phreatic line based on the lake level. Thus, soils are considered to be saturated below the El+630.0 based on this assumption; however a more accurate prediction can be done by performing seepage analysis which is outside of the scope of this work.

The next condition is the characterization of earthquake loading capable of producing ground motion at the Eagle Mountain dam. PSHA results depicted, 1% probability of 0.3g to be exceeded within a one-year time frame. Also, based on the recent seismicity events, the approximate magnitude of earthquake expected is ~M4.0 (i.e., maximum earthquake in the region, Venus, TX in 2014). Therefore, liquefaction

evaluation for this scenario can be estimated by using a ground motion of 0.3g in the CSR calculations.

5.4.1 Liquefaction Based on CPT

This section includes several plots used to evaluate the liquefaction potential using three different approaches for the first case scenario. A CPT test located at Station 10.50 on the crest of the dam is considered for the analysis. The raw CPT data (q_t, f_s and R_f) is shown in Figure 5-1 and it will be used in each methodology to calculate the liquefaction potential at that location.

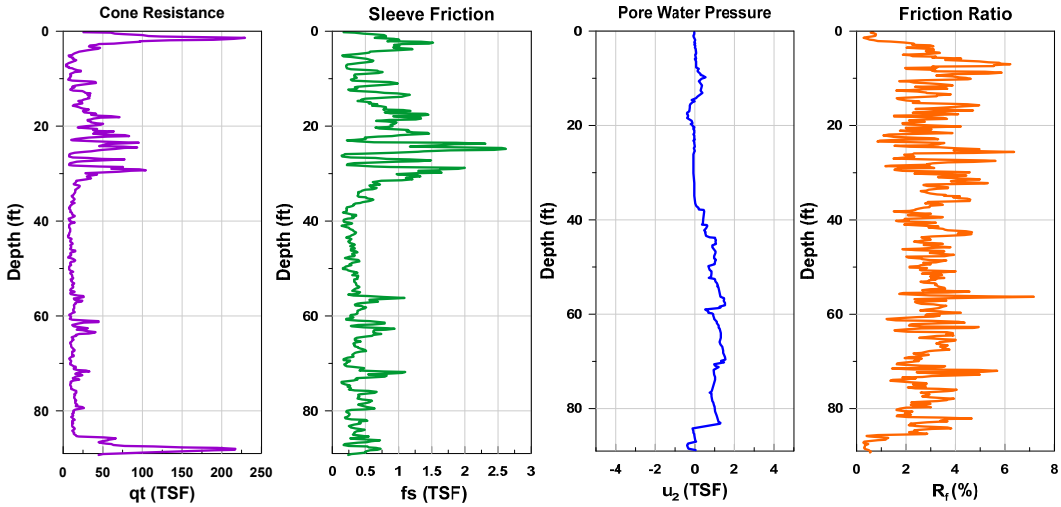

Figure 5-1 Raw CPT data obtained at Station 10.50 at the crest of the dam

5.4.1.2 Analysis based on Approach I

Initially, the raw CPT data was normalized by several conventional correction factors that are related to projected area of the cone and pore water pressure effects. Normalized plots and corresponding Soil Behavior Type Index (I_c) for the CPT performed at Station 10.50 are shown in Figure 5-2. Figure 5-3 illustrates the corrected normalized tip resistance ($Q_{tn,cs}$) by using the grain characterization factor (K_c) for estimation of $CRR_{7.5}$ in sandy-like soil and transition regions. Both, CRR and CSR can be estimated as

well as the FOS calculations at Station 10.50 are shown in Figure 5-4. It may be noted that cyclic liquefaction was also evaluated in the unsaturated zone (above 50 ft.) CRR values were found to be beyond the threshold value (CRR=4.0) as shown in Figure 5-4.

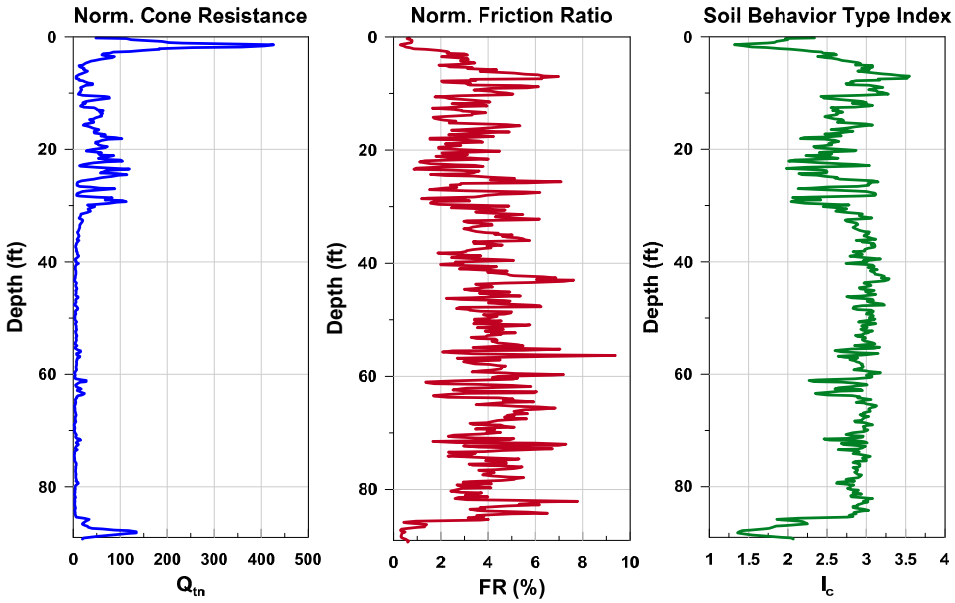

Figure 5-2 Normalized CPT values and Soil type at Station 10.50 – Robertson (2009)

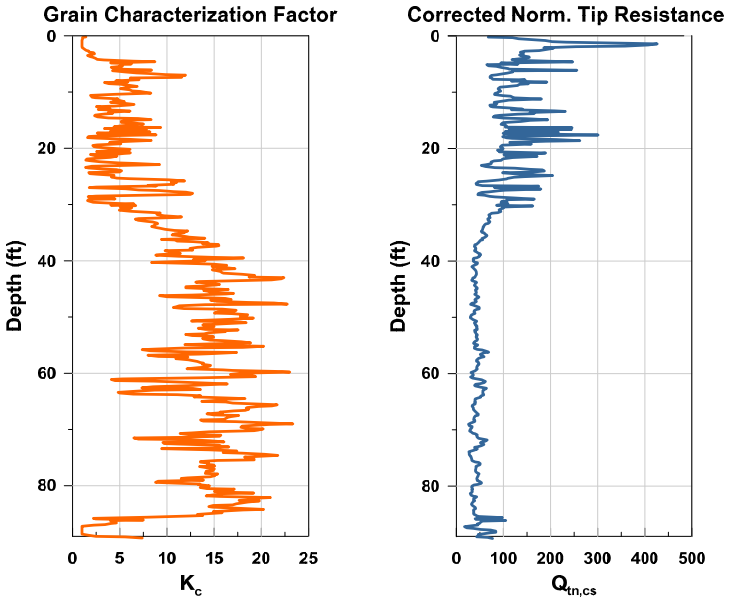

Figure 5-3 Corrected Normalized tip resistance ($Q_{tn,cs}$) – Robertson (2009)

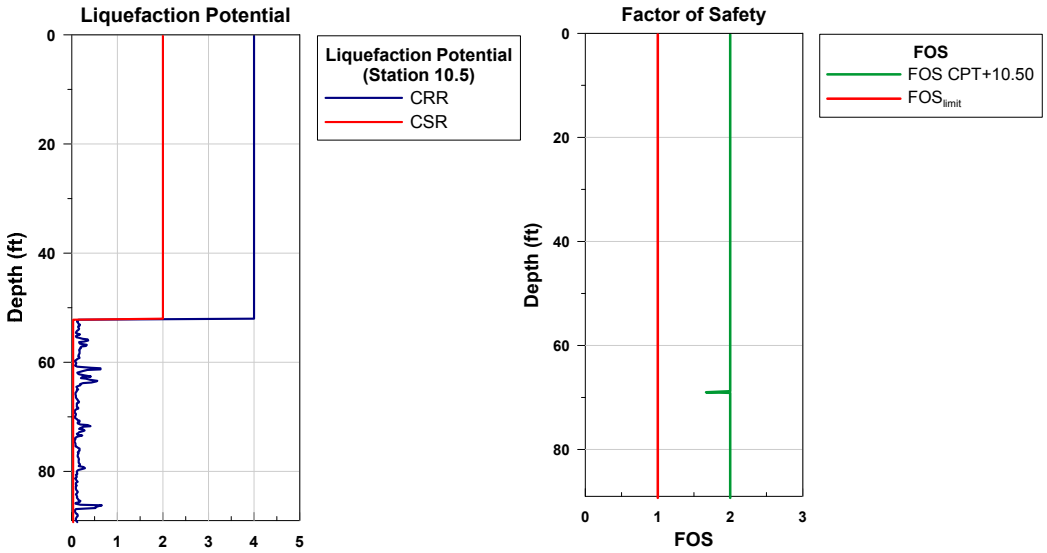

Figure 5-4 Liquefaction Potential at Station 10.5 at the crest of the dam using Robertson (2009)

Factor of safety against liquefaction potential using Roberson (2009) approach for the present case scenario depicted high values (FOS>2.0) in all soils. Liquefaction potential is defined by the FOS plots for each CPT data collected at EM dam. For unsaturated soil zones, the FOS values are much higher and hence high FOS of 2 are mentioned in those zones which indicate no liquefaction issues. Three-dimensional visualization models of FOS interpolation are further performed by incorporating their spatial variability using Geostatistics.

5.4.1.2 Analysis based on Approach II

This section includes several plots used to evaluate the liquefaction potential using the Boulanger and Idriss (2014) approach. For the sake of comparison with other methods, plots corresponding to CPT located at Station 10.50 on crest of the dam under first case scenario conditions, are presented herein. The following sequence of plots aim to understand the liquefaction evaluation using this approach. Figure 5-5 shows plots for the equivalent clean sand term obtained from raw CPT data as well as the fines content

estimation. These two terms are used for calculation of the fines adjustment term and the corrected tip resistance (Figure 5-6) used for computation of $CRR_{7.5}$ as shown in Figure 5-7.

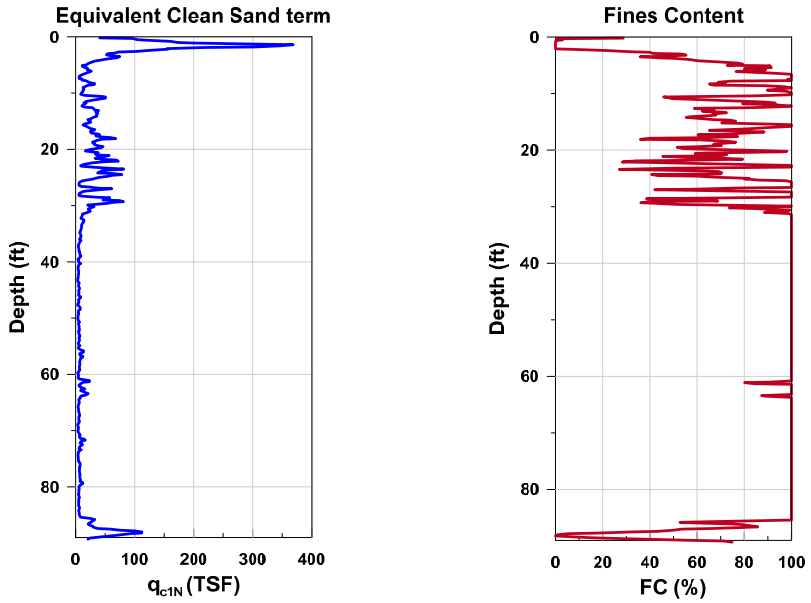

Figure 5-5 Equivalent clean sand and Fines Content, FC – Boulanger&Idriss (2014)

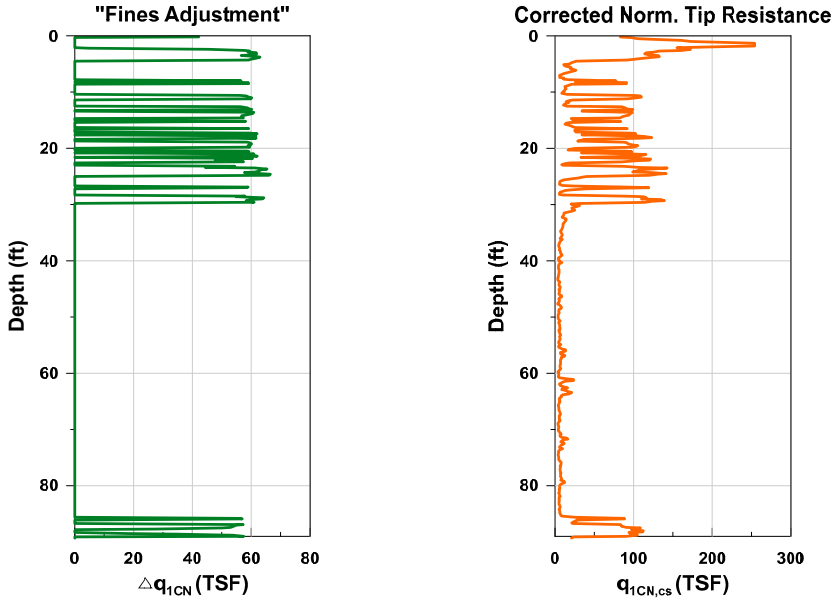

Figure 5-6 Fines adjustment and Correc. Norm. Tip resistance - Boulanger&Idriss (2014)

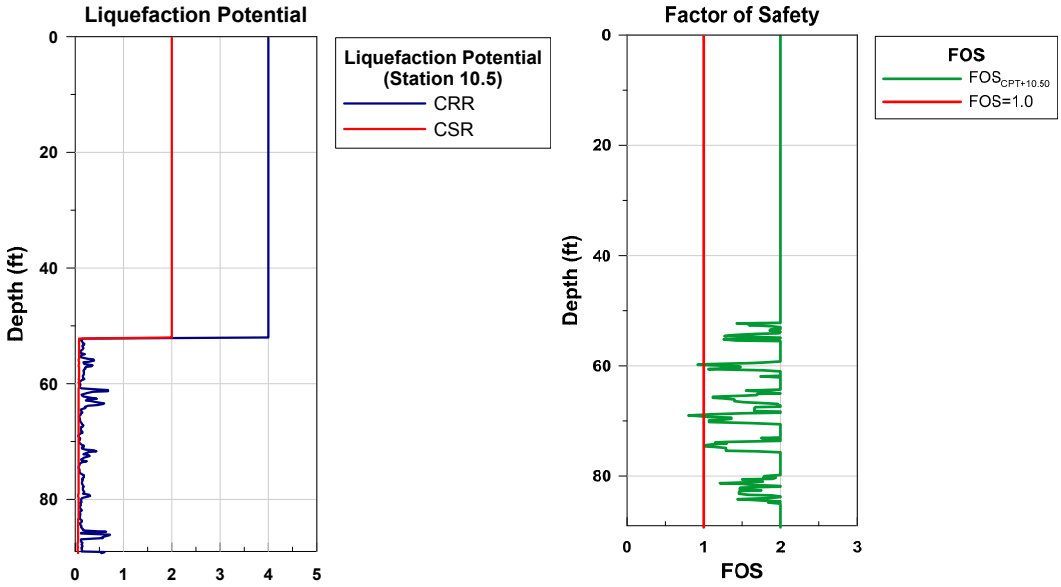

Figure 5-7 Liquefaction Potential at Station 10.5 at the crest – Bounlanger&Idriss (2014)

Liquefaction potential is also shown in Figure 5-7 in terms of factor of safety. The CPT depicted lower values of FOS than Robertson (2009) method and hence higher liquefaction potentials are obtained. In the present case (Figure 1-8), only a handful of locations yielded a FOS value of 1, still these are thin zones and hence do not appear to cause significant damage to the dam embankments. Interpolation of FOS obtained using this approach will provide higher number of data points for interpolation and visualization purposes.

5.4.1.2 Analysis based on Approach III

In an attempt to compare different liquefaction approaches by using some information available from SCPTu, an approach developed by Kayen et al. (2013) is presented. This approach is primarily developed when direct measurements of shear wave velocities are collected using different in-situ methods (i.e., SCPTu, DMT). SCPTu data were collected at four locations in the EM dam and shear wave velocities are used for the analysis. In an attempt at performing interpolation using Geostatistics, CPT raw

data can be used for computation the shear wave velocity at locations where SCPT is not available to increase the number of data. This approach estimates the liquefaction potential by using the normalized shear wave velocity (V_{s1}) and is better illustrated by generating several plots as shown in Figure 5-8 and Figure 5-9. Information collected at Station 10.50 is used for the sake of comparison with the other two methodologies.

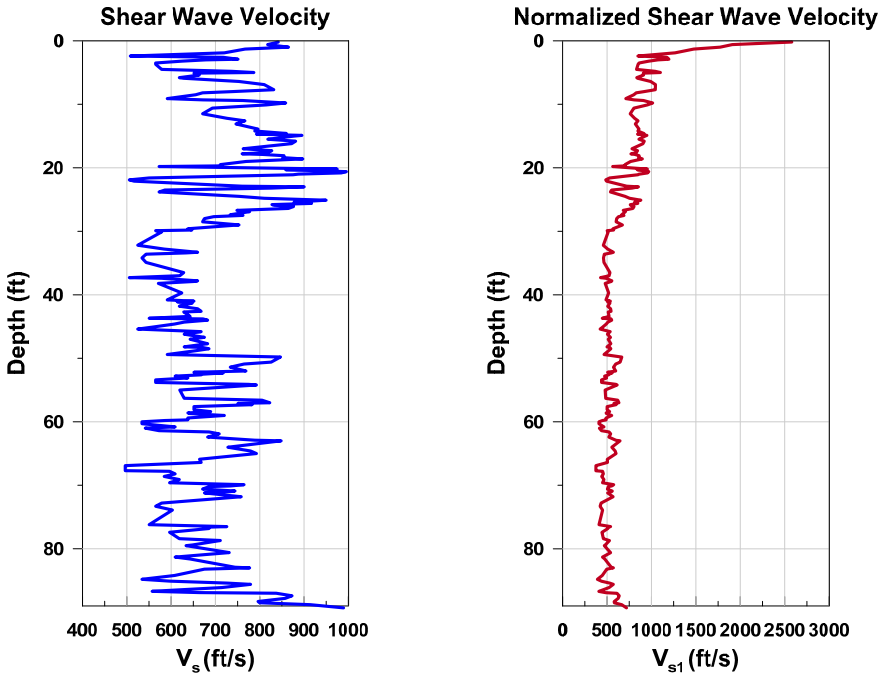

Figure 5-8 Normalization of Shear Wave Velocity

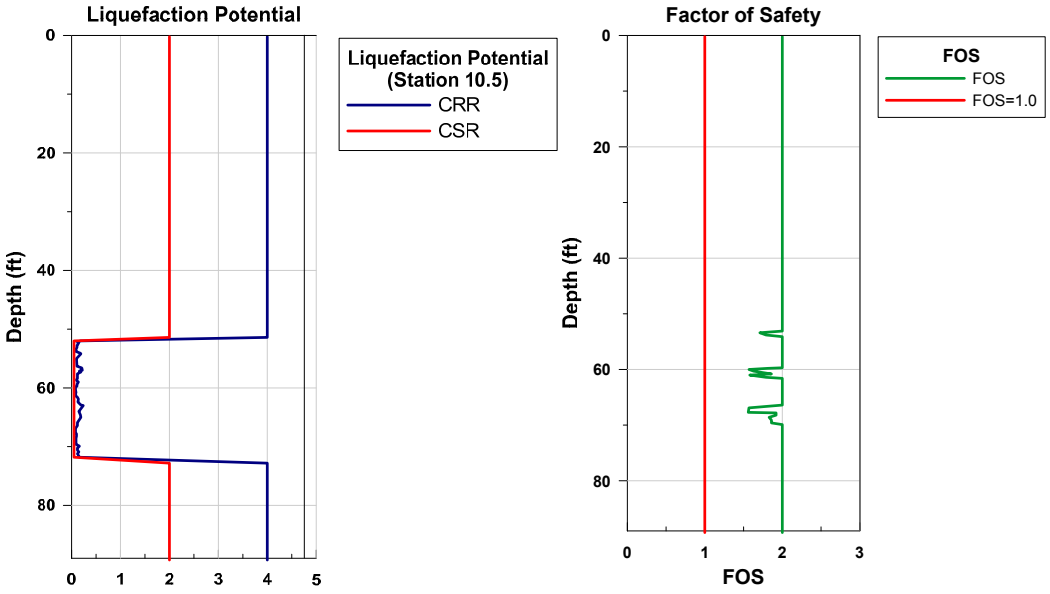

Figure 5-9 Liquefaction Potential at Station 10.5 at the crest - Kayen et al. (2013)

Factors of safety obtained from shear wave velocity approach are presented in Figure 5-9. When comparing FOS results with the other two methodologies, shear wave velocity does not show any similarity. It is expected to have a low quality interpolation due to the limited number of data resulting from the approach. Results can be attributed to the inherent variability in predicting shear wave velocity from CPT or to the lack of considering transition zones in the methodology. The present study includes this approach for comparison purposes only. Three-dimensional models based on Geostatistics are generated; however visualization quality can be decreased due to the kriging interpolation of limited number of data values as shown in the following section.

5.4.2 Three-Dimensional Visualization Model of FOS

Three-dimensional visualization models were generated based on the conditions described above for the present case scenario. Figure 5-10 presents the visualization model of liquefaction potential calculated using three different approaches: Robertson

(2009), Boulanger and Idriss (2014) and Kayen et al (2013). The colored legend corresponding to each visualization model is assigned to define liquefaction potential.

Results from visualization models using all three methodologies indicate that there is no liquefaction of soils in the Eagle Mountain dam based on the actual field conditions and the CPT interpretation results. The legend in the visualization results shows a full color of blue depicting high factors of safety within the body of the dam. If had liquefaction been triggered, some areas would be colored green showing factors of safety less than 1.0. The Eagle mountain dam is stable under local seismic conditions expected (M4, a_{max}=0.3g) and based on the assumption that lake level remains at the conservation pool elevation (EL+649.0).

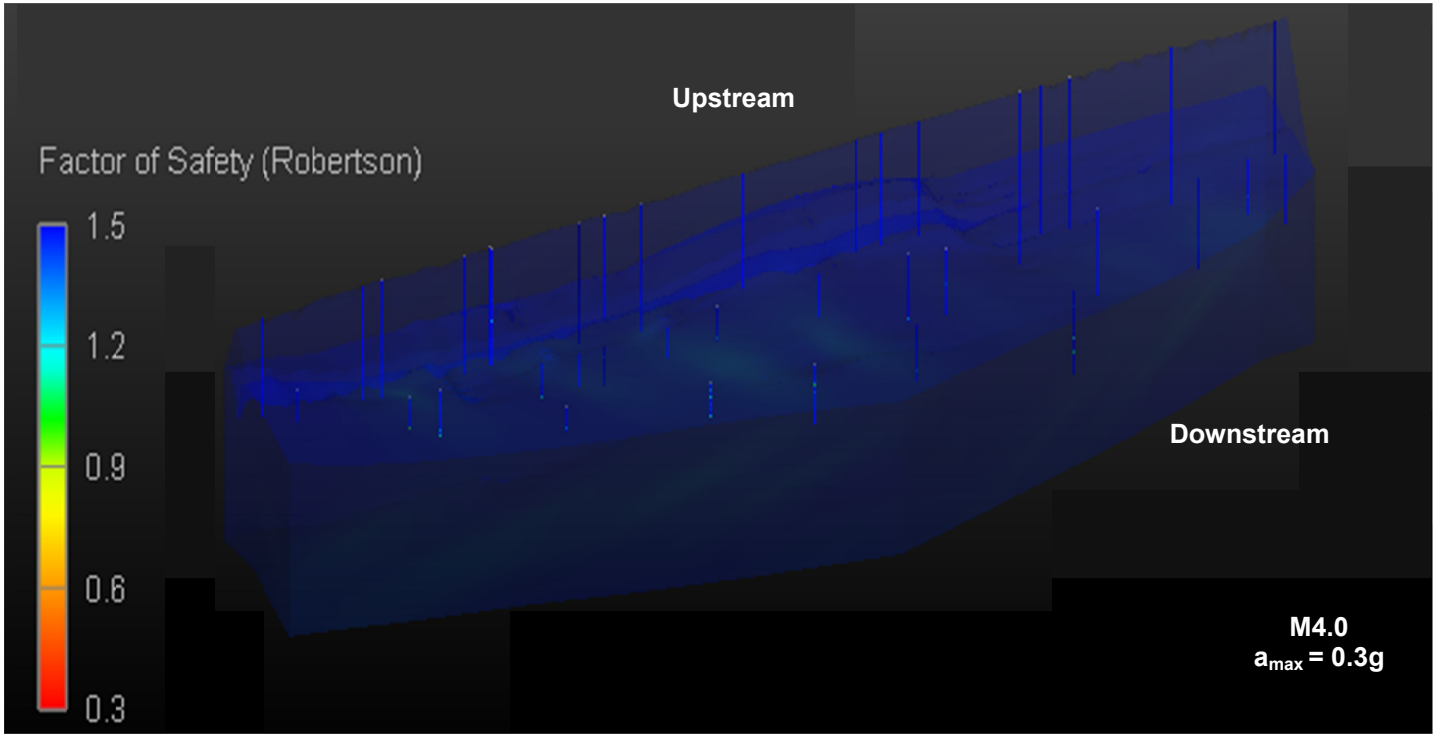
Upstream
Factor of Safety (Robertson)
1.5
1.2
0.9
0.6
0.3
Downstream
M4.0
a_{max} = 0.3g

(a)

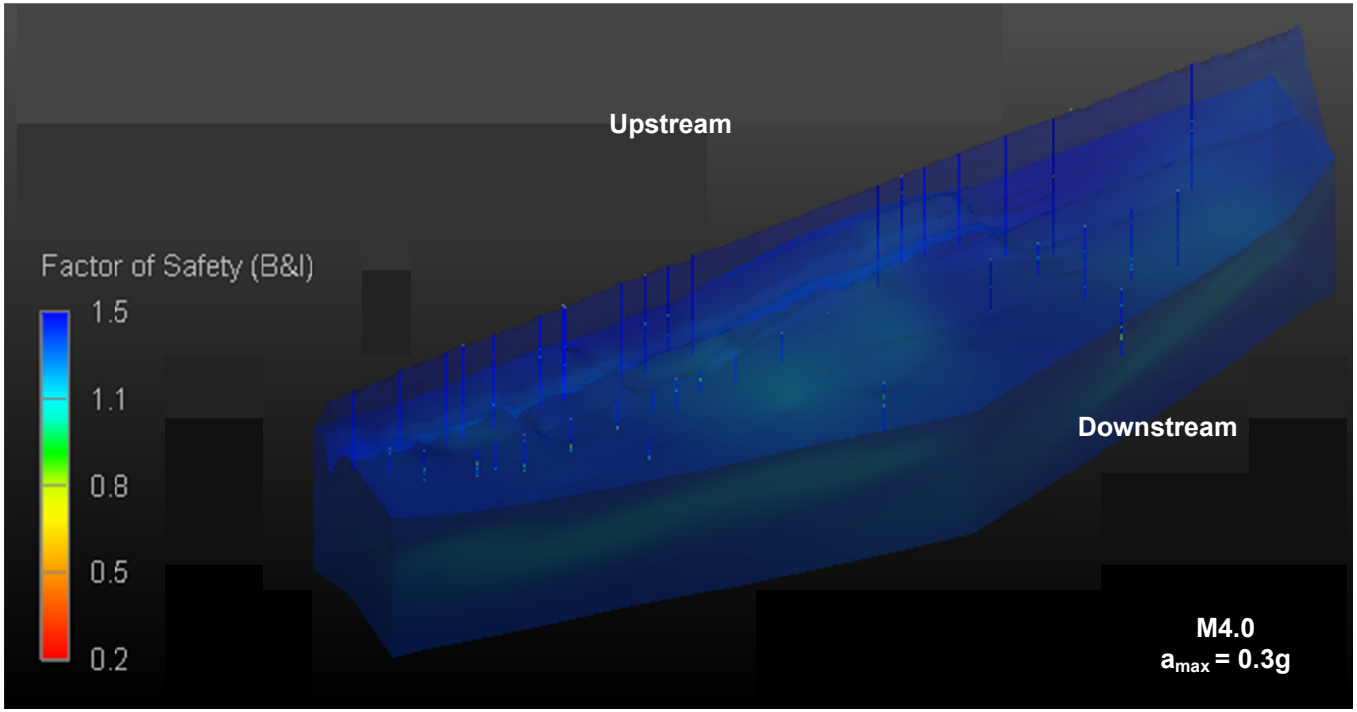
Upstream
Factor of Safety (B&I)
1.5
1.1
0.8
0.5
0.2
Downstream
M4.0
a_{max} = 0.3g

(b)

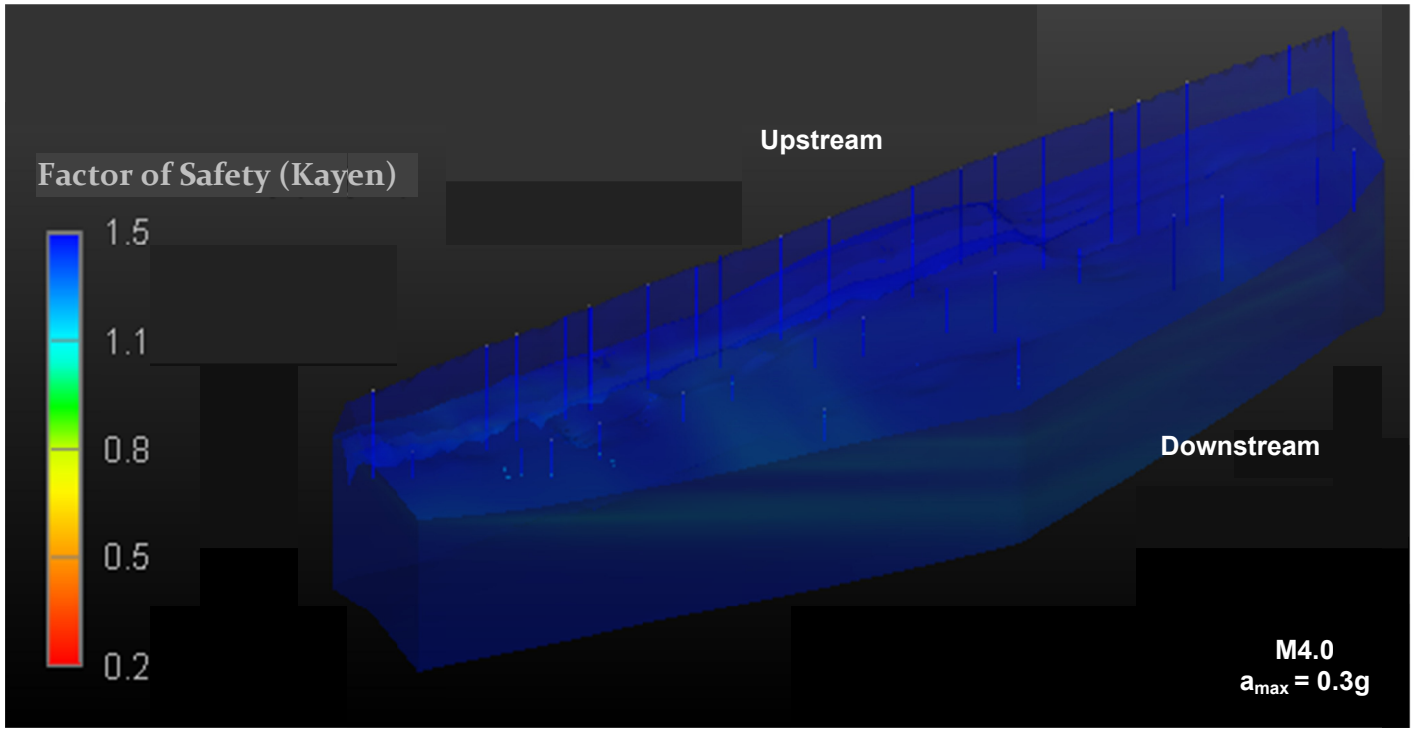

(c)

Figure 5-10 Visualization of Liquefaction potential for actual field conditions using three methodologies

5.5 Liquefaction Potential of EM Dam: Hypothetical Scenarios

This section presents three-dimensional visualization models of liquefaction potential for different hypothetical scenarios. The main objective is to visualize the influence in the increase of earthquake magnitude (M), peak ground acceleration (a), and the lake level that could lead to produce liquefaction in the dam. Seismicity with similar conditions in near locations (i.e., Oklahoma, Colorado) present higher magnitudes and accelerations as compared with the a_{max}=0.3g obtained from PSHA at the Eagle Mountain Dam. Both approaches are performed at different magnitudes of earthquakes (M4.5, M5.5 and M6.5) assumed to occur in North of Texas for comparison purposes only. The Robertson (2009) liquefaction approach is used for evaluating the liquefaction potential considering hypothetical scenarios.

The increase in earthquake loading will result in an increase in peak ground acceleration. The calculation of CSR is performed at Station 10.50 for each increase of acceleration (i.e., 0.3g, 0.4g and 0.5g) as well as for each magnitude of earthquake (M4.5, M5.5. and 6.5). It should be noted that both increase of earthquake magnitude and a hypothetical acceleration parameter are not directly correlated but they are considered as a potential transpiring scenario of earthquakes of different magnitudes that could occur in a larger area around the EM dam. The lake level remains constant for all cases. As shown in plots (Figure 5-11), CSR values above 50 ft. (unsaturated zone) are not shown in the plot due to scale limitations. The analysis performed by plotting CSR variation with acceleration and magnitude at the same location, provides a better insight of each hypothetical scenario herein presented. It should be noted that for the first three hypothetical scenarios where the lake level is at El+649.0, CRR values remain constant. The CRR changes for the fourth case scenario where the lake level is assumed to be high to consider soils in upper layers in saturated conditions.

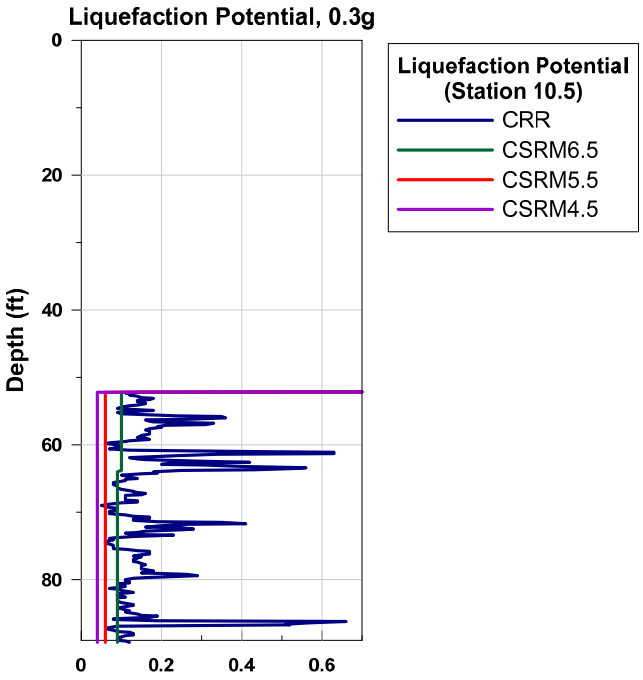
Liquefaction Potential, 0.3g
Depth (ft)
0
20
40
60
80
0
0.2
0.4
0.6
Liquefaction Potential
(Station 10.5)
CRR
CSRM6.5
CSRM5.5
CSRM4.5

(a)

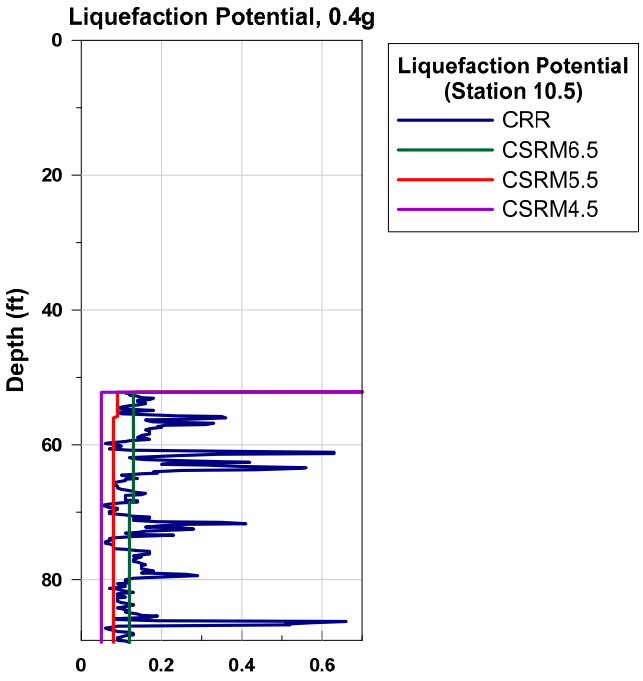
Liquefaction Potential, 0.4g
Depth (ft)
0
20
40
60
80
0
0.2
0.4
0.6
Liquefaction Potential
(Station 10.5)
CRR
CSRM6.5
CSRM5.5
CSRM4.5

(b)

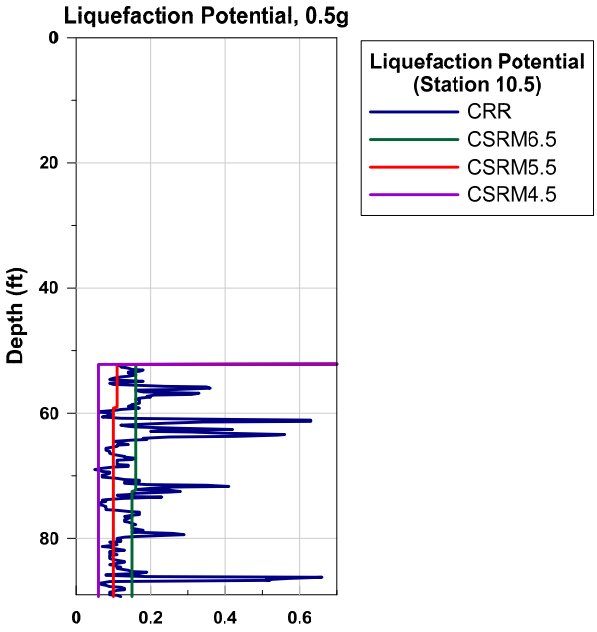

(c)

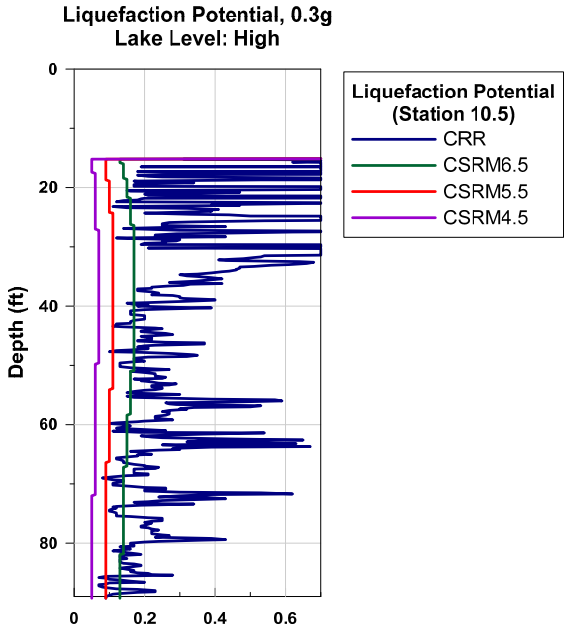

(d)

Figure 5-11 CSR at different magnitudes (a) 0.3g, (b) 0.4g, (c) 0.5g and (d) 0.3g – Lake level high – Roberson (2009)

5.5.1 Scenario I: a_{max} - 0.3g; M- 4.5, 5.5, 6.5; Flood Level- El+649

This section presents the generation of visualization models by assuming an increase in the magnitude of earthquakes in North Texas, but with the same peak ground acceleration a=0.3g obtained from PSHA. This condition, as noted earlier, can again transpire when larger EQ magnitudes occur beyond the 40-mile radius or due tore changes in geological and environmental conditions or both. The lake level still remains the same as the first case scenario considering the conservation pool levels reported by USGS (El+649.0). Results of liquefaction visualization models showed that for these defined conditions and with an increase in earthquake up to M5.5 (Figure 5-12), there is no liquefaction in the body of dam even when earthquake magnitude increases to M5.5. Results can be seen in Figure 5-12.

However, under an earthquake of M6.5, some liquefaction is triggered at deeper depths (55-60 ft.) at Sector 3 and 4 as shown in Figure 5-13. The contour or shaded cyan areas represent the locations where the factors of safety are less than 1.0 within the body of the dam. It is noted that the phreatic level was assumed to be at El+630 approximately 50 ft. below the crest and it was expected for liquefiable zones to be at locations below that elevation.

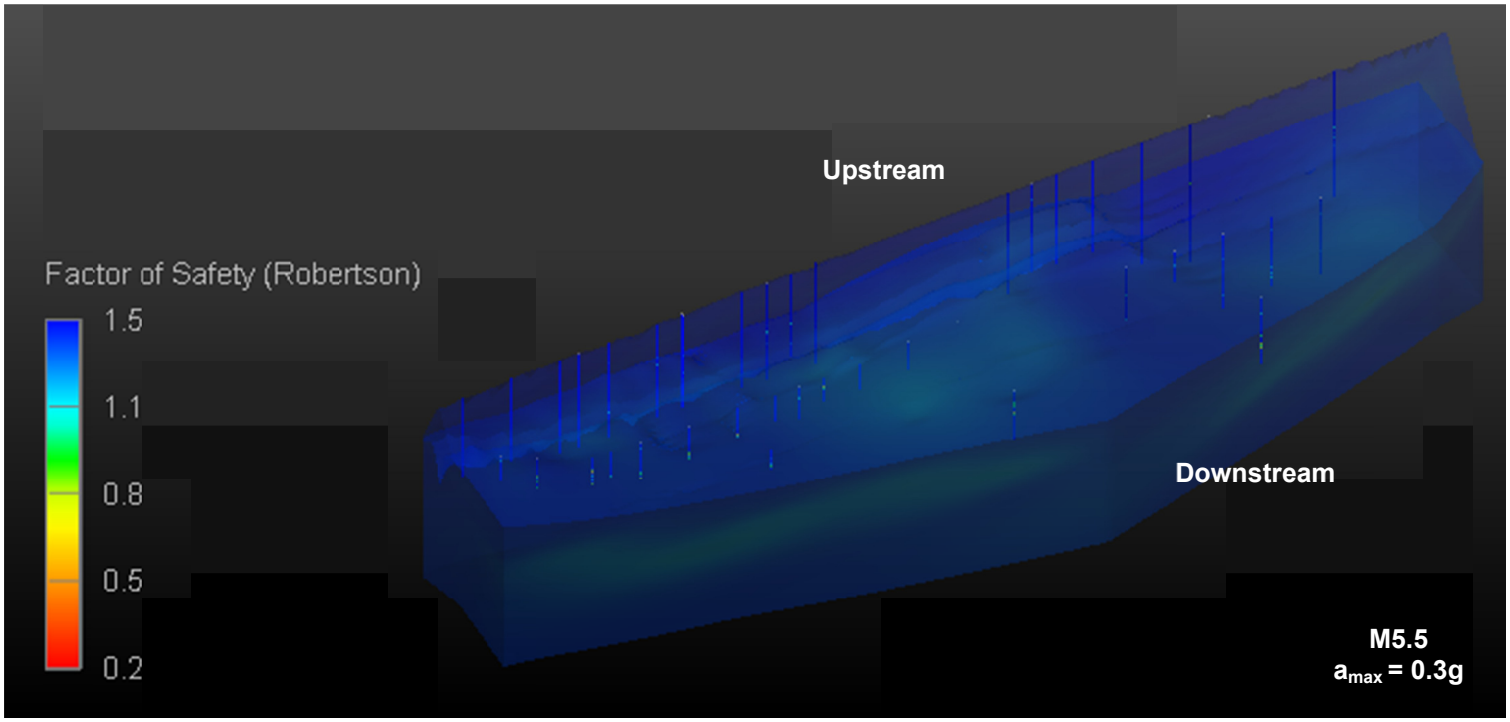

Figure 5-12 Visualization of liquefaction potential, M5.5, 0.3g – Roberson (2009)

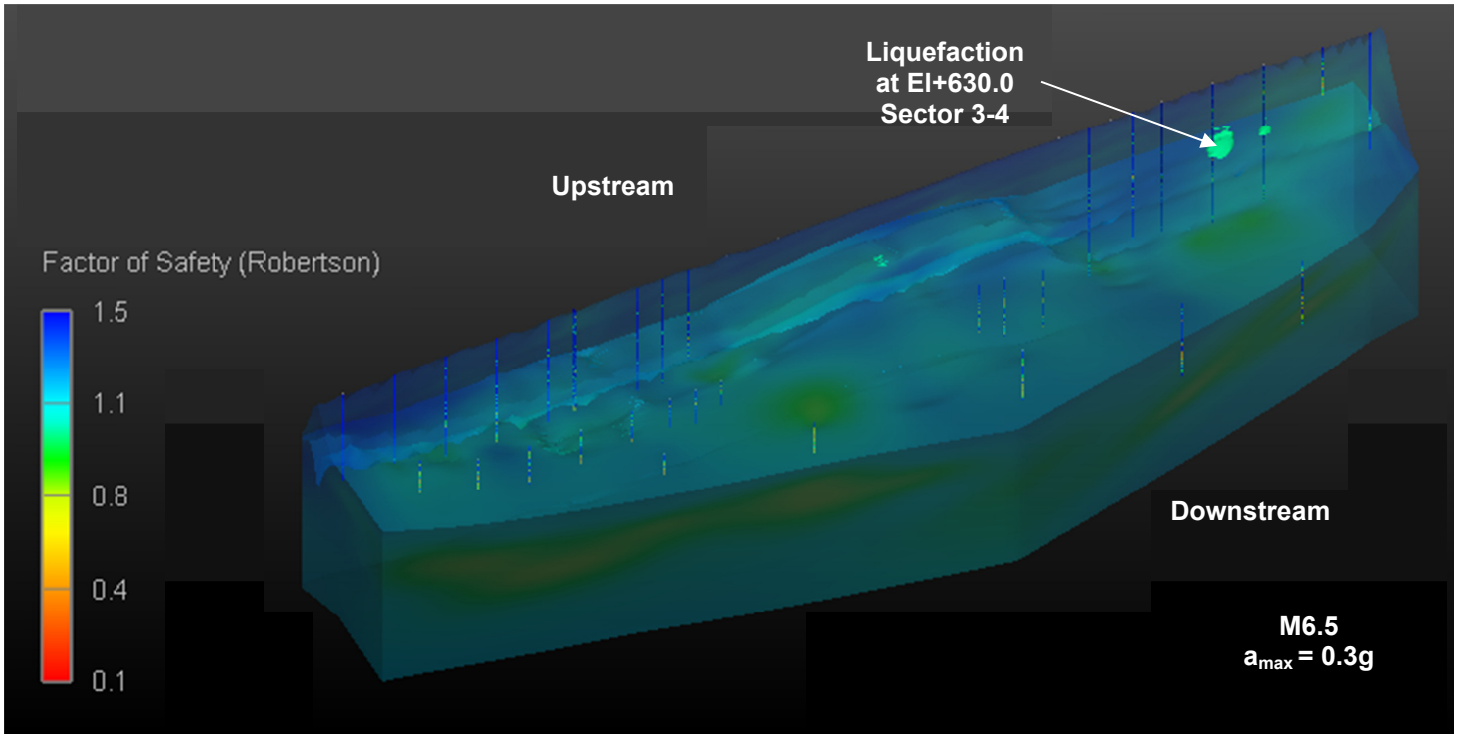

Figure 5-13 Visualization of liquefaction potential, M6.5, 0.3g – Roberson (2009)

5.5.2 Scenario II: a_{max} - 0.4g; M- 4.5, 5.5, 6.5; Flood Level- El+649

The second hypothetical scenario analysis is performed based on the assumption that the peak ground acceleration is increased to 0.4g at the Eagle Mountain Dam. Higher peak ground acceleration increases the cyclic stress ratio, and hence increases the liquefaction problem in the dam. The lake level remains constant for the present scenario, as the actual condition based on the conservation pool levels presented by USGS (El+649.0). The evaluations is developed for a series of earthquakes of magnitudes, M4.5, M5.5 and M6.0 to visualize at which earthquake liquefaction is triggered in the dam.

Results of visualization are shown to illustrate that an increase in earthquake magnitudes (M4.5, M5.5 and M6.5) has increased the cyclic liquefaction. The hypothetical scenario presented herein depicted that the initiation of liquefaction occurred in small areas at magnitudes of M5.5 at an acceleration of 0.4 g. In the visualization model for an earthquake magnitude M5.5, the liquefaction zone with factor of safety less than 1.0 (cyan color) is primarily located at Sector 3 at very large depths (~60 ft. below). Visualization models generated based on SBT, I_c and friction angle can be used for the interpretation of soil type at those locations. Results showed that soils are classified as silts; however liquefied area also includes some clayey-like soils which may be susceptible to cyclic softening.

At higher magnitudes (M6.5), the increase in liquefaction potential is shown at similar depths (60-70 ft.). Cyclic liquefaction occurs on soils that are mainly located in the shells as well as at certain locations within the core. In this hypothetical scenario, the stability of the dam may be affected due to large deformations that may occur in the clayey core after cyclic softening in clayey-like soils and cyclic liquefaction in sand-like soils located at the shells.

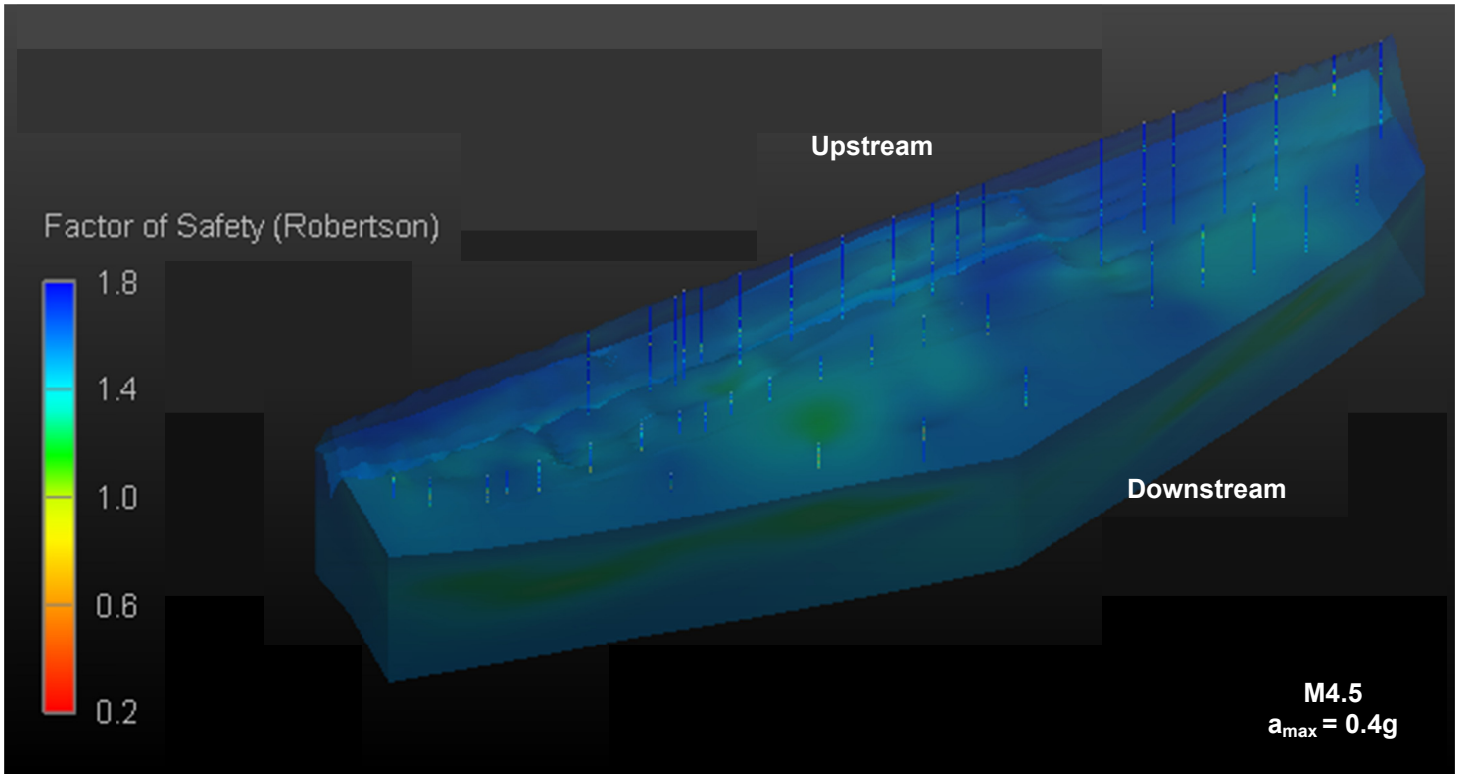
Upstream
Factor of Safety (Robertson)
1.8
1.4
1.0
0.6
0.2
Downstream
M4.5
a_{max} = 0.4g

(a)

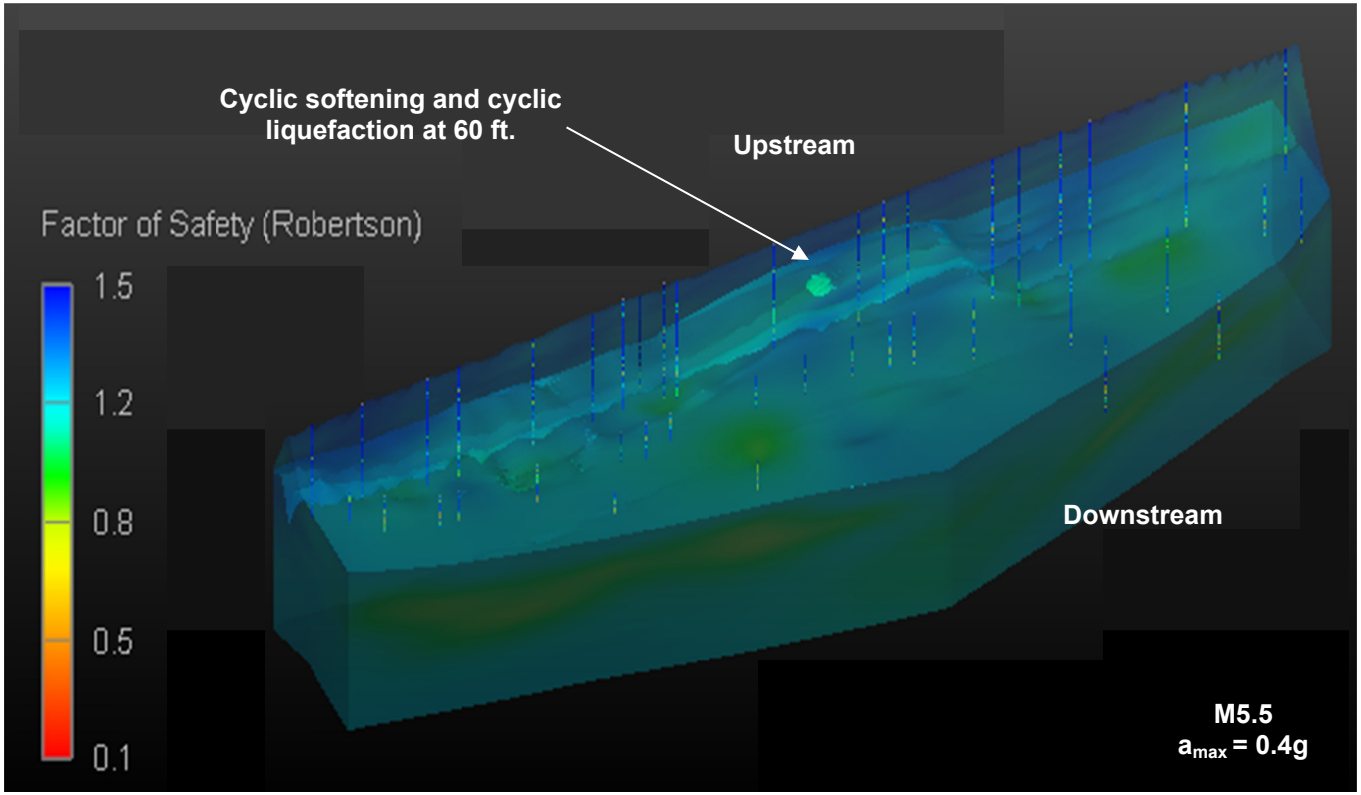
Cyclic softening and cyclic liquefaction at 60 ft.
Upstream
Factor of Safety (Robertson)
1.5
1.2
0.8
0.5
0.1
Downstream
M5.5
a_{max} = 0.4g

(b)

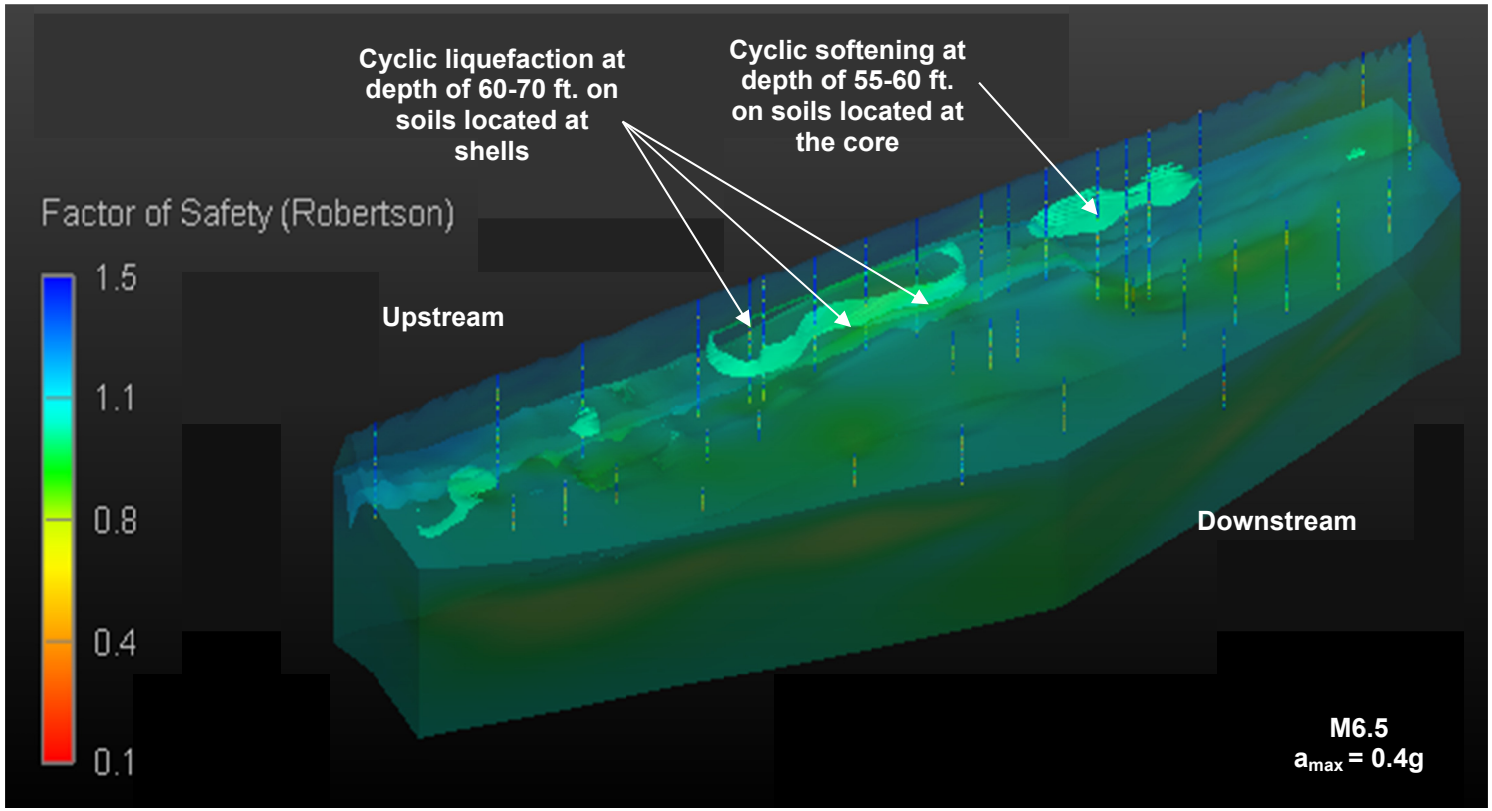

Figure 5-14 Visualization of liquefaction potential, 0.4g – Roberson (2009)

5.5.3 Scenario III: a_{max} - 0.5g; M- 4.5, 5.5, 6.5; Flood Level- El+649

The third hypothetical scenario is to provide the liquefaction condition at an increased acceleration of 0.5g at different earthquake magnitudes. Other condition such as the lake level remains constant as the previous case scenario. The effect on liquefaction is similar but slightly higher level as compared to the condition with acceleration of 0.4g. While maintaining these conditions, the initiation of liquefaction can be visible in magnitudes of earthquake M5.5 at certain depths (~55-65 ft.) as shown in Figure 5-15. Soil types at those locations are corroborated with visualization models developed for SBT and others soil properties. The presence of clayey-like materials present is susceptible to cyclic softening under a seismic event with these high acceleration conditions.

At higher magnitudes (M6.5), liquefaction zones expand along the dam at depths of 55-75 ft. Except for Sector 3 and 4 that consisted of sandy-like soils which experience cyclic liquefaction, the rest of the soils are mostly clayey-like materials that may be susceptible to cyclic softening at these conditions. Based on the color legend and in terms of the contours, it may be noted that the FOS of the entire dam is decreasing with an increase in the acceleration (a_{max} – 0.4g to 0.5g). This effect is also shown when the EQ magnitude is increased from M4.5 to M6.5.

Despite the fact that visualization results shown to have some liquefaction zones at higher earthquake magnitudes with higher accelerations, the probability to have these conditions at the North Texas is very low. The objective of reproducing these conditions is to highlight the importance of visualization approach using Geostatistics to provide a better overview of geotechnical hazards in a series of realistic and hypothetical scenarios. A worst case scenario is presented in the next section to show conditions at which the resilience of the dam is affected.

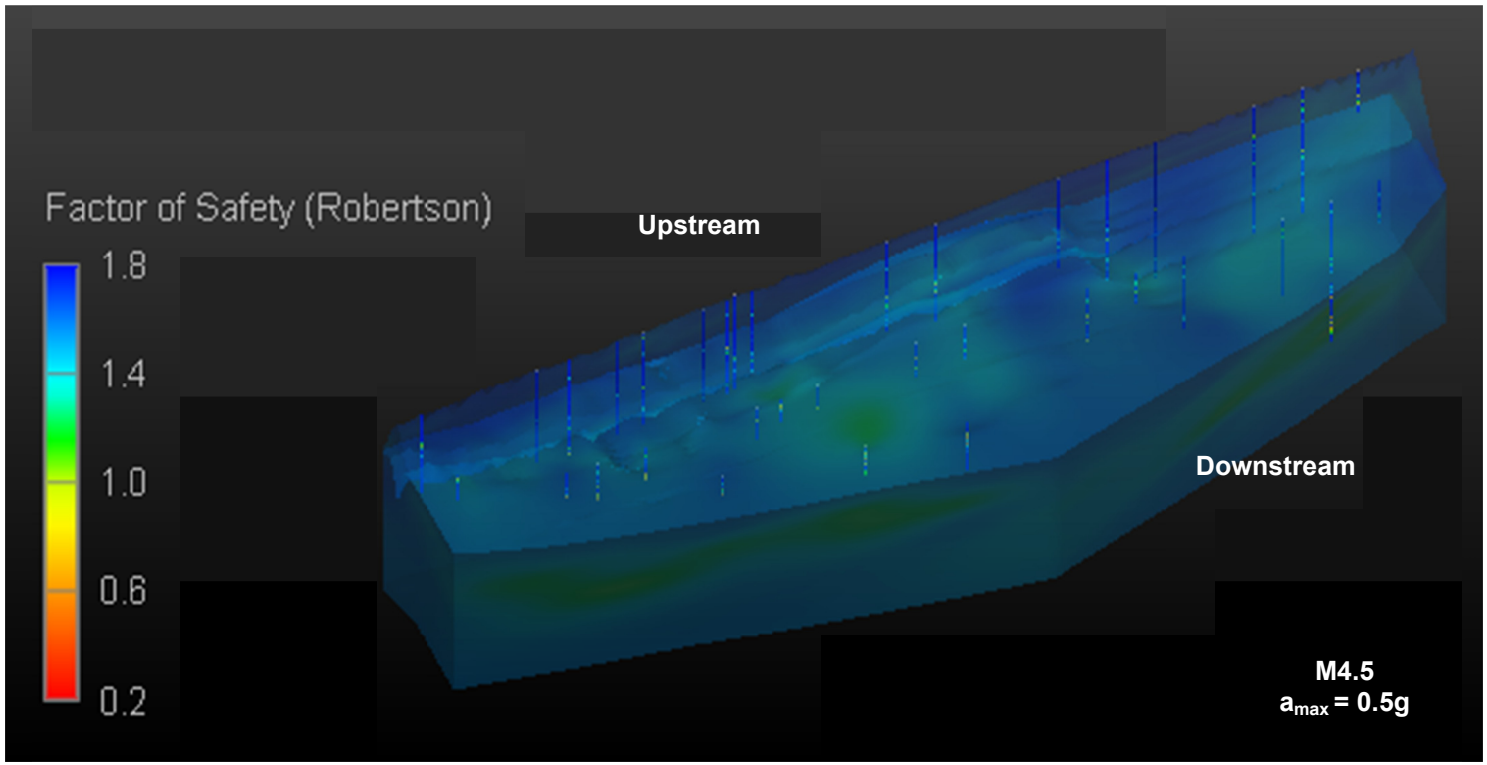
Factor of Safety (Robertson)
1.8
1.4
1.0
0.6
0.2
Upstream
Downstream
M4.5
a_{max} = 0.5g

(a)

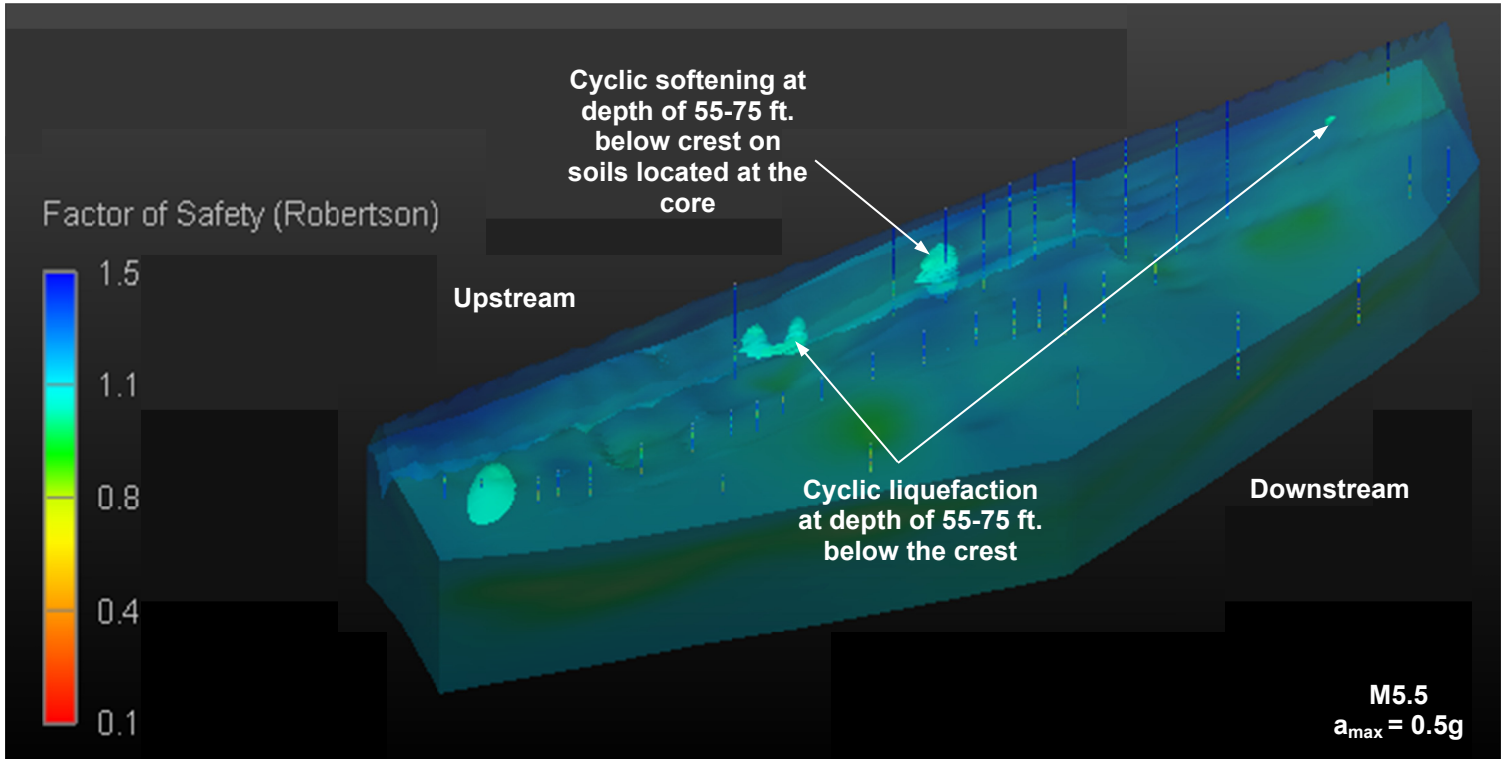
Cyclic softening at depth of 55-75 ft. below crest on soils located at the core
Factor of Safety (Robertson)
1.5
1.1
0.8
0.4
0.1
Upstream
Cyclic liquefaction at depth of 55-75 ft. below the crest
Downstream
M5.5
a_{max} = 0.5g

(b)

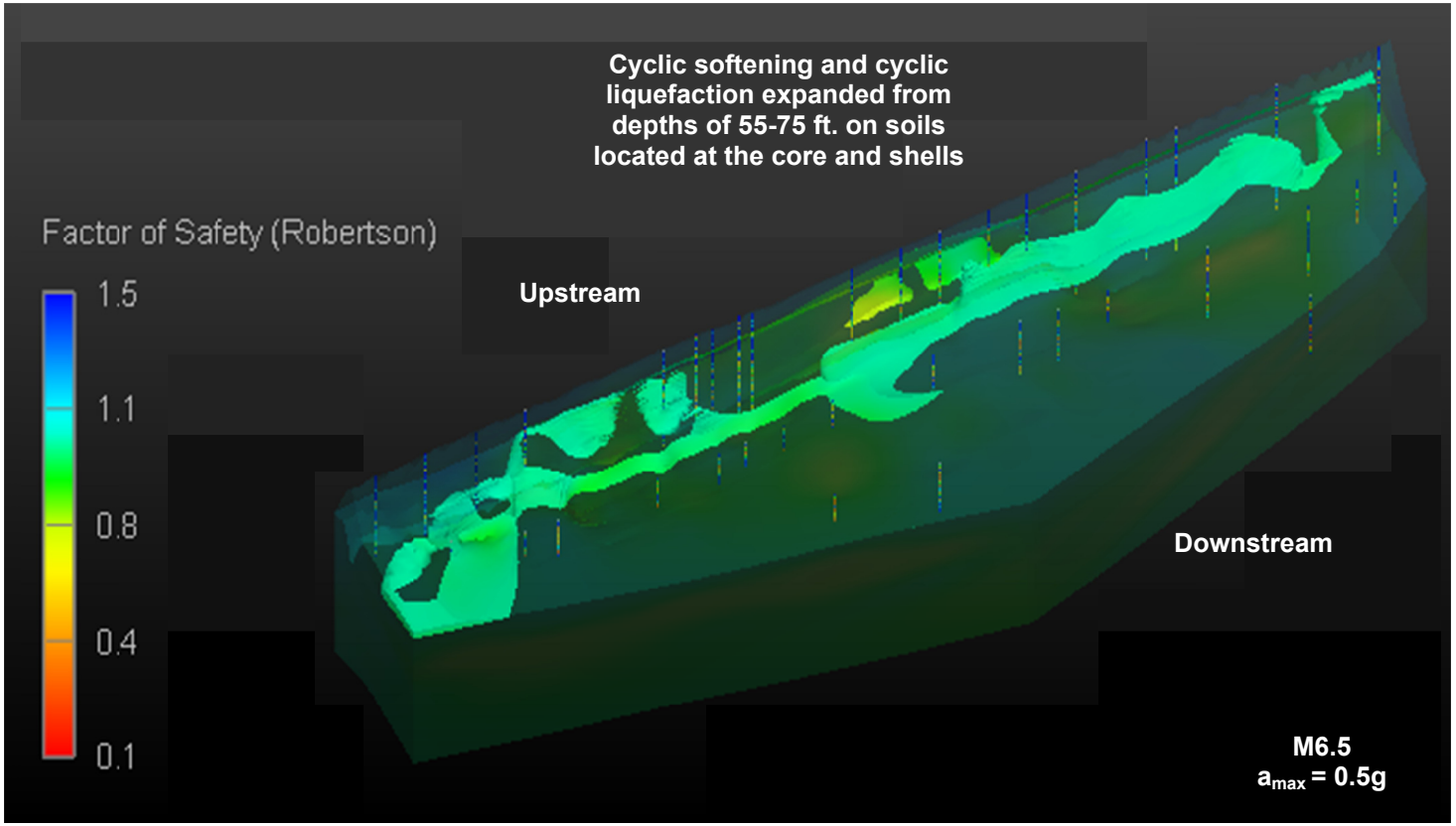

(c)

Figure 5-15 Visualization of liquefaction potential, 0.5g – Roberson (2009)

5.5.4 Scenario IV: a_{max} - 0.3g; M- 4.5, 5.5, 6.5; Flood Level- El+665

This section presents the liquefaction evaluation based on extreme conditions at the Eagle Mountain Dam. Previous sections presented hypothetical scenarios to illustrate the effects of increasing acceleration at the site as well as having earthquakes of higher magnitudes. All cases assumed that the water lake level remains at the conservation pool levels reported by USGS (El+649.0). Seepage line was reasonably assumed within the dam (average El+630.0) and it contemplates that soils were saturated below that elevation. Thus, the effect of saturation in soil hence the lake levels, have a significant effect on the liquefaction potential expected in the EM dam.

The present section is based on the condition that lake level rises up to the elevation of El+665.0 (i.e., above the maximum flood value) during the time an earthquake strikes the site with a higher earthquake magnitude (M4.5, M5.5 and M6.5) and with acceleration at the ground of 0.3g (PSHA). A seepage line is also assumed (~El+665) and soils are considered to be saturated below that level. The analysis is performed at three-different magnitudes (M4.5, M5.5 and M6.5). Since it is expected to have some liquefaction within the body of the dam because of the present conditions; the liquefaction potential is again evaluated using three same methodologies. This task aims to demonstrate the effect of each methodology on the interpolation and visualization results within the body of the dam.

Unlike the visualization results obtained from Robertson (2009) and Kayen et al. (2013) methods, Boulanger and Idriss (2014) approach depicts few zones of liquefaction at lower magnitudes (M4.5). Results can be attributed to the Magnitude Scaling Factor used in the model which considers duration of seismic events, soil type and state of the soil. Similar results are found in Sector 3 and 4, and it is noted to be one of the most critical regions in the dam, where maximum thickness of hydraulic fill is present. At higher

magnitudes (M5.5 and M6.0), liquefaction and areas of this distress increase in the dam and some of these areas can be considered susceptible to cyclic softening (i.e., clay-like soils).

While increasing the earthquake magnitude up to M5.5, liquefaction potential is expanded primarily in soils located in Sectors 3 and 4 as shown in Figure 5-17. Visualization models of soil properties are used to evaluate soil types at those locations. This sector was already identified in previous Chapters as critical since sands and silts were placed at the core location. At higher magnitude of earthquake M6.5, the stability of the dam is affected in Sectors 3 and 4 as shown in Figure 5-18.

The Robertson (2009) approach was found to give more conservative results when compared with the other two methodologies. Even though, Robertson (2009) considered in his updated work, the potential of cyclic softening in clayey-like soils, only few spots of cyclic softening areas are visualized. On the other hand, Boulanger & Idriss (2014) approach which initially considered the cyclic softening in clay-like soils showed a higher liquefaction potential for this type of materials.

The visualization models using Kayen et al. (2013) depicts low quality in the results (i.e., colored large blocks in visualization). This is mainly attributed to the low number of shear wave velocities data points (i.e., FOS values) used for the interpolation. However, the initiation of liquefaction can be identified in sands or silts located in Sectors 3 and 4 at same magnitudes at other approaches. Unlike the other two methodologies where few areas depict cyclic softening of the core at higher magnitudes (M6-M7), the shear wave velocity approach does not show any cyclic softening until an earthquake of Magnitude M7 is triggered as shown in Figure 5-18. The analysis is not performed for higher magnitudes since the dam is already showing liquefaction failures in the body of the dam at a=0.3g for the present high water table condition.

Analyses showed that higher saturation in the embankment of a dam would lead to liquefaction with the induced seismicity at the current PSHA level of 0.3g. In order to reduce these failures, it is important to maintain the phreatic line elevations levels well below the hypothetical level assumed here. Based on the current sets of water elevation readings, it is safe to assume that the embankment of the dam is less susceptible to liquefaction from induced seismicity occurring in the region. This analysis must also be considered within the maintenance and operational recommendations at the Eagle Mountain Dam. The lake level shall be conserved to ensure that soils are not fully saturated below certain elevation which minimizes the liquefaction potential.

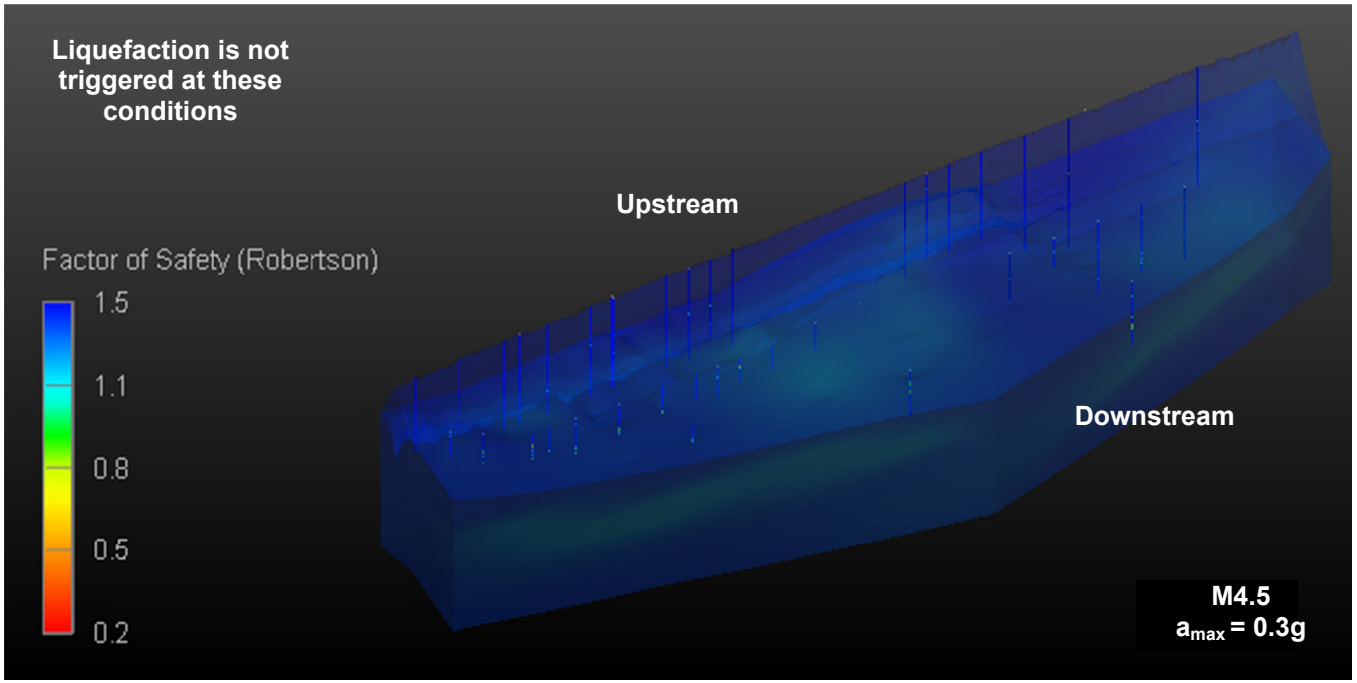
Liquefaction is not triggered at these conditions
Upstream
Factor of Safety (Robertson)
1.5
1.1
0.8
0.5
0.2
Downstream
M4.5
amax = 0.3g

(a)

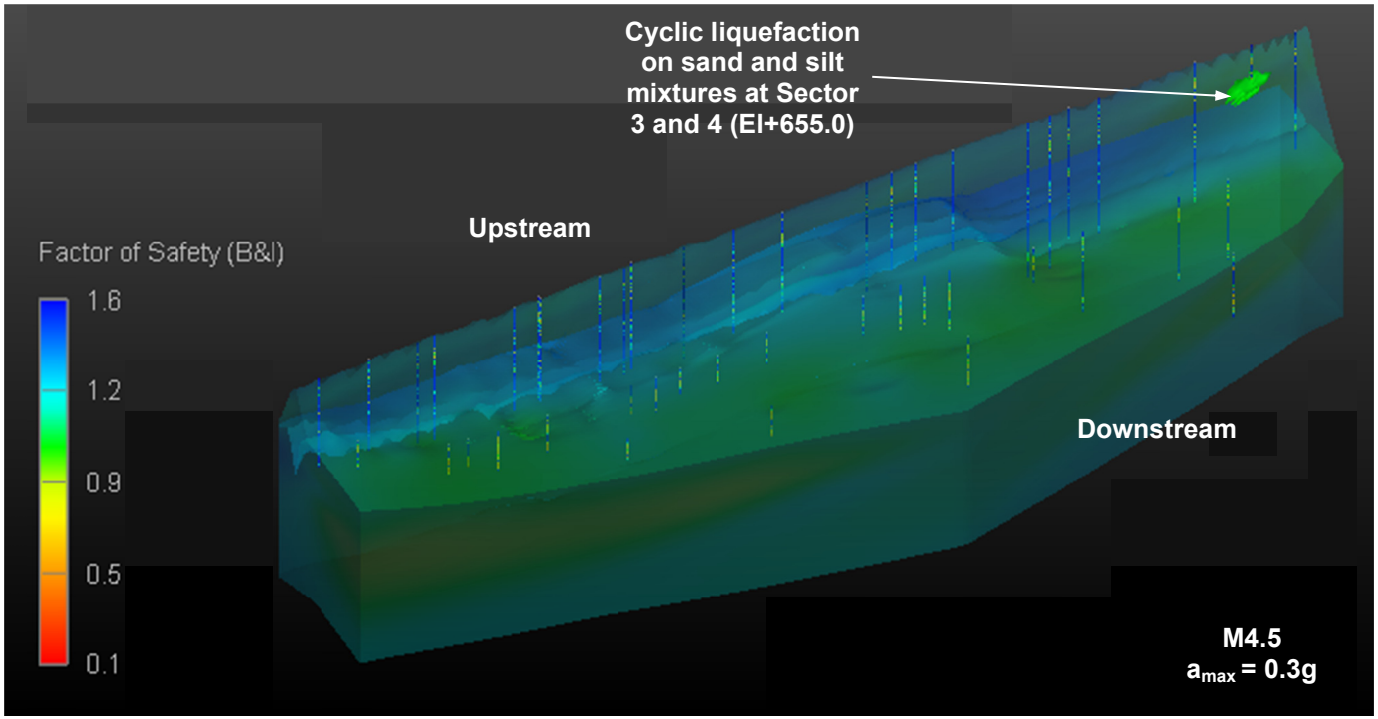
Cyclic liquefaction on sand and silt mixtures at Sector 3 and 4 (El+655.0)
Upstream
Factor of Safety (B&I)
1.6
1.2
0.9
0.5
0.1
Downstream
M4.5
a_{max} = 0.3g

(b)

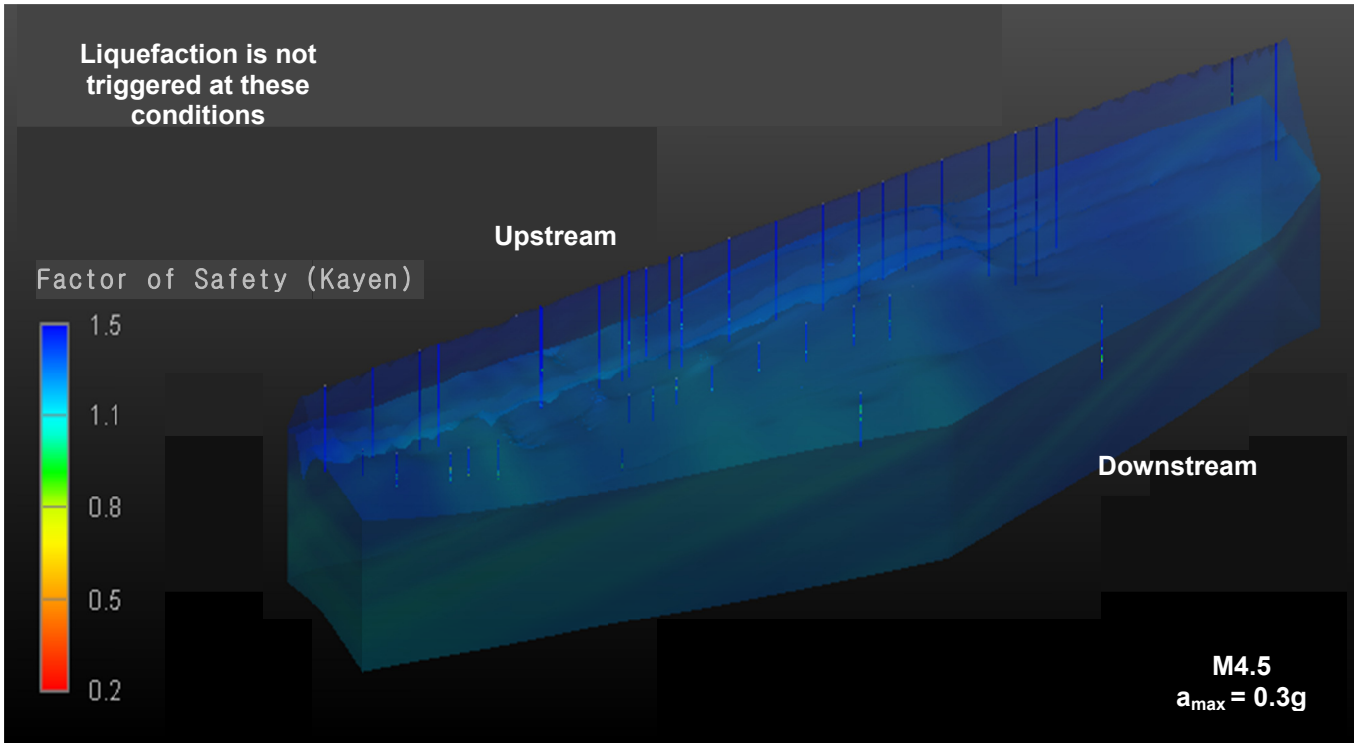

(c)

Figure 5-16 Visualization of LP using three methodologies at M4.5, 0.3g

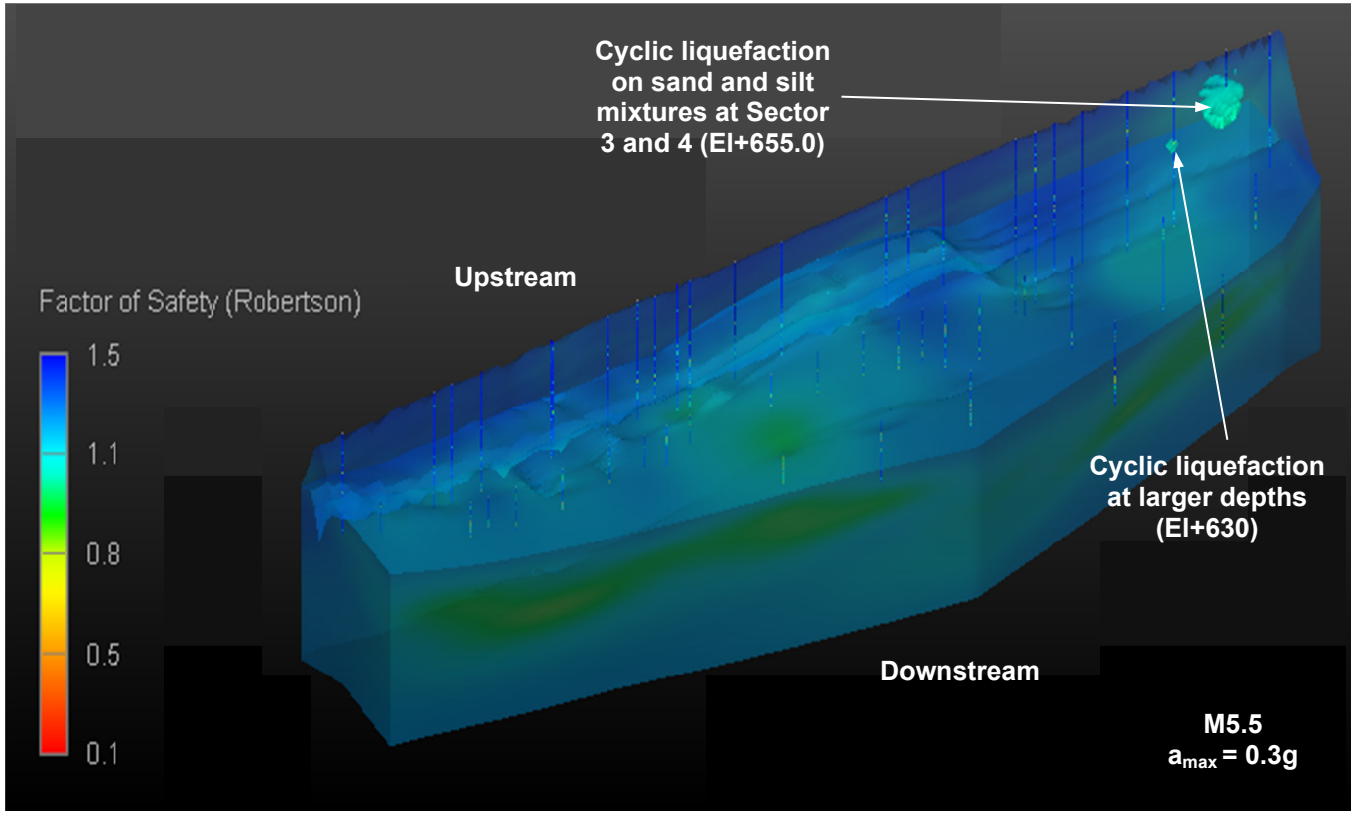
Cyclic liquefaction on sand and silt mixtures at Sector 3 and 4 (El+655.0)
Upstream
Factor of Safety (Robertson)
1.5
1.1
0.8
0.5
0.1
Cyclic liquefaction at larger depths (El+630)
Downstream
M5.5
a_{max} = 0.3g

(a)

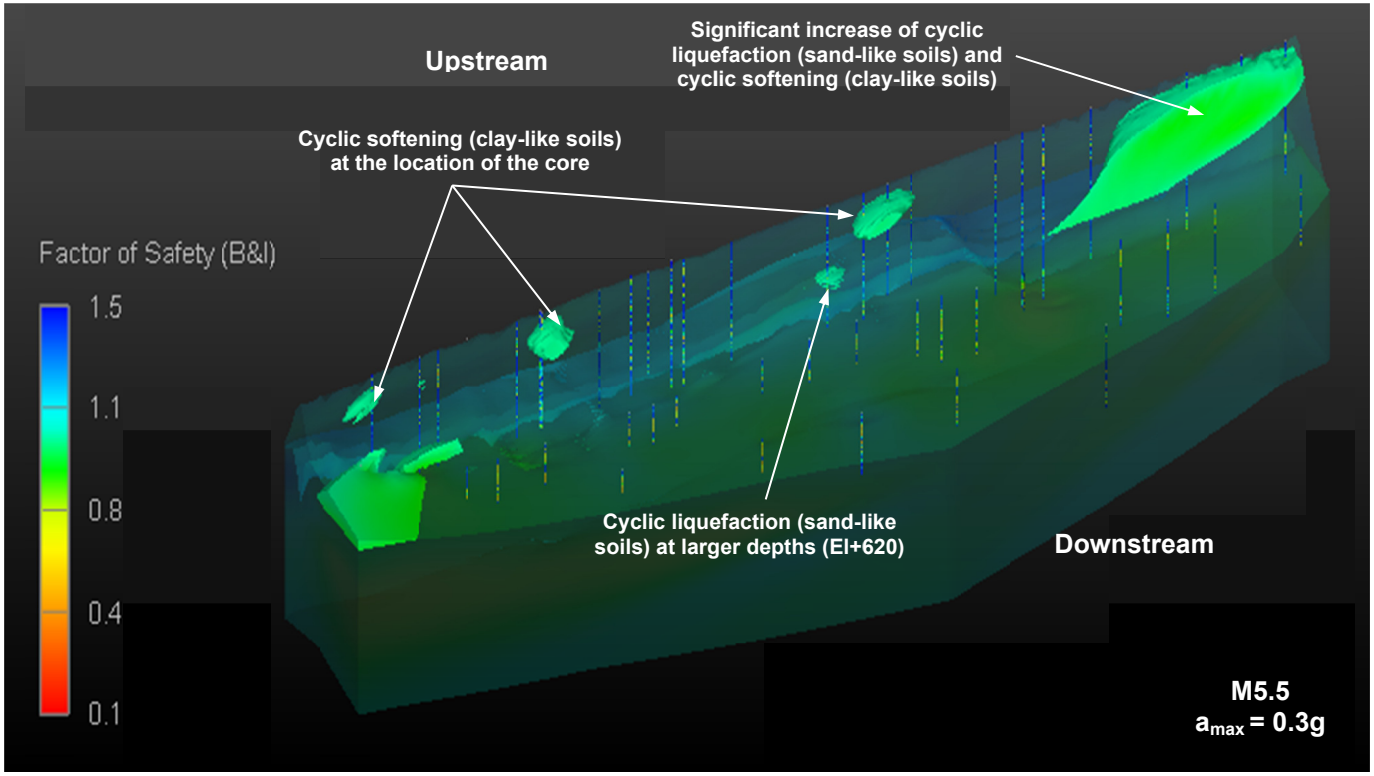
Upstream
Significant increase of cyclic liquefaction (sand-like soils) and cyclic softening (clay-like soils)
Cyclic softening (clay-like soils) at the location of the core
Factor of Safety (B&I)
1.5
1.1
0.8
0.4
0.1
Cyclic liquefaction (sand-like soils) at larger depths (El+620)
Downstream
M5.5
a_{max} = 0.3g

(b)

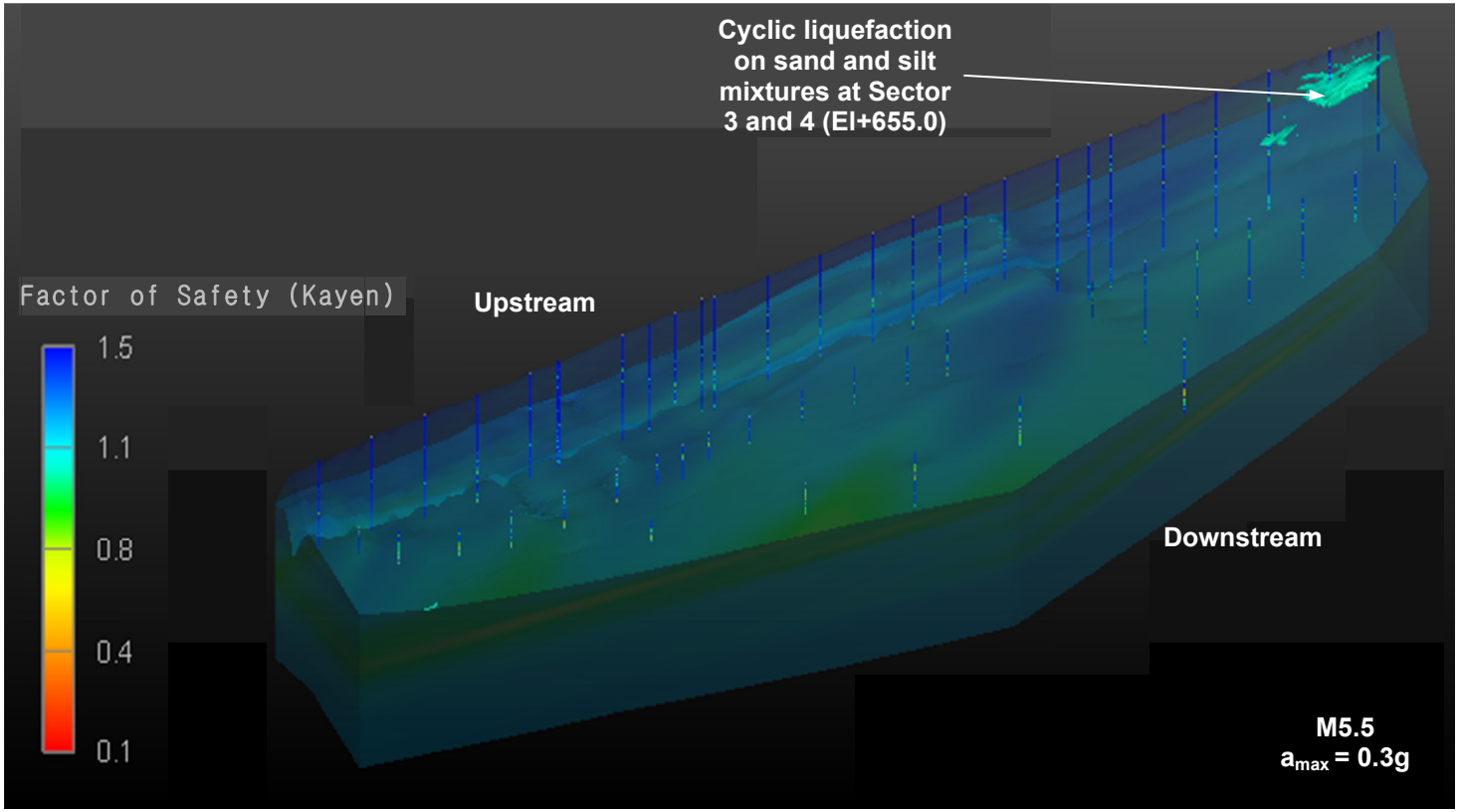

(c)

Figure 5-17 Visualization of LP using three methodologies at M5.5, 0.3g

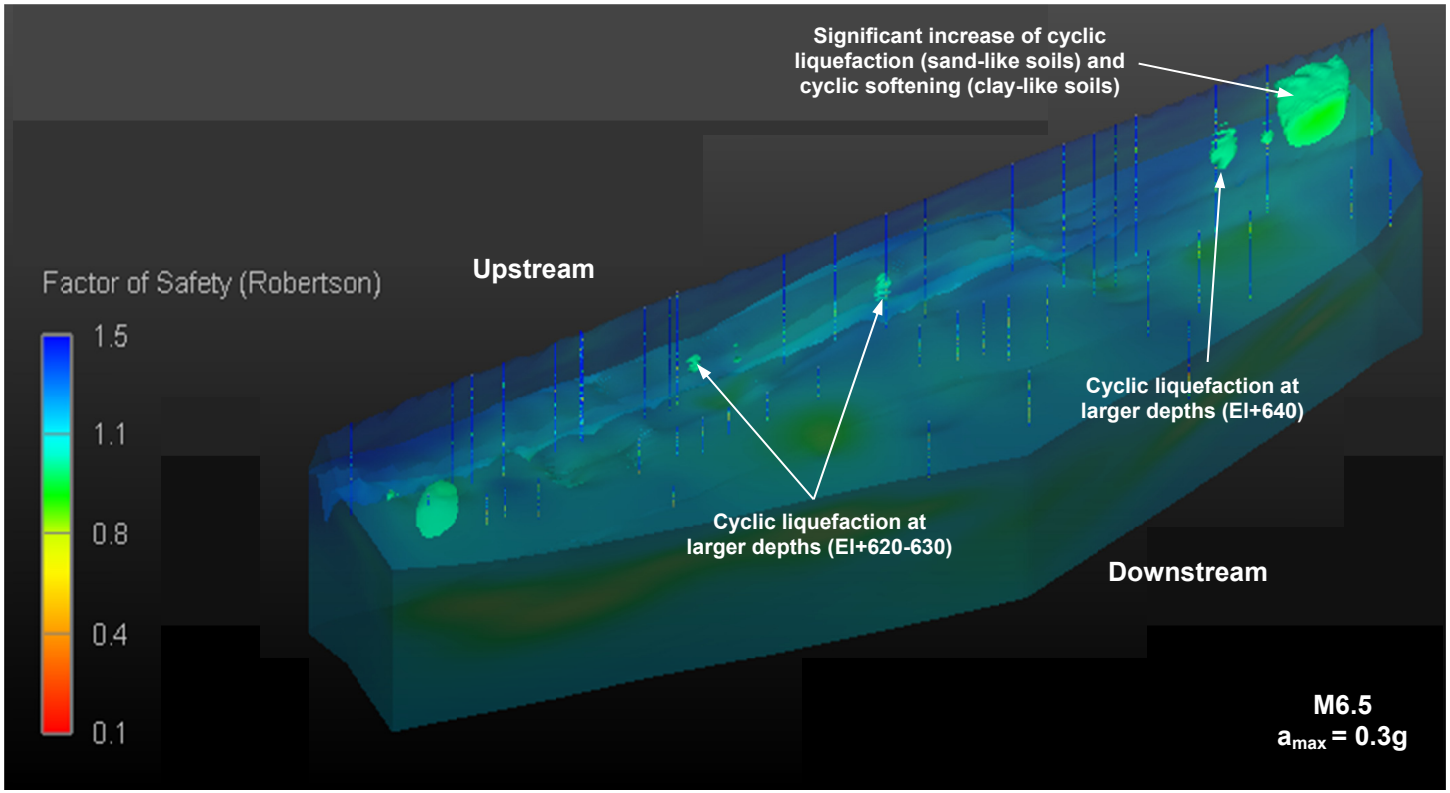
Significant increase of cyclic liquefaction (sand-like soils) and cyclic softening (clay-like soils)
Factor of Safety (Robertson)
1.5
1.1
0.8
0.4
0.1
Upstream
Cyclic liquefaction at larger depths (El+640)
Cyclic liquefaction at larger depths (El+620-630)
Downstream
M6.5
a_{max} = 0.3g

(a)

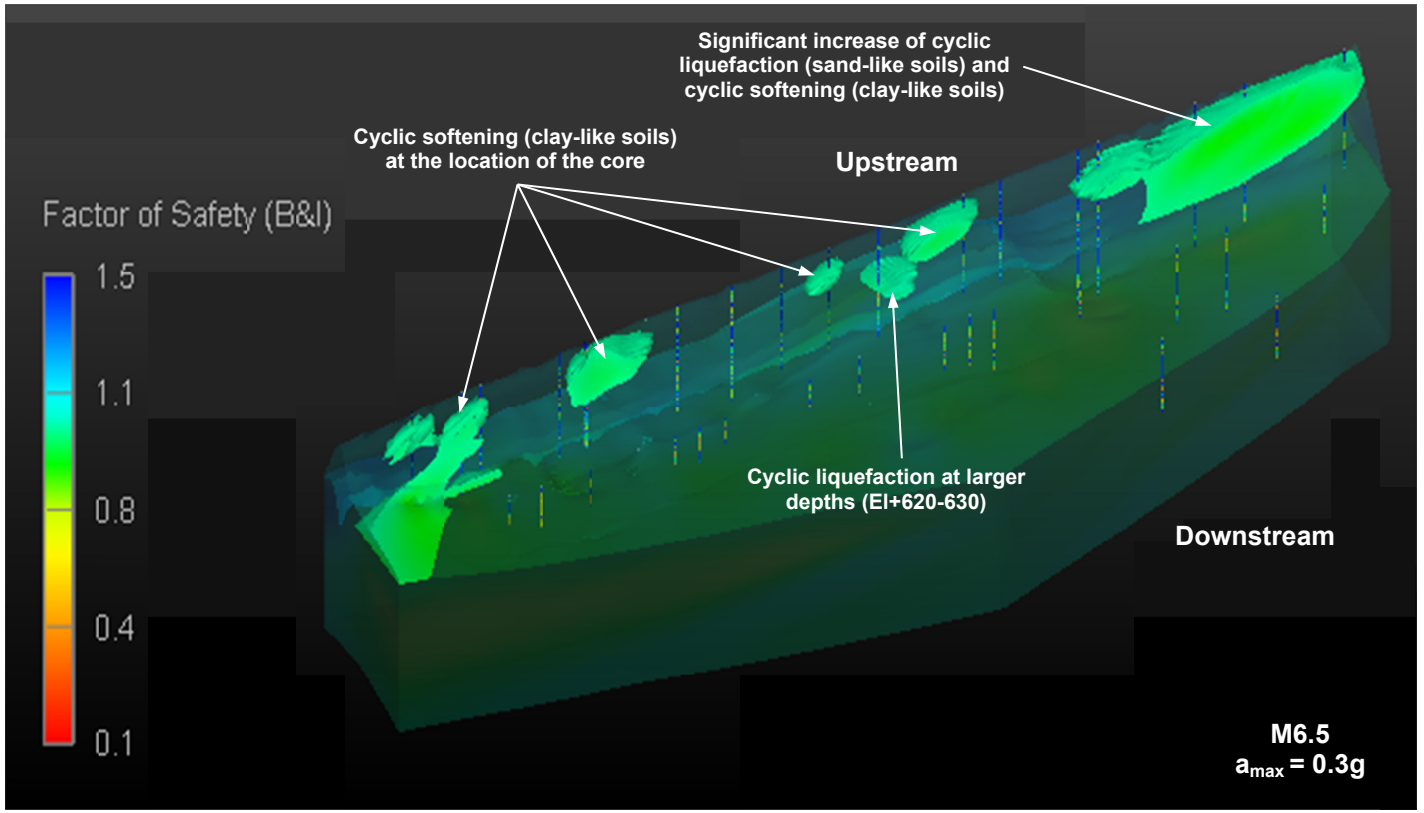
Significant increase of cyclic liquefaction (sand-like soils) and cyclic softening (clay-like soils)
Cyclic softening (clay-like soils) at the location of the core
Upstream
Factor of Safety (B&I)
1.5
1.1
0.8
0.4
0.1
Cyclic liquefaction at larger depths (El+620-630)
Downstream
M6.5
a_{max} = 0.3g

(b)

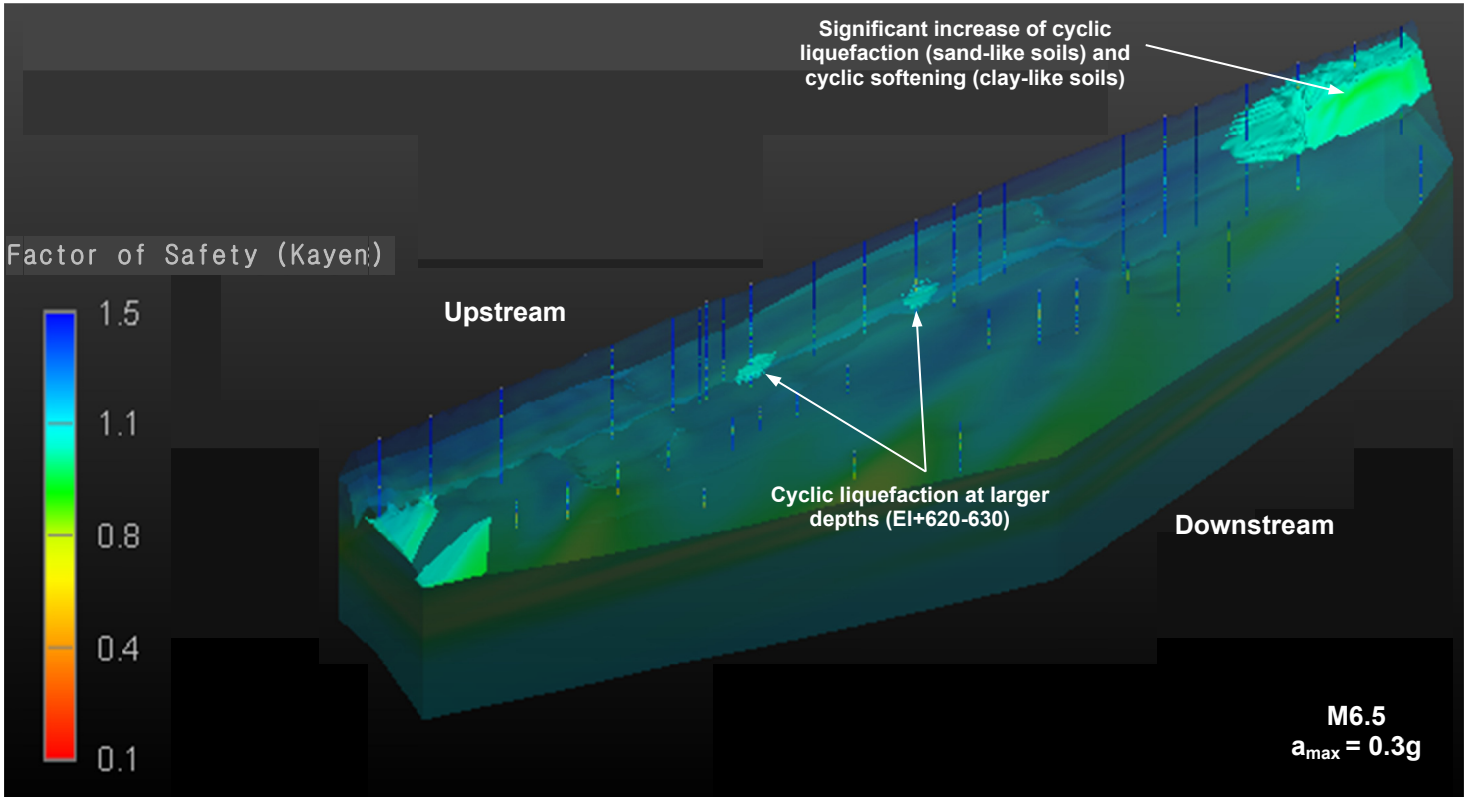

(c)

Figure 5-18 Visualization of LP using three methodologies at M6.5, 0.3g

5.7 Summary of Liquefaction Evaluation

A series of visualization models were developed to estimate the liquefaction potential at the Eagle Mountain dam. Three different liquefaction evaluation procedures were used in the analysis: Robertson (2009), Boulanger and Idriss (2014) and Kayen et al. (2013. Seismic activity in North Texas depicts relatively low magnitude earthquakes (M<4); however, since the rate of earthquakes is non-stationary and the main cause of seismicity has not been identified, earthquakes of larger magnitudes may also occur.

A series of different scenarios are presented based on ground motion expected and the conditions of soils within the dam (i.e., saturated or non-saturated). Initially, visualization models are generated based a real case scenario (~M4.0, 0.3g and Lake level +649.0). Several hypothetical scenarios are also considered and presented to account for the effect of increase in accelerations, earthquake magnitudes and lake levels. Some of these are hypothetical and are based on much larger influence areas around the dam. The estimation of CSR is primarily based on the simplified procedure presented by Seed (1971); however each liquefaction evaluation procedure presents a different set of correction factors such as the MSF and $K\sigma$.

Based on the comparisons of the three methodologies, Boulanger and Idriss (2014) approach seemed to be the most conservative method for evaluating liquefaction among all three methods. This approach depicts lower factors of safety and the probability to identify more spots susceptible to cyclic earthquake loading is higher as compared to the other two approaches. Shear wave velocity based liquefaction approach did not depict good quality visualization results for two main reasons: the first is that the approach developed by Kayen et al. (2013) is primarily used when direct measurements of shear wave velocity are available. In the present study, only four SCPTu were performed which were not sufficient to interpolate shear wave velocity values for the

entire dam. In an attempt to generate liquefaction visualization models, shear wave velocities were estimated using CPT raw data (i.e., fs) at other locations. However, the inherent variability in the correlation increases the uncertainty in the value of factor of safety and hence produces low quality results.

The second reason is that the approach does not consider the evaluation of liquefaction at transition zones as compared to the other two methodologies which recognize transition zones as valuable data for interpolation. The effect of transition zone in the three methodologies (green dotted lines in Figure 5-19) can be illustrated by the comparison of CSR estimation using the three methodologies. For the sake of comparison, CSR up to 50 ft. depth is only shown in Figure 5-19.

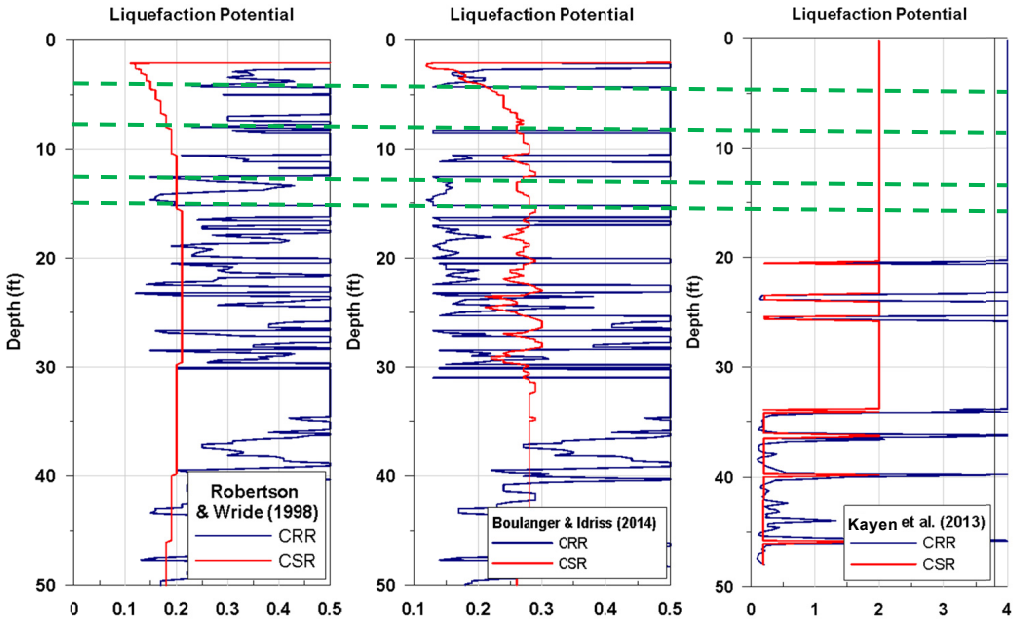

Figure 5-19 Comparison of liquefaction potential at 50 ft. depth (Station DCC10.50)

It may be noted that the shear wave velocity based approach has provided several restrictions in the generation of visualization models, yet is still included in the estimation of probability of liquefaction occurring in the present scenarios. It is important to clarify that probability of liquefaction potential from all three approaches was estimated

by considering all scenarios. Based on the analysis, the probability of liquefaction is close to 15%. In other words, results presented herein represent a probability of 15% for liquefaction to occur within the dam. The 15% probability has been assumed by several authors as a conservative factor for the computation of CSR (Robertson and Wride 1998; Idriss and Boulanger 2008, Kayen et al. 2013; Young et al. 2001).

Several insights can be gained based on the generation of liquefaction potential models at the Eagle Mountain Dam which are described in Table 5-1. Cyclic liquefaction mostly occurs where hydraulic fill is located. A comprehensive evaluation of visualization models is developed to identify critical sections that may be unstable due to liquefaction phenomena. Slope stability analysis is also performed on critical zones as described in the following sections. The present work includes a series of interactive figures shown in Appendix C, where users can fully visualize through some of the three-dimensional models of liquefaction potential.

Table 5-1 Sumarry of Liquefaction Potential Results at EM dam

DESCRIPTION		LAKE LEVEL EL (FT.)	PGA (g)	APPROACH	EARTHQUAKE MAGNITUDE, M			
					4	4.5	5.5	6.5
Hypothetical Scenarios	ACTUAL FIELD CONDITIONS	+649.0	0.3	Robertson (2009) / Boulanger & Idriss (2014) / Kayen et al. (2013)	No liquefaction	-	-	-
	SCENARIO I	+649.0	0.3	Robertson (2009)	-	No liquefaction	No liquefaction	Small amount of liquefaction of soils at ~El+630 ft. and below at Sector 3 and 4
	SCENARIO II	+649.0	0.4		-	No liquefaction	Few layers exhibit cyclic softening at Sector 3 (El+620)	Liquefaction is extended. Both, cyclic softening and liquefaction mostly in Sector 3
	SCENARIO III	+649.0	0.5		-	No liquefaction	Both, cyclic softening and liquefaction mostly in Sector 3 at depths of 55 to 75 ft. below the crest	Cyclic liquefaction and cyclic softening increases significantly in Sector 2 3 and 4
	SCENARIO IV	+665.0	0.3	Robertson (2009)	-	No liquefaction	Initiation of cyclic liquefaction in Sector 3 and 4 at depths of ~20 ft. and few layers at 50 ft. below the crest	Liquefaction potential extends at Sector 3 and 4. Cyclic liquefaction is exhibit at larger depths (El+620-640)
				Boulanger & Idriss (2014)	-	Initiation of liquefaction in few spots Sector 3 and 4 at depths of ~25 ft.	Cyclic liquefaction tends to increase in Sector 3 and 4 in inner soils. Cyclic softening is also exhibited in few seams within the core	Liquefaction potential extends significantly in Sector 3 and 4. Surface soil layers are liquefied. Cyclic softening is susceptible in clayey soil in the core in Sector 1 to 3.
				Kayen et al. (2013)	-	No liquefaction	Cyclic liquefaction increases in Sector 3 and 4. However, the increase is not significant as other two methods.	Liquefaction potential extends towards the surface at Sector 4. Cyclic liquefaction is exhibited at larger depths in Sector 3 (El+620-630)

5.8 Slope Stability Analysis

The main objective of this section is to study the effect of liquefiable soil zones on slope stability of the dam. Since, for actual site conditions, there were no liquefiable zones observed from the three approaches presented in section 5.4, the slope stability analysis is performed for the worst case hypothetical scenario. In order to perform this analysis, two main research tasks have been formulated: Identification of critical sections based on liquefaction analysis and slope stability analysis for worst case scenario (this is based on liquefaction analysis). The details of the analysis and results are provided in the sections below.

5.8.1 Identification and characterization of Critical Sections

This section presents the identification of critical sections based on the worst case scenario (scenario 4). In an attempt to perform the slope stability analysis for the EM dam, worst case conditions are considered and hence critical sections susceptible to liquefaction can be obtained from the body of the dam. From the evaluation of soil properties to the assessment of liquefaction, several insights can be gained to identify critical zones.

1. The absence of clayey soil in the core at Section 3 and 4 depicted from SBT and I_c visualization models was probably the path for seepage to occur in the EM dam. The presence of sands or silts in this region can be affected after strong seismic events (M>5.5). This is corroborated by the visualization models of soil properties. Also, since the elastic modulus is low due to sands and silts in Sectors 3 and 4, larger deformations may occur once liquefaction is triggered.
2. Liquefaction evaluation from Scenario IV depicts that cyclic liquefaction primarily occurs in soils located at depth of 10-15 ft. in Sectors 3 and 4 under an earthquake of M>5.0 at a_{max}=0.3g. The increase in peak ground acceleration,

PGA increases the amount of liquefiable soil layers but it does not result in cyclic liquefaction at magnitudes M<5.0. Based on the considerations, two sections are obtained from visualization models to address the stability of the dam by performing slope stability analysis.

3. Figure 5-20 illustrates two critical sections obtained from evaluating visualization models using three different CPT-based triggering approaches. These sections are located at Sector 3 and 4 and shows that initiation of liquefaction (FOS<1) is triggered under an approximate earthquake magnitude of M5.0 and a_{max}=0.3g. Critical sections identified are characterized for slope stability analysis based on the visualization models of different soil properties. Figure 5-21 illustrates the material type based on the SBT interpretation results. Foundations soils are mainly characterized as dense and compacted sands. However, the dam body includes several regions of sands and silts. Since soils within the dam are mainly characterized as sands, the strength for slope stability analyses must be provided by regionalizing visualization models of the effective drained friction angle shown in Figure 5-22.

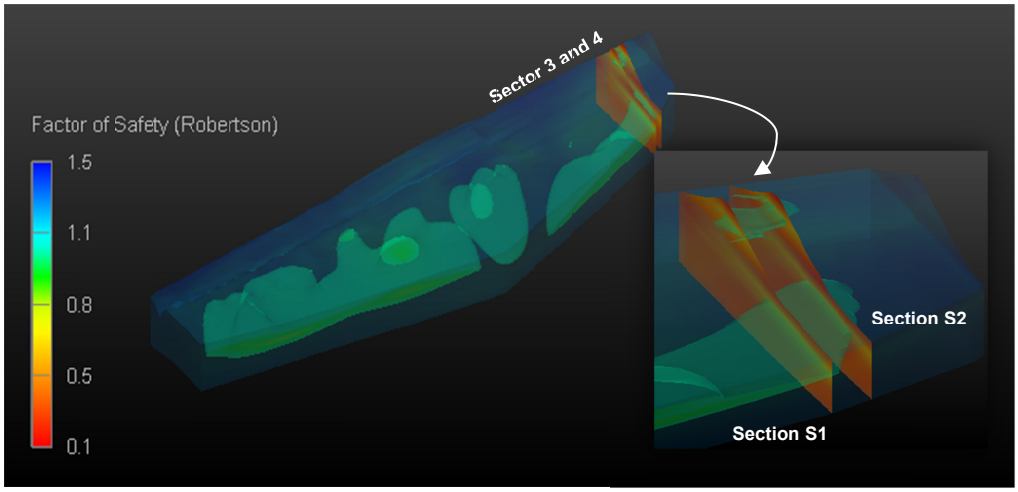

Figure 5-20 Critical sections susceptible for cyclic liquefaction, S1 and S2

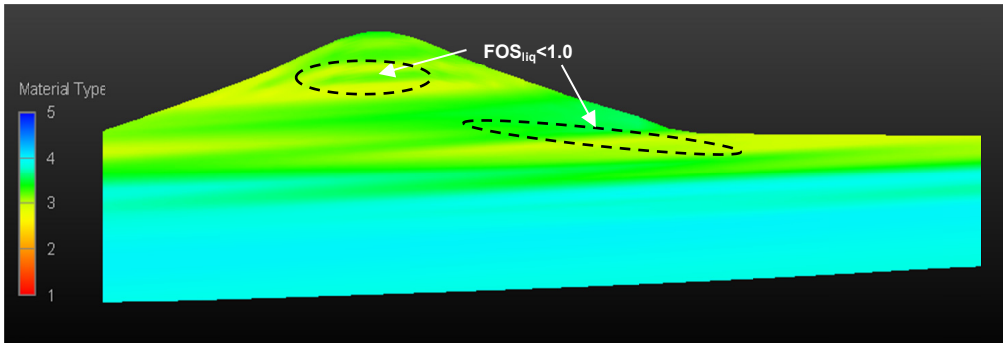

(a)

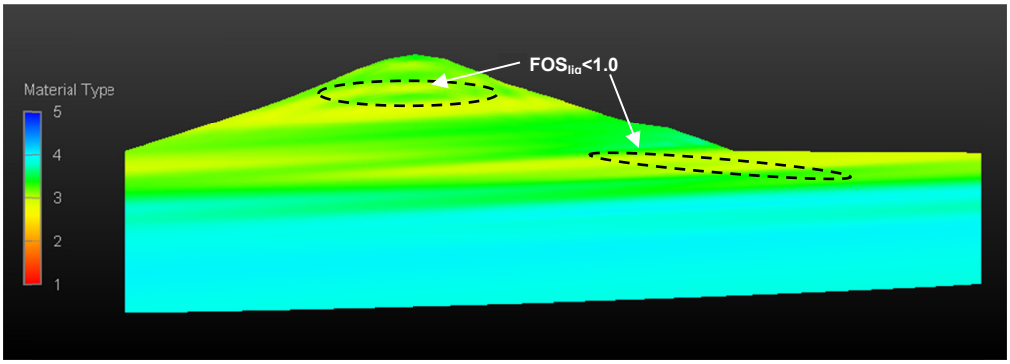

(b)

Figure 5-21 Material type based on SBT (Robertson 1998) at Sections (a) S1 and (b) S2

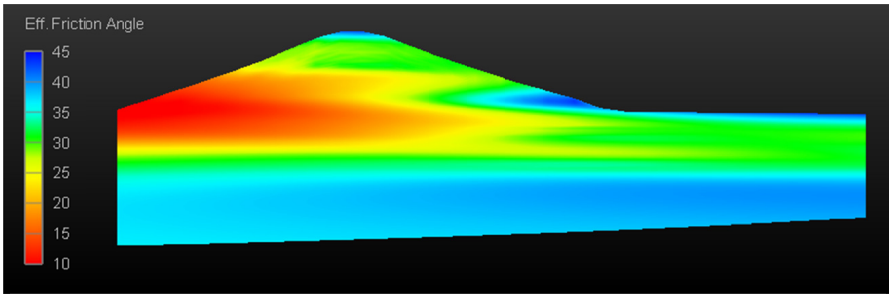

(a)

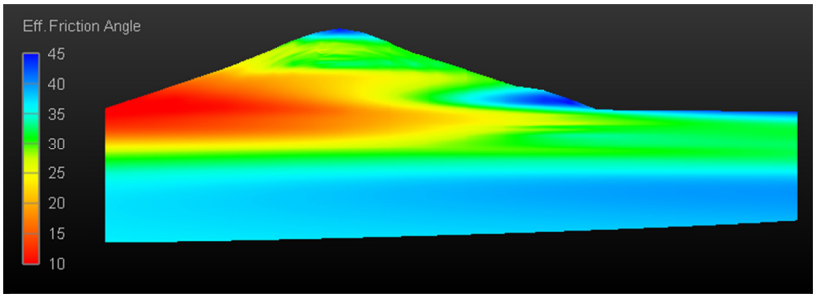

(b)

Figure 5-22 Effective drained shear strength at Sections (a) S1 and (b) S2

Figure 5-22 provides a reasonable visualization model of the effective drained friction angle (ϕ') at Sections S1 and S2 from where simplified regions can be addressed for slope stability modeling. Section S1 and S2 depicts a type of the soil to be in the group of sands and silts. If SBT visualization model shows the presence of significant amount of clay material, the undrained shear strength (S_u) visualization model will provide a more accurate estimation of regions for slope stability modeling.

5.8.2 Two-Dimensional Slope Stability and Deformation Analysis

Previous section identified Sectors 3 and 4 as critical and two cross-sections at these locations are used for the slope stability analysis. The slope stability model is based on the generation of regions using visualization results of effective drained friction angle (ϕ') as discussed in the previous section. Figure 5-23 shows the interpretation and

generation of regions for Section S1 based on visualization results, as well as the slope stability modeling for the analysis. The level of the reservoir is assumed to be at Elevation El+665 to have a conservative analysis. The maximum level of the reservoir reported until 2015 is at El+649 (USGS). Phreatic level is assumed based on the consideration that a core wall is constructed right at the centerline of the dam beneath the crest.

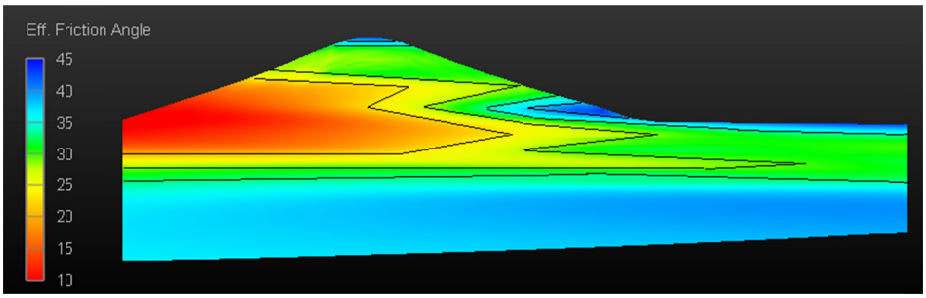

(a)

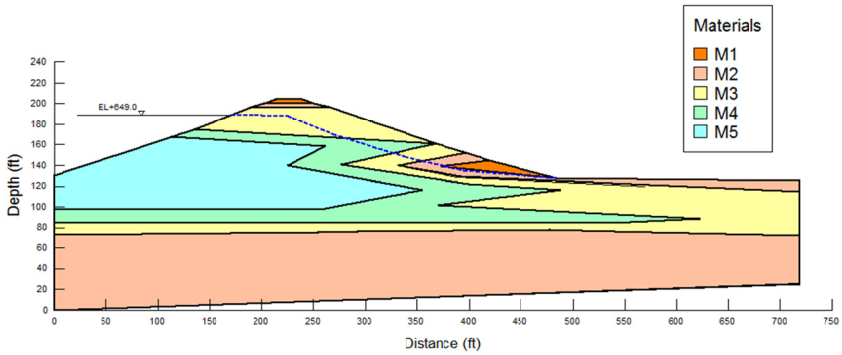

(b)

Figure 5-23 Regions for slope stability modeling based on visualization results of ϕ' at Section S1 (a) Visualization results and, (b) 2D slope stability modeling

Liquefaction potential can be incorporated in the slope stability modeling by using the visualization results obtained in the previous chapter as shown in Figure 5-24. Cyclic evaluation is performed up to the elevation El+625.00 since the cyclic stress approach is performed for gently slope or level ground surfaces (i.e., slope< 5 degrees). Additionally,

liquefaction zones obtained from the interpolation are also used for the slope stability analysis. Similar process was employed for slope stability modeling at Section S2. Slope stability was performed in two stages: before liquefaction is triggered (static condition), and after liquefaction was triggered (i.e., undrained conditions). Phreatic level remains the same in both stages. Slope stability analysis results are presented in Figure 5-25 and Figure 5-26 for both Sections S1 and S2 respectively. Results are summarized in Table 5-2.

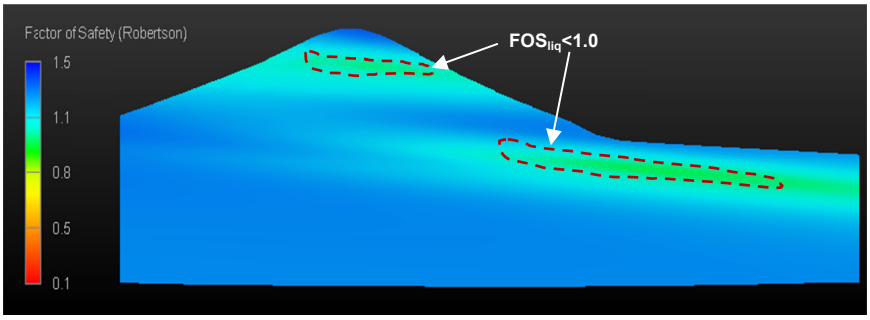

(a)

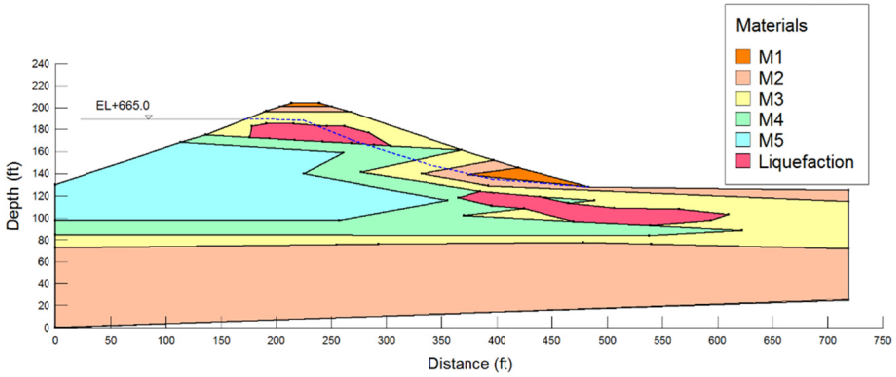

(b)

Figure 5-24 Liquefaction potential region included in slope stability modeling for Section S1 (a) Visualization results and, (b) 2D slope stability modeling

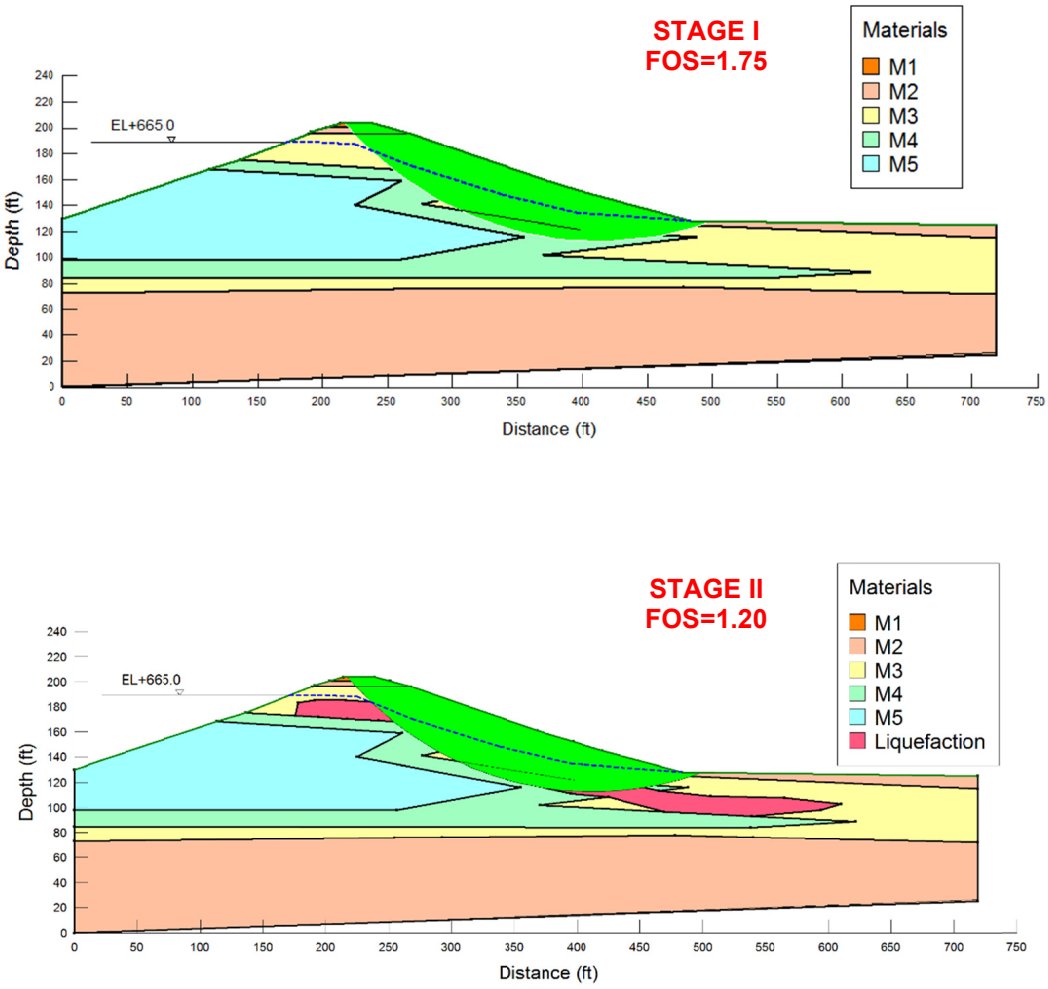

Figure 5-25 Slope Stability Analysis for Section S1 at Eagle Mountain Dam

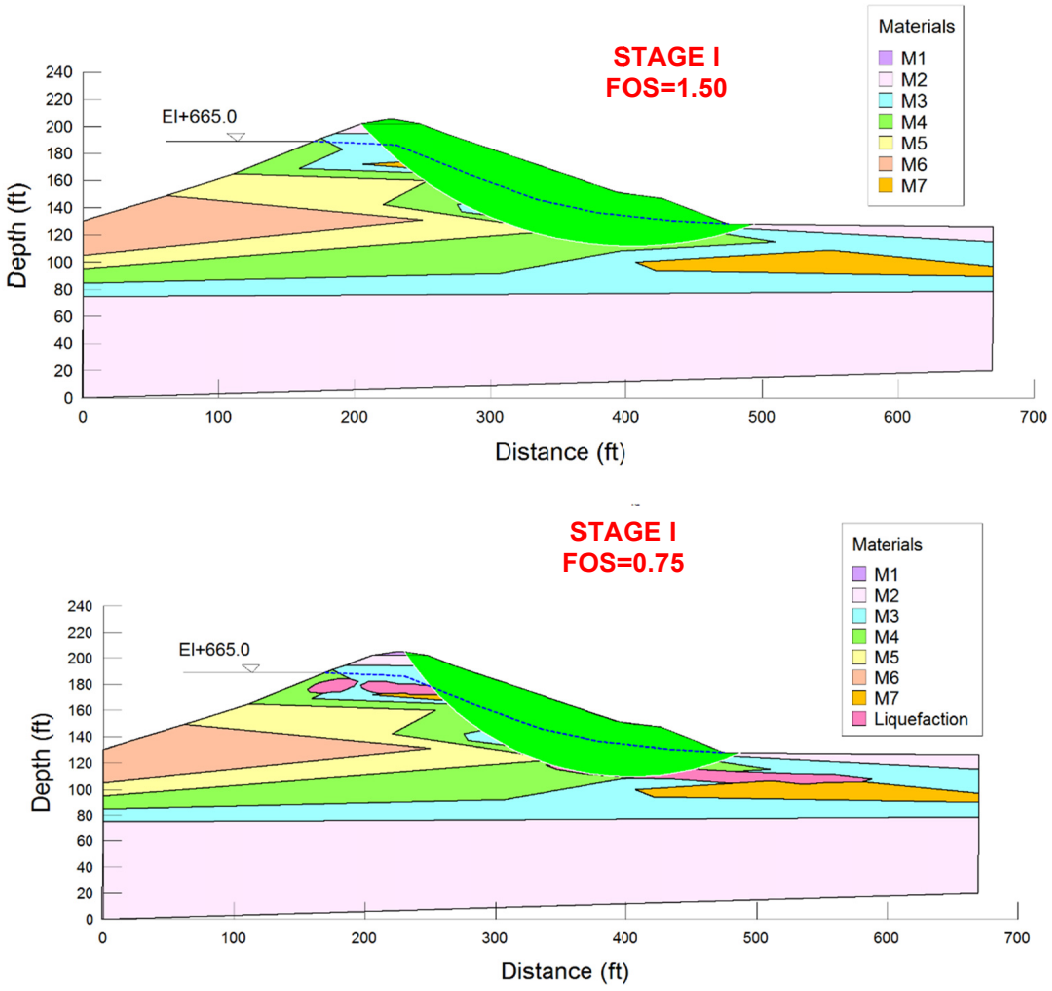

Figure 5-26 Slope Stability Analysis for Section S2 at Eagle Mountain Dam

Table 5-2 Sumarry of Slope Stability Analysis

Section	Factor of Safety	
	Stage I	Stage II
S1	1.75	1.20
S2	1.50	0.75

Slope stability analysis of two critical sections at the Eagle Mountain dam is presented in this section. The visualization model of liquefaction potential is used to

create a regionalized material which includes steady state strength parameters due to the strength loss developed after liquefaction. Slope stability analysis is based on the calculation of liquefaction under an earthquake magnitude M5.0-M5.5 with a maximum acceleration of 0.3g at the surface. Factor of safety for slope stability reduces after liquefaction is triggered in zones where high amount of hydraulic fill material was identified in Chapter 4. Liquefaction mostly occurs in areas where the shell is formed by hydraulic fill material. However, the present study is based on conservative assumptions such as the level of the lake at the time of liquefaction occurs (El+665) and the likely occurrence of an earthquake magnitude M5.0-M5.5 with a 0.3g. It is only presented to illustrate and highlight the importance of modern visualization in geotechnical engineering.

The intent of this analysis is not to evaluate the real stability of the Eagle Mountain dam; however it provides a comprehensive and modern visualization framework that can be applied to any geotechnical project. The incorporation of spatial variability in soils using Geostatistics aims to generate three-dimensional visualization models of soil properties and liquefaction potential using in-situ test data (i.e., CPT). Models can be further used to find critical locations within the dam to further perform slope stability analysis combined with the flow liquefaction analysis (i.e., loss of strength).

5.9 Summary

This chapter provides a comprehensive summary of liquefaction analysis of EM dam using both realistic and hypothetical conditions of the EQ events in the EM zones. Liquefaction assessments based on three models are presented in a visualization format. These data are further screened and evaluated for slope stability assessments and studies.

Chapter 6 Summary, Conclusions and Recommendations

6.1 Summary and Conclusions

This dissertation focuses on a comprehensive analysis of cyclic liquefaction assessment of a major dam in North Texas by first using kriging and visualization analysis for determining soil layer configuration followed by liquefaction analysis of the in situ cone testing data with probabilistic seismic hazard assessments. The Eagle Mountain dam, a hydraulic fill dam located in Fort Worth Texas, was the focus of this dissertation research and was fully analyzed in this work.

Three-dimensional visualization models were generated based on Geostatistics and kriging analyses of SCPTu results and this was followed by comprehensive cyclic liquefaction assessment. Based on these studies performed, the following conclusions are drawn:

1. In the development of a simplified seismic hazard analysis, a new methodology is proposed for the identification and characterization of seismic sources at North Texas. The method consisted of generating volumetric sources or prisms where the spatial occurrences are approximately uniformly distributed. The distribution of source-to-site distances (R) in each source was evaluated and checked for normality using the Chi-Square test. Three seismic sources capable of producing significant ground motion were identified and characterized for the seismic hazard. These three sources at North of Texas include events at Azle, TX; Irving, TX and Venus TX, respectively. Results of the deterministic seismic hazard analysis (DSHA) depicted very low values of PGA (0.02g) resulting from an earthquake of M3.6 located at Source 1 (Azle, TX) at a distance of 4.2 miles from the site.

2. North Texas seismicity presents a high uncertainty in the seismic activity and hence, a probabilistic seismic hazard analysis (PSHA) is more appropriate and hence PSHA steps were performed to determine seismic parameters for liquefaction analysis. A finite period of 1 year is used for the calculation of PSHA since the rate of earthquakes is non-stationary and it can change year to year. PSHA results depicted a hazard of 0.27g with 1% probability to be exceeded in one-year. Results are validated with the recently released USGS Hazard maps for the central United States (USGS 2016) which shows 0.25 to 0.28g with 1% probability to be exceeded in one-year for the area of North Texas. The proposed methodology to generate volumetric seismic sources has been shown to be successful to be used in areas where seismic activity has increased and there is no additional information about faults. The seismic hazard of 0.3g (an average value obtained from present seismic hazard analysis and USGS recent hazard map) was hence used for the computation of liquefaction potential at Eagle Mountain Dam.
3. A comprehensive characterization of soils at the Eagle Mountain Dam was performed by incorporating the spatial variability of soil properties using Geostatistics. A high variability in soil properties was found in the EM dam. It was evaluated by using construction drawings collected from 1930s and comparing the configuration of layers with the distribution of normalized tip resistance at same range of depths. Ordinary Kriging was used for the interpolation of data by constructing variograms that considered spatial variability and a fully three-dimensional analysis of anisotropy. An enhanced visualization was developed for soil behavior type, soil behavior type index, effective drained friction, undrained shear strength and elastic moduli. Visualization models

developed provided insights about of the construction methodology adopted in 1930s at Eagle Mountain Lake site. Four construction stages or sectors were identified in visualization models that are validated based on construction drawings information. Sector 3 and 4 were identified as critical sectors since it contains high amount of sands and silts at depths where the core is located.

4. Three-dimensional visualization models of the Eagle Mountain dam are also developed for the cyclic liquefaction patterns at the Eagle Mountain dam. Models feature the cyclic liquefaction potential of the dam as a function of factors of safety obtained from analyses based on Robertson (2009), Boulanger & Idriss (2014) and Kayen et al. (2013) approaches by using the cyclic stress approach. Cyclic stress approach is valid for level ground surfaces (El+625), however by the interpolation performed, cyclic liquefaction potential can be identified in zones within the body of the dam at higher magnitudes and higher accelerations. This assumption must be validated with the strength loss potential obtained from flow liquefaction analysis which is not covered in the present research. The interpolation for modeling used “factors of safety” obtained from the 15% probability of liquefaction occurrence considered in all three methodologies. The liquefaction evaluation was performed for three cases: the first, a realistic case when water level at the time of earthquake is as in field conditions under and earthquake of magnitude M4.0 (~max. earthquake expected in North Texas) which produces a ground motion of 0.3g (PSHA); the second and third cases are hypothetical scenarios, when water level at the time of earthquake is similar to in field dam conditions and the dam is subjected to hypothetical earthquakes of magnitude M4.5, M5.5 and M6,5 that produced ground motions of 0.3g, 0.4g and 0.5g. A worst case scenario was when water in the dam level at the time of

earthquake is ~10 ft. below the crest of the dam (soils are saturated) and the dam is subjected to an earthquake loading event of a_{max} =0.3g. Visualization results showed that liquefaction is not triggered in the first case scenario using three methodologies. For the second case scenario, there is no sign of liquefaction in soil layers up to a=0.3g at none of the earthquake magnitudes; however for a=0.4g and a=0.5g some liquefaction of layers is triggered at high earthquake magnitudes (M5.5-M6.0). For the worst case scenario, liquefaction is triggered for a=0.3g at magnitudes of M5-M5.5. It can be concluded overall that by including current spatial variability of soil properties, the EM dam is stable against earthquakes including those of a_{max}=0.3g under actual field conditions (first scenario).

5. In an attempt to highlight the importance of this visualization framework, third case scenario was used as a particular severe case study. From this scenario, visualization models show that Sectors 3 and 4 are critical. Two cross-sections depicting locations where the major parts of liquefaction zones were found (FOS_{liq}=1.0) are later used for performing slope stability analyses to study the effects of internally liquefied soil layers on global slope stability of the dam.
6. Regionalized sections were generated for slope stability modeling and the assignment of strength properties were based on three-dimensional visualization models. Two-dimensional slope stability analysis was performed using the limit equilibrium analysis approach in three different scenarios: under static loading (before liquefaction), right after liquefaction is triggered and a post liquefaction scenario. A region of liquefiable soil is assigned in the modeling with steady state strength values (i.e., approximately 10-20% of the maximum strength of soil) for the third case scenario. A significant decrease in the factor of safety is detected

after liquefaction occurs. Again, it may be noted that this is a worst case scenario condition where water table rises close to the crest of the dam, a condition that is not expected to occur in field operations.

7. Geostatistics was effectively used for the generation of an enhanced three-dimensional visualization of subsurface and soil configuration for the EM dam. It addressed the spatial variability, probabilistic distribution and the geostatistical anisotropy of the grid for the generation of the variogram. Kriging was comprehensively used along with the variogram models to effectively deal with high variability of soils presented in the hydraulic fill dam. The prediction of liquefaction was effectively addressed by using in-situ based approaches and by generating models to visualize its potential in terms of factors of safety at different scenarios. The above geostatistical framework as well as the seismic hazard analysis developed can be used for addressing geotechnical hazards of dams and levee structures at similar locations in North Texas.

6.2 Limitation of the Seismic Hazard Analysis Framework

The seismic hazard analysis is simplified by the generation of volumetric seismic sources which are used for the computation of DSHA and PSHA. However, the methodology for developing those seismic sources is based on a catalog of earthquakes obtained until November 2015. More recent seismic events (after November 2015) are not considered in the generation of volumetric seismic sources. Also, since the rate of earthquakes is considered as non-stationary seismic hazards curves (PSHA) are generated for a probability within a short period of time (one-year) as compared with other seismic hazards maps calculated with a probability of 50 years (i.e., California and New Madrid area). Therefore, the seismic hazard may increase if the rate of earthquakes

increases over the next years. The present simplified seismic hazard analysis can be used to address the seismic hazard at similar sites in North Texas only.

6.3 Recommendations for Future Research

Several recommendations can be made based on the framework developed:

1. The three-dimensional visualization information of soil properties in the EM Dam can be successfully incorporated to the evaluation other important geotechnical hazards (i.e., slope stability, lateral spreading, and seepage). The estimated liquefaction potential shown in visualization models is referred to a volume of liquefiable soils (FOS_{liq}=1.0).
2. Liquefaction Potential Index (LPI) can also be addressed based on this framework. It is recommended that visualization models can be generated based on the LPI interpolation using geostatistics for future research.
3. It is recommended to evaluate the strength loss potential of soils (flow liquefaction potential) by using the undrained shear strength ratio to verify the liquefaction potential locations at elevation higher than El+625.0 in this framework. Slope stability analysis can be evaluated by combining the cyclic liquefaction potential of layers at elevations lower than El+625.0 and the flow liquefaction potential evaluated by the strength loss of soils.
4. A 3D slope stability analysis can be developed by considering a comprehensive material characterization based on properties presented in the visualization models. The analysis can be performed by incorporating acceleration-time history or accelerograms to check the stability of the dam against earthquakes. A transient seepage analysis is also recommended to identify level at which soils are saturated within the dam.

5. A risk and reliability analysis of the EM dam can be developed by compiling the results from all geotechnical hazards expected at the site. Visualization models can be enhanced by incorporating image-based technology such as LiDAR and UAV.

Appendix A

Seismic Hazard Analysis - Catalog of Earthquakes

A1. Catalog of earthquakes within 60 km radius from Eagle Mountain Dam

(January, 2007 to October, 2015)

time	latitude	longitude	depth	M	M (type)	nst	gap	dmin	rms
2015-01-02T02:29:03.610Z	32.8438	-96.9034	2.25	2.4	mb_lg		64	0.567	0.45
2013-11-26T20:03:28.540Z	32.9594	-97.6176	2.27	2.8	mb_lg		57	0.974	0.99
2014-11-25T22:39:22.980Z	32.8404	-96.8922	2.58	2.7	mb_lg		64	0.552	0.88
2014-12-12T03:25:38.030Z	32.8501	-96.8902	3.02	2.7	mb_lg		64	0.568	0.63
2014-12-30T14:10:09.220Z	32.8372	-96.9132	3.09	2.7	mb_lg		64	0.535	0.57
2014-12-20T05:08:11.390Z	32.8304	-96.9188	3.18	2.4	mb_lg		78	0.554	0.48
2014-07-20T11:43:55.460Z	32.8386	-96.8669	3.23	2.2	mb_lg		75	0.588	0.81
2014-11-23T03:15:47.770Z	32.8346	-96.8932	3.96	3.3	mb_lg		34	0.552	0.46
2014-09-07T08:56:11.070Z	32.7397	-97.1132	4.12	2.4	mb_lg		41	0.438	0.53
2014-12-15T12:00:59.380Z	32.8412	-96.9009	4.16	2.7	mb_lg		64	0.566	0.52
2015-01-07T07:24:29.160Z	32.8473	-96.8896	4.27	2.3	mb_lg		77	0.57	0.27
2013-03-10T13:47:35.400Z	32.503	-97.499	4.3	2.7	mblg	20	62.3		0.53
2014-02-02T07:32:51.140Z	32.6451	-97.4354	4.99	2.4	mb_lg		97	0.232	0.62
2013-12-08T06:10:04.010Z	32.9144	-97.5817	4.99	3.6	mb_lg		88	0.926	0.53
2012-06-24T17:46:44.450Z	32.474	-97.289	5	3.5	mblg	61	46.3		1.04
2012-07-10T02:22:44.160Z	32.476	-97.266	5	2.4	mblg	9	82.2		1.18
2012-07-13T12:27:50.410Z	32.499	-97.323	5	2.7	mblg	13	84.1		0.78
2012-11-20T04:50:34.290Z	32.622	-97.157	5	2.3	mblg	11	79.9		1.02
2012-12-13T02:10:22.870Z	32.645	-97.32	5	2.6	mblg	12	76.3		0.68
2011-09-23T04:21:22.360Z	32.648	-97.135	5	2.4	mblg	12	90.4		1.25
2014-09-12T23:03:46.430Z	32.7335	-97.1299	5	2.5	mb_lg		69	0.43	0.68
2008-10-31T05:46:31.000Z	32.755	-97.017	5	2.5	mblg	4	169.9		1.08
2008-11-01T11:53:46.650Z	32.766	-97.035	5	2.5	mblg	4	169.3		1.02
2009-05-16T17:53:09.360Z	32.77	-97.117	5	2.7	mblg	7	110.6		1.43
2008-10-31T21:01:01.770Z	32.788	-97.028	5	2.9	mblg	5	132.4		0.8
2009-05-16T18:02:23.000Z	32.795	-97.016	5	2.6	mblg	5	108.5		
2008-10-31T06:23:44.120Z	32.799	-97.045	5	2.6	mblg	4	168.2		0.69
2008-10-31T04:25:52.290Z	32.8	-97.016	5	2.6	mblg	4	168.7		0.63
2012-09-30T04:09:02.720Z	32.815	-96.962	5	3.1	mblg	29	55		0.72
2014-09-11T08:21:58.780Z	32.8153	-96.9178	5	2.8	mb_lg		65	0.535	0.93
2015-01-12T01:46:06.570Z	32.8175	-96.8769	5	2.4	mb_lg		65	0.044	0.54
2014-11-10T09:04:05.600Z	32.8183	-96.8902	5	2.3	mb_lg		79	0.58	1.1
2013-11-01T21:57:23.680Z	32.8213	-97.2095	5	2.1	mb_lg		125	0.853	0.72
2015-09-20T23:25:08.930Z	32.8279	-96.9556	5	2.6	mb_lg		65	0.029	0.92
2015-09-12T12:16:16.840Z	32.8281	-96.933	5	2.2	mb_lg		65	0.01	0.95

CONTINUATION A1

2015-01-08T13:24:31.750Z	32.8282	-96.9008	5	2.3	mb_lg		96	0.066	0.34
2008-10-31T20:54:18.810Z	32.831	-97.028	5	2.9	mblg	4	167.6		1.32
2011-08-07T04:45:31.350Z	32.832	-97.037	5	2.6	mblg	18	56.5		0.63
2008-10-31T07:58:23.910Z	32.832	-97.012	5	2.9	mblg	4	167.9		0.56
2015-07-13T11:03:56.270Z	32.8351	-96.939	5	2.4	mb_lg		65	0.015	0.89
2014-12-02T15:36:21.880Z	32.836	-96.893	5	2.7	mb_lg				1.23
2008-10-31T05:01:54.910Z	32.836	-97.029	5	3	mblg	5	163.6		0.67
2015-08-25T20:18:31.760Z	32.8363	-96.9467	5	2.1	mb_lg		77	0.022	0.47
2015-03-08T03:12:22.340Z	32.8364	-96.9026	5	2.2	mb_lg		92	0.016	0.61
2015-01-07T14:34:02.760Z	32.8367	-96.9063	5	2.7	mb_lg		64	0.572	1.19
2015-08-31T08:15:37.160Z	32.8379	-96.9038	5	1.8	ml		77	0.011	0.77
2015-01-14T19:02:34.140Z	32.8396	-96.8998	5	1.9	mb_lg		92	0.056	0.5
2015-01-08T10:08:24.730Z	32.8408	-96.9143	5	2.1	mb_lg		96	0.05	0.52
2012-10-01T03:41:09.970Z	32.841	-96.93	5	2.3	mblg	11	91.4		1.13
2015-09-16T21:55:24.080Z	32.8411	-96.9448	5	2.1	ml		76	0.022	0.52
2015-01-07T06:59:03.320Z	32.8417	-96.9131	5	3.1	mb_lg		38	0.565	0.72
2012-09-30T04:05:00.930Z	32.842	-96.976	5	3.4	mblg	29	55		0.68
2015-09-12T09:34:20.660Z	32.8427	-96.9185	5	2.5	mb_lg		59	0.011	0.56
2014-10-28T07:15:01.840Z	32.8431	-96.9058	5	2.4	mb_lg		77	0.561	0.74
2014-11-24T13:06:36.030Z	32.846	-96.8955	5	2.4	mb_lg		77	0.569	0.15
2015-01-07T00:52:09.050Z	32.847	-96.8922	5	3.6	mb_lg		36	0.551	0.52
2014-11-25T05:47:54.460Z	32.8481	-96.9013	5	2.2	mb_lg		96	0.564	0.55
2014-11-15T19:19:46.410Z	32.8481	-96.9576	5	2.6	mb_lg		76	0.518	0.53
2015-01-07T02:12:16.390Z	32.8485	-96.9375	5	2.7	ml		130	0.513	0.2
2015-01-06T13:37:15.180Z	32.8487	-96.8883	5	2.3	mb_lg		77	0.57	0.33
2009-05-16T16:58:37.690Z	32.85	-97.095	5	3	mblg	6	100.7		1.18
2015-06-28T05:40:35.630Z	32.8505	-97.0002	5	2.1	mb_lg		75	0.034	0.52
2014-12-17T22:19:00.790Z	32.8507	-96.9193	5	2.6	mb_lg		76	0.548	0.41
2015-05-03T15:11:16.150Z	32.8511	-96.9514	5	3.2	mb_lg		64	0.024	0.56
2015-01-07T05:02:52.910Z	32.8512	-96.8844	5	1.6	ml		97	0.569	0.16
2015-01-18T02:00:04.200Z	32.852	-96.9378	5	2.2	ml		64	0.013	0.55
2015-07-16T00:17:49.460Z	32.8533	-96.9417	5	1.8	ml		65	0.017	0.57
2015-05-09T16:12:38.390Z	32.854	-96.8903	5	2.7	mb_lg		64	0.067	0.68
2015-04-02T10:38:06.000Z	32.8543	-96.9392	5	2.7	mb_lg		61	0.015	0.52
2015-08-25T20:59:47.930Z	32.8552	-96.9412	5	2.2	mb_lg		58	0.027	0.65
2015-05-03T16:12:04.480Z	32.8561	-96.891	5	2.5	mb_lg		76	0.009	0.7
2015-01-07T03:54:17.460Z	32.8564	-96.8819	5	1.7	ml		97	0.566	0.5
2015-03-14T07:31:16.290Z	32.8565	-96.9251	5	2.7	mb_lg		43	0.008	0.63

CONTINUATION A1

2015-10-27T13:01:07.430Z	32.8583	-96.9124	5	2.3	mb_lg		63	0.014	0.61
2015-01-07T04:05:14.350Z	32.8588	-96.9174	5	2.4	mb_lg		76	0.548	0.56
2015-11-03T02:37:41.520Z	32.86	-96.9426	5	2.2	mb_lg		59	0.033	0.45
2015-10-28T01:33:37.110Z	32.8606	-96.95	5	2.2	mb_lg		65	0.018	0.52
2015-05-04T13:57:59.870Z	32.8613	-96.8716	5	2.7	mb_lg		76	0.026	0.78
2015-04-03T03:04:49.640Z	32.8614	-96.9087	5	2.5	mb_lg		63	0.017	0.71
2014-12-10T04:44:48.610Z	32.8621	-96.9338	5	2	ml		75	0.534	0.5
2015-10-04T05:57:09.220Z	32.8633	-96.9174	5	2.1	ml		67	0.021	0.81
2014-04-17T19:44:20.040Z	32.8634	-96.9079	5	2.4	mb_lg		76	0.548	0.33
2015-10-19T23:12:03.180Z	32.8659	-96.9394	5	2.3	mb_lg		58	0.024	0.44
2015-05-18T18:14:29.920Z	32.8675	-96.9566	5	3.3	mb_lg		65	0.009	0.73
2015-10-18T00:17:36.710Z	32.8684	-96.8652	5	2.4	mb_lg		63	0.025	0.72
2008-10-31T05:33:45.620Z	32.871	-96.971	5	2.6	mblg	4	167.6		0.22
2015-06-27T10:19:02.930Z	32.8723	-96.907	5	2.3	mb_lg		60	0.024	0.82
2015-06-13T13:34:47.480Z	32.8726	-96.9038	5	2.3	mb_lg		78	0.024	0.93
2008-11-01T11:54:30.190Z	32.874	-96.968	5	2.7	mblg	4	167.6		0.61
2015-10-19T22:39:47.980Z	32.8755	-96.9134	5	2.7	mb_lg		57	0.029	0.61
2015-09-14T21:04:59.040Z	32.8785	-96.901	5	2	ml		86	0.029	0.59
2015-04-03T08:58:11.070Z	32.8826	-96.8772	5	2.2	mb_lg		169	0.047	0.28
2015-09-22T10:18:43.020Z	32.8838	-96.9187	5	2.4	mb_lg		49	0.013	0.4
2015-03-12T14:41:14.790Z	32.8839	-96.9075	5	2	ml		90	0.022	0.37
2013-11-09T03:34:07.100Z	32.8873	-97.618	5	2.3	mb_lg		58	0.903	1.18
2013-11-06T17:05:47.700Z	32.8884	-97.6784	5	2.6	mb_lg		105	0.914	0.83
2013-01-23T04:16:18.860Z	32.894	-97.004	5	3	mblg	12	74.3		0.74
2013-12-10T15:39:49.450Z	32.8951	-97.5437	5	2.7	mb_lg		99	0.904	0.85
2013-11-26T14:24:03.850Z	32.908	-97.5587	5	2.7	ml		112	0.918	0.52
2013-11-19T18:03:37.000Z	32.9086	-97.5903	5	2.8	mb_lg		59	0.921	0.78
2013-11-29T06:14:09.070Z	32.9093	-97.5205	5	3.1	mb_lg		39	0.917	1.29
2013-11-20T00:40:34.950Z	32.9116	-97.5509	5	3.6	mb_lg		30	0.921	0.71
2011-08-01T04:33:26.360Z	32.913	-96.929	5	2.2	mblg	5	147.1		1.4
2013-11-23T09:43:32.440Z	32.9152	-97.5983	5	2.9	mb_lg		88	0.929	0.63
2013-11-06T03:32:08.600Z	32.9194	-97.5175	5	2.6	mb_lg		62	0.926	0.58
2013-11-25T07:43:02.950Z	32.9195	-97.6182	5	3.4	mb_lg		43	0.935	0.63
2013-11-09T19:54:31.820Z	32.9197	-97.6665	5	3	mb_lg		38	0.942	0.91
2013-11-21T05:53:57.040Z	32.9232	-97.578	5	2.1	mb_lg		111	0.934	0.46
2013-12-03T15:44:32.210Z	32.9387	-97.5545	5	2.7	mb_lg		98	0.948	0.63
2014-01-13T17:40:21.580Z	32.9391	-97.5529	5	3.1	mb_lg		53	0.014	0.61
2013-11-19T17:57:18.940Z	32.9437	-97.5992	5	2.5	mb_lg		105	0.957	0.71

CONTINUATION A1

2014-01-28T17:54:44.300Z	32.9453	-97.5339	5	2.5	mb_lg		113	0.016	0.59
2013-11-26T01:55:21.460Z	32.9479	-97.5353	5	2.8	mb_lg		61	0.956	0.59
2013-12-17T20:09:04.870Z	32.9543	-97.5546	5	2.1	mb_lg		90	0.027	0.69
2013-11-08T04:32:56.870Z	32.9556	-97.6719	5	2.8	mb_lg		38	0.978	0.56
2013-11-13T09:01:33.890Z	32.9574	-97.5029	5	2.6	mb_lg		62	0.964	0.49
2013-12-09T09:23:14.340Z	32.9576	-98.0594	5	3.7	mb_lg		35	1.09	0.85
2013-12-22T17:31:54.990Z	32.9619	-97.5552	5	3.3	mb_lg		38	0.028	0.58
2013-11-28T07:58:35.690Z	32.9735	-98.0894	5	3.7	mb		35	1.116	1.33
2013-11-11T08:30:54.280Z	32.9923	-97.5436	5	2.8	mb_lg		41	1	0.8
2015-01-09T17:39:14.500Z	32.8418	-96.8936	5.03	2.4	mb_lg		64	0.057	0.49
2013-12-15T04:54:16.010Z	32.9379	-97.6196	5.05	2.9	mb_lg		57	0.954	0.9
2015-04-03T04:28:37.020Z	32.8678	-96.934	5.74	2.3	mb_lg		59	0.021	0.49
2015-01-06T21:10:31.550Z	32.835	-96.9027	5.93	3.5	mb_lg		38	0.547	0.19
2014-01-11T20:55:25.250Z	32.9125	-97.4787	6.24	2.2	mb_lg		133	0.054	0.36
2013-12-23T13:11:34.040Z	32.9284	-97.5789	6.39	3.3	mb_lg		42	0.013	0.44
2014-10-01T21:32:18.700Z	32.8499	-96.9824	6.56	2.1	mb_lg		93	0.497	0.45
2015-01-07T15:57:30.110Z	32.8464	-96.9171	7.24	2.7	mb_lg		64	0.533	0.36
2015-04-02T22:36:21.040Z	32.8588	-96.9356	7.67	3.3	mb_lg		56	0.015	0.49
2015-02-27T12:18:21.710Z	32.8336	-96.9098	7.93	3.1	mb_lg		47	0.009	0.55
2014-11-23T21:40:46.520Z	32.8449	-96.9343	8.01	2.5	mb_lg		56	0.537	0.5
2014-12-19T16:38:30.010Z	32.8245	-96.9317	8.13	2.4	mb_lg		78	0.545	1.26
2015-03-12T01:55:02.270Z	32.8775	-96.9129	8.17	2.4	mb_lg		56	0.02	0.22
2015-01-07T02:11:17.810Z	32.8085	-96.8962	8.24	2.9	mb_lg		65	0.554	0.55
2015-01-20T20:50:02.540Z	32.8526	-96.9265	8.32	2.5	mb_lg		56	0.005	0.43
2015-10-29T22:24:39.420Z	32.8439	-96.9121	8.48	2.5	mb_lg		77	0.014	0.4
2009-05-16T16:24:06.570Z	32.795	-97.016	8.7	3.3	mblg	19	66.5		0.84
2015-01-23T15:16:01.500Z	32.8904	-96.8967	8.74	2.2	mb_lg		66	0.03	0.43
2015-01-20T19:37:04.150Z	32.8615	-96.9093	8.77	2.6	mb_lg		63	0.031	0.44
2015-01-20T20:25:49.390Z	32.8221	-96.9055	9.04	3	mb_lg		65	0.015	06
2015-08-12T11:13:28.340Z	32.8465	-96.9122	9.78	2.7	mb_lg		64	0.008	0.3
2015-01-20T14:04:03.170Z	32.8492	-96.9152	9.83	2.3	mb_lg		64	0.006	0.17
2015-01-20T20:43:17.470Z	32.8536	-96.9029	10.4	2.4	mb_lg		76	0.027	0.16
2015-07-18T15:30:09.260Z	32.8484	-96.9172	10.69	2.6	mb_lg		59	0.004	0.15
2015-10-01T21:28:25.800Z	32.8343	-96.8929	12.14	2.7	mb_lg		78	0.015	0.59

Appendix B

Boring Log Information for Validation

B.1 Soil Consolidated-Undrained Triaxial Strength (TRWD Records)

Station DBC-16.06 – Sector 3

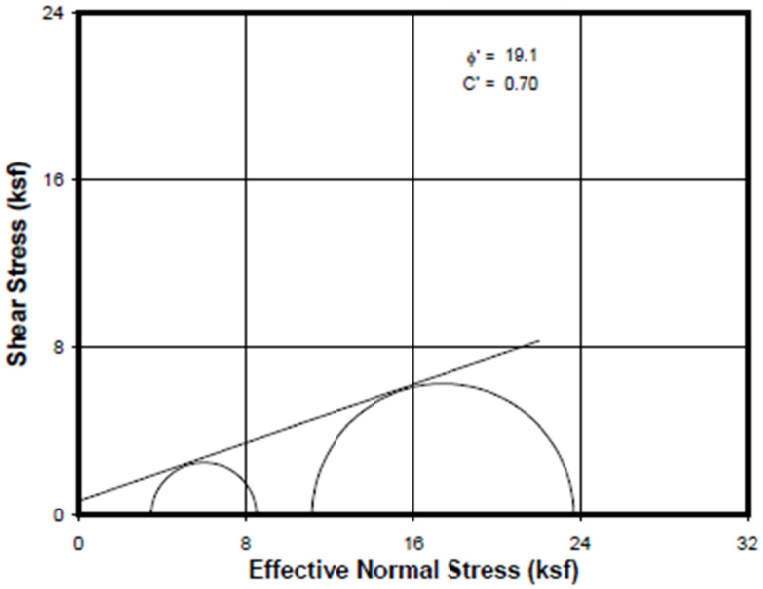

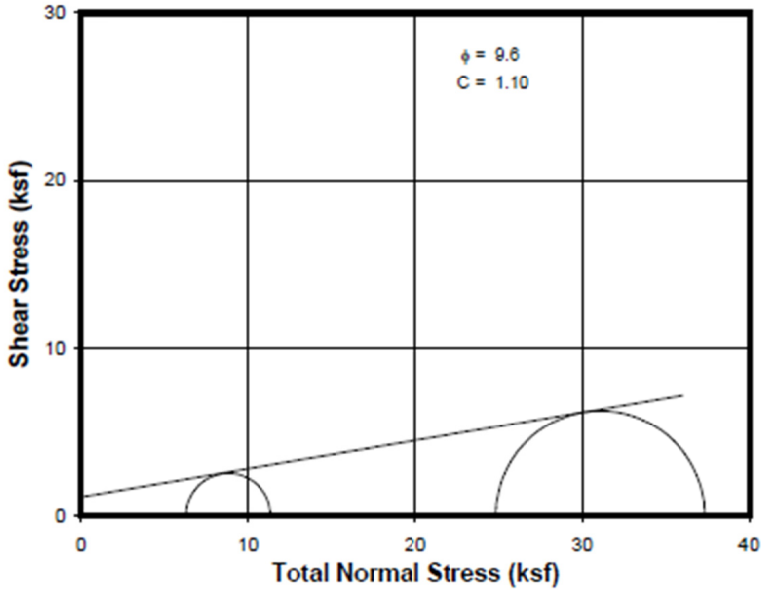

CONSOLIDATED-UNDRAINED TRIAXIAL COMPRESSION TESTS
Isotropically Consolidated
Sample: U24 - Depth: 51.55-52.25 ft
Boring: DBC-16.05
Eagle Mountain Dam

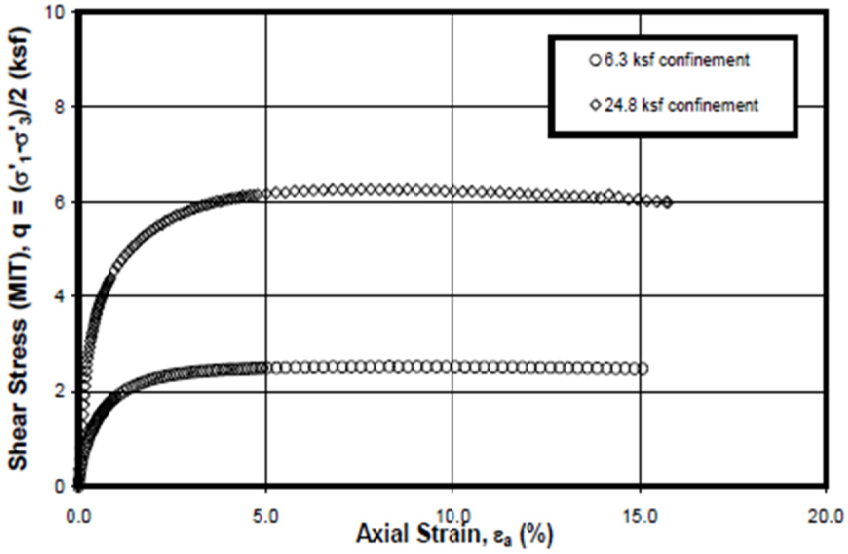

Initial/Consolidated Specimen Conditions

Specimen	Confinig Pressure (ksf)	Depth (ft)	Height (mm)	Volume (cm^3)	Area (cm^2)	Water Content (%)	Density Total (lbf/ft^3)	Density Dry (lbf/ft^3)	Saturation (%)	Void Ratio e
1	6.3	52.25	75.82	75.05	9.90	21.4	125.55	103.45	91.0	0.64
			75.09	72.12	9.60	20.7	129.96	107.65	98.1	0.57
2	24.8	51.55	75.80	75.02	9.90	21.5	126.22	103.87	92.6	0.63
			74.75	67.80	9.07	16.6	134.03	114.93	95.2	0.47

Test Summaries

Specimen		ε_a (%)	q (MIT) (ksf)	p' (MIT) (ksf)	ΔU (ksf)	σ'_1 (ksf)	σ'_3 (ksf)
1	Max. Shear Stress	8.32	2.52	5.98	2.84	8.50	3.45
	Max. Obliquity	6.80	2.52	5.94	2.86	8.46	3.42
2	Max. Shear Stress	7.56	6.26	17.41	13.65	23.68	11.15
	Max. Obliquity	14.18	6.15	16.71	14.25	22.85	10.56

CONSOLIDATED-UNDRAINED TRIAXIAL COMPRESSION TESTS
Isotropically Consolidated
Sample: U24 - Depth: 51.55-52.25 ft
Boring: DBC-16.05
Eagle Mountain Dam

B.2 Soil Consolidated-Undrained Triaxial Strength (TRWD Records)

Station DBC-37.05 – Sector 3

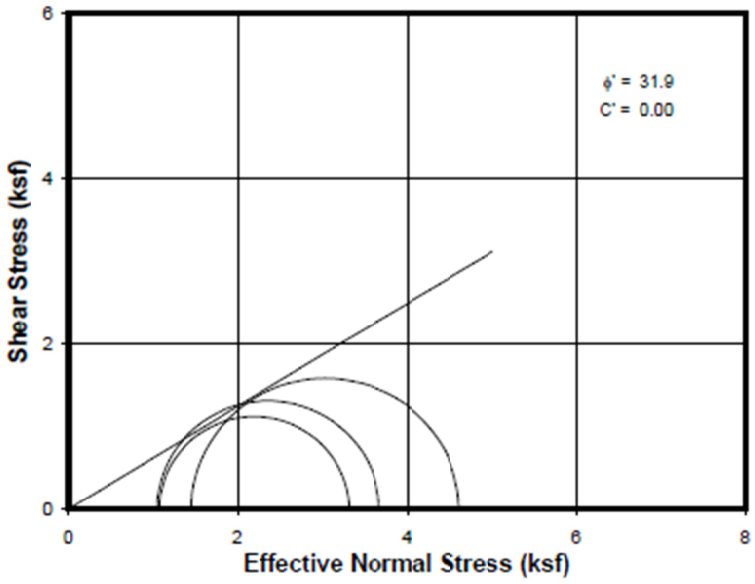

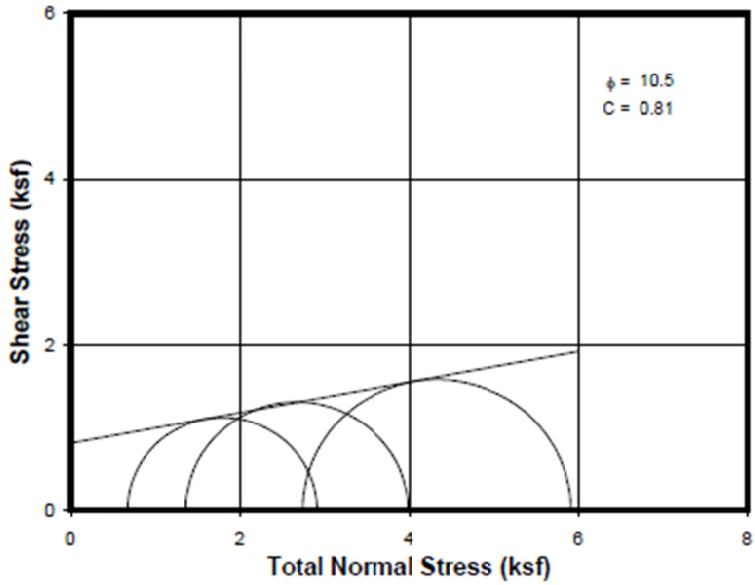

CONSOLIDATED-UNDRAINED TRIAXIAL COMPRESSION TESTS
Isotropically Consolidated
Sample: P2 - Depth: 10.0-12.0 ft
Boring DBC-37.05
Eagle Mountain Dam

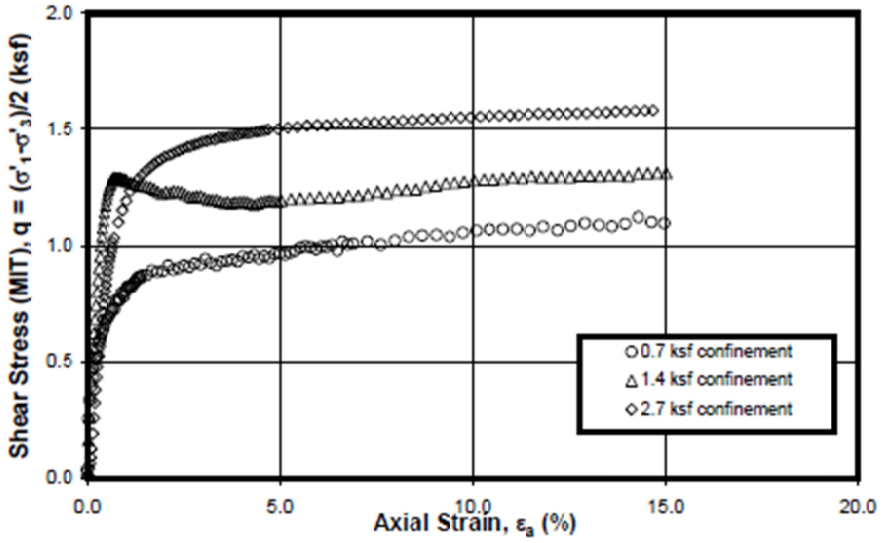

Initial/Consolidated Specimen Conditions

Specimen	Sample	Depth (ft)	Height (mm)	Volume (cm^3)	Area (cm^2)	Water Content (%)	Density Total (lbf/ft^3)	Density Dry (lbf/ft^3)	Saturation (%)	Void Ratio e
1	P2	11.20	76.15	75.4	75.4	22.8	123.4	100.5	91.4	0.675
			76.13	75.3	75.3	25.1	125.9	100.6	100.9	0.672
2	P2	11.60	107.70	221.7	221.7	21.6	121.2	99.7	84.6	0.688
			107.52	219.7	219.7	23.9	124.7	100.6	95.9	0.672
3	P2	12.00	109.31	223.3	223.3	21.1	117.1	96.6	77.0	0.741
			109.12	219.4	219.4	23.5	121.4	98.3	89.2	0.711

Test Summaries

Specimen		ε_a (%)	q (MIT) (ksf)	p' (MIT) (ksf)	ΔU (ksf)	σ'_1 (ksf)	σ'_3 (ksf)
1	Max. Shear Stress	14.29	1.12	2.20	-0.40	3.32	1.08
	Max. Obliquity	1.10	0.82	1.13	0.31	1.95	0.31
2	Max. Shear Stress	14.79	1.31	2.36	0.31	3.67	1.05
	Max. Obliquity	0.60	1.26	1.91	0.70	3.17	0.65
3	Max. Shear Stress	14.67	1.58	3.04	1.30	4.62	1.45
	Max. Obliquity	4.38	1.49	2.71	1.53	4.19	1.22

CONSOLIDATED-UNDRAINED TRIAXIAL COMPRESSION TESTS
Isotropically Consolidated
Sample: P2 - Depth: 10.0-12.0 ft
Boring DBC-37.05
Eagle Mountain Dam

Appendix C

Interactive Three-Dimensional Models of Liquefaction Potential

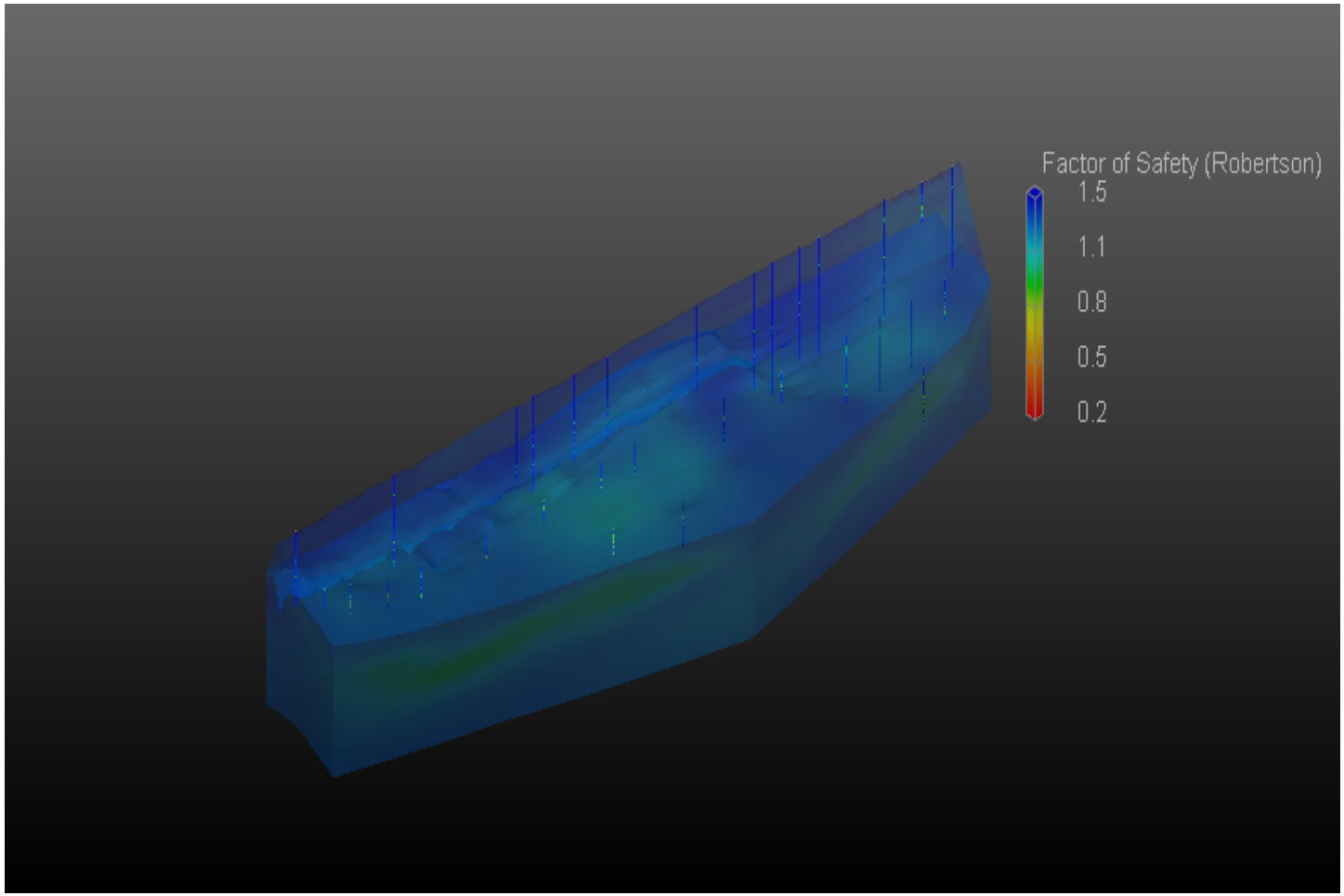

C1. Scenario I: amax - 0.3g; M- 4.5, 5.5; Flood Level- El+649 (Click on the figure to activate the object)

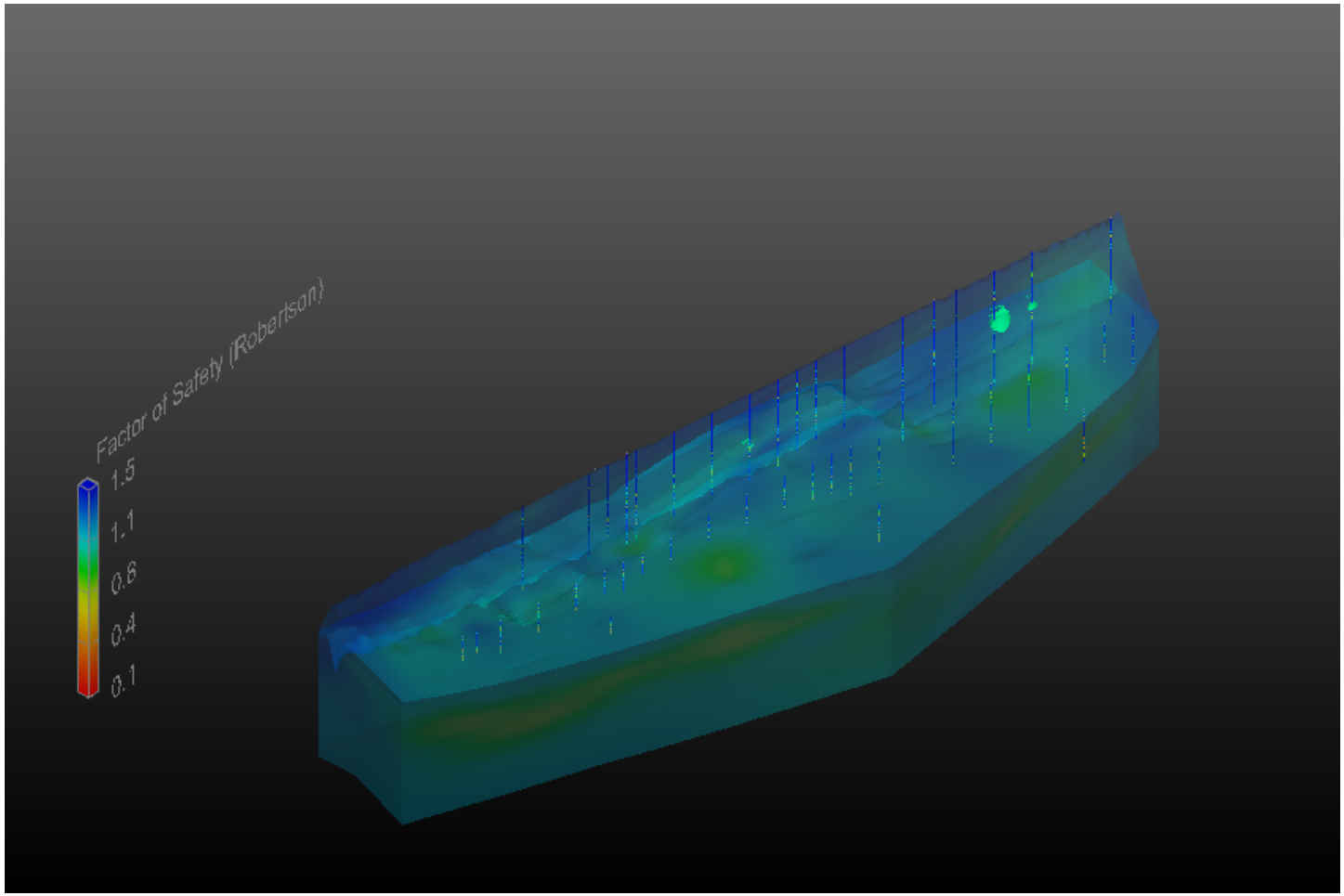

C2. Scenario I: amax - 0.3g; M- 4.5, 5.5; Flood Level- El+649 (Click on the figure to activate the object)

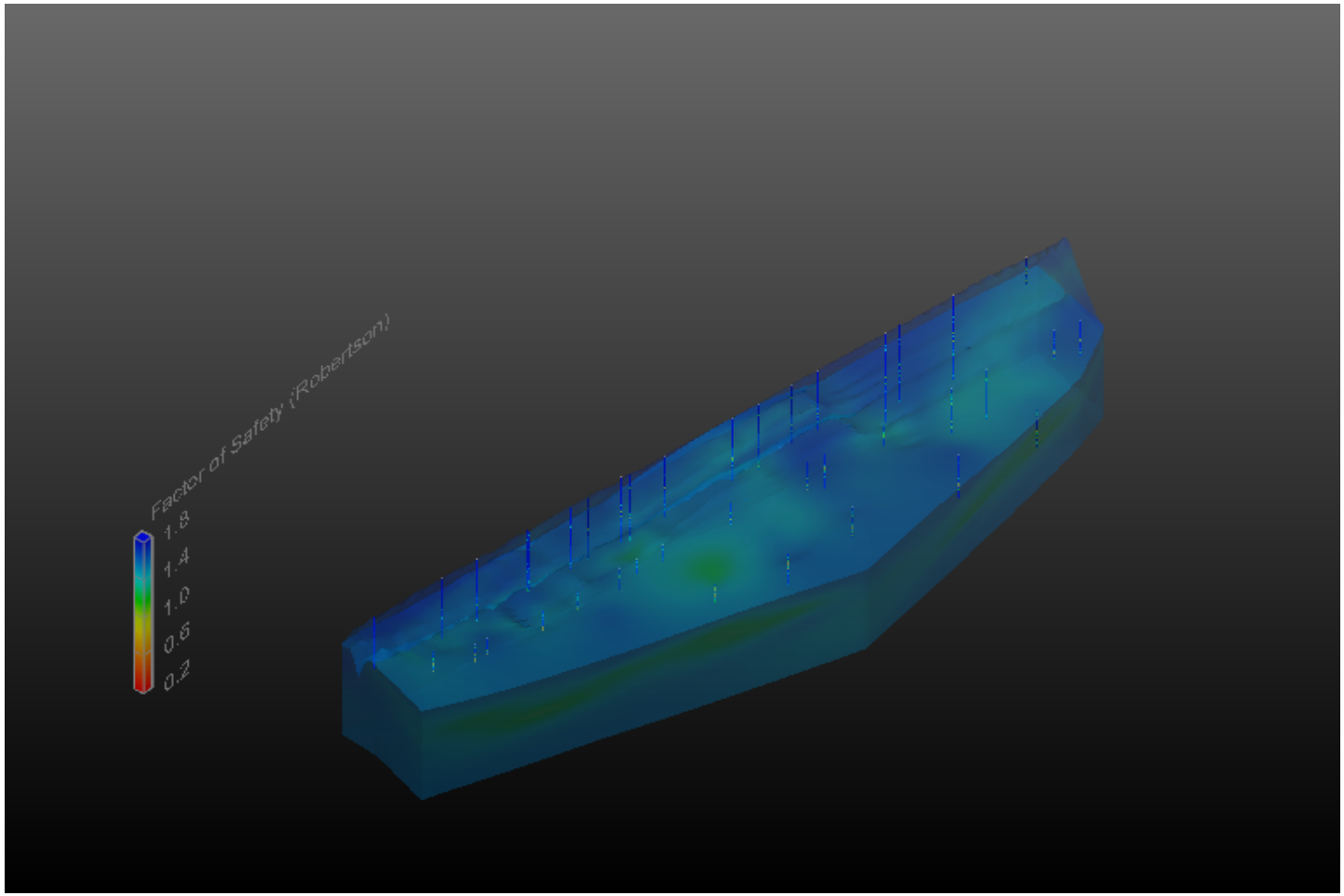

C3. Scenario II: amax - 0.4g; M- 4.5; Flood Level- El+649 (Click on the figure to activate the object)

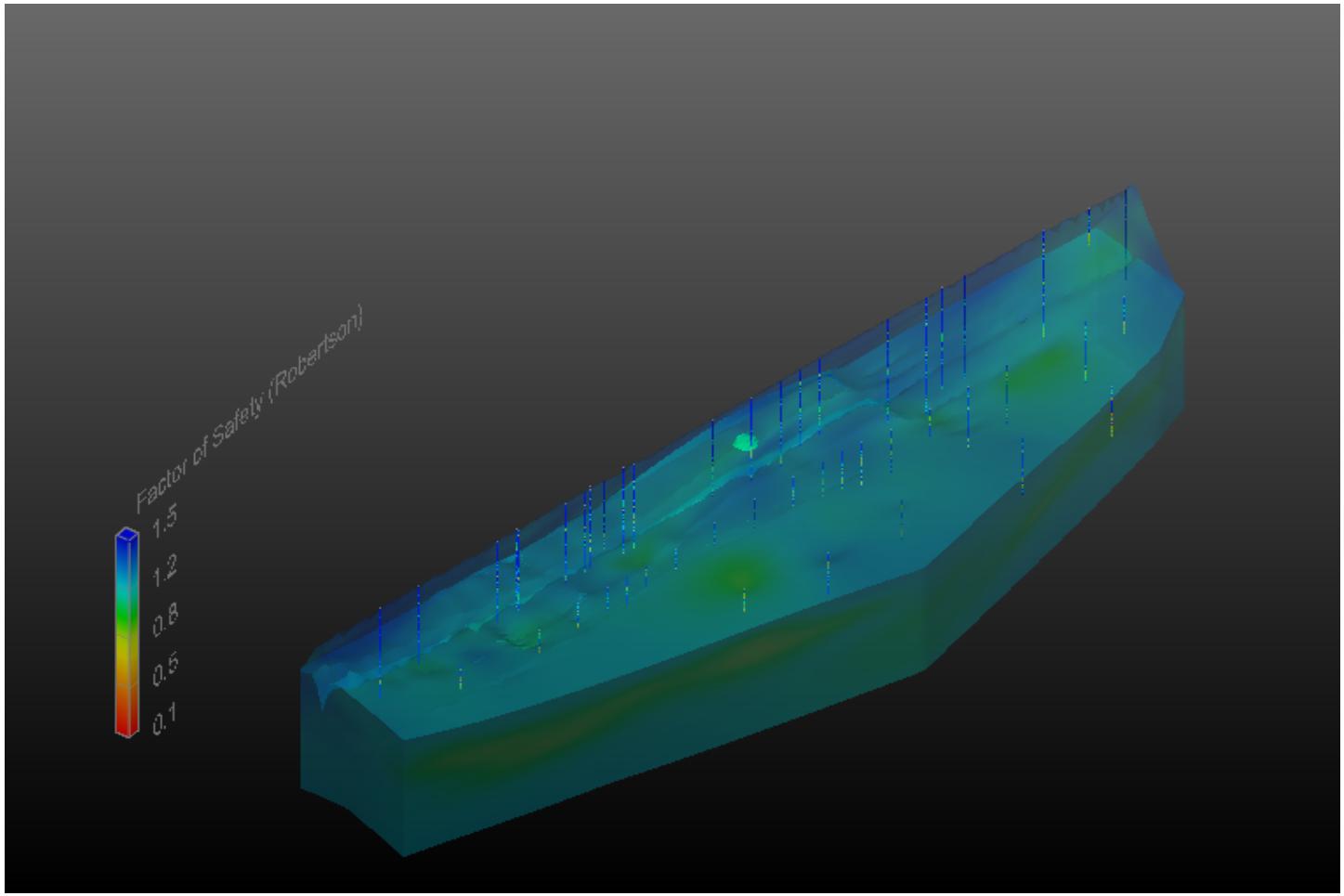

C4. Scenario II: amax - 0.4g; M- 5.5; Flood Level- El+649 (Click on the figure to activate the object)

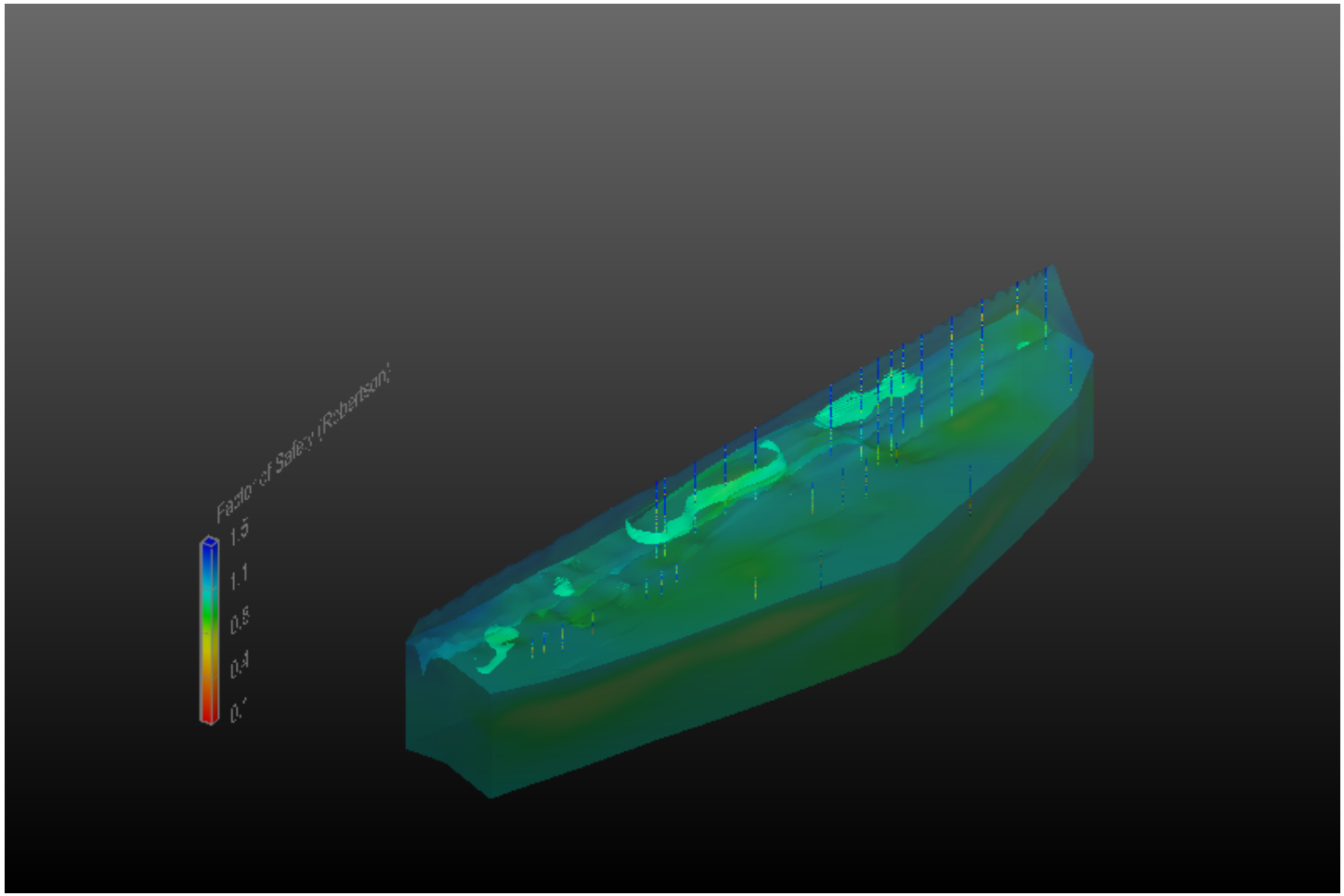

C5. Scenario II: amax - 0.4g; M- 6.5; Flood Level- El+649 (Click on the figure to activate the object)

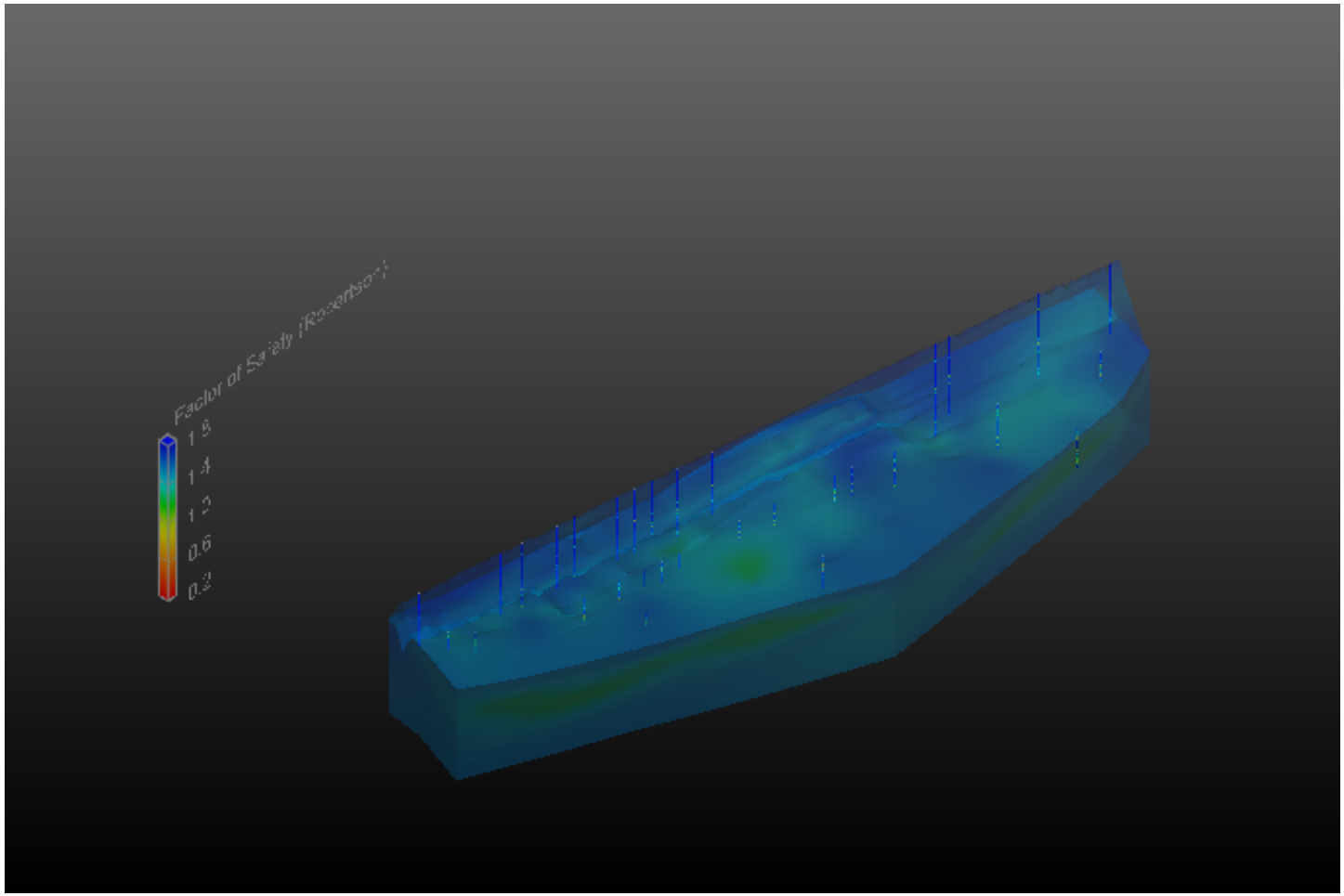

C6. Scenario III: amax - 0.5g; M- 4.5; Flood Level- El+649 (Click on the figure to activate the object)

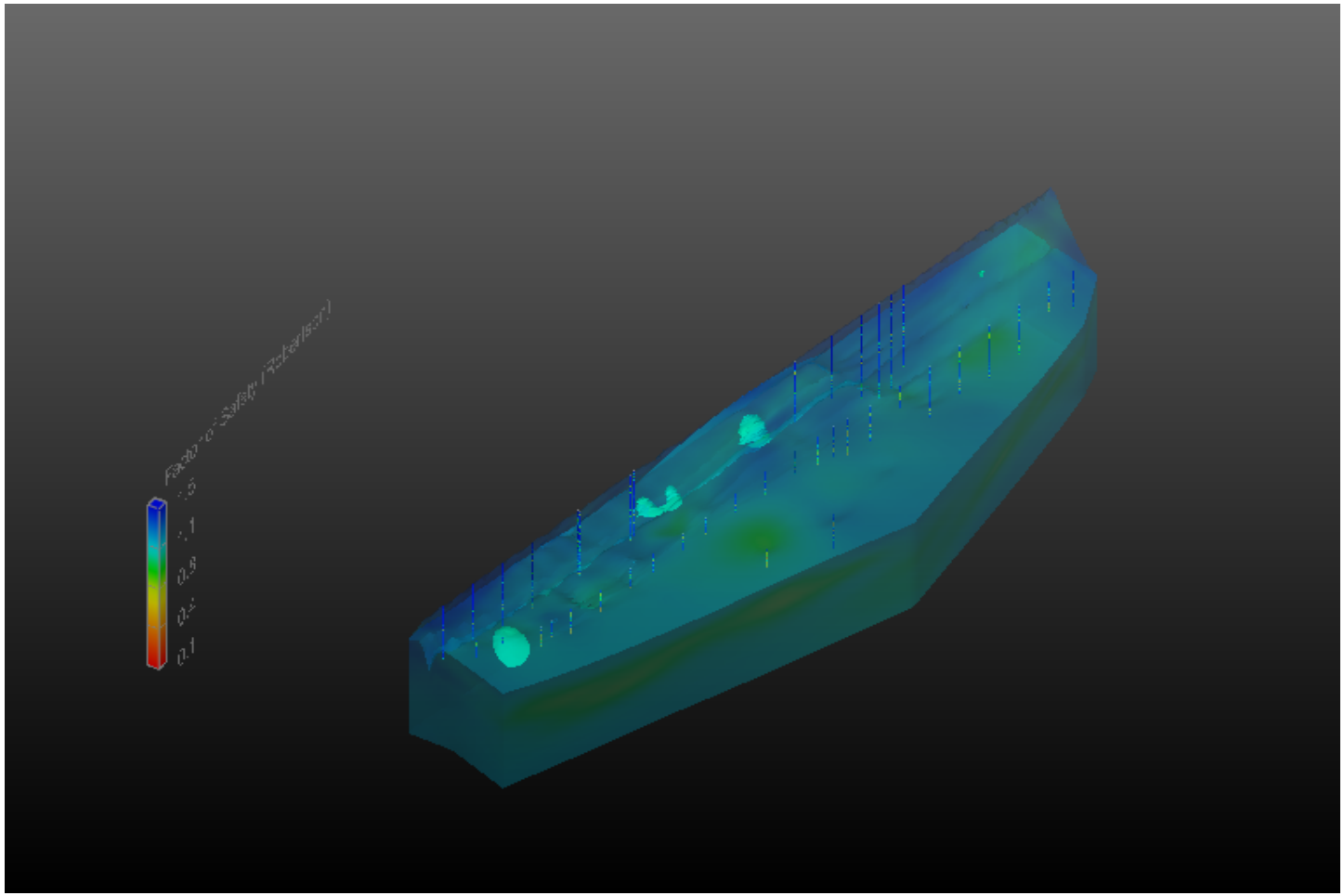

C7. Scenario III: amax - 0.5g; M- 5.5; Flood Level- El+649 (Click on the figure to activate the object)

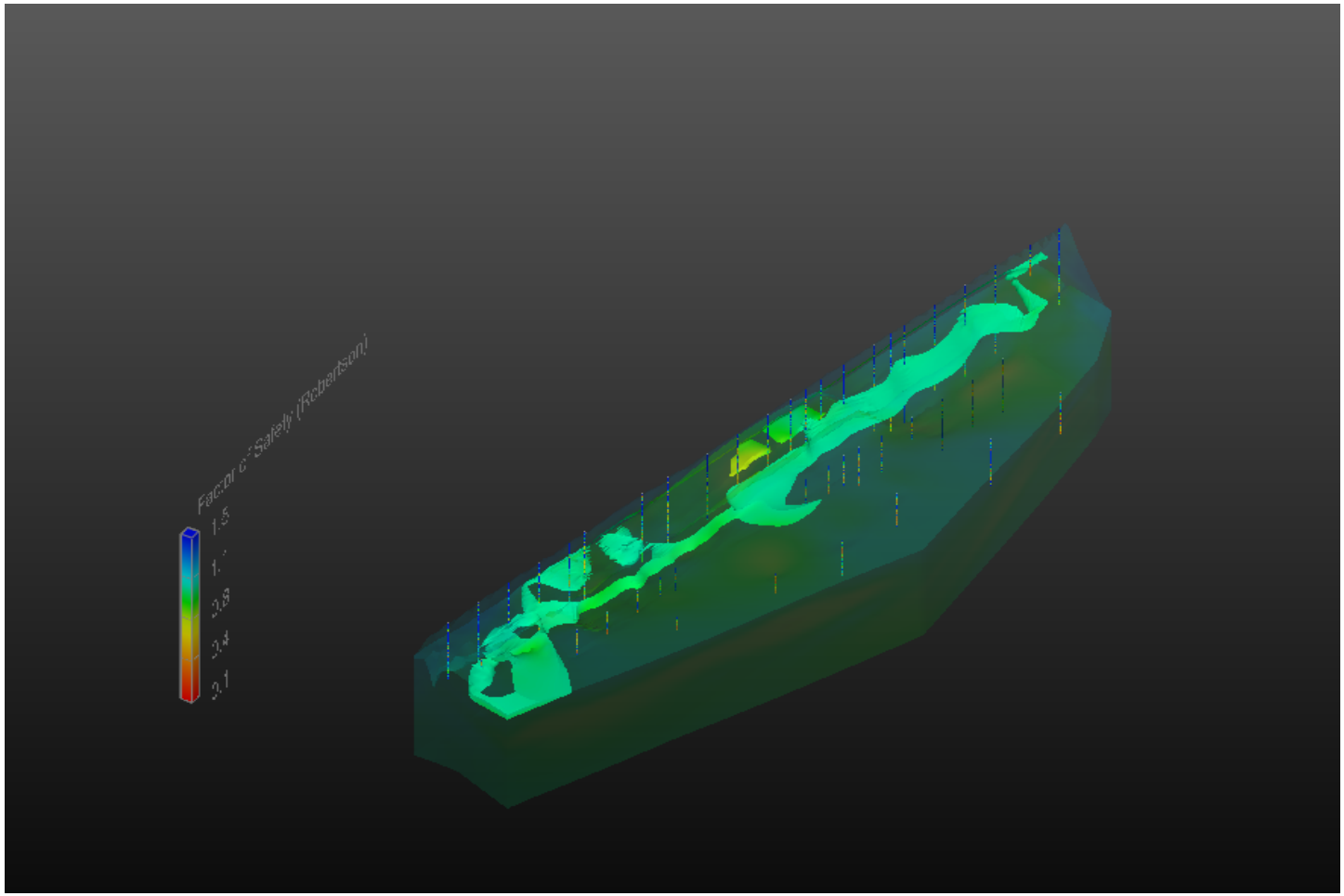

C8. Scenario III: amax - 0.5g; M- 6.5; Flood Level- El+649 (Click on the figure to activate the object)

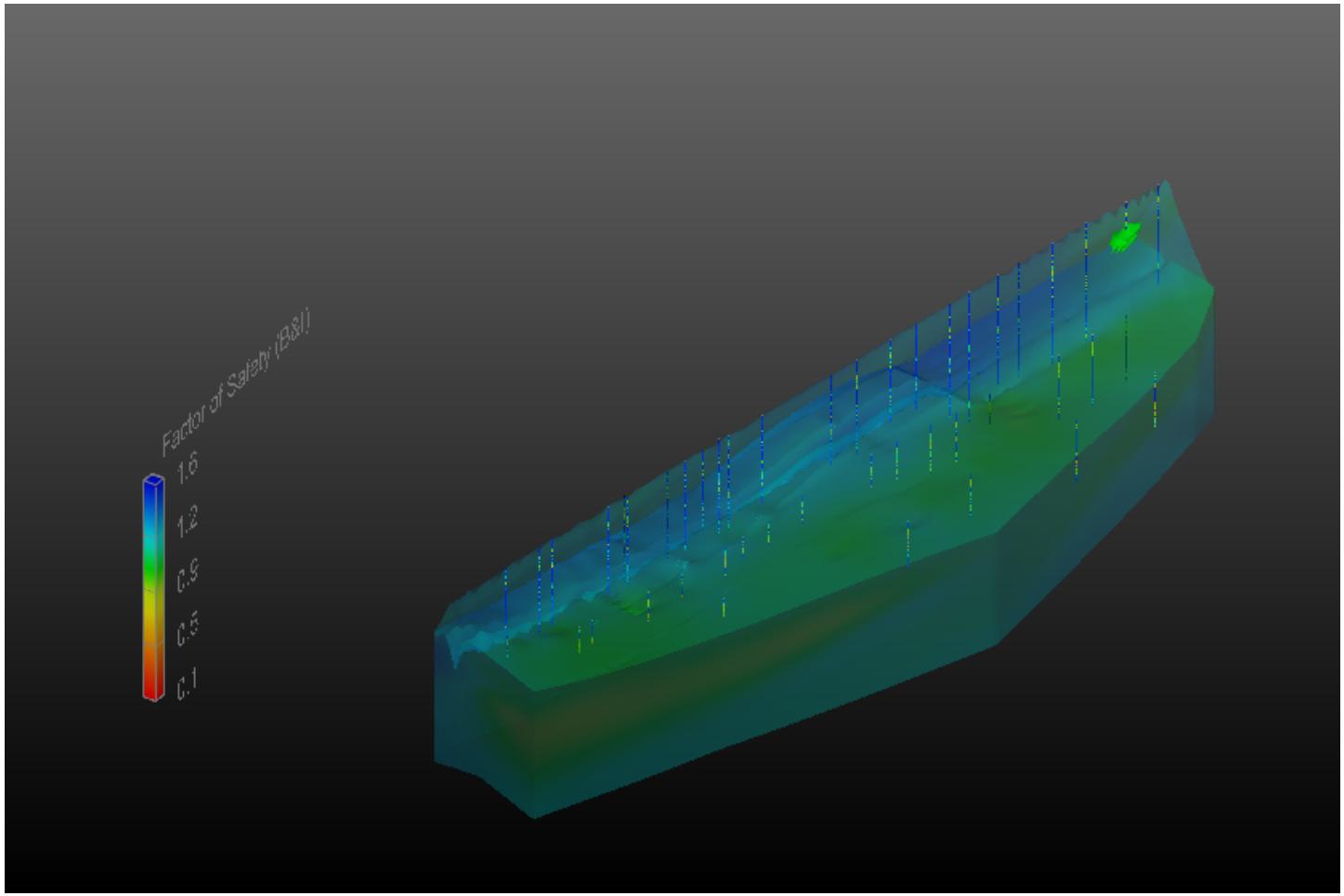

C9. Scenario IV: amax - 0.3g; M- 4.5, Boulanger & Idriss (2014); Flood Level- El+665
(Click on the figure to activate the object)

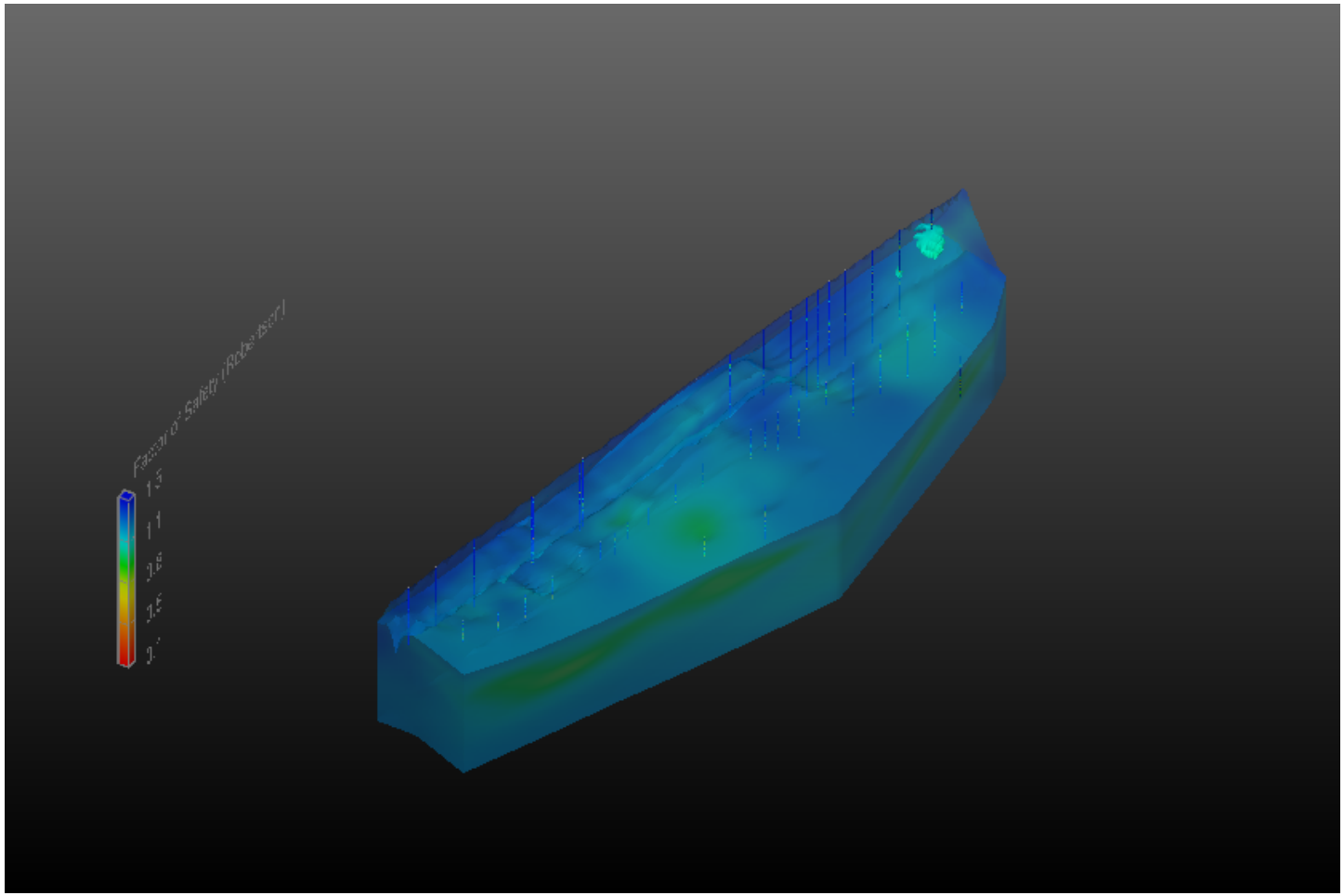

C10. Scenario IV: amax - 0.3g; M- 5.5, Robertson (2009); Flood Level- El+665
(Click on the figure to activate the object)

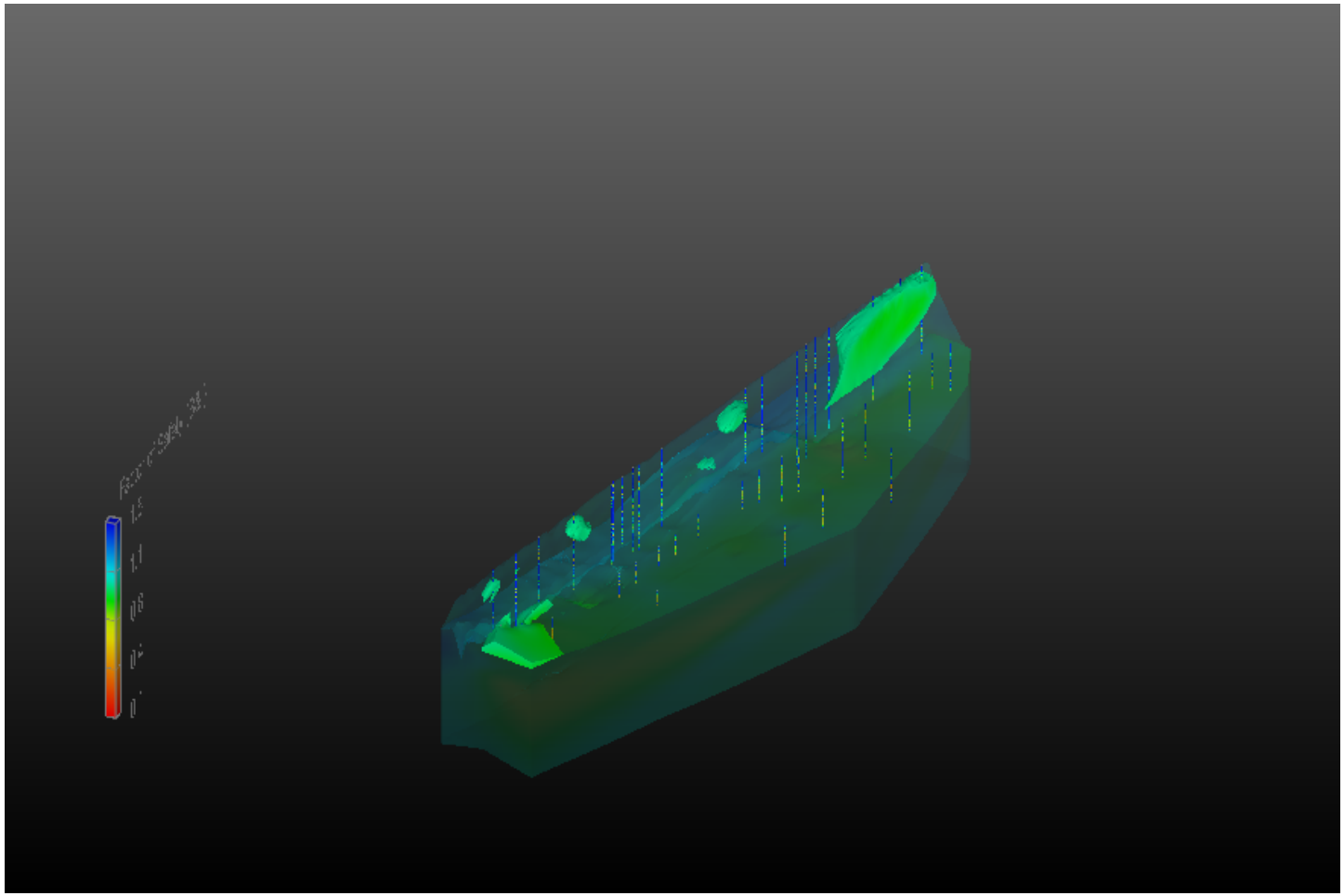

C11. Scenario IV: amax - 0.3g; M- 5.5, Boulanger & Idriss (2014); Flood Level- El+665
(Click on the figure to activate the object)

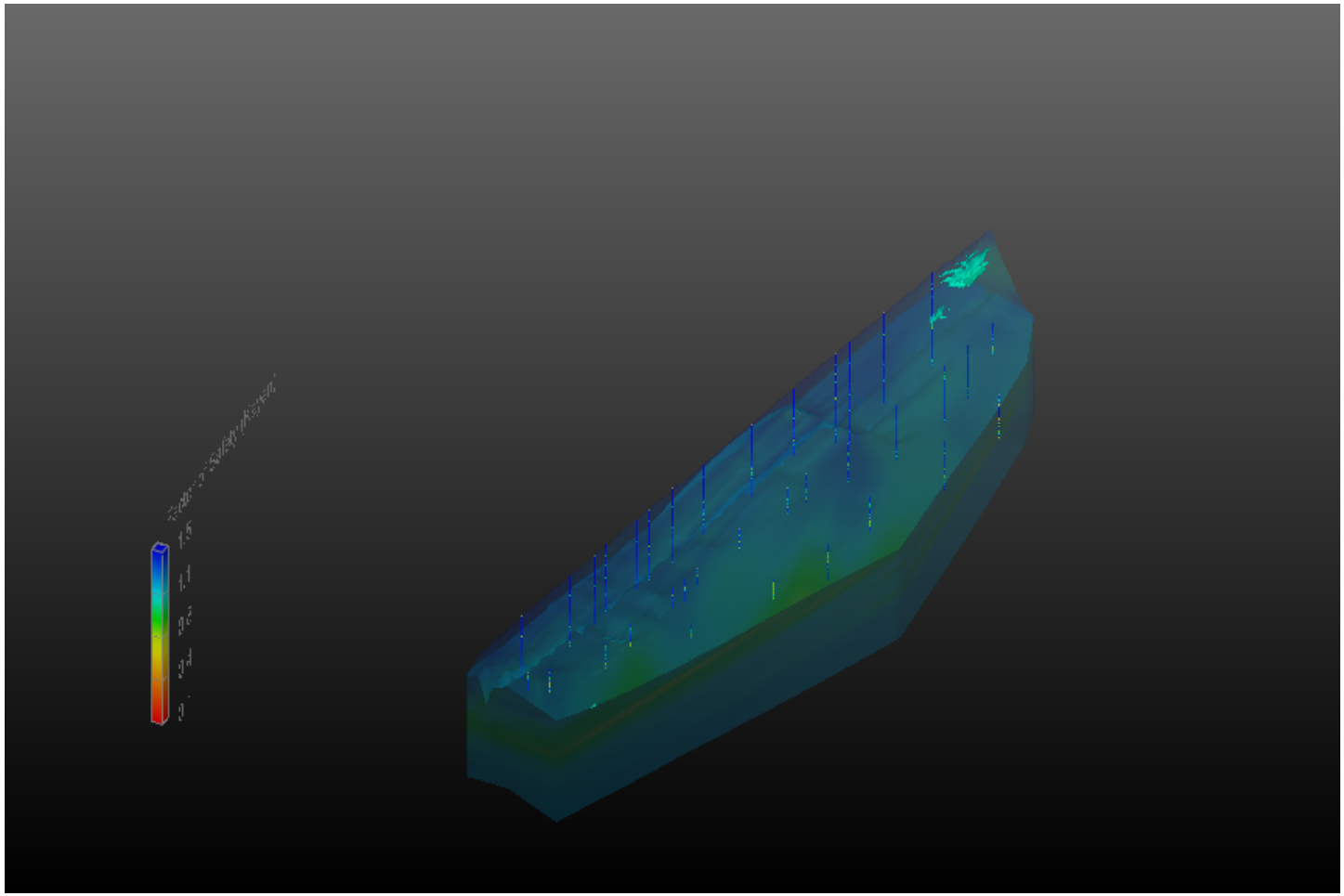

C12. Scenario IV: amax - 0.3g; M- 5.5, Kayen et al. (2013); Flood Level- El+665
(Click on the figure to activate the object)

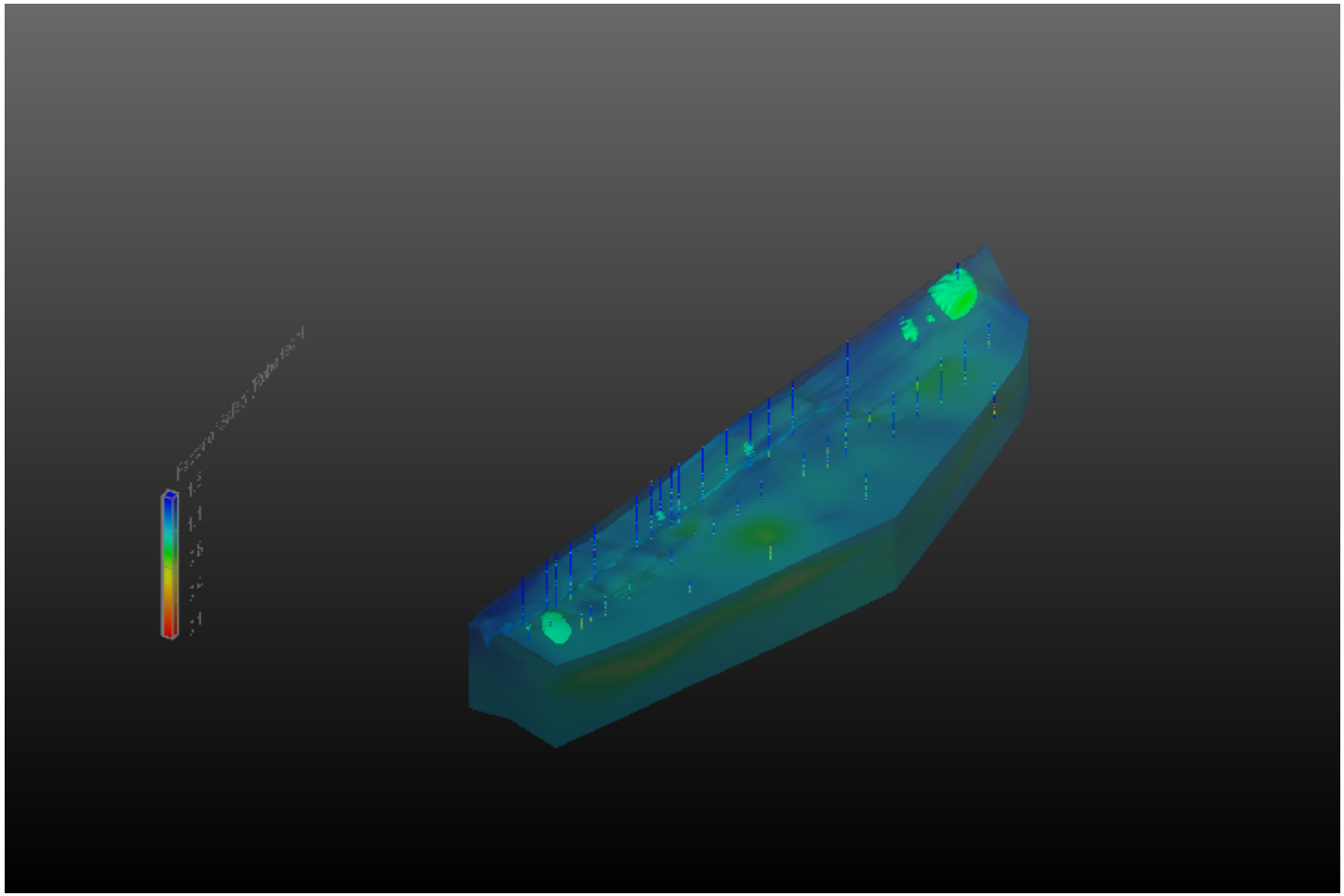

C13. Scenario IV: amax - 0.3g; M- 6.5, Robertson (2009); Flood Level- El+665
(Click on the figure to activate the object)

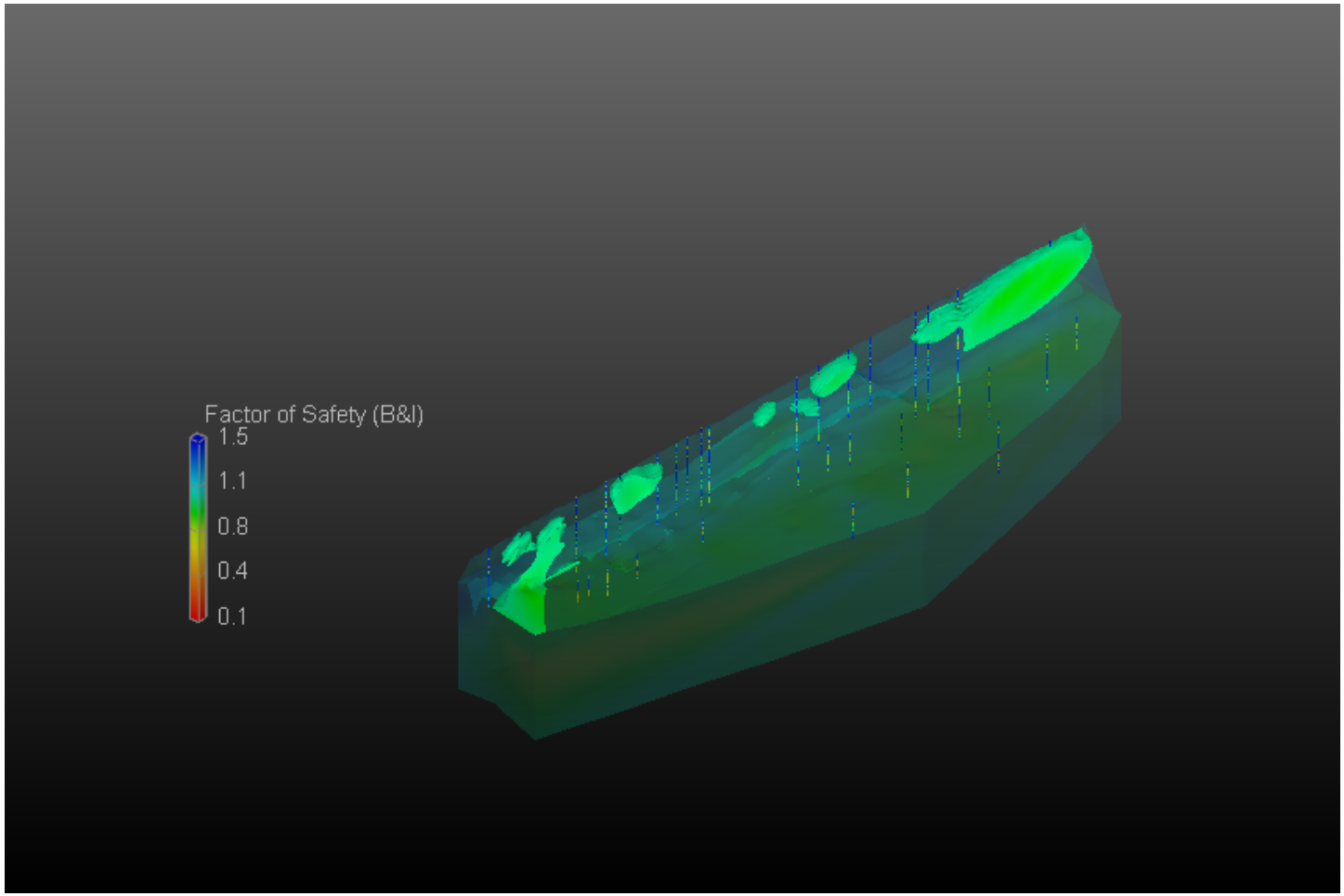

C14. Scenario IV: amax - 0.3g; M- 6.5, Boulanger & Idriss (2014); Flood Level- El+665
(Click on the figure to activate the object)

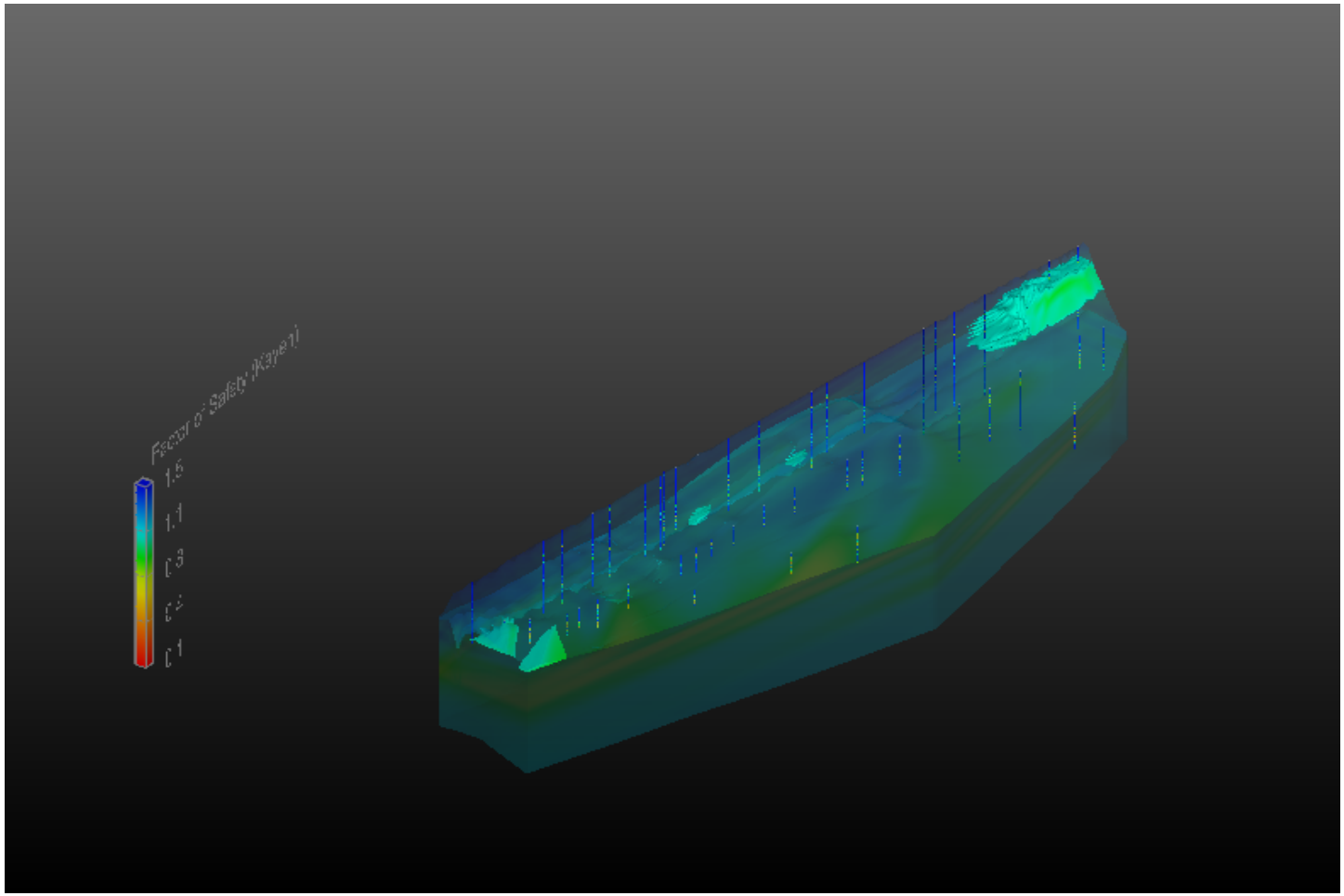

C15. Scenario IV: amax - 0.3g; M- 6.5, Kayen et al. (2013); Flood Level- El+665
(Click on the figure to activate the object)

References

Armstrong, M., 1994. Is Research in Mining Geostats as Dead as a Dodo? In: Dimitrakopoulos, R. (Ed.)., Geostatistics for The Next Century, Kluwer Academic, Dordrecht, pp. 303–312.

Akhlaghi, T. and A. Nikkar (2014). "Evaluation of the pseudostatic analyses of earth dams using Fe simulation and observed earthquake-induced deformations: case studies of Upper San Fernando and Kitayama dams." ScientificWorldJournal 2014: 585462.

Algermissen, S. T., et al. (1982). "Probabilistic estimates of maximum acceleration and velocity in rock in the contiguos United States." U.S. Geological Survey: 99.

Amundaray, J. I. (1994). Modeling Geotechnical Uncertainty by Bootstrap Resampling. West Lafayette. IN, Purdue University. PhD.

ASDSO (2017). "Association of State Dam Safety Officials." from http://www.damsafety.org/news/?p=412f29c8-3fd8-4529-b5c9-8d47364c1f3e.

Atkinson, G. (2015). Ground-Motion Prediction Equation for Small-to-Moderate Events at Short Hypocentral Distances, with Application to Induced-Seismicity Hazards, Bulletin of the Seisimological Society of America. 105: 981-992.

Atkinson, G., and W. Silva (2000). Stochastic modeling of California ground motions, Bull. Seismol. Soc. Am. 90, 255–274

Bair, J. M., et al. (2003). SEISMIC EVALUATION OF THE SEMI-HYDRAULIC FILL SALUDA DAM. USSD Annual Conference, Charleston, SC.

Baker, J. W. (2008). An introduction to Probabilistic Seismic Hazard Analysis (PSHA), US Nuclear Regulatory Commission.

Bheemasetti, T. V. (2014). Spatial Variability Models and Prediction Analysis of Soil Properties using Geostatistics. Deepartment of Civil Engineering. Arlington, TX, The University of Texas at Arlington. PhD.

Bialek, E. Z., et al. (2007). A New Solution for a Hydraulic Fill Dams - The Case of San Pablo Dam V Water Sysem Seismic Conference.

Billington, D., et al. (2005). The History of Large Federal Dams: Planning, Design, and Construction. Denver, Colorado, U.S. Department of Interior, Bureau of Reclamation.

Bommer, J. J. and N. A. Abrahamson (2006). "Why Do Modern Probabilistic Seismic-Hazard Analyses Often Lead to Increased Hazard Estimates?" Bulletin of the Seismological Society of America 96(6): 1967-1977.

Boore, D. M. (2009). Comparing stochastic point-source and finite-source-ground-motion simulations: SMSIM and EXSIM, Bull. Seismol. Soc. Am. 99, 3202–3216.

Boulanger, R. W. and I. M. Idriss (2004). State normalization of penetration resistances and the effect of overburden stress on liquefaction resistance. 11th International Conference on Soil Dynamics and Earthquake Engineering, and 3rd International Conference on Earthquake Geotechnical Engineering, Stallion Press.

Boulanger, R. W. and I. M. Idriss (2014). CPT AND SPT BASED LIQUEFACTION TRIGGERING PROCEDURES. Davis, California, University of California, Davis.

Bray, J., et al. (2004). "Subsurface characterization of ground failure sites in Adapazari." Journal of Geotechnical and Geoenvironmental Engineering, ASCE 130(7): 673-685.

Caballero, S. R., et al. (2016). Three-Dimensional Visualization Model of the Eagle Mountain Dam Using Cone Penetration Test Data Based on Geostatistic. GeoFrontiers, Orlando, Florida.

Campbell, K. W. (1985). Strong ground motions attenuation relations: A ten-year perspective. Earthquake Spectra. 1: 759-804.

Casagrande, A. (1936). "Characteristics of Cohesionless Soils Affecting the Stability of Slopes and Earth Fills." Journal of Boston Society Civil Engineers 23(1): 13-32.

Casagrande, A. (1975). Liquefaction and Cyclic Deformation of Sands - A Critical Review. V Panamerican Conference on Soil Mechanics and Foundation Engineering: 81-133.

Castro, G. (1969). Liquefaction of Sands. Cambridge, Massachusetts, Harvard University.

Cho, S. E. (2012). "Probabilistic Analysis of Seepage that Considers the Spatial Variability of Permeability for an Embankment on Soil Foundation." Engineering Geology 133: 30-39.

Choi, Y. and H. Park (2006). "Integrating GIS and 3D geostatistical methods for geotechnical characterization of soil properties." IAEG.

Clayton, P., et al. (2016). The Geotechnical Aspects of the September 3, 2016 M5.8 Pawnee, Oklahoma Earthquake, NSF - GEER.

Cornell, C. A. (1968). "Engineering seismic risk analysis." Bulletin of the Seismilogical Society of America 58: 1583-1606.

Das, B. M. (1998). Principles of Geotechnical Engineering, PWS.

Davidoff, B., et al. (1986). "A Method to Verify the Presence of a Trend in Studying Spatial Variability of Soil Temperature1." Soil Science Society of America Journal 50(5): 1122-1127.

Davis, J. C. (1986). Geostatistics and Data Analysis in Geology, John Wiley & Sons.

Dismuke, J. (2002). SEISMIC SLOPE STABILTY AND ANALYSIS OF THE UPPER SAN FERNANDO DAM. T. U. o. C. a. Davis, University of California at Davis.

Douglas, J. (2011). Ground-motion prediction equations 1964-2010. BRGM: 444.

Edwards, B. and J. Douglas (2013). "Selecting ground-motion models developed for induced seismicity in geothermal areas." Geophysical Journal International 195(Oxford University Press (OUP)): 1314-1322.

Einstein, H. H. and G. B. Baecher (1982). "Probabilistic and Statistical Methods Engineering Geology, I. Problem Statement and Introduction to Solution. Rock Mechanics and Rock Engineering Vol. 12 pp. 47-61 of Soil Heterogeneity Quatification and Implication on Geotechnical Field Problems." Canadian Geotechnical Engineering 40(1): 1-15.

Ellis, H. L. and M. J. Vessely (2015). Visualization of Geotechnica lData for Hazard Mitigationand Disaster Response. A Synthesis of Highway Practice. N. S. 467. Washington D.C., NATIONAL COOPERATIVE HIGHWAY RESEARCH PROGRAM.

Ellsworth, W. L., et al. (2015). "Increasing seismicity in the U. S. midcontinent: Implications for earthquake hazard." The Leading Edge 34(6): 618-626.

EPRI (1986). Seismic hazard methodology for the central and eastern United States. Palo Alto, California, Electric Power Research Institute, Palo Alto, California.

FEMA (2005). Federal Guideliones for Dam Safety. Earthquake Analyses and Design of Dams, FEMA.

FEMA (2007). Instructional Material Complementig FEMA 451, Design Examples, FEMA.

Fenton, G. A. (1999a). "Estimation for Stochastic Soil Models." ASCE Journal of Geotechnical and Environmental Engineering 125(6): 470-485.

Fernandez, A. (2013). 3D SEISMIC ATTRIBUTE EXPRESSION OF THE ELLENBURGER GROUP KARST-COLLAPSE FEATURES AND THEIR EFFECTS ON THE PRODUCTION OF THE BARNETT SHALE, FORT WORTH BASIN, TEXAS. Norman, Oklahoma, The University of Oklahoma. Master of Science.

Finn, W. D. L. (1981). Liquefaction potential: developments since 1976. Conference on Recent Advances in Geotechnical Earthquake Engineering and Soil Dynamics, St. Louis, MO.

Gringarten, E. and C. V. Deutsch (2001). "Teacher's Aide Variogram Interpretation and Modeling." International Association for Mathematical Geology 33(4).

Guttenberg, B. and C. F. Richter (1944). "Frequency of earthquakes in California." Bulletin of the Seismilogical Society of America 34(4): 185-188.

Hack, R., et al. (2007). "Influence of earthquakes on the stability of slopes." Engineering Geology 91(1): 4-15.

Haining, R. P. (2010). Geography, Spatial Data Analysis and Geostatistics: An Overview. Geographical Analysis. 42: 7-31.

Hammah, R. E. and J. H. Curran (2006). Geostatistics in Geotechnical Engineering: Fad or Empowering? GeoCongress 2006: Geotechnical Engineering in the Information Technology Age. v 2006: 102.

Hasofer, A. M. (1993). Probabilistic Methods in Geotechnical Engineering. Balkema, Rotterdam.

Hazen, A. (1920). "Hydraulic Fill Dams." ASCE Transactions 83: 1713-1745.

Heuvelink, G. B. M., et al. (2016). "Geostatistical prediction and simulation of European soil property maps." Geoderma Regional 7(2): 201-215.

Hohn, M. E. (1999). Geostatistics and Petroleum Geology.

Holchin, J. D. and L. E. Vallejo (1995). The Liquefaction of Sand Lenses Due to Cyclic Loading. Third International Conference on Recent Advances in Geotechnical Earthquake Engineering & Soil Dynamics.

Holland, A., et al. (2013). Probabilistic Seismic Hazard Assessment and Observed Ground Motions for the Arcadia, Oklahoma, Dam Site. Special Publication 2013-01 (SP2013-01). O. G. Survey. Norman, Oklahoma, The University of Oklahoma.

Holmes, J. A. (1921). "Some Investigations and Studies in Hydraulic-Fill Dam Construction." transactions of the American Society of Civil Engineers 84 84: 331.

Hornbach, M. J., et al. (2015). "Causal factors for seismicity near Azle, Texas." Nat Commun 6: 6728.

Hsu, S. (1988). "Review of Practice in Hydraulic Fill Construction, In Hydraulic Fill Structures." ASCE Geotechnical Special Publication No. 21: 884-901.

Huang, J. S., et al. (2010). System Reliability of Slopes by RFEM. S. a. Foundations. 50: 343-353.

Idriss, I. M. and R. W. Boulanger (2008). Soil liquefaction during earthquakes. E. E. R. Institute. Oakland, CA: 261.

Isaaks, E. H. and R. M. Srivastava (1989). An Introduction to Applied Geostatistics. O. U. Press. New York.

Ishihara, K. (1993). "Liquefaction and flow failure during earthquakes. The 33th Rankine Lecture." Geotechnique 43(3): 351-415.

Jamiolkowsky, M. and D. C. F. LoPrsti (1992). Discussion of "Correlation between liquefaction resistance and shear wave velocity" by K. Tokimatsu and A. Uchida. Soils and Foundations. 32: 144-145.

Jones, A. L., et al. (2002). Estimation of Uncertainty in Geotechnical Properties for Performance-Based Earthquake Engineering, University of California, Berkeley

Kayen, R., et al. (2013). "Shear-Wave Velocity–Based Probabilistic and Deterministic Assessment of Seismic Soil Liquefaction Potential." Journal of Geotechnical and Geoenvironmental Engineering 139(3).

Kollgaard, E. B., et al. (1988). Development of dam engineering in the United States / prepared in commemoration of the Sixteenth Congress of the International Commission on Large Dams by the United States Committee on Large Dams. New York, Pergamon Books.

Kramer, S. L. (1996). Geotechnical earthquake engineering. Upper Saddle River, N.J., Prentice Hall.

Laccasse, S. and F. Nadim (1996). ""Uncertainties in Characterizing Soil Properties" in Uncertainty in the Geologic Environment (GSP 58), edited by Shackelford, C.D., Nelson, P.P., and Roth, M.J.S." ASCE, New York: 49-75.

Lawson, J. J. (1985). Expected Earthquake Ground-Motion Parameters at the Arcadia, Oklahoma, Dam Site. Special Publication 85-1. O. G. Observatory. Oklahoma. ISSN 0275-0929.

Li, K. S. and W. White (1987). Probabilistic Characterization of Soil Profiles. Canberra, UNSW, ADFA.

Lowe III, J. (1970). Embankment Dams. New York, McGraw-Hill Book Co.

M., K., et al. (1996). Artificial Neural Networks and Spatial Estimations of Chemobul Fallout. Geoinformatics. 7: 5-11.

Magneron, C., et al. (2009). Noise Reduction by M-Factorial Kriging. IAMG'09: 23-28.

Matheron, G. (1982). Pour une Analyse Krigeante des Donnees Regionalisees. C. d. Geostatistique. Fontainebleau, France, ENSMP.

Mayne, P. (2007). Cone Penetration Testing. Washington, D. C., NATIONAL COOPERATIVE HIGHWAY RESEARCH PROGRAM, Transportation Research Board.

McGuire, R. K. and W. J. Arabasz (1990). An introduction to probabilistic seismic hazard analysis. S.H. Ward, Society of Exploration Geophysics. 1: 333-353.

Mesic, I. (2016). Comparison of Ordinary and Universal Kriging interpolation techniques on a depth variable (a case of linear spatial trend), case study of the Šandrovac Field. The Mining-Geology-Petroleum Engineering Bulletin.

Minasny, B. and A. B. McBratney (2007). "Spatial prediction of soil properties using EBLUP with the Matérn covariance function." Geoderma 140(4): 324-336.

Mitchell, J. K. (2014). Lessons from the Lives of Two Dams. Soils and ROck. 37-2: 99-109.

Mogami, T. and K. Kubo (1953). The behaviour of soil during vibration 3rd International COnference on Soil Mechanics and Foundation Engineering.

Montgomery, S. L., et al. (2005). Mississippian Barnett Shale, Fort Worth Basin, north-central Texas: Gasshale play with multi-trillion cubic foot potential. AAPG Bulletin. 89: 155-175.

Mostyn, G. R. and K. S. Li (1996). Probabilistic Slope Stability Analysis - State-of-Play. Conference on Probabilistic Methods in Geotechnical Engineering, Canberra, Australia.

National Research, C. and C. o. t. S. o. E. Dams (1983). Safety of existing dams : evaluation and improvement. Washington, D.C., National Academy Press.

Olea, R. A. (2009). A Practical Primer on Geostatistics, USGS.

Omran, E.-S. E. (2012). "Improving the Prediction Accuracy of Soil Mapping through Geostatistics." International Journal of Geosciences 03(03): 574-590.

Ortiz, J. M. R. and J. O. Serra, C. (1986). Curso Aplicado de Cimentaciones. Madrid, Colegio de Arquitectos de Madrid.

Pail, C. H. (1922). "Core Studies in the Hydralic-Fill Dam of the Miami COnservancy District." Transactions of the American Society of Civil Engineers 85 85: 1181.

Pando, M. and P. K. Robertson (1995). Evaluation of shear stress reversal due to earthquake loading for sloping ground. 48th Canadian Geotechnical Conference, Vancouver.

Petersen, M. D., et al. (2016). "2016 one-year seismic hazard forecast for the Central and Eastern United States from induced and natural earthquakes."

Pezeshk, S., et al. (2011). "Hybrid Empirical Ground-Motion Prediction Equations for Eastern North America Using NGA Models and Updated Seismological Parameters." Bulletin of the Seismological Society of America 101(4): 1859-1870.

Phoon, K. K. and F. H. Kulhawy (1999). "Characterization of Geotechnical Variability." Canadian Geotechnical Engineering 36: 625-639.

Pollastro, R. M. (2003). Geologic and production characteristics utilized in assessing the Barnett Shale continuous (unconventional) gas accumulation, Barnett-Paleozoic total petroleum system, Fort Worth Basin, Texas. Barnett Shale Symposium, Ellison Miles Geotechnology. Dallas, Texas, Institute at Brookhaven College.

Reiter, L. (1990). "Earthquake Hazard Analysis - Issues and Insights." Columbia University Press, New York: 254.
Robertson, P. K. (2010). "Evaluation of Flow Liquefaction and Liquefied Strength Using the Cone Penetration Test." Journal of Geotechnical and Geoenviromental Engineering 136(6): 842-853.

Robertson, P. K. (2009). "Interpretation of cone penetration tests - a unified approach." Canadian Geotechnical Engineering 46: 1337-1355.

Robertson, P. K. (2009). Performance based earthquake design using the CPT, Gregg Drilling & Testing Inc., Signal Hill, California, USA.

Robertson, P. K. and K. L. Cabal (2012). Guide to Cone Penetration Testing for Geotechnical Engineering, Gregg Drilling & Testing, Inc.

Robertson, P. K. and R. G. Campanella (1983). "SPT–CPT Correlations." Journal of the Geotechnical Engineering Division 108(GT 11): 1449-1459.

Robertson, P. K. and C. Fear (1994). Liquefaction of sand and its evaluation. Earthquake Geotechnical Engineering. Rotterdam, Balkema.

Robertson, P. K. and C. E. Wride (1998). "Evaluating cyclic liquefaction potential using the cone penetration test." Canadian Geotechnical Engineering 35: 442-459.

Rubinstein, J. L. and A. B. Mahani (2015). "Myths and Facts on Wastewater Injection, Hydraulic Fracturing, Enhanced Oil Recovery, and Induced Seismicity." Seismological Research Letters 86(4): 1060-1067.

Schuyler, J. D. (1907). "Recent Practice in Hydraulic-Fill Dam Construction." Transactions of the American Society of Civil Engineers 63 63: 196-252 with discussion 253-177.

Schwartz, D. P. (1988). Geology and seismic hazards: Moving into 1990s. Earthquake Engineering and Soil Dynamics II: Recent Advances in Ground Motion Evaluation. G. S. P. 20. New York, ASCE: 1-42.

Schwartz, D. P. and K. J. Coppersmith (1984). "Fault behavior and characteristic earthquakes: examples from the Wasatch and San Andreas fault zones." Journal of Geophysical Research 89(B7): 5681-5698.

Seed, H. B. (1979). "Soil liquefaction and cyclic mobility evaluation for level ground during earthquakes." Journal of Geotechnical Engineering Division, ASCE 105(gt2): 201-255.

Seed, H. B. and P. Alba (1986). "Use of SPT and CPT tests for evaluating the liquefaction resistance of sands. In Use of in situ tests in geotechnical engineering." aSCE Geotechnical Special Publication No. 6: 281-302.

Seed, H. B. and I. M. Idriss (1971). "Simplified procedure for evaluating soil liquefaction potential." Journal of the Soil Mechanics and Foundation Division, ASCE 97(SM9): 1249-1273.

Seed, H. B., et al. (1973). Analysis of the Slides in the San Fernando Dams During Earthquake of Feb. 9, 1971, University of Berkeley, California.

Seed, H. B., et al. (1985). "Influence of SPT procedures in soil liquefaction resistance evaluations." Journal of Geotechnical Engineering, ASCE 111(12): 1425-1445.

Sharma, H. D. (1991). Embankments Dams. New Delhi, Oxford & IBH Publishing CO. PVT. LTD.

Sherards, J. L. and L. P. Dunnigan (1985). Filters and leakage control in embankments. Seepage and Leakage from Dams and Impoundments. Proc. Symposium Sponsored by Geotechnicall Engineering Division in Conjunction with ASCE National Convention Denver, Colorado.

Silver, N. L. and H. B. Seed (1971). "Volume changes in sands during cyclic loading." Journal of the Soil Mechanics and Foundation Division, ASCE 97(No. SM9): 1171.

Sowers, G. F. and H. L. Sally (1962). Earth and Rockfill Dam Engineering, by George F. Sowers and H.L. Sally. Published Under the Auspices of the Water Resources Development Training Centre, University of Roorkee, India.

START (2003). The Chi-Square: a Large-Sample Goodness of Fit Test. Selected Topics in Assurance Related Technologies. Rome, NY. 10.

Stepp, J. C. (1972). Analysis of completeness in the earthquake sample in the Puget Sound area and its effect on statistical estimates of earthquake hazard. International Conference on Microzonation, Seattle, Washington.

Stokoe, K. H., et al. (1994). Characterization of geotechnical sites by SASW method. Geophysical Characterization of Sites. Rotterdam, R.D. Woods: 15-25.

Sturges, H. A. (1926). "The Choice of a Class Interval." Journal of the American Statistical Association: 65-66.

Tang, T. N. (2015). Seismic Hazard Analysis. New Mexico.

Terzaghi, K. and R. B. Peck (1967). Soil Mechanics in Engineering Practice. New York, John Wiley & Sons, Inc.

Tezcan, S., Bhatia, S. K., & Fiegle, S. (2001). Seismic Stability and Rehabilitation Analysis of a Hydraulic Fill Dam: International Conferences on Recent Advances in Geotechnical Earthquake Engineering and Soil Dynamics.

Tokimatsu, K., et al. (1991). Liquefaction potential evaluation based on Rayleigh wave investigation and its comparison with field behavior. 2nd International Conference on

Recent Advances in Geotechnical Earthquake Engineerin and Soil Dynamics, St Louis, MO.

Torild van, E., et al. (2006). "Seismic hazard fue to small-magnitude, shallow-source induced earthquakes in The Netherlands." Engineering Geology 87: 105-121.

Uddin, Nasim and Baltz, J. F., "Seismic Evaluation and Remediation of Embankment Dam" (2001). International Conferences on Recent Advances in Geotechnical Earthquake Engineering and Soil Dynamics. 3.
http://scholarsmine.mst.edu/icrageesd/04icrageesd/session05/3

URS (2008). Risk Prioritization Tool for Dams - Users Manual, Federal Emergency Management Agency. Release Version.

USACE (1994). Arch Dam Design. D. o. t. A. U. S. A. C. o. Engineers. Washington D.C.

USACE (1995). Gravity Dam Design. E. a. Design. Washington D.C., Department of the Army U.S. Army Corps of Engineers. 20314-1000.

USACE (2016). Earthquake Design and Evaluation for Civil Works Projects. U. A. C. o. E. Department of the Army. Washington D.C., US ARMY CORPS OF ENGINEERS.

USACE (2017). "NID National Map." from http://nid.usace.army.mil/cm_apex/f?p=838:5:0::NO.

USDA Engineering Field Manual. Natural Resource Conservation Service, USDA.

USDI (1983). Dams and Public Safety. A Water Resources Techincal Publication, Bureau of Reclamation, Revised Reprint.

USDI (1987). Design of Small Dams, U.S. Dept. of the Interior, Bureau of Reclamation.

USDI (2010). Internal Erosion. B. o. R. U.S. Dept. of the Interior. Dam Safety Risk Analysis Best Practices.

USDI (2012). Embankment Dams. Embankment Design.

USNRC (1985). Safety of Dams. C. o. S. C. o. D. United States National Research Council, Water Science and Technology Board, Commission on Engineering and Technical Systems. Washington. D.C., National Academy Press.

Valenzuela, L. (2015). Tailings Dams and Hydraulic Fills, The 2015 Casagrande Lecture. Geotechnical Synergy in Buenos Aires 2015, Buenos Aires, Argentina, IOS Press.

Vanmarcke, E. H. (1977). "Probabilistic Modeling of Soil Profiles." Journal of the Geotechnical Engineering Division, ASCE 103(GT11)(Electric Power Research Institute, Palo Alto, CA., Report EL-5507(3)): 1227-1246.

Vanmarcke, E. H. (1977). "Probabilistic modeling of soil profiles." Journal of the Geotechnical Engineering Division, ASCE 103((GT11)): 1227-1246.

Vanmarcke, E. H. (1984). Random Fields: Analysis and Synthesis. Cambridge, M.I.T. Press.

Vennapusa, K. R. P., et al. (2010). "Geostatistical Analysis for Spatially Referenced Roller-integrated Compaction Measurement." Journal of Geotechnical and Geoenvironmental Engineering, ASCE 136(6): 813-822.

Verdugo, R. (1992). Discussion of "Correlation between liquefaction resistance and shear wave velocity" by K. Tokimatsu and A. Uchida. Soils and Foundations. 32: 144-145.

Wan, C. F. (2006). Experimental investigation of piping erosion and suffusion of soils in embankment dams and their foundations, University of New South Wales. PhD.

Weichert, D. (1980). "Estimation of the earhquake recurrence parameteres for unequal observation periods for different magnitudes." Bulletin of the Seismilogical Society of America 70(4): 1337-1347.

Whitman, R. V. (1984). "Organizing and evaluating uncertainty in geotechnical engineering." Uncertainty in the Geologic Environment(Madison: ASCE): 1-28.

Wiltshire, R. (2002). 100 Years of Embankment Dams. Denver, Colorado, U.S. Bureau of Reclamation.

Wilson, S. D. and R. Squier (1969). Earth and Rockfill dams - State of the Art Report. 7th. ICSMFE. Mexico. State of the Art Volume: 138-141, 182-190.

Yamazaki, F. and M. Shinozuka (1988). "Digital generation of non-Gaussian stochastic fields." Journal of Engieering Mechanics 114(7): 1183-1197.

Yang, et al. (1993). General Monte Carlo Procedure.

Yenier, E. and G. M. Atkinson (2014). "Point-source modeling of mdoerate-to-large magnitude earthquakes and associated ground-motion saturation effects." Bulletin of the Seismilogical Society of America 104: 1458-1478.

Yoshimi, Y., et al. (1977). Soil dynamics and its application to foundation engineering. 9th International Conference on Soil Mechanics and Foundation Engineering, Tokyo.

Youd, T. L. (1972). "Compaction of sands by repeated shear strianing." Journal of the Soil Mechanics and Foundation Division, ASCE 98(No. SM7): 709-725.

Youd, T. L. and I. M. Idriss (1998). Workshop on Evaluation of Liquefaction Resistance of Soils. Proceedings of the National Center for Earthquake Engineering Research (NCEER), Salt Lake City, Utah, NCEEER.

Youngs, R. R. and K. J. Coppersmith (1985). "Implications of fault slip rates and earthquakes recurrence models to probabilistic seismic hazards assessments." Bulletin of the Seismilogical Society of America 75(4): 939-964.

Zhu, H., et al. (2013). "Two-dimensional Probabilsitic Infiltration Analysis with a Spatially Varying Permeability FUnction." Computers and Geotechnics 48: 249-259.

Zou, H., et al. (2017). "Mapping probability of liquefaction using geostatistics and first order reliability method based on CPTU measurements." Engineering Geology 218: 197-212.

Biographical Information

Santiago Caballero is a geotechnical engineer originally from Ecuador, South America. He received his Bachelor in Civil Engineering at Pontifical Catholic University of Ecuador (Universidad Católica del Ecuador) in 2010 and upon the completion of his undergraduate studies, he worked in the two important engineering firms in Ecuador for almost 3 years. He received his Master's Degree in Civil Engineering with concentration in Geotechnical Engineering in 2014 at California State University, Fullerton under the supervision of Dr. Binod Tiwari. His work consisted on the effect of rainfall and seepage on slope stability and deformation analyses of partially saturated clays by implementing experimental studies. He was the instructor for the Soil Mechanics Lab and the Engineering Technical Drafting courses at CSU Fullerton.

He just recently obtained his Doctoral Degree in Geotechnical Engineering at The University of Texas at Arlington under the supervision of Dr. Anand Puppala. His doctoral research is presented in this work and it consisted on the development of a seismic resilience framework for hydraulic fill dams located in induced seismic areas, primarily focused in the area of North Texas. The project is part of a comprehensive framework presented to the Tarrant Regional Water District (TRWD) for this type of structures. He had several presentations at regional and international conferences regarding his research work. His motivation and future plans are to get licensed at several states to contribute in the area of induced seismicity and dam and levee safety using novel approaches that serves our geotechnical community. His plans also include the contribution with his country, Ecuador, to develop a more trustworthy and detailed regulation framework for the seismic and geotechnical resilience of structures. His main goal is to establish his own geotechnical consulting firm that aims the development of innovative geotechnical projects in the United States, Ecuador and other countries.